Synthesis, Isolation, and Characterization of Tb-based Large Cage TNT-EMFs and Dimetallic Endohedral Metalloazafullerenes

Tianming Zuo

Dissertation submitted to the faculty of the Virginia Polytechnic Institute and State University in partial fulfillment of the requirements for the degree of

Doctor of Philosophy
In
Department of Chemistry

Dr. Harry C. Dorn, Chair
Dr. Larry T. Taylor
Dr. Alan R. Esker
Dr. Diego Troya
Dr. Randy Heflin

January 09, 2008
Blacksburg, VA

Keywords: Tb-based large cage TNT-EMFs, Dimetallic endohedral metalloazafullerenes, Retention behavior and mechanism

Synthesis, Isolation, and Characterization of Tb-based Large Cage TNT-EMFs and Dimetallic Endohedral Metalloazafullerenes

Tianming Zuo

ABSTRACT

A family of novel large cage Tb-based TNT-EMFs $Tb_3N@C_{2n}$ ($40 \leq n \leq 44$), and a family of novel dimetallic endohedral metalloazafullerenes with the molecular formula of $M_2@C_{79}N$ (M=Y, Tb, and La), were for the first time systematically synthesized, isolated, and structurally characterized. The protocol developed in this thesis provides an effective and systematic method for the synthesis, purification, and characterization of TNT-EMFs and other novel EMFs.

Structural information about this family of Tb-based TNT-EMFs strongly supports the TNT formation mechanism of TNT-EMFs. It also demonstrates for the first time that EMFs do not necessarily choose an IPR-obeying cage even if the IPR cages are available. At room temperature and in a non-polar organic solvent, the fluorescence of the hydrogenated product of $Tb_3N@C_{80}$ was for the first time successfully obtained based on the proposed idea: de-shielding the screen effect of the fullerene cage on the metal ions or clusters inside the fullerene cage.

The structural characterization of $Tb_2@C_{79}N$ using single crystal X-ray diffraction crystallography demonstrated that the fullerene cage of $M_2@C_{79}N$ is an I_h eighty-atom cage. The presence of the N atom in the molecule was further confirmed by mass spectra of the ^{15}N labeled samples. ESR data demonstrated that there is a single-electron bond between the two Y atoms in $Y_2@C_{79}N$ molecules. Theoretical calculations showed for the first time that the single-electron bond is low-lying at the HOMO -2 orbital and thereby resulting in a large HOMO-LUMO gap. It is, in fact, this large HOMO-LUMO gap and the low-lying single-electron orbital (hidden at

HOMO-2) that are jointly responsible for the stability of $M_2@C_{79}N$. The single-electron bonds are the longest metal-metal bond reported so far.

The chromatographic retention behavior of TNT-EMFs was also systematically studied on 5PBB and 5PYE columns. Both experimental and theoretical data demonstrated that the 5PBB column is sensitive to a fullerene's predicted cage size but indifferent to its cage symmetry, while the 5PYE column is more sensitive to the density and distribution of π electrons in a fullerene cage. Therefore, the 5PYE column is more suitable for separating structural isomers. The combination of the 5PBB column in the first stage and the 5PYE column in the second provides a highly effective way for isolating specific isomers.

Acknowledgements

When I was a child in early 1970's, I read a news article in a Chinese newspaper that my parents had actually used to decorate the wall of my house. The headline for the particular article read: "Chairman Mao met Dr. Tsung-Dao Lee." I was very curious and asked my father, "What does the word "Dr." mean?" My father, who was well educated compared with other people in his generation, told me that "Dr." refers to a person who knew everything. Since that time, the concept of "Dr." has been rooted in my mind. Much later in 2005, I read another news article concerning Dr. Tsung-Dao Lee, in which he elucidated his own understanding of the title "Dr." According to him, a person designated in that way was well trained and knowledgeable in his particular research field, but beyond that he was probably a very average person. As a Ph.D candidate in 2005, who at that point had only completed half of the degree process, I had to completely agree with Dr. Lee.

The completion of my doctoral marathon would have been impossible without the advisement and support of many people. First, my deepest gratitude and my earnest respect are given to Professor Harry C. Dorn, the inventor of TNT-EMFs. His expertise and knowledge of this field, as well as many other academic disciplines, continues to amaze me. Moreover, his overall academic manner, serious attitude toward research results, and patience with his students have established Dr. Dorn as the primary role model for my academic career. As a result of his thorough and perceptive training, I am now very confident to face any challenges in my future academic career. Second, I extend my profound gratefulness to my committee members: Professor Larry T. Taylor, Professor Alan R. Esker, Professor Diego Troya, and Professor Randy Heflin. Their rigorous scientific approach and encouragement were always to remind me to work hard, to question results, and to persist despite any setbacks or disappointments. I also owe a

great deal of appreciation to Professor Harry W. Gibson, Professor Richard D. Gandour, Professor T. Daniel Crawford, Professor John R. Morris, Professor Patricia G. Amateis, Professor James M. Tanko, Professor Brian Tissue, and Professor Mark R. Anderson. Their academic nurturing and support were always available to me and have given me much needed confidence along the way. To the same extent, the advisors of my master's program, Professor Thomas T. Huang and Professor William L. Stone, are also gratefully acknowledged herein. Their kindness and support laid a solid foundation for my pursuit of this doctoral program.

My Ph.D study has been enhanced by support from Professor Alan L. Balch and Professor Marilyn M. Olmstead. Their expertise in single crystal X-ray diffraction crystallography has made this research amazingly productive. The timely analytical support from Mr. Kim Harich, Ms. Anne Campbell, Dr. Carla Slebodnick, Dr. Mehdi Ashraf-Khorassani, and Dr. Keith Ray has also been invaluable. I would like to acknowledge the following individuals for their help: Ms. Melody Windsor, Jessica Weidgin Lu, Ms. Tammy Jo Hiner, Ms. Laurie Good, Ms. Claudia Brodkin, Mr. Frank Cromer, Mr. Tom Glass, Mr. Rob Russell, Mr. Thomas E. Bell, Mr. Geno Iannaccone, Ms. Jan McGinty, Mr.Tom Wertalik, and Ms. Angie Miller. Their assistance and support made my life at Virginia Tech much easier.

My great appreciation also goes to my colleagues in Dr. Dorn's vigorous and dynamic research group: Liaosa Xu, Wujun Fu, Ting Cai, Jianfei Zhang, Dr. Chunying Shu, and Mr. Jonathon Reid. Academic interactions with them often helped me to make surprising progress in my research.

I would be remiss if I did not acknowledge the love and support of my family, from whom I have received the greatest encouragement for this accomplishment. Support from my siblings and in-laws in China has enabled me to concentrate on realizing my dream of a PhD,

especially since they have been largely responsible for taking care of our aging mother, disabled by a stroke more than fifteen years ago. My mother always encouraged me to remember that "Where there is a will, there is a way," and that has sustained me during the last four years of this academic journey. In this country, my wonderful son and wife provided a warm and comfortable harbor for me. Their high expectations and belief in me always gave me confidence and renewed energy for my research. It is only due to their consideration and support that this "work maniac" was able to spent days and nights in the lab for years in order to explore the nano-world in such a productive and meaningful way. In acknowledgement of their constant love, support, and help, I dedicate this dissertation to my dear son, Howard, and to my amazing wife, Juhong.

TABLE OF CONTENT

List of Figures

List of Tables

Chapter 1 — Literature Review

1.1. Introduction

The concept of a fullerene was introduced by Kroto, Heath, O'Brien, Curl and Smalley (the Smalley team) in a paper published in *Nature* in 1985.[1] In order to explain the prominent intensity of peak *M/Z*=720 of a C_{60} stable carbon cluster in mass spectra (see Figure 1-2), they suggested a truncated icosahedron structure for C_{60} (see Figure 1-1). This structure is a polygon with 60 vertices, 32 faces and 90 edges. In this truncated icosahedron of C_{60}, each of the 60 carbon atoms was placed at each of the 60 vertices, hence, each edge is a bond between two carbon atoms. Of the 32 faces, 12 faces must be pentagons and the remainders are hexagons.

In an attempt to model a stable structure for the C_{60} cluster, Kroto et al. were inspired by the work of American architect R. Buckminster Fuller, whose geodesic dome is constructed on the same stable structural principles (Figure 1-1a). They built a paper model of a truncated icosahedron representing the C_{60} cluster (I_h),[2] and named it the Buckminsterfullerene (or, more simply, the Buckyball). Fullerene is the comprehensive name for the family of carbon clusters that includes $C_{60,}$ $C_{70,}$ and $C_{84,}$ etc. The suffix "-ene" indicates that there are some carbon-carbon double bonds in the stable C_{60} cluster that satisfy the bonding requirement for sp^2 hybrid carbon atoms. Actually, the C_{60} (I_h) structure is easier to visualize if one replaces each vertex on the seams of a soccer-ball with a carbon atom (Figure 1-1b).

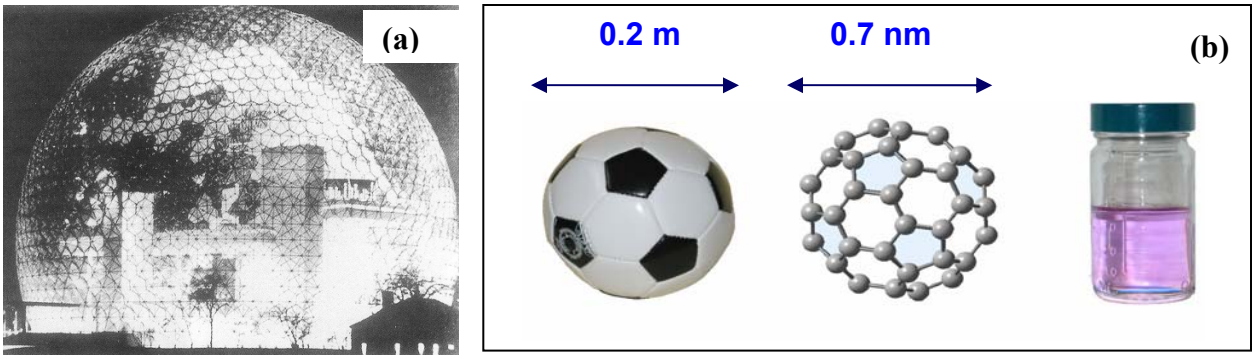

Figure 1-1. (a) Geodesic dome designed by Buckminster Fuller. (b) Comparison of soccer ball and C_{60} (I_h). Both the soccer ball and C_{60} (I_h) are composed of 12 pentagons and 20 hexagons. Each pentagon is surrounded by 5 hexagons. Thus, each of the 12 pentagons is all isolated. The diameter of C_{60} (I_h) is about 0.71 nm. Therefore, it is a typical nano-particle. C_{60} (I_h) in toluene is purple in color (reprinted from Ref. 2).

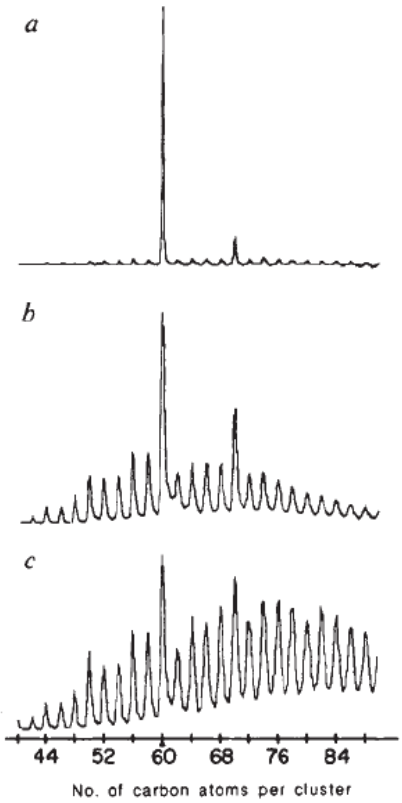

Figure 1-2. Mass spectra of carbon clusters obtained at different experimental conditions (reprinted from Ref. 1). (a) In the condition of maximizing the cluster thermalization and cluster-cluster reactions. (b) About 760 Torr helium present over the graphite target vaporized. (c) Less than 10 Torr helium present over the graphite target vaporized.

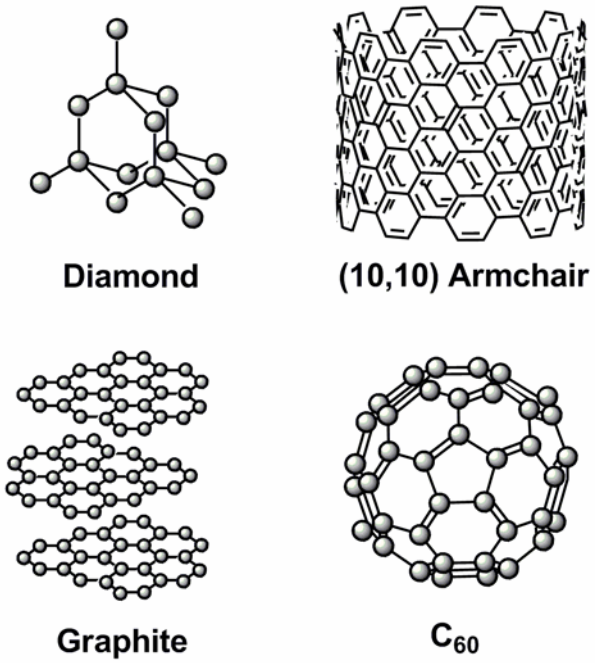

Figure 1-3. The structures of carbon allotropes: diamond, graphite, C_{60} (I_h) fullerene (diameter is about 710 nm), and (10,10) single-wall carbon nanotube (SWNT) (diameter is about 1360 nm)[3]. Both diamond (sp^3 hybrid) and graphite (sp^2 hybrid) have boundaries, while the third form of carbon, a fullerene (sp^2 hybrid), has no boundary due to the satisfaction of all the bond formation requirements in its structure. SWNT is a special form of a fullerene.

Prior to the C_{60} (I_h) –Buckminsterfullerene concept, two allotropic forms of carbon—diamond and graphite—were well known to chemists (see Figure 1-3). However, the soccer-ball form of C_{60} had, in fact, already been conjectured by E. Osawa in 1970.[4] It was later studied theoretically by Bochvar and Gal'pen using Hückel theory in 1973.[4] Their work showed that the soccer ball configuration of C_{60} could be stable. Although intriguing, neither report really caught the attention of the scientific world, perhaps because they were published in Japanese and were not supported by sufficient experimental data. In addition to the theoretical studies noted above, other researchers investigated carbon clusters at high temperatures, particularly with respect to a new allotropic form of carbon. Specifically, they suggested that the third carbon allotrope had the structure of a carbyne (see references of Ref. 5).[5]

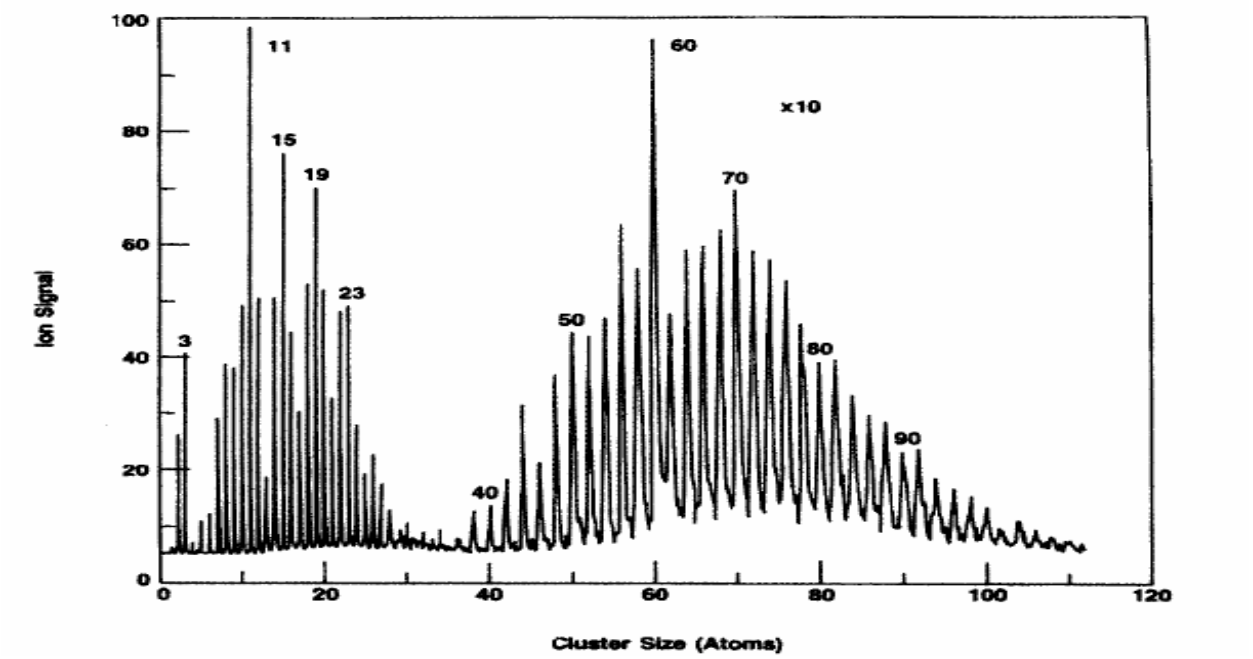

Figure 1-4. Time-of-flight (TOF) mass spectrum of carbon clusters (C_n) produced by laser ablation of graphite (reprinted from Ref.5). There are three areas in this mass spectrum: the fullerene zone (n≥ 36), where all peaks correspond to the even number of carbon atoms; the forbidden zone (n is about 28~35); and the small cluster zone (n≤28, n can be even or odd numbers).

In 1984, Rohlfing, Cox, and Kaldor in an Exxon research group reported the prominent intensity of peaks C_{60} and C_{70} clusters in the TOF mass spectrum of carbon clusters ablated by lasers[5] (See Figure 1-4). This beautiful mass spectrum clearly demonstrated a bimodal cluster distribution. As the carbon cluster sizes exceeded C_{36}, the carbon clusters were only composed of an even number of carbon atoms. Rohlfing et al. interpreted this phenomenon by proposing a carbyne structure with alternating long (single) and short (triple) carbon-carbon bonds for the clusters. Their argument was that since the basic unit of the carbyne is C_2 (-C≡C- unit), the high temperature crystalline form of carbon (namely, the carbyne form) has an even number of carbon atoms. In the same publication, they also documented the mass spectra of metal-carbon complex clusters.[5, 6] These experimental conditions were similar to those later adopted by the Smalley team to demonstrate the existence of metallofullerenes. After Smalley et al. published their Buckminsterfullerene research in 1985,[1] the Exxon group carried out a systematic study of

carbon clusters under variable experimental conditions in 1988.[7] In this publication, another famous mass spectrum of a "magic number" of carbon clusters was reported (see Figure 1-16) (This mass spectrum was later used by Kroto as additional evidence to support their Buckminsterfullerene proposal).[2] Based on their work with carbynes, however, they concluded that: *"Our observations and explanations proposed neither confirm nor refute the claim that C_{60} may possess the structure of a truncated icosahedron. Positive structural determination most likely must await further characterization studies of chemically isolated C_{60}."* [7]

In 1990, another exciting chapter in fullerene history was written. Specifically, Krätschmer, Lamb, Fostiropoulos and Huffman invented a method for synthesizing and purifying macroscopic quantities of fullerenes[8]— the so called Krätschmer-Huffman arc-discharge method. They isolated a macroscopic amount of a pure C_{60}, which was the dominant component in the extractable mixture using an organic solvent, and obtained an infrared spectrum of a solid C_{60} sample. The resulting four-band IR vibrational absorption spectrum is perfectly consistent with the theoretical prediction of the IR vibrational pattern of I_h-C_{60} based on its icosahedral symmetry. This means that Smalley et al.'s research on the Buckminsterfullerene[1] was at last confirmed by experimental evidence.

Due to the availability of macroscopic amounts of fullerenes, other characterization using Raman, ^{13}C NMR and photoelectron spectra were soon reported. These results were all consistent with the proposed fullerene structure. Just a couple of months after Krätschmer-Huffman's innovation, the first single crystal X-ray diffraction structural determination of C_{60}'s derivative, $C_{60}(OsO_4)$(4-tert-butylpyridine)$_2$, was reported (see Figure 1-5).[9] The structure of C_{60} was exactly the same as the one originally proposed by the Smalley team. The Smalley team not only discovered the important relationships between the structure of C_{60} (I_h) and its outstanding

stability, they also delivered compelling theoretical and experimental evidence to support their Buckminsterfullerene proposal. Indeed, their work has withstood all scientific challenges, and has inspired expanded research in the field of fullerenes by scientists throughout the world. For these reasons, they were awarded the Nobel Prize in Chemistry in 1996.

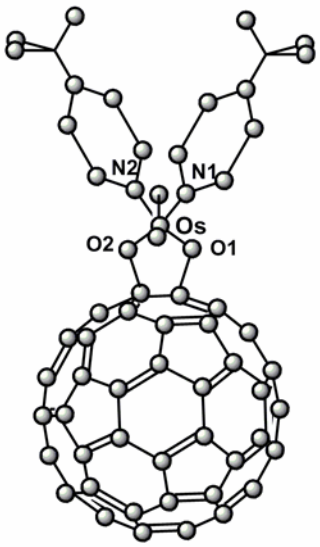

Figure 1-5. First single crystal X-ray diffraction structure of a C_{60} derivative. It confirmed that C_{60} was constructed by 20 hexagons and 12 pentagons without a fused pentagon pair, as was originally proposed.

1.2. Fullerene Cage

1.2.1 Application of Euler's Theorem to Fullerene Cages

Fullerenes (C_n) are defined as polyhedral closed cages made up entirely of *n* three-coordinate carbon atoms and having 12 pentagonal and (*n*/2-10) hexagonal faces, $n \geq 20$.[10] Each carbon atom in a fullerene C_n is placed at the vertex of the polyhedron and connected to three other carbon atoms on the surface of the closed carbon cage. The carbon cage is a convex polyhedron with only pentagons and hexagons, which means that a fullerene cage assumes the shape of an Archimedean solid.[11] Since fullerenes are polyhedrons, they obey Euler's theorem, which states that in a spherical polyhedron the sum of vertices (*v*) and faces (*f*) equals the edges (*e*) plus two,[12] i.e.

$$f + v = e + 2 \text{ ----------(Equation 1.1)}$$

For a fullerene C_n, by definition, we know that:

$$v=n \text{ ---------- (Equation 1.2)}$$

Since each carbon atom bonds to three other carbons, we have the following equation

$$3n=2e \text{ ---------- (Equation 1.3)}$$

Equation 1.3 means that *3n* counts each edge two times.

By incorporating Equations 1.2 and 1.3 into Equation 1.1 and eliminating *v* and *e*, we now have the following relationship:

$$f = n/2 + 2 \text{ ---------- (Equation 1.4)}$$

Equation 1.4 tells us that for any fullerene C_n, *n* must be an even number since *f* is an integer. Therefore, with respect to Figure 1-4, we know why only an even number of carbon peaks in the fullerene zone can exist when *n* is larger than the forbidden zone (*n* is about 28~35).[3]

Using Equations 1.3 and 1.4, we can immediately determine the numbers of edges and faces once *n* is known for C_n. For example, for C_{60}, $n=60$, it has $3n/2=3\times60/2=90$ edges and $60/2 + 2 = 32$ faces. Using the same equations for C_{70}, we know that it has 105 edges and 37 faces.

Since fullerenes can only have pentagonal faces (*p*) and hexagonal faces (*h*), we have:

$$h+ p = f \text{ ---------- (Equation 1.5)}$$

We can also have:

$$5p + 6h = 3n \text{ ---------- (Equation 1.6)}$$

We have Equation 1.6 because both $3n$ and $(5p + 6n)$ count each edge twice ($=2e$), therefore, $(5p + 6h)$ equals to $3n$.

By incorporating Equations 1.5 and 1.6 into Equation 1.4 and eliminating *f* and *n*, we can state:

$$p = 12 \text{ ----------(Equation 1.7)}$$

$$h = n/2 - 10 \text{ ----------(Equation 1.8)}$$

Equation 1.7 tells us that fullerenes must have 12 pentagons. Using Equation 1.8 enables us to calculate the number of hexagonal faces in a fullerene. For example, any C_{60} has 20 (hexagons) + 12 (pentagons) = 32 faces; while any C_{70} has, pentagons =12 and hexagons = 70/2-10 = 25; hence, there are *37* faces in a C_{70} cages.

Equation 1.8 also tells us that $n \geq 20$ since $h = n/2 - 10$ and *h* cannot be a negative integer. Therefore, we know that the smallest possible fullerene is C_{20}. For C_{20}, $n=20$, $h=0$, which means that C_{20} consists of only twelve pentagons (no hexagons). Therefore, fullerene C_{20} has the shape of a Platonic solid.[11] One exception to this definition of a fullerene is that C_{22} cannot exist because there is no way to build a polyhedron with a hexagon and 12 pentagons.

1.2.2 Rationale for the Necessity of Pentagons

Carbon atoms in fullerene cages are all bonded to three other carbons (all sp^2 hybrid). Therefore, hexagons are the natural result of connecting sp^2 hybrid carbon atoms without strain. The question is: why must there be pentagons and not other poly-lateral faces—for example, square (quadrilateral faces) and heptagonal faces? To answer this question, several factors must be taken into account. First, only hexagons cannot form a closed-cage because they can only form planar sheets (graphene in graphite) and bucket walls of carbon nanotubes. Second, carbon atoms are all sp^2 hybrids in a fullerene cage, so each carbon atom also has one π-electron. These π-electrons on the cage surface form a conjugated system, which is highly stabilized by hexagons, but less stabilized by pentagons and heptagons. Moreover, the further away the structure is from a hexagon, the less stabilized the π-conjugated system becomes. When a

pentagon is fused with two hexagons, as shown in Figure 1-6, δ_{23} $(=3\pi/5)$ is an angle in the pentagon, while δ_{34} $(=2\pi/3)$ and δ_{24} $(=2\pi/3)$ are angles in the hexagons, resulting in the following equation: $\delta_{23}+\delta_{34}+\delta_{24}=29\pi/15<2\pi$. Therefore, C_1, C_2, C_3, C_4 cannot be coplanar and C_1 will be a vertex. In addition, the introduction of a pentagons to hexagons will cause pyramidalization, resulting in strain energy for both the σ-bonds and the π-bond on the surface of the fullerene cage.

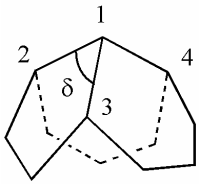

Figure 1-6. Curvature caused by the incorporation of a pentagon to hexagons.

Calculating the vertex defect angles will show the relationship between the sum of these angles and the solid angle of a closed cage (4π). The vertex defect angle (ϕ) is the amount by which a full rotation (2π radian) exceeds the sum of the bond angles at that vertex.[10] By this definition, at vertex 1 in Figure 1-6, we have the following relationship:

$$\phi = 2\pi - (\delta_{23}+\delta_{34}+\delta_{24}) = 2\pi - 29\pi/15 = \pi/15 \text{ ------ (Equation 1.9)}$$

$$\sum_{n=1}^{60}\phi = 60\times\pi/15 = 4\pi \text{ ----------(Equation 1.10)}$$

The integer 60 in Equation 1.10 refers to 12 pentagons with a total of 60 inner angles. Equation 1.10 tells us that the total vertex defect angle in a fullerene cage is equal to the total solid angle of a fullerene cage. [13] Therefore, we understand that there must be 12 pentagons in a fullerene cage. The introduction of 12 pentagons to hexagons is necessary and sufficient to form a closed fullerene cage.[14]

The pyramidalization of the σ -bond skeleton of the fullerene cage will cause the rehybridization of the π-orbital system. The effects of pyramidalization and rehybridization are shown in Figure 1-7.

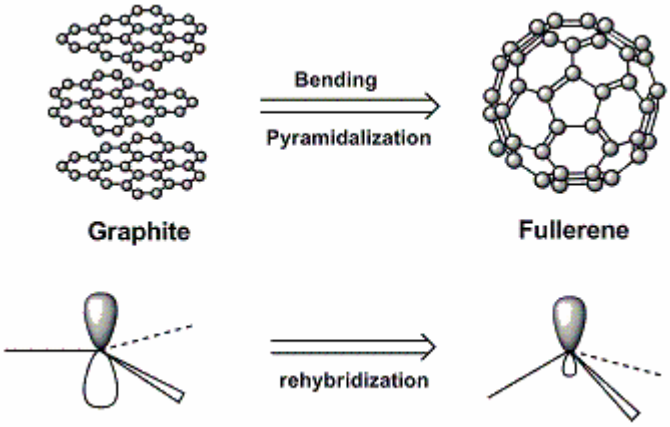

Figure 1-7. Relationship between pyramidalization and rehybridzation.

More generally, Equations 1.1 and 1.6 can be written, respectively, as:

$$v + \sum_n f_n = e + 2 \text{ --------- (Equation 1.11)}$$

and

$$\sum_n n f_n = 3n \text{ ----------(Equation 1.12)}$$

where f_n refers to a face with *n* sides.[15-17] For example, f_5 indicates a pentagonal face, f_6 corresponds to hexagonal face, etc. If we allow a polyhedron of a fullerene to have pentagonal faces, hexagonal faces, and heptagonal faces, i.e. a polyhedron of fullerene with *n=5, 6, 7,* the following equations will result:

$$f_5 = 12 + f_7 \text{ ----------(Equation 1.13)}$$

$$f_6 = \frac{n}{2} - 10 - 2 f_7 \text{ ----------(Equation 1.14)}$$

Equations 1.13 and 1.14 tell us that if we introduce a heptagonal face into a fullerene cage, we will have an extra pentagonal face and two less hexagonal faces than a fullerene cage with only pentagonal and hexagonal faces. Since pentagons and heptagons have σ-strain and hexagons have no σ-strain, clearly, the incorporation of a heptagonal face to a fullerene cage will cause more strain than evidenced in a fullerene cage with only pentagonal and hexagonal faces. Indeed, these suppositions concerning fullerene cages with only pentagonal and hexagonal faces have been confirmed by *IR*[8] and *NMR*[3, 18] of C_{60} (I_h) and C_{70} (D_{5h}).[19] If heptagonal faces exist in the cages of fullerenes C_{60} and C_{70}, the *NMR* of C_{60} (I_h) and C_{70} (D_{5h}) cannot have just 1 and 5 peaks, respectively (see Figure 1-8). If the single ^{13}C NMR peak of C_{60} cluster can be rationalized by another possibility, for example, a sixty member ring of *sp* hybrid carbons,[20] the 5 peaks (3×10, 2×20) in the ^{13}C NMR of a C_{70} cluster provides conclusive evidence for the validity of the Buckminsterfullerene proposal; it also reinforces the legitimacy of the fullerene conjecture.

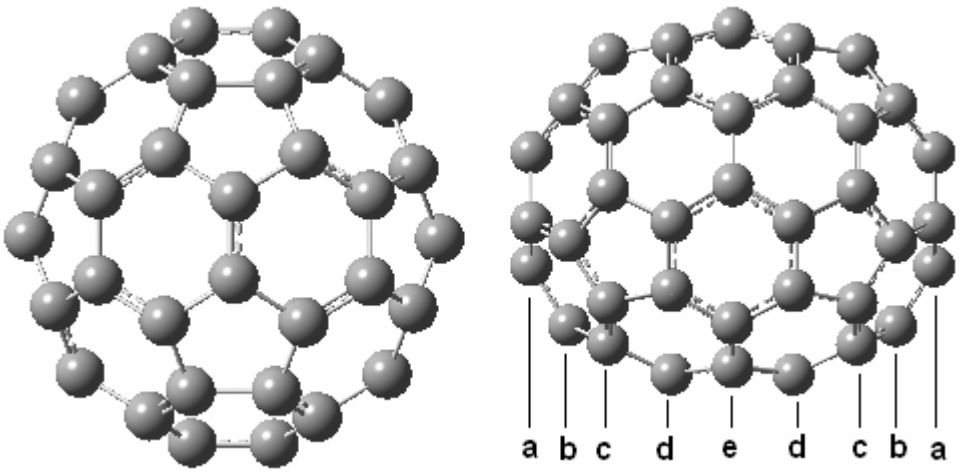

Figure 1-8. Structures of C_{60} (I_h) (left) and C_{70} (D_{5h}) (right). All sixty carbon atoms in C_{60} (I_h) are identical while there are five kinds of carbon atoms (3×10, 2×20) in C_{70} shown as a(10), b(10), c(20), d(20), e(10).[19]

Recently, Rubin and co-workers reported the detection of $C_{62}^{\cdot -}$ by the LD-FTMS spectrum of its precursor. As a result, they proposed a mechanism by which the precursor formed

the C_{62}, which involved the incorporation of a four-membered ring in the gas phase. However, due to the complexity of gas phase reactions during the mass spectometry,[21] their proposed mechanism could not be conclusively proved, thus rendering the four-membered ring of the C_{62} strongly in question. The resulting C_{62} cluster may anneal to other classical fullerene structures.

1.2.3 Isolated Pentagon Rule (IPR), Pentagon Index and Hexagon Index

1.2.3.1 IPR and the Steric Strain Energy of Fullerene Cage

According to the definition of a fullerene C_n, when *n* increases, the number of possible isomers will increase rapidly. For example, C_{20}, C_{24}, and C_{26}, all have only 1 isomer; C_{36} has 15 isomers; C_{60} has 1812 fullerene isomers when enantiomers are regarded as equivalent, but it has 3532 fullerene isomers when enantiomers are regarded as distinct.[12] However, for fullerene C_{60}, only 1 isomer I_h-C_{60} was experimentally isolated, which means I_h-C_{60} must have a thermodynamic and/or kinetic energy advantage compared to other fullerene isomers of C_{60}. [14]

We already know that the incorporation of a pentagonal face to hexagonal faces causes the pyramidalization of carbon atoms in fullerene cages. Pyramidalization of a σ-bond network and rehybridation of a π-orbital system are sources of strain energy.[22-26] Thus, if two pentagonal faces are fused together, there will be more local strain. Isolated pentagon rule (IPR) was developed according to that logic. IPR states that the most stable fullerenes are those in which all (12) pentagons are isolated by hexagons. In other words, there are no fused pentagons in the stable fullerenes. Apparently, a natural extension of IPR is that the isomer with the lowest energy of fullerene C_n will be the one that has the minimum achievable number of fused pentagon pairs (a.k.a. the pentagon adjacency penalty rule, PAPR).[27-29] Before fullerenes were experimentally isolated, theoretical chemists had already suggested some constraining criteria for stable fullerenes and their isomers. These criteria include: "(1) three-valent (sp^2 hybrid) σ-network, (2)

cage homeomorphic to a sphere, (3) five- and six- sided rings only, (4) higher symmetry, (5) non-abutting five-sided rings, (6) uniform curvature spreads over the cage."[16]

So far, the isolated and well characterized empty cage fullerenes are all classical fullerenes containing five- or six-membered rings and following IPR. However, after capturing metal atoms and clusters or exo-functionalization, IPR may not be obeyed and other membered rings may also be present.[30] Non-IPR structural fullerenes can be obtained through the exo-passivation of the highly active sites of an otherwise extremely unstable cage. An example of the exo-passivation of a non-IPR structural fullerenes is $C_{50}Cl_{10}$.[26] Non-IPR structural fullerenes can also be obtained through endo-passivation by a metal atom sitting in the folder of pentalene and coordinating with the carbon atoms of the pentalene folder. Examples of the endo-passivation of a non-IPR structural fullerenes include $Sc_3N@C_{68}$,[28] $Tb_3N@C_{84}$,[31] and $Sc_2C_2@C_{66}$.[32]

Due to the introduction of pentagons to hexagons, the carbon atoms are no longer co-planar. In other words, the carbon atoms have pyramidalized. Since the carbon atoms are non-planar, the π-orbitals are no longer parallel, as shown in Figure 1-9.

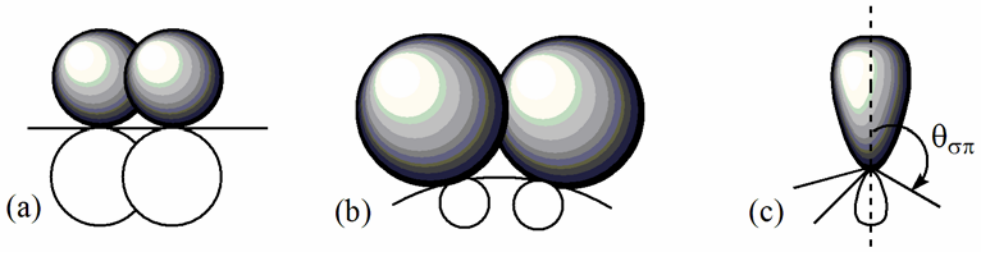

Figure 1-9. (a) π-orbitals in graphite, (b) π-orbitals in fullerene, (c) angle between π-orbital and σ-bond due to the pyramidalization.

In order to overlap with each other in the fullerene, the π-electron orbital must be rehybridized. In Figure 1-9 (a) the π-electrons are in the pure *p*-orbitals, which are parallel to each other. However, in Figure 1-9 (b) the lobes of the π-electron orbitals are no longer pure *p*-orbitals. They are rehybridized to contain partial *s*-orbital character. The strain due to the non-

planarity is shown in Figure 1-9(c). Apparently, the larger the $\theta_{\sigma\pi}$, the more severe the pyramidalization and the more curvature expressed in the fullerene cage. When $\theta_{\sigma\pi} = \pi/2$, the carbon atoms are pure sp^2 hybrids and co-planar. Consequently, there is no strain. Therefore, $\sum^{n}(\theta_{\sigma\pi} - \frac{\pi}{2})^2$ was used to assess the strain due to the non-planarity of fullerene C_n.

Approximately:

$$\sum^{n}(\theta_{\sigma\pi} - \frac{\pi}{2})^2 = 4\pi/(3\sqrt{3}) = 2.418 \text{----------(Equation 1.15)}$$

According to π-orbital axis vector theory (POAV) approximation,[22] the π-orbital rehybridization ($s^m p$) is related to the pyramidalization angle:

$$m = \frac{2\sin^2(\theta_{\sigma\pi} - \frac{\pi}{2})}{1 - 3\sin^2(\theta_{\sigma\pi} - \frac{\pi}{2})} \text{ ----------(Equation 1.16)}$$

$$\frac{m}{m+1} = 2tg^2(\theta_{\sigma\pi} - \frac{\pi}{2}) \approx 2(\theta_{\sigma\pi} - \frac{\pi}{2})^2 \text{ -------(Equation 1.17)}$$

$$\sum^{n}\frac{m}{m+1} \approx 2\sum^{n}(\theta_{\sigma\pi} - \frac{\pi}{2})^2 \approx 2 \times 4\pi/(3\sqrt{3}) = 4.837 \text{ ------- (Equation 1.18)}$$

Equations 1.15 and 1.18 show that both pyramidalization and rehybridization in fullerenes are approximately conserved. Thus, the total strain in fullerenes, including pyramidalization and rehybridization, is approximately conserved at the POAV level.[22] However, the total strain per carbon atom changes greatly from one fullerene to another. Kinetic stability will mainly depend on the local strain.[33] Figure 1-10 shows how the trend of rehybridization changes with the number of increasing pentagons.

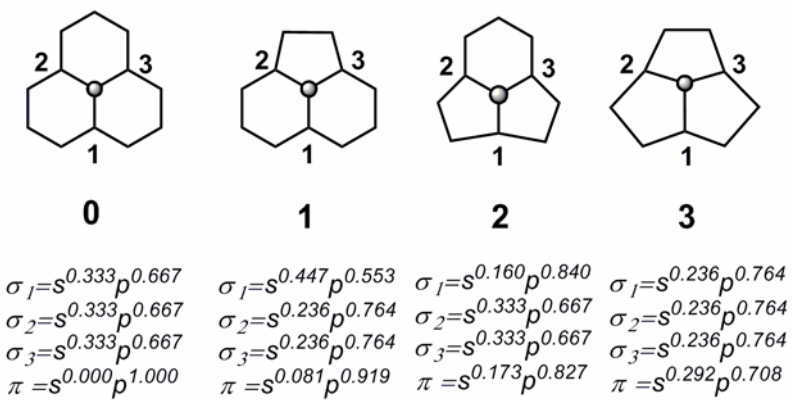

Figure 1-10. The change of s and p components of σ and π hybrid orbitals on the central carbon atom with increasing number of fused pentagons.[12]

1.2.3.2 Pentagon Index and Hexagon Index[12]

The pentagon index was developed to compare the stabilities between isomers of a fullerene. The pentagon neighbor index of each pentagon is defined as the number of other pentagons to which it is adjacent. The pentagon neighbor index can be expressed in the form of a pentagon signature: (P_0, P_1, P_2, P_3, P_4, P_5), where P_k denotes the number of pentagons with pentagon neighbor index k. For example, fullerene C_{20} has the pentagon signature (*0, 0, 0, 0, 0, 12*) since each of the *12* pentagons is adjacent to five other pentagons and the pentagon neighbor indices of *12* pentagons are all *5* (P_5); Conversely, for C_{60} (I_h), which abides by IPR, each of the *12* pentagons is adjacent to *5* hexagons (no fused pentagon), and their pentagon neighbor indices are all 0 (P_0). Hence, its pentagon signature is (*12, 0, 0, 0, 0, 0*). Therefore, the pentagon signature can clearly show the local and global topography of a fullerene cage.

To use the pentagon signature to compare the stabilities between isomers, we should also know that the smaller the maximum pentagon neighbor index in the pentagon signature, the lower the energy of the isomer. In other words, most stable non-IPR cages contain the minimum achievable number of pentagon adjacency since each [5,5] junction greatly increases the local ring strain of the cluster (see Section 2.3.1). The cost per pentagon adjacency (pentagon

adjacency penalty) increases when the cage size becomes larger. For example, the energy penalty grows linearly from 72 kJ/mol for C_{30} to 111 kJ/mol for C_{60}.[29] The pentagon adjacency penalty rule (PAPR) suggests that the energetic driving force for maintaining the IPR will grow stronger with larger fullerene cages. Therefore, ignoring cages with fused pentagons in the screening of low-energy structures for larger fullerene isomers will become a better and better approximation. PAPR can be rationalized on both steric and electronic grounds because fused pentagon pairs introduce both cage skeleton strain and an anti-aromatic pentalene folder into a fullerene.[27] According to the definition of pentagon neighbor index, it is easily understood that

$$P_0 + P_1 + P_2 + P_3 + P_4 + P_5 \equiv 12 \text{ ---------(Equation 1.19)}$$

However, in the case of some of the larger fullerenes, the pentagon neighbor index becomes useless. For example, C_{80} has seven isomers, *80:1 (D_{5d}), 80:2(D_2), 80:3(C_{2v}), 80:4(D_3), 80:5(C_{2v}), 80:6 (D_{5h}), 80:7 (I_h)*, which all follow IPR, so the pentagon signature for each of these seven isomers is (*12, 0, 0, 0, 0, 0*). Therefore, another index is needed —namely, the hexagon index— to analyze the implication of steric strain in larger fullerenes.

The hexagon neighbor index of each hexagon in a fullerene is the number of other hexagons to which it is adjacent. Similar to the pentagon index, the hexagon index can be expressed in the form of a hexagon signature: ($h_0, h_1, h_2, h_3, h_4, h_5, h_6$). Since a hexagon index is used for fullerenes abiding by IPR (i.e. $h_0=h_1= h_2=0$ for all IPR fullerene), a hexagon signature can be simplified as (h_3, h_4, h_5, h_6). According to the definition of hexagon index, therefore, we can make the following association:

$$3h_3 + 2h_4 + h_5 = 60 \text{ ---------(Equation 1.20)}$$

where ($3h_3 + 2h_4 + h_5$) is the total number of edges in all pentagons. consequently, the total edges of pentagons should be 12×5=60 edges. In order to obtain the optimum solution for IPR

fullerenes with minimum steric strain, Raghavachari's argument is needed. Raghavachari's argument states that for IPR fullerenes with minimum steric strain, the indices of all the hexagons in the structure should be as similar to one another as possible. The nature of Raghavachari's argument is that for a stable fullerene cage, the strain should be averaged over the entire cage and the cage should seek as a high symmetry as possible (see Section 2.3.1). For example, in the case of C_{60} (I_h), hexagons =60/2-10=20. Using Raghavachari's argument, h_4=20 and h_5=20 cannot satisfy Equation 1.20; instead, only h_3=20 can satisfy this equation. Specifically, h_3=20 means that each of the 20 hexagons is adjacent to 3 hexagons and 3 pentagons in alternative pattern (without any fused pentagons). This structure mirrors the I_h isomer of C_{60}, which had already been proven experimentally and theoretically to be a stable isomer of the C_{60} fullerene.

With respect to physical chemistry, stable isomers of fullerenes should exhibit their thermodynamic and/or kinetic energy advantages. However, the peak intensity of C_{70} (D_{5h}) is lower than that of C_{60} (I_h) in Figure 1-4, even though C_{70} (D_{5h}) has lower energy per carbon atom compared to C_{60} (I_h).[34] This fact suggests that the kinetic stability, which corresponds to chemical inertness or nonreactivity,[23, 33, 35-38] may play a more important role than thermodynamic energy in the formation of fullerenes. However, a stable isomer of a fullerene normally has a structure with both thermodynamic and kinetic stabilities. This is easily understood since fullerenes screened by IPR, PAPR and other methods exhibited minimal global and local steric strains, reflecting their thermodynamic and kinetic stability, respectively.

In addition to topological structural rules (IPR, PAPR, etc.), which correspond to the stability of the fullerenes, their electronic structures, including HOMO-LUMO gap, multiplicity (open shell or closed shell), and low-lying single-electron molecular orbital, etc., are all strongly

associated with the stability of the fullerenes. For example, among all the 31924 empty C_{80} fullerenes, seven isomers, *80:1 (D_{5d}), 80:2(D_2), 80:3(C_{2v}), 80:4(D_3), 80:5(C_{2v}), 80:6 (D_{5h}), 80:7 (I_h)*, obey the IPR. However, only two of these, *80:2(D_2)* and *80:1 (D_{5d}),* are experimentally isolated. This experimental evidence clearly proves that one can successfully predict for the fullerenes' stability using IPR. However, according to Raghavachari's argument, the *80:7 (I_h)* isomer, which has the highest symmetry among the seven IPR-obeying isomers, should be more stable than *80:2(D_2)* and *80:1 (D_{5d})*. However, *80:7 (I_h)* isomer has not yet been isolated. Thus, the invalidity of the topological structural rule in this case suggests that other considerations may be important and necessary. High level theoretical calculations, in fact, have demonstrated that the instability of the empty *80:7 (I_h)* isomer is due to its small HOMO-LUMO gap and open-shell electronic configuration in the HOMO. The HOMO of the empty *80:7 (I_h)* should be four-fold degenerate orbitals, but there are only two electrons in them. The Jahn-Teller distortion thus results in a small HOMO-LUMO gap. However, after acquiring six electrons, C_{80}^{6-} (I_h) has a closed-shell electronic configuration and a large HOMO-LUMO gap. Thus C_{80}^{6-} (I_h) is very stable with temperature and chemical reagents as in the case of $[Sc_3N]^{6+}@C_{80}^{6-}$ (I_h).

1.2.4 Symmetry and Theoretical Calculation

1.2.4.1 Symmetry Assignment and Point Groups of Fullerene

As discussed in Section 2.1, we know that for fullerene C_n, there are *n* vertices (carbon atoms), 3*n*/2 edges (bonds) and (*n*/2+2) faces (pentagons and hexagons). Therefore, there are a total of (3*n* + 2) special points on the fullerene cage.[12, 39, 40] The (3*n*+2) special points are *n* vertices, 3*n*/2 edge mid-points and (*n*/2 +2) face centers (see Figure 1-11). When a computer is used to assign a symmetry to a fullerene, it should first generate the coordinates for the (3*n*+2) special points, as well as find all vectors from the coordinate origin to the special points, all

possible rotation axes, and all possible reflection planes (σ_d *and* σ_v). With these geometrical data in hand, a series of symmetry operations can be performed. Using a symmetry tree chart, a computer can easily figure out the point group for specific fullerene cages. In total, there are only 28 fullerene point groups which are listed in Table 1-1.

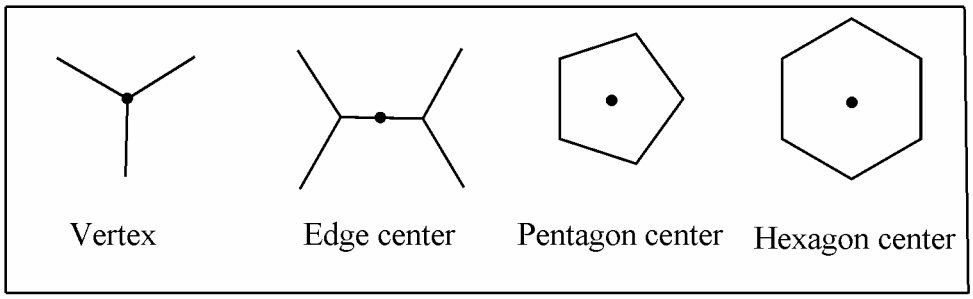

Figure 1-11. The (3n+2) special points in a fullerene cage. The special points include vertices, edge centers, and pentagon and hexagon centers.

Table 1- 1. The 28 fullerene point groups and their subgroups (reprinted from Ref. 39)

Group	Order	Subgroups	Group	Order	Subgroups
I_h	120	I, T_h, D_{5d}, D_{3d}	D_{2h}	8	C_{2v}, C_{2h}, D_2
I	60	T, D_5, D_3	D_{2d}	8	C_{2v}, D_2, S_4
T_d	24	T, D_{2d}, C_{3v}	D_2	4	C_2
T_h	24	T, D_{2h}, S_6	S_6	6	C_3, C_i
T	12	D_2, C_3	S_4	4	C_2
D_{6h}	24	D_{3d}, D_{3h}, D_6, D_{2h}	C_{3h}	6	C_3, C_s
D_{6d}	24	D_6, D_{2d}	C_{3v}	6	C_3, C_s
D_6	12	D_3, D_2	C_3	3	C_1
D_{5h}	20	D_5, C_{2v}	C_{2h}	4	C_2, C_s, C_i
D_{5d}	20	D_5, C_{2h}	C_{2v}	4	C_2, C_s
D_5	10	C_2	C_2	2	C_1
D_{3h}	12	C_{3v}, C_{3h}, D_3, C_{2v}	C_s	2	C_1
D_{3d}	12	C_{3v}, D_3, S_6, C_{2h}	C_i	2	C_1
D_3	6	C_3, C_2	C_1	1	–

The carbon atoms in fullerene cages are all located at the vertices. Thus, the site symmetries for each carbon atom can only have four possibilities: C_{3v}, C_3, C_s and C_1 (see Figure 1-11). In Table 1-1, C_{3v} and C_3 are mutually exclusive among the 28 point groups; therefore, for each fullerene cage, there are only three site symmetries available for carbon atoms. The ^{13}C

NMR intensity is directly proportional to the number of equivalent nuclei, which is inversely proportional to the order of the site group. Consequently, for a pure fullerene isomer, there are at most three different peak intensities in its carbon-13 NMR spectrum. In other words, more than three peak intensities can be associated with impurity of the sample or an endohedral carbide metallofullerene. The ^{13}C NMR peak intensity patterns of the 28 point groups are list in Table 1-2.

Table 1-2. The ^{13}C NMR peak intensity patterns of the 28 point groups of fullerenes[39, 40]

Symmetry	**Peak intensity**
C_1, C_i, C_2, S_4, D_2, D_5, D_6	1 peak intensity (All peak intensities are equal)
C_s, C_3, C_{2h}, C_{2v}, S_6, D_3, D_{2h}, D_{5h}, D_{6h}, D_{2d}, D_{5d}, D_{6d}, T, I	$\leq$ 2 peak intensities
C_{3h}, C_{3v}, D_{3h}, D_{3d}, T_h, T_d, I_h	$\leq$ 3 peak intensities

1.2.4.2 Procedure of Theoretical Calculation

An Atlas of Fullerenes, by Fowler and Manolopoulos, provides the spiral codes and pentagon indices for most fullerenes under C_{100}. As they reported, a spiral code can be generated by the "fullerene surface unwind conjecture," which states that "the surface of a fullerene polyhedron may be unwound in a continuous spiral strip of edge-sharing pentagons and hexagons such that each new face in the spiral after the second shares an edge with both (a) its immediate predecessor in the spiral and (b) the first face in the preceding spiral that still has an open edge." [12]

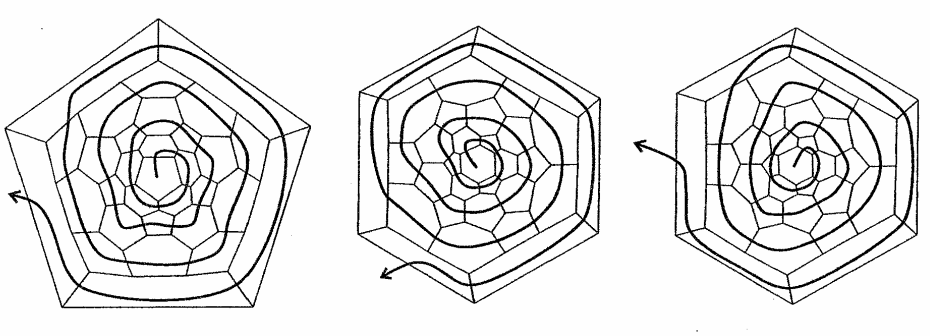

Figure 1-12. Two Schlegel diagrams of C_{60} (I_h) and three symmetry-distinct spirals which successfully unwind (reprinted from ref. 12).

Three spiral codes of C_{60} fullerene in Figure 1-12 are as follows:

Full spiral code		Simplified spiral code (pentagon positions)
5666665656565656656565656566666 5	↔	1 7 9 11 13 15 18 20 22 24 26 32
6565656665665665656656565656566	↔	2 4 6 10 13 16 18 21 24 26 28 30
6656565656656656565665666565656	↔	3 5 7 9 12 15 17 20 23 27 29 31

Since a fullerene cage consists of only pentagons and hexagons, the number of hexagons that can be obtained for fullerene C_n is determined by (n/2-10). Therefore, the full spiral code and simplified spiral code can be easily inter-converted because all other positions except for the 12 pentagons are hexagons.

By utilizing the spiral code, a Schlegel diagram of a fullerene can be built. A Schlegel diagram is a topological planar diagram showing the connectivity of carbon atoms in a fullerene (see Figure 1-12). Through the use of Schlegel diagram[41] and a molecular mechanics program, a primary three-dimensional cage can be optimized as an input file for further higher level calculations—for example, ab initio calculations. The coordinate structures of various fullerene cages can now be freely downloaded from the Internet and can be recognized and edited using GaussianView as an input structural file. Another basic task that must precede higher level calculations is determining the multiplicity of the corresponding input files. This can be accomplished using the Hückel program, which is provided freely on the Internet.[42] Once the

electron distribution in the HOMO is known by Hückel theory, the spin multiplicity can be calculated using:

$$Multiplicity = 2s+1 \text{----------(Equation 1.21)}$$

and

$$s = number\ of\ unpaired\ electrons \times \frac{1}{2} \text{----------(Equation 1.22 [43])}$$

A useful rule in figuring out multiplicity is that fullerene C_n with n=60+6k (k≠1, k is integer) and carbon cylinders with n=2p(7+3m) (p=5 or 6, m is integer) will have closed-shell electronic structure, which means that its multiplicity is one.[12]

1.2.5 The Mechanisms of Fullerene Formation

Fullerene can be generated by the vaporization of carbon materials at high temperature (over 4000 ˚C) in an inert gas environment. Under such conditions, the carbon material will be vaporized as carbon atoms or small carbon clusters. Rationally, the resulting random collisions of the small clusters should entropically favor the formation of unorganized products. Interestingly, however, well ordered, highly symmetrical fullerenes, such as C_{60} (I_h) and C_{70} (D_{5h}), were the main products after extraction using organic solvents. Thus, the mechanism of fullerene formation was initially somewhat of a mystery. Based on experimental evidence and theoretical simulations, several mechanisms for fullerene formation were proposed in the early 1990's, with the "Pentagon Road" and the "Fullerene Road" mechanisms most widely discussed.[44-49]

1.2.5.1 The "Pentagon Road" Mechanism

The main points of the "Pentagon Road" mechanism include the following: [50]

(1) Whenever the number of carbon atoms in a carbon cluster is ~ *30* or higher, it is energetically favored to form a carbon network in the form of a "bowl." The bowl-like

surface formed by the small C_n chain clusters increases the coordination numbers of carbon atoms and thus is a more stable structure.

(2) This "bowl" consists of only pentagons and hexagons.

(3) The pentagons should avoid being fused. In other words, each pentagon should be surrounded by hexagons to form a so-called "isolated pentagon" via the isolated pentagon rule (IPR). The rationale of IPR is that the fused pentagons introduce an energy penalty for fullerene cages (See Sections 2.2 and 2.3).

(4) Pentagons should be as numerous as possible so that the "bowl" is effectively curved to reduce the number of "dangling bonds" (free valences on the periphery of the bowl). Above a certain size, the rearrangement of the bonding pattern will drastically reduce the dangling bonds and eventually form the first IPR structure, C60 (I_h), followed by the second IPR structure, C_{70} (D_{5h}). The energy released as a result of reducing the dangling bonds is the driving force for the closure of a fullerene cage.

Although the "Pentagon Road" mechanism can explain many experimental facts, its weakest point (compared with the "Fullerene Road" mechanism described below) is that the so-called "bowl" is still very energetic due to dangling bonds on its periphery. However, the supporting evidence for the existence of a "bowl-like" structure is the existence of a trace amount of corannulene in the fullerene-rich soot.

1.2.5.2 The "Fullerene Road" Mechanism

The main points of the "Fullerene Road" mechanism include the following:[51]

(1) Whenever the number of carbon atoms in carbon clusters is ~ *28* or higher, it starts to form closed fullerene cages rather than to stay open as "bowls."

(2) The small fullerene cages (smaller than C_{60}) inevitably have fused pentagons, which do not conform with IPR because the smallest fullerene satisfying IPR is C_{60}.

(3) The small and closed fullerenes are expected to have lower energies than the open "bowls" because the dangling bonds disappear in the closed fullerene cages.

(4) From the smaller fullerene cages to the larger cages, the Stone-Wales rearrangement, C_2 gain (Endo-Kroto insertion) and C_2 loss (O' Brien exclusion) may be required in the annealing process.

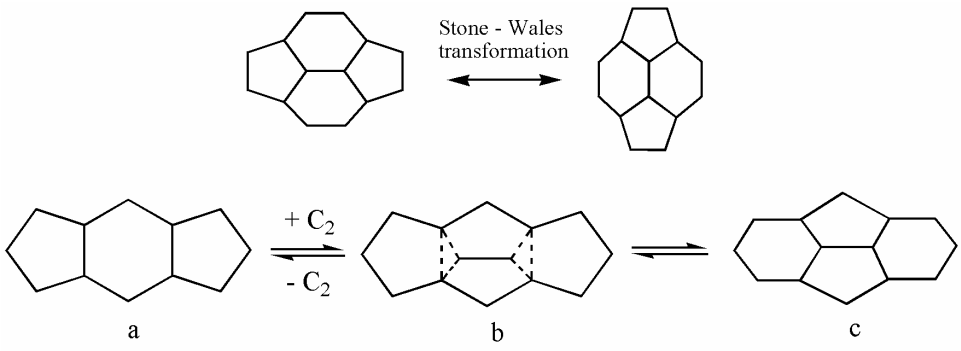

Figure 1-13. Stone-Wales rearrangement,[3, 15] Endo-Kroto insertion (a→b→c),[12] and O' Brien exclusion (c→b→a).[3, 52]

Before carbon clusters can form open bowls or small, closed fullerene cages, they exist in different sizes at different stages. C_1—C_7 clusters exist as atoms and/or small clusters. C_7—C_{10} are mainly linear chains, C_{10}—C_{20} clusters are monocyclic rings, and C_{21}—C_{28} exist in the form of different rings or loops or even as bi-cyclic carbon structures. Newton and co-workers reported the formation energy per carbon of carbon clusters, including linear, planar, and polyhedral carbon clusters[24, 53] (see Figure 1-15). The crossover in the energy preference from planar to polyhedral structures is at about C_{40}, which is fairly consistent with the observations that fullerenes start to form at C_{36}~C_{40} (see Figure 1-4).

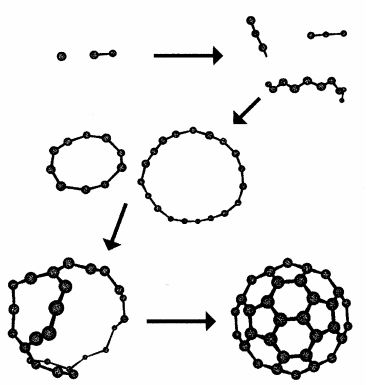

Figure 1-14. Carbon cluster structures of the different sizes in the process of fullerene formation (reprinted from Ref. 54).

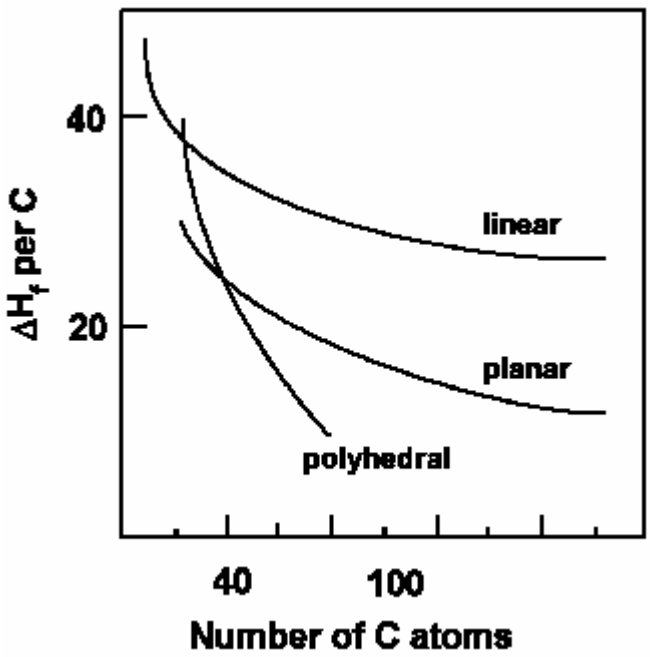

Figure 1-15. Formation energy per carbon of carbon clusters. The crossover in energy preference from planar to polyhedral structures is at about C_{40}.[24]

Since the formation of a fullerene was initially associated with the experiments in which the graphite was "vaporized" with a laser, many thought that graphite sheet fragments might have been ablated from the graphite target and rearranged into C_{60}. However, even after the graphite target (sp^2 hybrid) was replaced with a diamond (sp^3 hybrid),[4, 55] the same distribution of peaks (as shown in Figure 1-4) was still obtained. This experiment suggests that C_{60} was produced as a result of nucleation from carbon vapor consisting initially of carbon atoms and

very small carbon molecules, rather than by a process involving the ablation of bulk fragments from the target. This result was further confirmed by the $^{13}C/^{12}C$ isotope scrambling experiment.[56, 57]

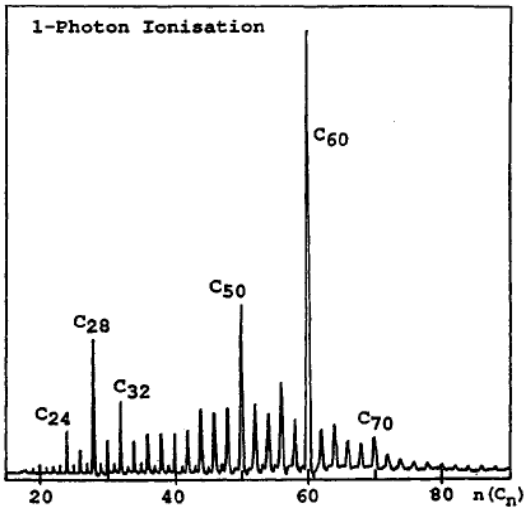

Figure 1-16. Magic number of smaller fullerenes (reprinted from Ref. 7). Fullerenes C_n with magic number n=24, 28, 32, 50, and 70 were expected to exhibit enhanced stability due to their minimal achievable number of abutting pentagons at their fullerene sizes. (see Figure 1-17)

As discussed earlier, in 1988 the Exxon research group reported an MS corresponding to a "magic number" of carbon clusters,[7] shown in Figure 1-16. They deduced that the carbon clusters with that "magic number" size would significantly reflect their electronic character. Kroto, however, believed that carbon clusters with a "magic number" size reflected their structural stability, based on the Buckminsterfullerene proposal. C_{60} and C_{70} are the predominant peaks in the mass spectrum because they are, respectively, the first and second IPR-obeying fullerene cages formed from small carbon clusters. Other magic numbers clusters, such as C_{24}, C_{28}, C_{32}, and C_{50}, all correspond to the minimal achievable number of abutting pentagons at their fullerene sizes. Thus, they have a minimal energy penalty compared to their neighboring carbon clusters. A more detailed explanation is provided graphically in Figure 1-16, as well as its descriptive caption.

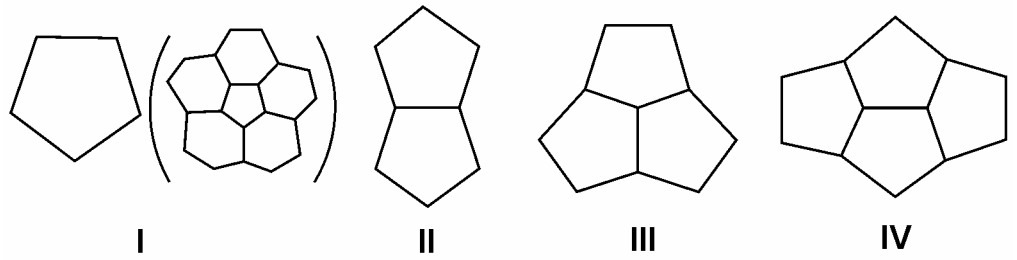

Figure 1-17. Types of the fused pentagons.[14] The local strain increases in order from I to IV. For type I, the smallest fullerene size is C_{60}; type II, the smallest size is C_{50}, Type III, the smallest size is C_{28}~ C_{36} (see Figure 1-16).

1.2.6. Production and Purification

1.2.6.1 Production of Fullerenes

In the laboratory setting, fullerenes are typically produced according to two methods: (1) the laser ablation method, and (2) the Krätschmer-Huffman method (see Figure 1-18). The advantage of the laser ablation method is that it is easier to use in conjunction with the analytical instruments needed for characterization, such as the mass spectrometer, etc. The Krätschmer-Huffman method is popular because it can produce macroscopic amounts of fullerenes required for further characterization and other applications.

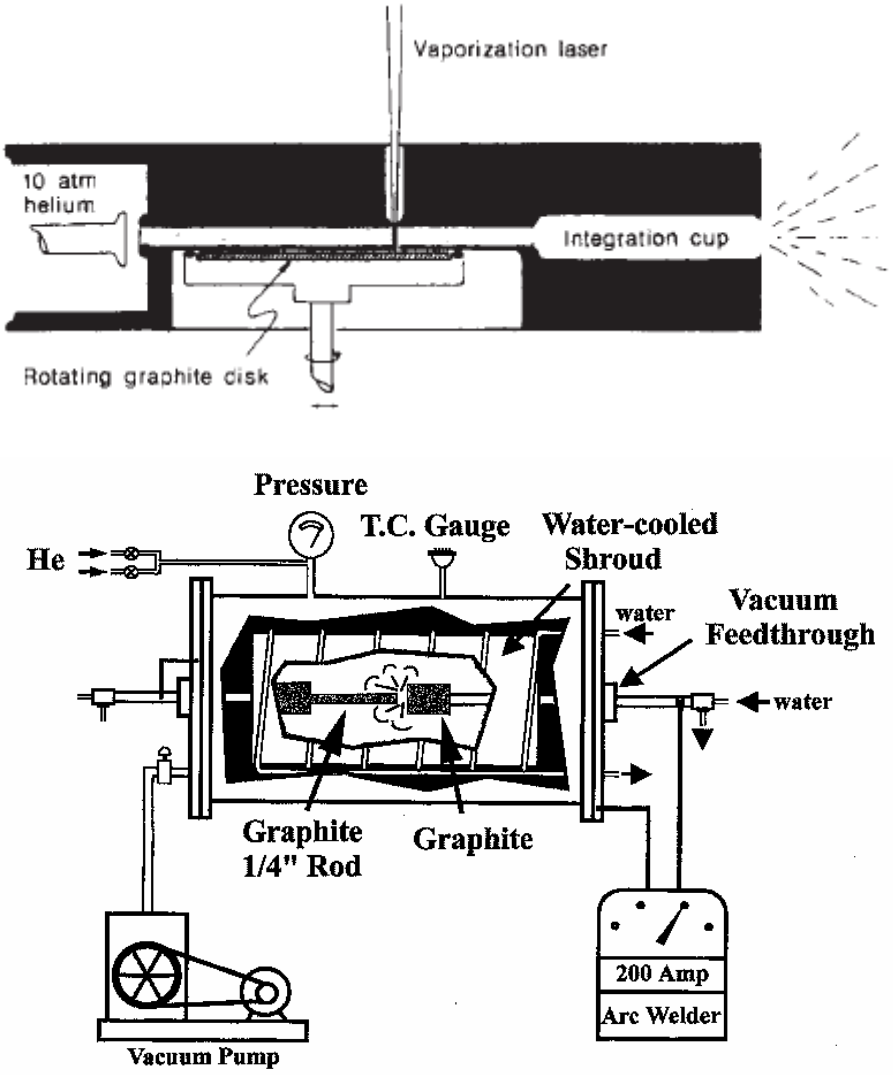

Figure 1-18. Laser ablation apparatus (upper, reprinted from Ref. 1) and Krätschmer-Huffman generator (bottom, reprinted from documents from the Dorn Lab)

Fullerenes can also be prepared at lower temperatures, for example, at 1800 K in a limited oxygen atmosphere in order to burn hydrocarbon precursors such as benzene, or by pyrolysis of the polycyclic aromatic hydrocarbons (PAHs), such as naphthalene, at 1300 K in an argon stream.[54] Recently, Scott reported the 12-step chemical synthesis of C_{60} using the starting compound, 4-bromo-chlorobenzene, with an overall C_{60} yield of 0.1~1%. The last step of this process involved the flash vacuum pyrolysis of a polycyclic aromatic precursor bearing chlorine

substitutes. Although in practice this method cannot supplant the graphite vaporization method, its rationale is very important to chemists.[58]

In the Krätschmer-Huffman method, the carbon rods (anode) are vaporized at above 4000°C (melting and boiling points of carbon are 3527°C and 4027°C, respectively) by DC electric arc-discharge between two electrodes in the noble gas atmosphere (normally helium) at about 100~200 Torr. The vaporized small carbon clusters are annealed to form fullerenes at the outer sphere of the arcing plasma. This area is called the fullerene formation zone, wherein the temperature ranges between 1000 and 2000°C. The choice of noble gas is also very important. Helium provides the highest fullerene yield compared with other noble gases, such as argon. This phenomenon is related to the dynamic annealing process in which the noble buffer gas passivates the nascent fullerenes by transferring their energy through collisions. As shown earlier in Figure 1-2, Kroto and co-workers demonstrated the effect of different helium pressures on the formation of fullerenes.

1.2.6.2 Solubility of C_{60} in Some Organic Solvents

After the anode is consumed, the soot is collected in a thimble and extracted using the Soxhlet method. The fullerene mixture is soluble in some non-polar solvents, such as benzene, carbon disulfide, chloro-benzene, hexane, chloroform, pyridine, carbon tetrachloride, etc. It should be noted that a fullerene mixture yield can change tremendously, depending on the solvent used in extraction. After rotary vaporization, the resulting solid sample needs to be washed several times using ether[8] or acetone[59] in order to remove the ubiquitous PAHs.

Table 1- 3. Solubility of C_{60} in some organic solvents (at 25˚C)[60]

Solvent	Solubility (μg/ml)
Hexane	37~52
Cyclohexane	35~54
Carbon tetrachloride	101~447
Mesitylene	994~1699
Toluene	2268~3197
Benzene	878~1858
Dioxane	41
Carbon disulfide	5162~12024
Acetone	0.72
Methanol	0.03
Water	1.3×10^{-18}
Chlorobenzene	5702~6998
1,2-dichlorobenzene	22896~27000
1,2,4-trichlorobenzene	4846~21312

Under optimized conditions of fullerene generation and using toluene as the solvent, the Krätschmer-Huffman method typically provides *5~15%* yields.[54] Parker, however, reported a *29~44%* yield of fullerene mixture from C_{60} to C_{200} via a multi-step extraction using a combination of solvents.[61] The fullerene mixture of C_{60} and C_{70} is about 95% with C_{60}:C_{70} being about 5:1, the higher fullerenes such as C_{76}, C_{78}, C_{82}, $C_{84,}$ etc. afford a yield of only about 5% together.[59]

1.2.6.3 Purification of Fullerenes

In a high vacuum or inert gas environment, C_{60} can be vaporized from the soot and collected using cooling finger by heating the soot to *300~400*°C.[8, 62] Further purification of a single component from a fullerene mixture normally involves the processes of LC[59] and HPLC.[63]

The HPLC columns routinely used to separate components in a fullerene mixture include the 3-[(pentabromobenzyl)oxyl]propylsilyl column (PBB),[64] the 2-(1-pyrenyl)ethylsilyl column (PYE),[65] the tripodal 2,4-dinitrophenyl ether column (Buckyclutcher), and the 3-(1-pyrenyl)propylsilyl column (Buckyprep).[66] PYE and Buckyprep, in particular, are used for high efficiency fullerene separation—for example, $Xe@C_{60}$ from C_{60} and fullerene structural isomer separations. PYE and Buckyprep have the largest conjugated π electronic systems (pyrene moiety) and thus have better π-π stacking interactions with fullerenes in the mobile phase. This improved π-π stacking interaction may be responsible for their enhanced ability to separate fullerenes efficiently. Buckyprep has one more $-CH_2-$ group than PYE in the chain connecting the silica supporting material and the pyrene moiety and thus is more hydrophobic than the PYE column. The advantage of the PBB column is that it can handle large sample loading and therefore be used in preparative separation, even with a small column. The retention behavior of a fullerene on a PBB column is very special in that its capacity factor is directly proportional to its fullerene cage size. Therefore, this property is very helpful in determining the structure of a fullerene. Since the Buckyclutcher has very polar moieties (tripodal 2,4-dinitrophenyl, DNP) in its stationary phase, metalloendofullerenes have longer retention times than empty cage fullerenes on the same column. Thus, the Buckyclutcher is used for separating endohedral metallofullerenes from empty cage fullerenes. However, the separation capabilities of the Buckyclutcher are poorer than the other three columns. For special separations, a combination of these columns is also desirable. The structures of the stationary phases of these columns are shown in Figure 1-19.

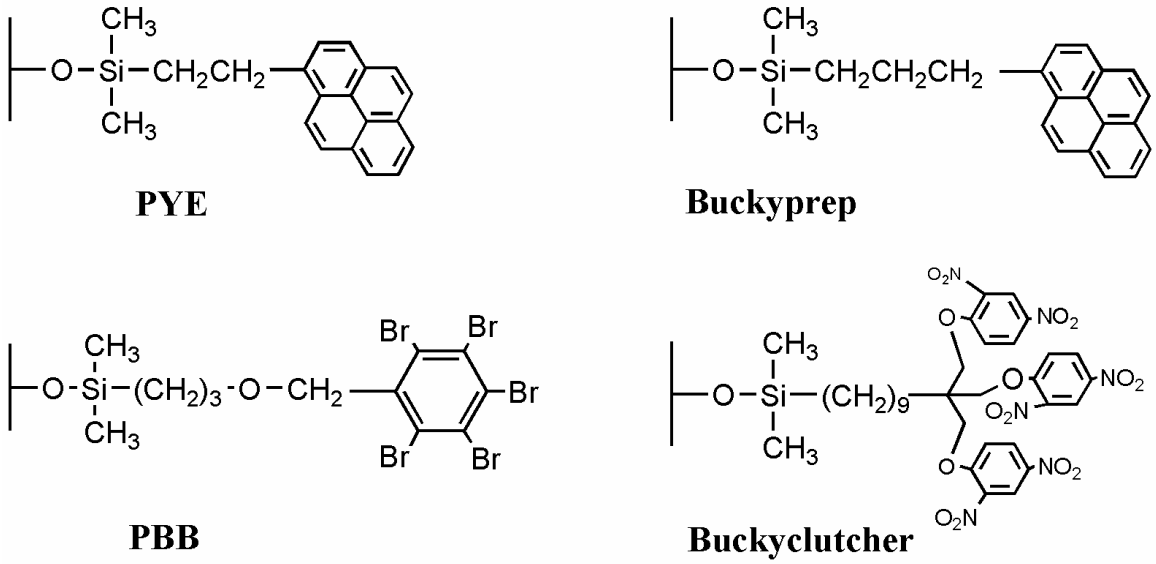

Figure 1-19. Frequently used stationary phases of HPLC columns in the purification of fullerenes.

As fullerene research has evolved, many new separation methods and strategies have emerged, including the electrochemical and retro-exofunctionalization methods. Recently, Echegoyen reported the electrochemical separation of I_h and D_{5h} isomers of $Sc_3N@C_{80}$ by taking advantage of the 270 mV difference in their first electrochemical oxidation potentials.[67] Since the D_{5h} isomer is less abundant than the I_h isomer, and its first electrochemical oxidation potential is 270 mV lower than the I_h isomer, the two isomers' purification was based on the selective oxidation of the D_{5h} isomer using tris(p-bromophenyl)ammonium hexachloroantimonate (TPBAH) with the subsequent removal of D_{5h} $Sc_3N@C_{80}^{\cdot+}$ from the mixture using liquid chromatography (LC) with a silica column. The retro-exofunctionalization method involves a three-step process. The first is the exo-functionalization of the isomers in a mixture. The second involves HPLC or LC separation. Since isomers have different symmetries and reactivities toward the selected functionalization reagent, the functionalized isomers generally have an enhanced difference in their retention times compared with those of isomers before the reaction. Furthermore, the organic exo-functionalized products have shorter retention times for separation.

Therefore, separating the products will be much easier with the functionalized sample than with the original sample. The third step corresponds to the retro reaction to remove the exo-groups on the fullerene cages. Although this method has not yet been published, a preliminary study in our research group demonstrated its potential application. Apparently, this method is suitable for large scale separations.

1.2.7. Fullerene Chemistry

Fullerene cages can be considered as three-dimensional building blocks in organic chemistry (compared with two-dimensional molecules, such as benzene). Although their π-orbitals in the cages are conjugated, their aromatic properties are still under discussion.[25, 68, 69] Due to the curvature of the cages, fullerenes are much more reactive than graphite. Moreover, the smaller the cages, the more reactive they are. For example, addition reactions for C_{60} occur more easily than for C_{70}. [70, 71] Since there is no hydrogen on a fullerene cage, substitution reactions cannot occur. However, two other kinds of chemical reactions—addition and redox—can take place with fullerenes. Since the discovery of the soccerball configuration of C_{60}, there has been a desire to encapsulate atoms or small clusters into a fullerene cage so that the buckyball conjecture could be confirmed. Therefore, endohedral fullerene chemistry has been a very important branch in fullerene science.[72-76] The replacement of carbon atoms with other atoms—for example, N atoms and B atoms (a.k.a. heterofullerene chemistry) is also an interesting field.[77-82] The various possible chemical transformations with fullerene are shown in Figure 1-20.

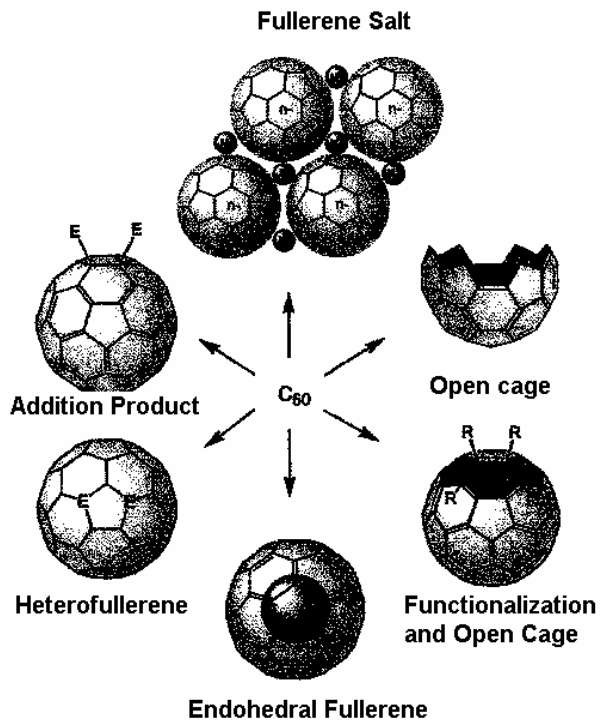

Figure 1-20. The possible chemical transformations with fullerene represented by C_{60} (reprinted from Ref. 82).

1.3. Endohedral Fullerenes

1.3.1 Confirmation of Endohedral Fullerene

When first identified, fullerenes were thought to have a hollow space in the carbon cage.[1] One test of this hypothesis is that some atoms or small clusters should be able to be inserted into the hollow cage. Actually, just a few days after the discovery of C_{60}, the Smalley team also found evidence of metal atoms being inserted into a fullerene. In the laser ablation of a La-doped graphite disc, a series of peaks of C_n^+ and La C_n^+ ion such as LaC_{60}^+ and $La_2C_{60}^+$ were observed by mass spectrometry.[6] Therefore, they suggested that the lanthanum atom had been encapsulated in the fullerene cage. However, this speculation could not be proven because there was also a possibility that the lanthanum atom had either combined with the cage or was still external to the cage. Later on, this group demonstrated the famous "shrink-wrapping" experiment

in which the critical smallest cage sizes occur at *n = 48, 44, 44~42* for Cs, K, and La, respectively, which are in accord with the sizes of the encapsulated atoms, as seen by multi-photon fragmentation of $C_{60}M^+$.[83] These results are shown in Figure 1-21.

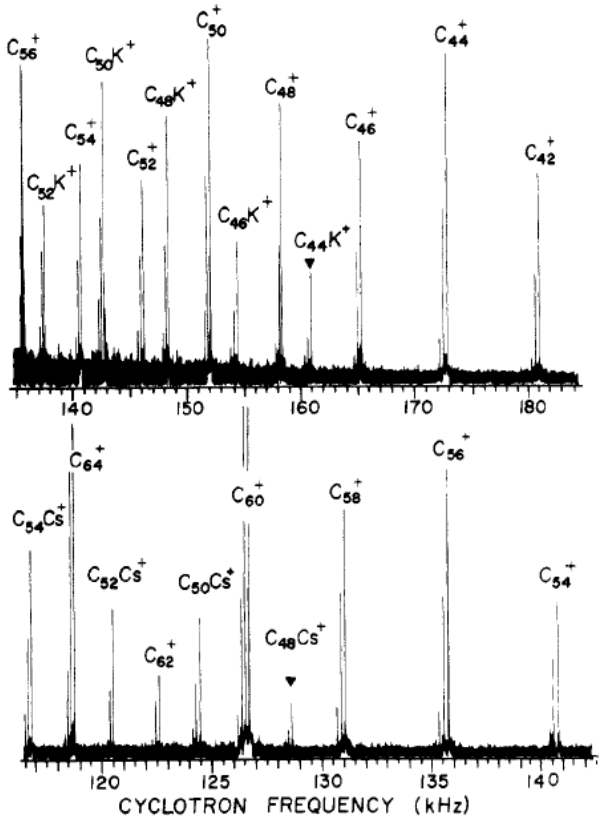

Figure 1-21. Fragmentation of $C_{60}K^+$ and $C_{60}Cs^+$ by intense laser excitation (reprinted from Ref. 83). The series of endohedral metallofuerenes created by O'Brien exclusion in which K-C clusters and Cs-C clusters stop at $C_{44}K^+$ and $C_{48}Cs^+$, respectively.

Based on two experimental observations that (1) a series of C_2 cluster exclusion without losing metal atoms and (2) critical cage sizes matching the sizes of corresponding metal atoms, Smalley team concluded that metal atoms were trapped inside fullerene cages. If the complexes were exohedral in structure, a series of C_2 exclusion without losing the metal atom could not be rationally explained. Therefore, this observation can only be justified by an endohedral model. Moreover, since the metal was encapsulated in a C_{60} fullerene cage, the C_2 exclusion can only reduce the cage size, preventing the metal atom from escaping. At the critical cage size, a cage

cannot become smaller because a metal atom of similar size was inside the cage. Thus, the cage would be completely destroyed by high energetic multiphotons. Therefore, the peaks of metal-enclosing fullerenes, which are smaller than the critical cage size, would disappear. In the early 1990's, many other reports also provided convincing evidence for this endofullerene model although they also provided indirect supports. Two examples are Saunder's helium releasing and neon encapsulating experiments[84] (see Section 3.2) and ESR studies of metallofullerenes.[85]

At this stage there was still some room for people to doubt the encapsulation of some atoms inside fullerene cage. After all, people did not directly see that the atoms had been entrapped in the fullerene cage. As a result, many researchers directed their efforts toward proving the existence of the endofullerene. In fact, in 1994, the Dorn group at Virginia Tech, together with two other research groups (IBM and Caltech), succeeded in preparing metallofullerene $Sc_2@C_{84}$ crystals. Following their structural determinations by electron diffraction and high-resolution transmission electron microscopy (TEM), they provided the first conclusive evidence that Sc atoms could be inevitably encapsulated in a fullerene cage since the additional charge density (compared with the simulated images of empty C_{84}) was observed within the fullerene cage of the $Sc_2@C_{84}$ sample.[86] Later in 1995, Shinohara's group also provided structural evidence for the endohedral metallofullerene $Y@C_{82}$ using the maximum entropy method (MEM) /X-ray powder diffraction techniques.[87] To show the endohedral nature of the $Y@C_{82}$, they compared the electron density distributions of $Y@C_{82}$ and empty C_{82}. as shown in Figure 1-22, there was a significant high electron density inside the C_{82} cage of $Y@C_{82}$ while there was none in the empty C_{82}. The number of electrons in the maximum region is about 38 (atomic number of Y is 39). The radius of the empty C_{82} is 4.10 Å, whereas the distance from the center of the $Y@C_{82}$ to the Y atom is 3.14 Å. These structural data clearly demonstrated that

the Y atom was encapsulated in the C_{82}. Meanwhile, it also showed that the Y was off the center in C_{82} cage of $Y@C_{82}$, which is consistent with the theoretical predictions for $Y@C_{82}$.[88, 89] The close contact of the Y atom with the C_{82} cage is due to the electrostatic attraction between Y^{3+} and C_{82}^{3-} by charge transfer model of $Y^{3+}@C_{82}^{3-}$.

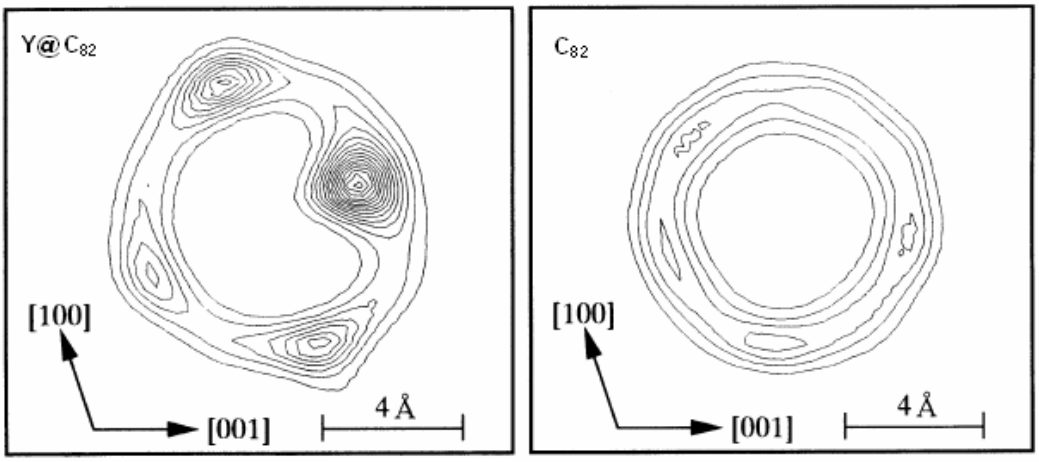

Figure 1-22. The electron density distributions of $Y@C_{82}$ (left) and empty C_{82} (right) using MEM /X-ray powder diffraction techniques (reprinted from Ref. 87).

1.3.2 Noble Gas Endohedral Fullerenes

In addition to endohedral metallofullerenes, noble gas atoms have also been encapsulated in fullerene cages.[84, 90-99] Examples of these encapsulations include $He@C_{60}$ and $Xe@C_{60}$. Similar to these types of endofullerenes, N and P atoms have also been encapsulated in fullerene cages via the ion-implantation method (see Figure 1-23). [100-104] The noble gases, N, and P endofullerenes have little or no charge transfer between the capturer and captive. The interactions between these intercalants and cages can be considered as van der Waals interactions. The global minimum energy structures of these endofullernes correspond to structures in which these intercalants are located at the center of the cages.[105] In addition to the ion-implantation method, the noble gases are more generally encapsulated via a high temperature (600~*650*°C) and a high pressure (~*3000* atm) procedure, which normally affords higher yields

as compared to the ion-implantation method. The high temperature and high pressure method are thought to thermally induce window opening on the cage, followed by a high pressure squeeze-in mechanism (window mechanism, see below).[90, 91, 105]

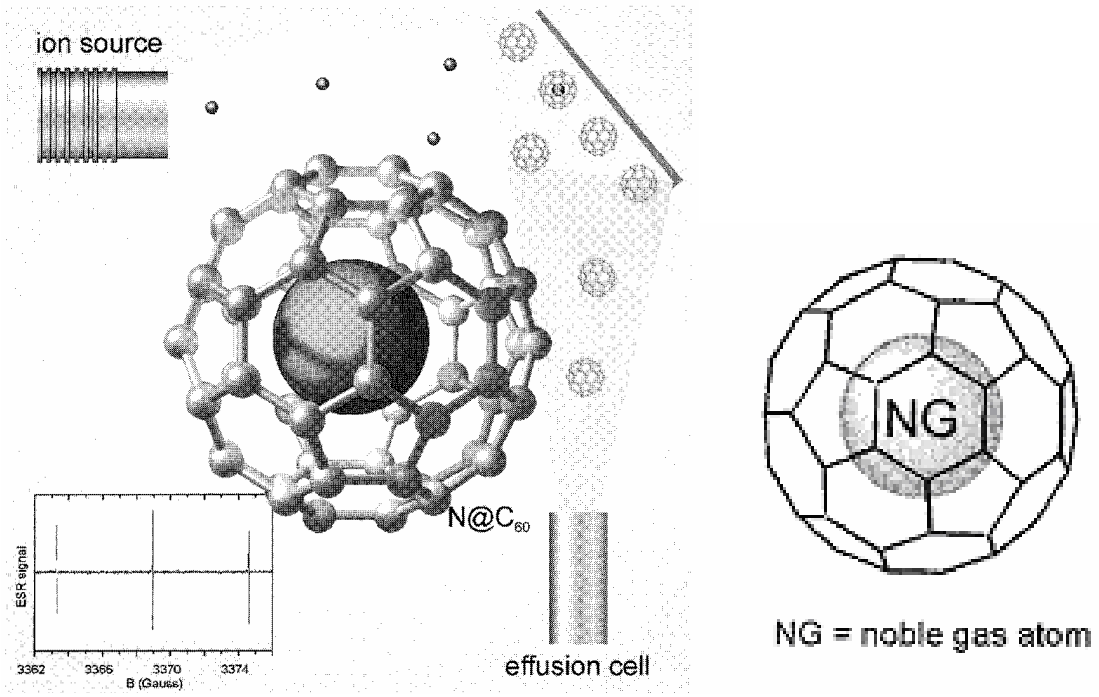

Figure 1-23. The illustration of noble gas endofullerene formation via the ion-implantation method (left part) and the model of noble gas endofullerenes without charge-transfer between the entrapped atom and the fullerene cage (right part) (reprinted from Ref.105).

The first two noble gas endofullerenes, He@C_{60} and Ne@C_{60}, were reported by the Saunders group in 1993.[84] Their experiment was based on the idea that He@C_{60} might already exist in commercial C_{60} samples because these samples had been produced by the Krätschmer-Huffman method in which the helium gas was used for cooling. In this experiment, 40mg commercial C_{60} sample (C_{60} >90%) was heated. They found that helium atoms were mainly released at 780~850°C. Helium gas was collected and measured with a mass spectrometer. The ratio of He@C_{60} to the C_{60} empty cage was at the parts-per-million (ppm) level and the isotopic ratio of ^{3}He/^{4}He in the collected helium gas was different from that of atmospheric helium. These

results demonstrated that the helium was indeed inside the C_{60} cage. They also heated a commercial C_{60} fullerene sample at 600°C under three atmospheric pressures of ^{22}Ne gas for one hour. The recovered fullerene sample weighing 22 mg was heated again at 200~900°C and the released neon gas was collected. They found that most of the ^{22}Ne atoms had been released at 700~900°C. These results indicated that the neon atoms were encapsulated when heated at 600°C in the presence of neon gas, and subsequently released when heated at a higher temperature (700~900°C) due to the damage to the fullerene cages. Based on these observations, they proposed a "window" mechanism. This "window" mechanism states that when fullerenes are heated to 600~650°C, some bonds on the fullerene cages undergo reversible breaking and reforming so that there is an equilibrium of the window opening and re-closing on the fullerene cages. Based on this mechanism, the Saunders group demonstrated the incorporation of helium, neon, argon, krypton and xenon into fullerene cages using the high temperature and high pressure method.[91] The yields of $Ne@C_{60}$, $Ar@C_{60}$, and $Kr@C_{60}$ were 0.2%, 0.3%, 0.3%, respectively. $Xe@C_{60}$ was detected but was difficult to quantify. The yield of $Xe@C_{70}$ was about 0.04% which is an order of magnitude lower than the yields of other noble gases in the C_{70} endofullerenes. These data showed that xenon is much more difficult to encapsulate in fullerene cages than other noble gases, especially for the C_{60} cage. These results are somewhat intuitive because the "window" on a fullerene cages may not be large enough for xenon atoms to pass through. For example, the van der Waals radius of a xenon atom is about 216 pm,[106] the calculated diameter of a C_{60} cage is about 710 pm, and the calculated radius of a carbon atom is about 67 pm.[106] Therefore, we can propose the following equation:

$$\frac{\text{Van der Waals diameter of Xenon atom}}{\text{Net diameter of } C_{60} \text{ cage}} = \frac{2 \times 216}{710 - 2 \times 67} \approx 75\%$$

The calculation above shows that xenon atoms are just slightly smaller than C_{60} molecules, making them very difficult to encapsulate in C_{60} cages.

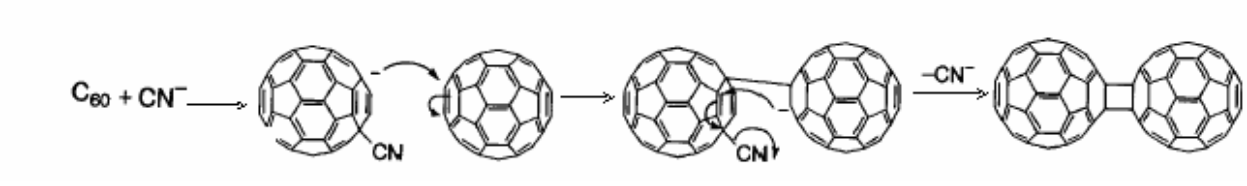

Figure 1-24. Nucleophilic addition of cyanide (reprint from Ref. 15)

The Saunders group also used an improved high temperature and high pressure method to demonstrate the inclusion of xenon atoms into C_{60} cages. Their improved methodology resulted in increased yield of noble gases into C_{60} cages by about an order of magnitude. Specifically, the yield of Xe@C_{60} was about 0.3%.[90] The only difference between the improved method and the prior method is that they used a ground mixture of a C_{60} sample and KCN material, instead of a pure C_{60} sample. Although the mechanism by which they improved the yield of Xe@C_{60} is not entirely clear, they suggested that the nucleophilic addition of cyanide on the C_{60} cage weakened the C-C bonds near the addition sites.[15] Therefore, a larger "window" on a cage might be easier to produce via this method. The nucleophilic addition of cyanide to a fullerene cage is shown in Figure 1-24.

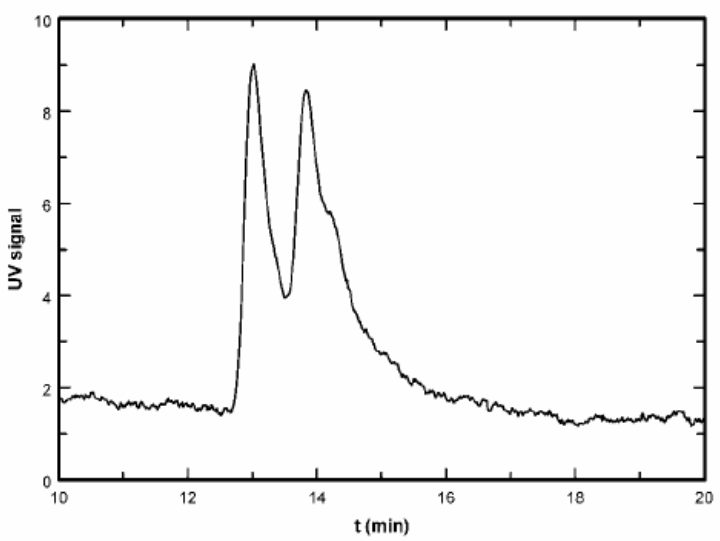

Figure 1-25. Chromatogram of Xe@C_{60} on PYE column (10×250 mm). Mobile phase is toluene, flow rate is 2 ml/min. The first peak at 13.0 min. is due to C_{60}, the second peak at 13.8 min. is due to Xe@C_{60}. The shoulder on the second is due to C_{60} epoxide (reprinted from Ref. 90)

Since no charge transfer exists between the encapsulated noble gas atoms and fullerene cages, noble gas endofullerenes and their corresponding empty cages have very similar retention times in an HPLC chromatogram. Therefore, the separation of noble gas endofullerenes from their corresponding empty fullerenes is very difficult. For example, as demonstrated in Figure 1-25, the retention time difference between the Xe@C_{60} and C_{60} peaks was only 0.8 minutes. PYE and Buckyprep columns are more effective for isolating noble gas endofullerenes (see Figure 1-19).[90, 96]

1.3.3 The Trimetallic Nitride Template (TNT) Endohedral Metallofullerenes (EMFs)

From 1999, the Dorn group at Virginia Tech has synthesized a series of trimetallic nitride template (TNT) endohedral metallofullerenes, which can be expressed by $L_{3-x}M_xN@C_{2n}$ (x=0~3; n=34, 39, 40; L and M are Sc, Y or Lanthanides).[28, 107-110] This series of TNT endofullerenes includes $Sc_3N@C_{68}$, $Sc_2ErN@C_{68}$, $Sc_3N@C_{78}$, $Sc_3N@C_{80}$, $Sc_{3-x}Er_xN@C_{80}$ (x=1~2), $Lu_3N@C_{80}$. These endofullerenes provide indirect support for the fullerene conjecture because with an increase in the captive cluster size, the cage size also increases. For example, Lu_3N clusters were

not found in C_{68} fullerene cages, but were found in the C_{80} cage. Since the C_{68} cage contains annelated pentagons, $Sc_3N@C_{68}$ and $Sc_2Er@C_{68}$ are called non-classical metallofullerenes.

1.3.3.1 Production and Purification of TNT-EMFs

Endohedral metallofullerenes are generally produced using the Krätschmer-Huffman method.[54, 111-113] To produce endohedral metallofullerenes, the graphite rod connected to the anode is drilled out and packed with a mixture of metals or metal oxides along with graphite powder. In order to minimize the production of polycyclic aromatic hydrocarbons, the packed rod should be baked for several hours under vacuum or an inert gas atmosphere at about 1200 °C.[59, 114] The rods are then vaporized by arc-discharge at about 4000 °C in a cooling gas (generally helium) at about 100~300 Torr. For the production of TNT-EMFs, about 20 Torr of nitrogen gas needs to be introduced into the chamber with the other cooling gas.

Dunsch and co-workers reported the alternating reactive nitrogen source-ammonia method.[112, 115, 116] The advantage of the ammonia method is that the empty cages are effectively depressed and converted to PAHs. Thus, after washing out the PAHs using acetone or ether, the task of separating the endofullerenes from the empty cage fullerenes would be much less than with the dinitrogen method.[112] The downside of this method, however, is that the ammonia is corrosive to gas tubes and gas flow meters. Moreover, the pollution of ammonia fumes in working environment is also a problem. To balance the positive and negative aspects of the dinitrogen and ammonia methods, a solid nitrogen source, such as melamine, might be a viable solution. The solid nitrogen source method is now under development in the Dorn lab. After vaporizing the rod, the soot is collected and extracted in Soxhlet extractor using non-polar organic solvents, such as CS_2 and toluene (see Section 2.6). The extract is a mixture of empty-cage and endofullerenes.[117] HPLC methods with various columns are generally used to purify the

endohedral metallofullerene, which is a very time-consuming process. For instance, HPLC purification may involve hundreds of injections in order to produce just enough material for one NMR sample. To purify $M_3N@C_{80}$ (M is metals in Group III B and lanthanide), the Dorn group recently developed a purification method based on the Diels-Alder reaction.[118] For these purifications, Merrifield's peptide resin is functionalized and connected with cyclopentadiene (CPDE-MPR). Since the C_{80} (I_h) cage is stabilized by the charge transfer of six electrons from the trimetallic nitride cluster[119] and the C_{80} (I_h) lacks a pyracylene reactive site (see Figure 1-28),[54] $M_3N@C_{80}$ will not react with the CPDE-MPR and is eluted by a mobile phase. In contrast, other empty cages and endofullerenes are more reactive and are connected to the CPDE-MPR so that they cannot be eluted. Aihara calculated the reactivities of empty cages and TNT-EMFs using the minimum bond resonance energy method and concluded that the TNT-EMFs are kinetically much more stable than empty cages.[35, 37] The procedures associated with this chemical separation methodology are shown in Figure 1-26.

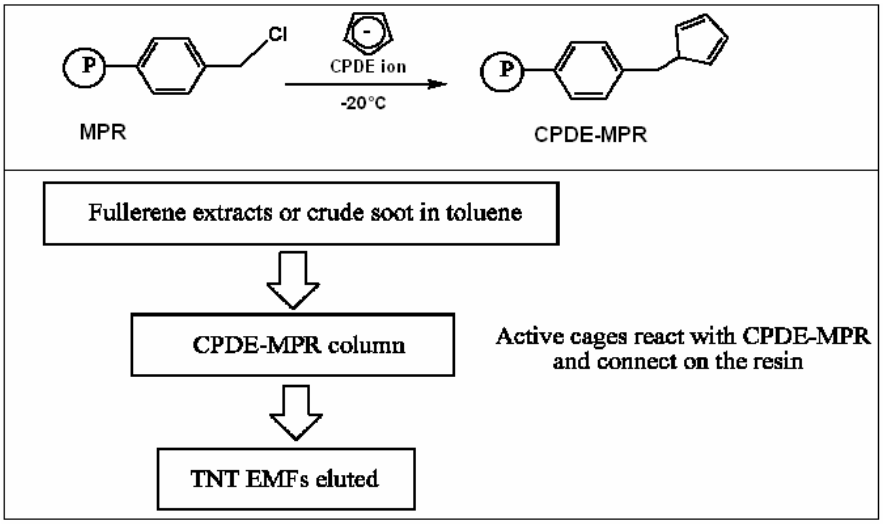

Figure 1-26. Synthesis of cyclopentadiene functionalized Merrifield peptide resin (CPDE-MPR) and principle of chemical separation process.

1.3.3.2 Discovery and Characterization of $Sc_3N@C_{2n}$ (n=34, 39, 40)

1.3.3.2.1 $Sc_3N@C_{80}$ (I_h)

$Sc_3N@C_{80}$ (I_h) was the first reported TNT-EMF, as documented by the Dorn group in 1999. The eventual assignment of the 1109 M/Z peak to the molecular formula $Sc_3N@C_{80}$ took quite sometime to determine. Once they finally realized that the nitrogen was due to air leaks, they intentionally added dinitrogen to the cooling gas (helium), which greatly improved the yield of $Sc_3N@C_{80}$. In fact, among all the endohedral metallofullerenes, $Sc_3N@C_{80}$ had the highest yield. Under optimized conditions, the peak area of $Sc_3N@C_{80}$ was even higher than that of C_{84}. This means that the yield of $Sc_3N@C_{80}$ is just lower than those of C_{60} and C_{70}, which are the most abundant. Moreover, $Sc_3N@C_{80}$ is very stable in air. By heating in vacuum, it can survive up to 600 °C. The ^{13}C NMR of $Sc_3N@C_{80}$ has only two peaks with a 3:1 peak area ratio. As judged by ^{13}C NMR data, the C_{80} cage of $Sc_3N@C_{80}$ should be I_h symmetry, in which there are only two types of carbon atoms, three hexagon [666] junction points (pyrene type, total 20 carbon atoms, with ^{13}C chemical shifts in the range of 130-138 ppm) and two hexagon and one pentagon [665] junction points (corannulene type, total 60 carbon atoms, with ^{13}C chemical shifts in the range of 138-145 ppm). ^{13}C NMR data also suggests that the Sc_3N cluster provides an averaged chemical environment for all the 80 carbon atoms in the NMR time scale. If this was not the case, the ^{13}C NMR spectrum could not maintain such a pattern (two ^{13}C peaks with a 3:1 peak area ratio). Based on this observation, Dorn and coworkers proposed that the Sc_3N cluster rotates as a wheel inside the $C_{80}(I_h)$ cage.

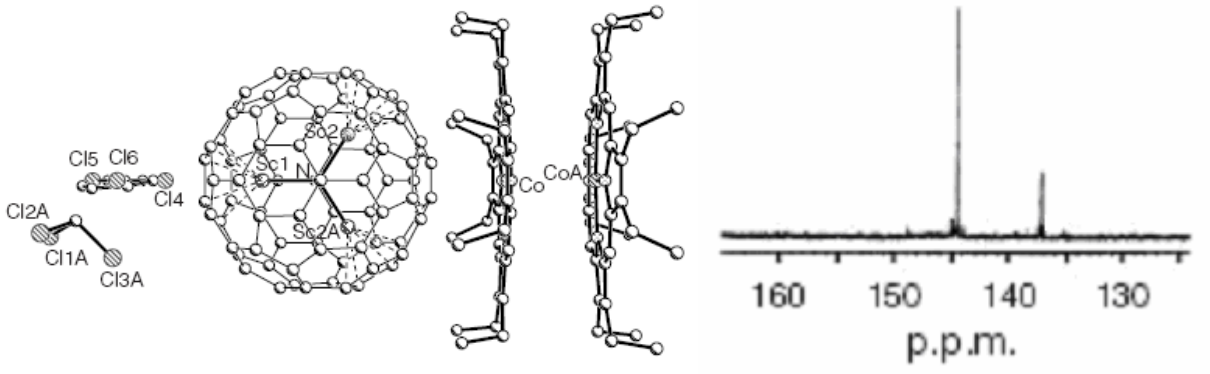

Figure 1-27. The X-ray diffraction structure of single crystal $Sc_3N@C_{80}(I_h)\cdot Co^{II}(OEP)\cdot 1.5CHCl_3\cdot 0.5C_6H_6$ and ^{13}C NMR spectrum of $Sc_3N@C_{80}(I_h)$ (reprinted from Ref.107)

This proposed structure was confirmed by the X-ray diffraction measurement of single crystal $Sc_3N@C_{80}(I_h)\cdot Co^{II}(OEP)\cdot 1.5CHCl_3\cdot 0.5C_6H_6$ (OEP is the dianion of octaethylporphyrin). Until now, the major occupation of Sc_3N cluster in the C_{80} (I_h) cage has not been found, even with good quality co-crystals similar in composition to the original. Theoretical calculations later showed that the C_{80}^{6-}(I_h) cage has a very smooth electrostatic potential interior surface (see Figure 1-35).[74, 111, 119, 120] Due to this iso-potential surface, there is barely a rotational barrier to force the Sc_3N cluster in any major orientation. The crystal structure of $Sc_3N@C_{80}(I_h)\cdot Co^{II}(OEP)\cdot 1.5CHCl_3\cdot 0.5C_6H_6$ demonstrated that $Sc_3N@C_{80}(I_h)$ was placed in the cradle formed by the eight ethyl groups and the plane of $Co^{II}(OEP)$. The crystal structure of pure $Co^{II}(OEP)$ showed that the eight ethyl groups of $Co^{II}(OEP)$ have two opposite orientations relative to the plane of $Co^{II}(OEP)$, with four ethyl groups in each side of the plane. These structures suggest that there are favorable van der Waals interactions between $Sc_3N@C_{80}$ (I_h) and $Co^{II}(OEP)$. This, in fact, was clearly demonstrated by the inter-molecular distances between them.[107] The detailed electronic structure of $Sc_3N@C_{80}$ (I_h) shows that each of the three Sc atoms donates two electrons to the C_{80} (I_h) cage and one electron to the central N atom. Thus, it can be formally expressed as $[Sc_3N]^{6+}@C_{80}^{6-}$. Furthermore, theoretical calculations showed that the

neutral C_{80} (I_h) cage has a four-fold degenerate HOMO and only two electrons associated with the HOMOs. Thus, it has an open-shell electronic structure. Because of Jahn-Teller distortion, it also has a very small HOMO-LUMO gap. Therefore, the neutral C_{80} (I_h) cage is very unstable.

Among the 31924 structural isomers, only seven isomers, 80:1 *(D_{5d}),* 80:2*(D_2),* 80:3*(C_{2v}),* 80:4*(D_3),* 80:5*(C_{2v}),* 80:6 *(D_{5h}),* 80:7 *(I_h)*, obey IPR (see Figure 1-33). Two of the seven isomers, *80:1 (D_{5d}), 80:2(D_2),* were experimentally isolated. C_{80} (I_h) *(80:7)* is the least stable isomer among these seven IPR structures. However, after obtaining 6e from a Sc_3N cluster, the four-fold degenerated HOMOs were fully occupied (closed-shell) and also resulted in a large HOMO-LUMO gap. Thus, $Sc_3N@C_{80}$ (I_h) is very kinetically stable. This is the reason that $Sc_3N@C_{80}$ (I_h) has an outstanding yield and is very stable in air and with heating.

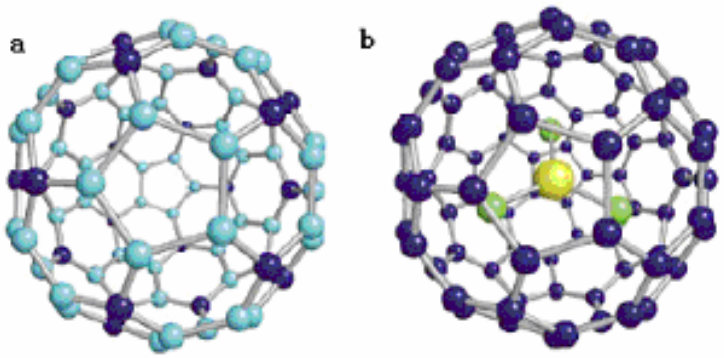

Figure 1-28. (a) empty C_{80} (I_h) cage which has no pyracylene patch and (b) $Sc_3N@C_{80}$ (I_h) in which the planar Sc_3N cluster rotates as a wheel (reprinted from Ref.107).

1.3.3.2.2 $Sc_3N@C_{80}$ (D_{5h})

The HPLC peak on the 5PYE column of component of $Sc_3N@C_{80}$, which was produced via the TNT process, has a small tail (see Figure 1-29).[110] The area of the tail peak is roughly 10% of the main peak. The mass peak of the tail also corresponds to1109 M/Z, making it another isomer of $Sc_3N@C_{80}$.[110] Since this small tail is situated behind a huge main peak in the HPLC trace, separating it from the main peak will be quite difficult. The first structural characterization

of this minor isomer was based on an NMR spectrum of a mixture of the main peak and the tail peak. In order to obtain sufficient NMR signals for the minor isomer, the sample was labeled with ^{13}C isotope when it was synthesized.[110] From the peak area ratio of 1:2:2:1:1:1 in the ^{13}C NMR of the minor isomer, its structure was assigned with D_{5h} symmetry.[110] The D_{5h} symmetry of the minor isomer was confirmed by the single crystal X-ray diffraction measurement.[121] Its HPLC trace and NMR spectrum were shown in Figure 1-29. The assignment of the six ^{13}C NMR peaks of $Sc_3N@C_{80}$ (D_{5h}) is listed in Table 1-4.

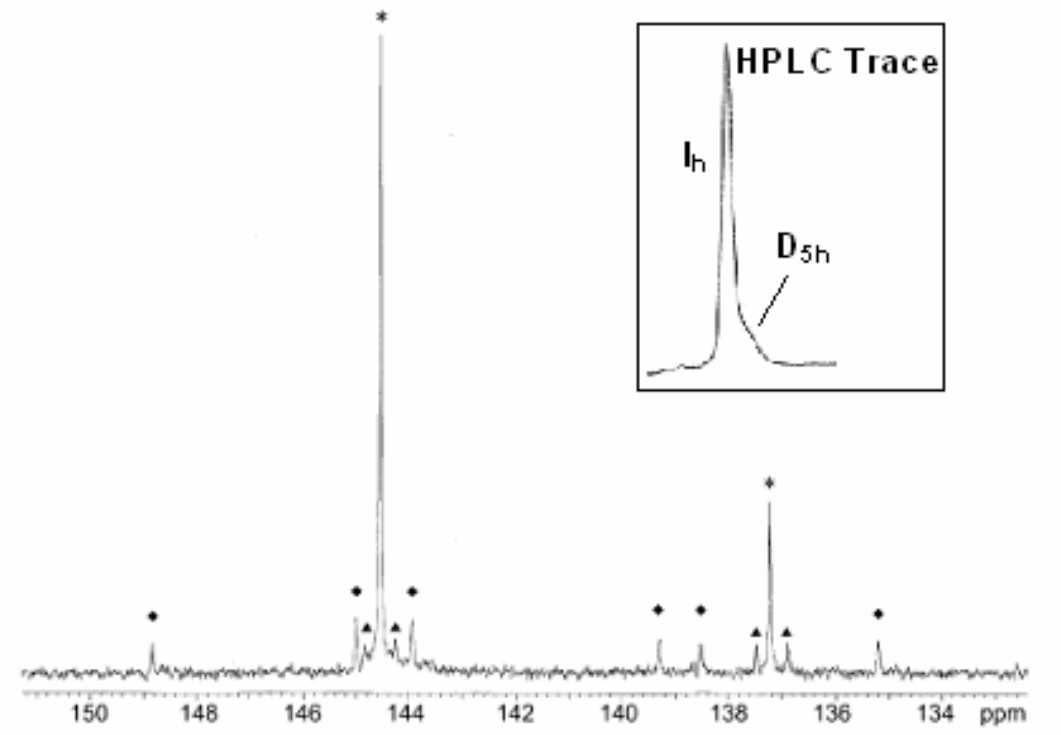

Figure 1-29. ^{13}C NMR of ^{13}C isotope labeled sample of $Sc_3N@C_{80}$ (I_h and D_{5h}). Peaks marked with * and ▲ are due to the well characterized $Sc_3N@C_{80}$ (I_h) isomer and its J-J carbon coupling, respectively. Six peaks marked with ♦ are due to the $Sc_3N@C_{80}$ (D_{5h}) isomer (reprinted from Ref. 110).

Table 1- 4.The assignment of the ^{13}C NMR peaks of $Sc_3N@C_{80}$ (D_{5h}) (reprinted from Ref. 110)

Experiment	Theory	Site
149.8	150.7	Corannulene
145.0	149.8	Corannulene
143.9	148.2	Pyracylene
139.3	145.7	Corannulene
138.5	141.6	Pyrene
135.2	141.4	Pyrene

1.3.3.2.3 $Sc_3N@C_{68}$ (D_3)

Based on the reported $Sc_3N@C_{80}$ (I_h), the mass peak of 965 M/Z can be easily assigned to the formula $Sc_3N@C_{68}$. For fullerene cages smaller than C_{70}, only C_{60} (I_h) follows IPR. Apparently, C_{68} of $Sc_3N@C_{68}$ must have a non-IPR structure. ^{45}Sc and ^{13}C NMR spectra of the $Sc_3N@C_{68}$ have one single symmetrical peak and 12 singlet lines (11 lines at full intensity and 1 line at one-third intensity), respectively.[28]

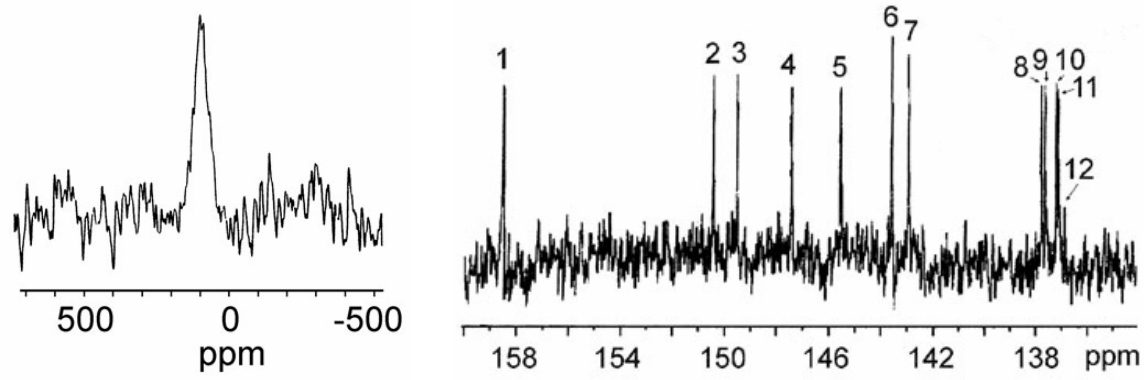

Figure 1-30. ^{45}Sc (left) and ^{13}C (right) NMR spectra of the $Sc_3N@C_{68}$ at 121.5 MHz and 150MHz, respectively (reprinted from the supporting information of Ref. 28).

Interpreted jointly, the ^{45}Sc and ^{13}CNMR spectra of the $Sc_3N@C_{68}$ clearly indicated that its likely structure assumes either a D_3 or an S_6 symmetry. Among the 6332 structural isomers of fullerene C_{68}, only 11 candidates are possibly consistent with both the experimental ^{45}Sc and ^{13}C NMR spectra shown in Figure 1-30. The 11 candidates are shown in Figure 1-31.

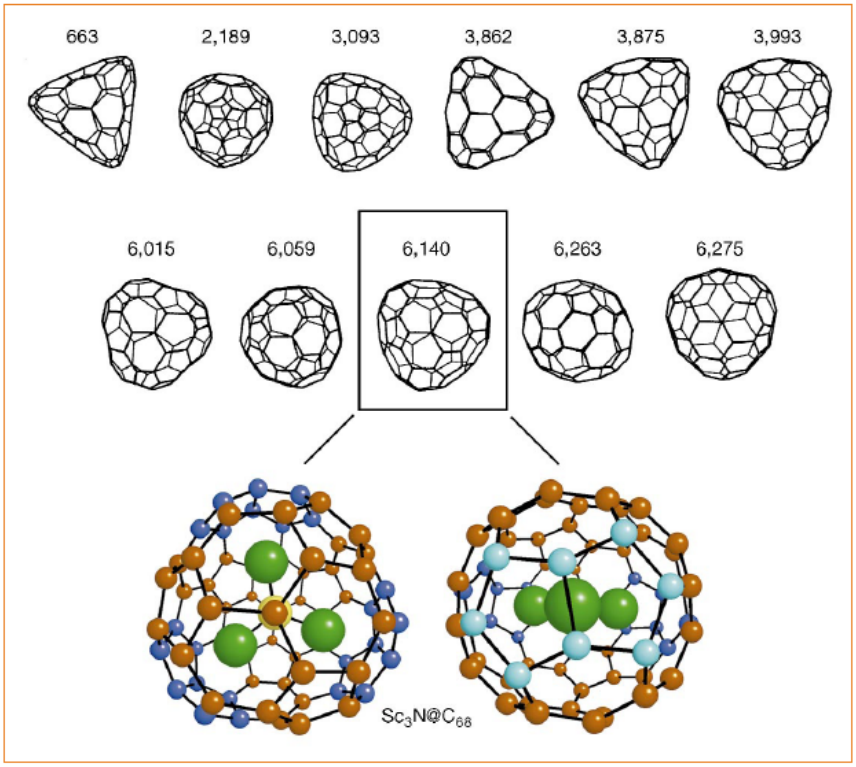

Figure 1-31. The structures of the eleven C_{68} candidates with 3-fold symmetry and the proposed the structure for $Sc_3N@C_{68}$ (reprinted from Ref. 28).

Among these 11 isomers, isomers 6140 and 6275 had the minimum fused pentagon pairs (N_p=3), while the N_p of the other candidates varied from 6 to 15. Since each pair of fused pentagons in a neutral fullerene cage will result in a 70~90 kJ/mol energy penalty, further screening of the candidates focused on isomer 6140 (D_3) and 6275 (D_3).[28] High level calculations using DFT demonstrated that the 6140 isomer had energy advantages larger than 120kJ/mol when both cages carried formal charges from -2 to -6. Thus, the final cage structure of $Sc_3N@C_{68}$ was proposed to be the 6140 (D_3) chiral isomer.

As shown in Figure 1-31, each Sc atoms of the Sc_3N core cluster sits in each of three pentalene patches of C_{68} (6140, D_3).[28] Theoretical calculations showed that 76% of the total charges transferred from the Sc_3N core cluster to the C_{68} cage were distributed in the three pentalene patches. Thus, the antiaromatic pentalene folder was converted to the aromatic form so

that the strain of the fused pentagon pair could be released.[27] At the B3LYP/6-31G* or higher level calculations, the Sc_3N neutral molecule had planar D_{3h} symmetry,[27] in contrast to the pyramidal C_{3v} geometry reported before.[122] The rotation of the Sc_3N cluster inside the $Sc_3N@C_{68}$ is hindered by the energy barrier of 4.52 eV,[27] suggesting that the Sc_3N cluster was completely stuck by the pentalene folders. So far the reported non-IPR endohedral metallofullerenes all share a common characteristic, namely, their fused pentagon pair is coordinated with one metal atom.

In addition to the $Sc_3N@C_{68}$, other similar examples include $Sc_2@C_{66}$ (C_{2v}),[123] $Sc_2C_2@C_{68}$ (6073,C_{2v}),[32, 124] and $Tb_3N@C_{84}$ (51365,C_s).[31] From neutral C_{68} (D_3) to C_{68}^{6-} (D_3), the average bond elongation was reported to be 1.33%, while it was only 0.39% from C_{68}^{6-} (D_3) to $Sc_3N@C_{68}$ (D_3).[27] Thus, the cage distortion from a hexaanionic model to an endohedral model is much smaller than that from a neutral cage to a hexaanionic charged cage. The complexation energy, as defined by the following formula, reflects the adiabatic bonding energy between the cage and the trimetallic nitride cluster:[27]

$$E_{complex}\ (Sc_3N@C_{2n}) = E\ (Sc_3N@C_{2n}) - E\ (Sc_3N) - E\ (C_{2n})$$

The calculated complexation energies for $Sc_3N@C_{2n}$ (n=34, 39, 40) at B3LYP/6-31G* are listed in Table 1-5. The high complexation energy reflects a substantial degree of interaction (hybridization) between the Sc_3N subunit and the fullerene enclosure.

Table 1-5. The calculated complexation energies for $Sc_3N@C_{2n}$ (n=34, 39, 40)

$Sc_3N@C_{2n}$	$E_{complex}$ (eV)
$Sc_3N@C_{68}$ (D_3)	-12.07[27]
$Sc_3N@C_{78}$ (D_{3h})	-9.37,[122] -9.62[27]
$Sc_3N@C_{80}$ (I_h)	-11.60,[122] -10.72[125]

1.3.3.2.4 $Sc_3N@C_{78}$ (D_{3h})[109]

$Sc_3N@C_{78}$ was one of the three TNT EMFs produced in the process of vaporizing graphite rods doped with Sc_2O_3 in the mixed cooling gases of helium and dinitrogen. Figure 1-32 shows the mass spectra and images of the three pure samples dissolved in carbon disulfide.

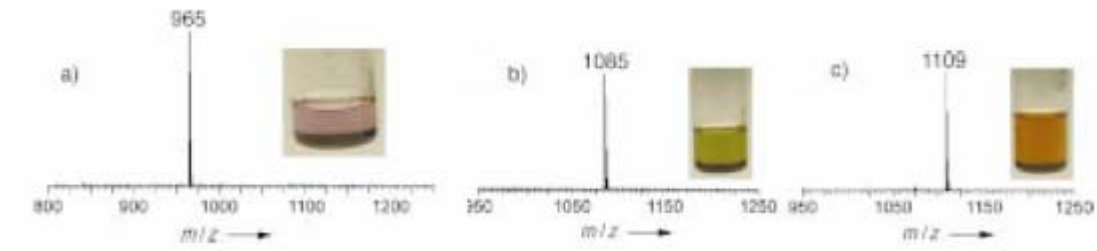

Figure 1-32. Mass spectra and images of the three scandium-based TNT EMFs. a) $Sc_3N@C_{68}(D_3)$, b) $Sc_3N@C_{78}(D_{3h})$, and c) $Sc_3N@C_{80}(I_h)$ (reprinted from Ref. 109).

The mass peak of 1085 corresponds to $Sc_3N@C_{78}$. Unlike the procedures used for the $Sc_3N@C_{68}$ (D_3) and $Sc_3N@C_{80}$ (I_h) reported earlier, the crystal structure of the $Sc_3N@C_{78}$ was first obtained and then confirmed by its ^{13}C NMR spectrum. There are a total of five isomers for the C_{78} fullerene obeying the IPR. The five isomers are listed in the order of their stabilities as follows: D_3 (78:1)>C_{2v} (78:2) > $C_{2v'}$(78:3)> D_{3h}(78:4)> $D_{3h'}$(78:5). The isolated isomers of empty C_{78} fullerenes are D_3 (78:1), C_{2v} (78:2), and $C_{2v'}$(78:3) following their stabilities. However, similar to the $Sc_3N@C_{80}$ (I_h), the crystal structure of the $Sc_3N@C_{78}$ demonstrated that the Sc_3N cluster was encapsulated in $D_{3h'}$(78:5), the least stable IPR cage. The planar Sc_3N cluster lies in the horizontal plane of $D_{3h'}$(78:5) with each of the three Sc atoms coordinated with each [6,6] ring junction of the three pyracylene patches of $D_{3h'}$(78:5). The coordination of the Sc atom with the double bond of the [6,6] ring junction is similar to the coordination of a metal ions with an alkene. The eight line ^{13}C NMR spectrum (five full intensity lines and three half intensity lines) suggests that the cage of the $Sc_3N@C_{78}$ has D_{3h} symmetry. Since there are two D_{3h} symmetry cages among the five IPR isomers listed above, the structure assignment using only ^{13}C NMR

spectrum is problematic. If no crystal structure is available, theoretical calculations must be involved to further screen the final structure, as was the case for the reported $Sc_3N@C_{68}$ (D_3). Therefore, the single crystal X-ray diffraction determination will often have the final "say" in resulting structural characterization. Theoretical calculations showed that the Sc_3N cluster of $Sc_3N@C_{78}$ can only swing along the three [6,6] ring junctions of the pyracylene patches in the horizontal plane of $Sc_3N@C_{78}$ (D_{3h}). If it is further away from the range of the equilibrium swing, it will face a rotational barrier of 1.12eV, in contrast to that of $Sc_3N@C_{80}$ (I_h), rotation barrier, 0.23 eV (5.3 kcal/mol). This 0.23 eV rotation barrier suggests that the Sc_3N cluster can freely rotate in $Sc_3N@C_{80}$ (I_h).

Although the $Sc_3N@C_{2n}$ (n=34, 39 and 40) can be formally expressed as $[Sc_3N]^{6+}@C_{2n}^{6-}$, the theoretical calculations showed that the ionic model is simplified in comparison with the actual situation. There exists a *d-π* orbital interaction between the Sc atoms of the core Sc_3N cluster and the interior surface of the fullerene cage;[126] nevertheless, the *d-π* orbital interaction may vary with the relative ratio of the Sc_3N cluster size to the fullerene cages' size (see Chapter 5).

As discussed above, a Sc_3N cluster was often adopted by the least stable and higher symmetry cage among the corresponding available isomers. The phenomenon can be theoretically explained by the $[Sc_3N]^{6+}@C_{2n}^{6-}$ model. When the six charges were transferred to the fullerene cage, the previous least stable neutral cage became a closed-shell electronic structure with large a HOMO-LUMO gap. Thus, its kinetic stability was dramatically improved and it is capable of surviving the arcing-discharge synthesis process with significant yield. However, the large HOMO-LUMO gap may not form a complete picture to explain the high yield of the TNT-EMFs.

Krause *et al* summarized possible reasons based on the reported experimental and theoretical observations for $Sc_3N@C_{80}$. They proposed that the high yield could be the result of : "(1) a significant charge transfer from the Sc_3N cluster to the C_{80} cage, (2) the strength of the three Sc-N bonds, (3) the chemical bond between the Sc_3N cluster and the C_{80} cage, and (4) a large HOMO-LUMO gap."[119] As the investigators have continued to explore the field of TNT-EMFs, new questions have emerged. For example, why does the $M_3N@C_{80}$ (I_h) always have the highest yield in the series of $M_3N@C_{2n}$ ($39 \leq n \leq 44$, M=Sc, Lu, Tm, Er, Ho, Dy, Y, Tb, and Gd) even though the size of M_3N becomes increasingly larger and even has a significant pyramidal geometry, as in the case of $Gd_3N@C_{80}$ (I_h) and $Tb_3N@C_{80}$ (I_h)? The recently reported $Nd_3N@C_{2n}$ is the first case in which $Nd_3N@C_{88}$ was shown to be dominant over the $Nd_3N@C_{80}$. However, its primary data suggest that $Nd_3N@C_{88}$ has a small HOMO-LUMO gap.[127]

1.3.3.2.5 Other TNT-EMFs: $M_3N@C_{2n}$ (M=Metals in Group III B and Lanthanide, $39 \leq n \leq 49$)

In addition to the TNT-EMFs examined in this study, many others have been reported, including: $Tm_3N@C_{2n}$ ($39 \leq n \leq 44$),[115, 119, 128] $Dy_3N@C_{2n}$ ($39 \leq n \leq 49$),[116, 129, 130] $Gd_3N@C_{80}$ (I_h),[131, 132] and $Y_3N@C_{80}(I_h)$.[133-136] Characterization studies, however, have focused primarily on the most abundant isomer, namely, $M_3N@C_{80}$ (I_h) and have typically included UV-Vis, IR, Raman, XPS, mass spectra, electrochemistry, magnetic property, and rare crystallography.

1.3.4 Endohedral Metallofullerenes ($M_x@C_{2n}$, M=metals, x=1~2) and Metallic Carbide Endohedral Metallofullerenes ($M_xC_2@C_{2n}$, M=metals, x=2~3)

$M_x@C_{2n}$ (M=metals, x=1~2) is the largest family of endofullerenes. Although the metal atom can be either Ca,[137, 138] Ba,[139] Ti,[140, 141] or Cu,[142, 143] Group III B and lanthanide elements are typically associated with endohedral metallofullerenes since they exhibit multiple ionizations.[74] In an extracted mixture of empty cage fullerenes, C_{60} (I_h),[1, 3, 8, 18] C_{70} (D_{5h}),[19] C_{76}

(D_2),[144] C_{78} (C_{2v}, D_3),[145] C_{82} (C_{2v}, C_{3v}),[146, 147] and C_{84} (D_2, D_{2d})[146, 148] are the most commonly observed fullerenes via a mass spectrum and a HPLC chromatogram, indicating they are more stable than others. However, for endohedral metallofullerenes, they generally do not adopt the fullerene cages mentioned above. For example, $La_2@C_{80}$ (I_h),[74, 149-151] $Sc_3N@C_{68}$ (D_3),[27, 28] and $Ba@C_{74}$ (D_{3h}).[139] These observations can be readily explained by the charge-transfer from the metal atoms to the fullerene cages, which would not otherwise survive in the empty cages themselves.[152] For neutral empty fullerene cages, the electrostatic potentials inside the cages are all positive. This means that the neutral empty cages are originally better suited for accommodating negative species. However, upon transferring electrons onto a fullerene cage,[153] the electrostatic potential inside the cage becomes highly negative,[74, 151, 154] making it capable of holding the cations inside. In order to identify the most suitable cage for endohedral metallofullerenes, one must assess the relative energy (thermodynamics) and HOMO-LUMO gap (kinetics) of the negatively charged cage. For example, C_{68}^{6-} (D_3) for $Sc_3N@C_{68}$ (6140, D_3)[28] and C_{80}^{6-} (I_h) for $La_2@C_{80}$ (I_h).[151] In this respect, empty cage fullerenes and endohedral metallofullerenes share a common characteristic, i.e. the most stable candidate is the one with both thermodynamic and kinetic advantages. However, with respect to a fullerene cage with negative charges, the most favorable cage isomer for it is often different from one for neutral empty cage in the same cage size. As reported, this is due to the fact that they will isomerize to their most favorable structure during the annealing process as they form.[152]

1.3.4.1 The Structure of $La_2@C_{80}$ (I_h)

The first experimental evidence (mass spectrum) for the existence of $La_2@C_{80}$ (I_h) was reported in 1991.[155] Since the only available data was the mass spectrum of $La_2@C_{80}$, the authors proposed that the two La atoms should be encapsulated in one of seven IPR isomers—based on

the principle of minimizing adjacent pentagons, namely, the pentagon adjacency penalty rule (PAPR). Instead of the oblate and quasi-spherical I_h-C_{80}, they proposed elongated or prolate structures, such as D_{5d}-C_{80} or the twisted D_2-C_{80} as the favored cages (see Figure 1-33).[155] Their reasoning for the proposed cages probably is that these cages can keep the two La cations as far away as possible. Since the empty C_{84} is a stable cage, they further proposed an electronic structure of $[La_2]^{4+}@[C_{80}]^{4-}$ so that the resulting fullerene cage can preserve the 84 P_π electron count, which is similar to that of the stable empty C_{84} fullerene cage.[155] The seven IPR isomers' structures of C_{80} are shown in Figure 1-33.

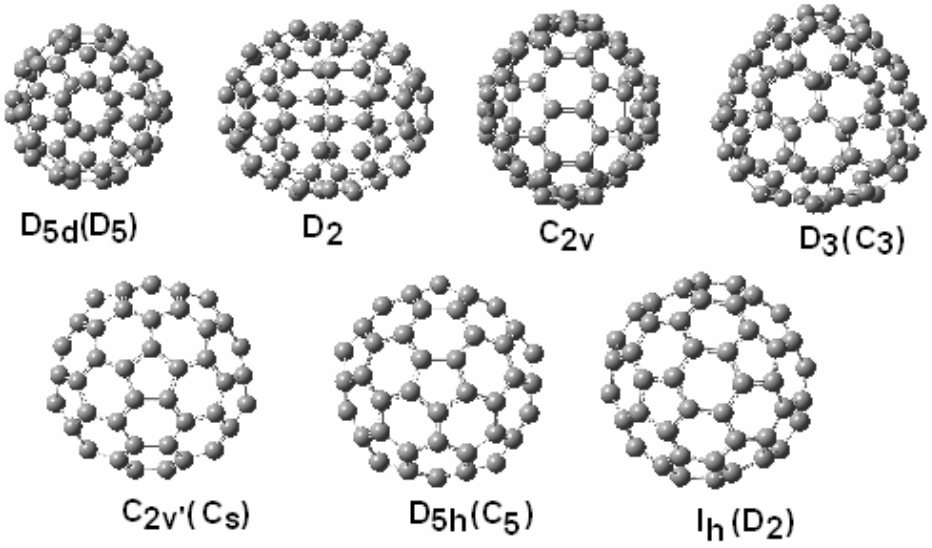

Figure 1-33. The structures and the symmetries of the seven IPR isomers of C_{80}. The relaxed lower symmetries resulting from the full structural optimization are list in parentheses.[74]

Fowler and Zerbetto calculated the negatively charged C_{80}^{n-} with n=2,4,6 for the seven IPR isomers. They found that $C_{80}^{6-}(I_h)$ had both thermodynamic and kinetic energy advantages compared with the other IPR isomers carrying different charges.[154] This finding was confirmed by ^{13}C and ^{139}La NMR spectra of $La_2@C_{80}$.[156] Thus, the electronic and geometric structure of $La_2@C_{80}$ (I_h) should be presented as $[La_2]^{6+}@[C_{80}(I_h)]^{6-}$. Figure 1-34 depicts the ^{139}La NMR spectrum of $La_2@C_{80}$. As shown, the single peak of the ^{139}La NMR spectrum suggests that the

two La atoms were equivalent. Theoretical calculations also showed that the electrostatic potential surface of the interior C_{80}^{6-} (I_h) had very smooth concentric circles without a clear local minima (see Figure 1-35) and that the barrier for the movement of La atoms was only about 5 kcal/mol (0.23 eV).[120] This smooth electrostatic potential surface further suggests that the placement of the La atoms in specific positions would not result in stable structures. Based on the ^{139}La NMR spectrum and theoretical calculations described above, the authors suggested a dynamic circular movement for the two La atoms inside the C_{80}^{6-} (I_h) (see Figure 1-35). The calculated and MEM/retrieved La-La distances were 3.655 Å[120] and 3.84 Å,[157] respectively. The circular motion of the two La atoms provides an average chemical environment for all the carbon atoms of the C_{80}^{6-} (I_h).[157] Thus, the ^{13}C NMR of the $La_2@C_{80}$ (I_h) would display minimum peaks due to the highest symmetry of the C_{80}^{6-} (I_h). However, the experimental ^{13}C NMR of $La_2@C_{80}$ (I_h) only showed one peak[156] (see Figure 1-36), although theoretically it should have had two peaks with a 3:1 ratio of the peak areas (60 atoms of [665] junctions and 20 atoms of [666] junctions).[54, 107]

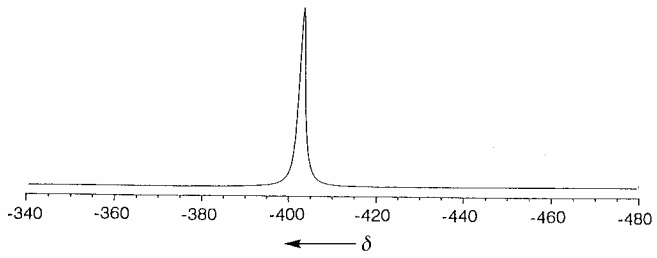

Figure 1-34. ^{139}La NMR spectrum of $La_2@C_{80}$ (I_h) (reprinted from Ref. [156]).

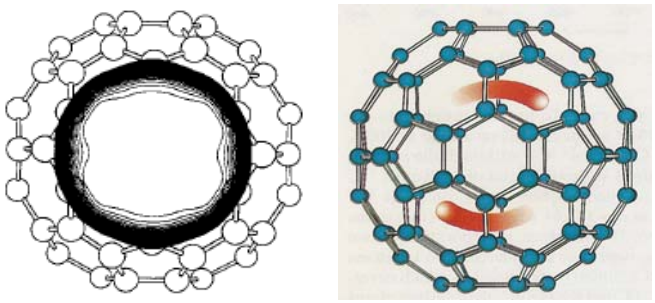

Figure 1-35. Left: The demonstration of the electrostatic potential surface inside the C_{80}^{6-} (I_h) (reprinted from Ref.120). Right: The dynamic circular movement of the two La atoms in C_{80}^{6-} (I_h) (Reprinted from Ref. [156]).

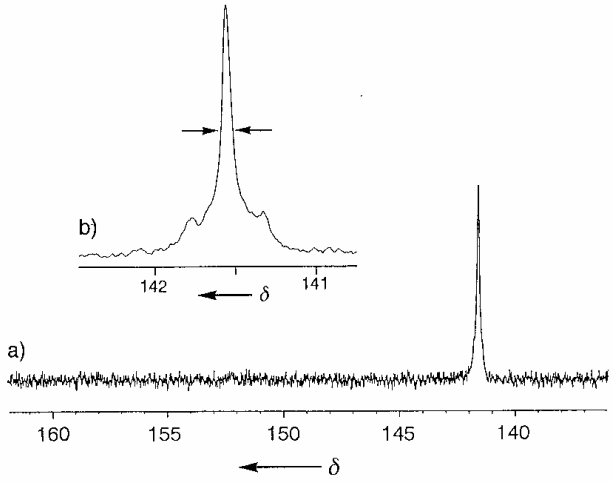

Figure 1-36. The experimental ^{13}C NMR spectrum of $La_2@C_{80}$ (I_h) (reprinted from Ref. [156]).

Kobayashi and Nagase calculated the structures of $M_2@C_{80}$ for other metals in Group III B and lanthanide.[74, 151] They found that the stability, structure and electronic states of $M_2@C_{80}$ are all strongly metal dependent. For example, $Sc_2@C_{80}$ (I_h) can only be expressed as $[Sc_2]^{4+}@[C_{80}\ (I_h)]^{4-}$. Thus, the four-fold HOMO orbitals cannot be fully occupied and will result in a low-energy LUMO orbital with small HOMO-LUMO gap, which leads to high reactivity for $Sc_2@C_{80}$ (I_h). The experimental evidence for the existence of $Sc_2@C_{80}$ (I_h) is, as yet, undiscovered.

With the development of fullerene research, several endohedral metallofullerenes—originally reported with a molecular formula of $M_x@C_{2n}$ (x = 2 ~ 3)—were instead found to be

metallic carbide endohedral metallofullerenes with a molecular formula of $M_xC_2@C_{2n}$ (x = 2 ~ 3). Examples include $Sc_3@C_{82}$[158, 159] vs. $Sc_3C_2@C_{80}$ (I_h),[160, 161] $Sc_2@C_{86}$[162] vs. $Sc_2C_2@C_{84}$ (D_{2d}),[163] and $Sc_2@C_{84}$ (III)[164] vs. $Sc_2C_2@C_{82}$.[165, 166] These misinterpretations could be the result of several factors, including complicated ^{13}C NMR due to low symmetric fullerene cages, the low resolutions of available instruments, as well as lack of understanding of the structures of fullerenes.

1.3.4.2 The Structure of $Sc_2C_2@C_{84}$ (D_{2d})

The first confirmed metallic carbide endohedral metallofullerene was identified as $Sc_2C_2@C_{84}$ (D_{2d}), which was reported by the Shinohara group via ^{13}C NMR and maximum entropy method (MEM) /X-ray powder diffraction techniques.[163, 167] $Sc_2C_2@C_{84}$ (D_{2d}) was previously reported as $Sc_2@C_{86}$ (I) by the same research group.[162]

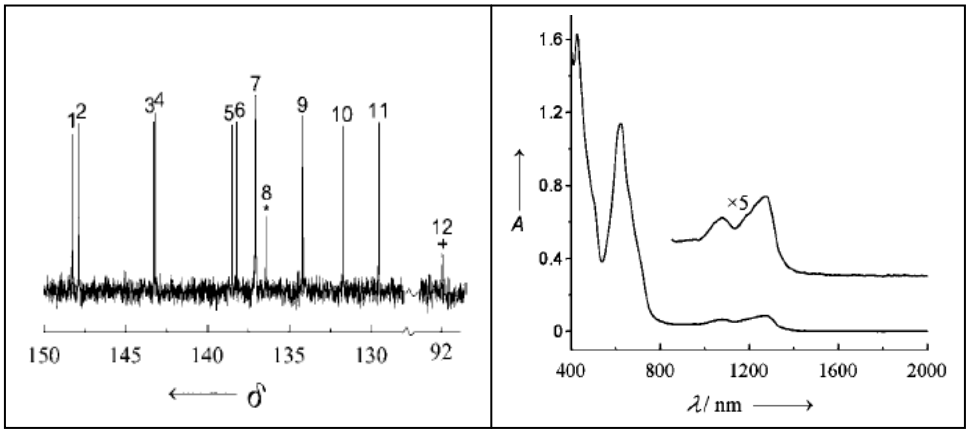

Figure 1-37. ^{13}C NMR spectrum (left) and UV/Vis/NIR spectrum (right) of $Sc_2C_2@C_{84}$ (D_{2d}) (reprinted from Ref.[167]).

As shown by ^{13}C NMR (Figure 1-37), there were a total of 12 lines in the pattern of (10×8, 1×4, 1×2) using the following notation: ([number of NMR lines] × [number of carbon atoms]). Line 12, showing an intensity of two carbon atoms, is attributed to the two carbon atoms of the core cluster Sc_2C_2. The other 11 lines (10×8, 1×4) are due to the C_{84} (D_{2d}) cage, which is the No. 23 IPR isomer of C_{84}. The assignment of the ^{13}C NMR spectrum was confirmed by

maximum entropy method (MEM) /X-ray powder diffraction measurement, which is shown in Figure 1-38.

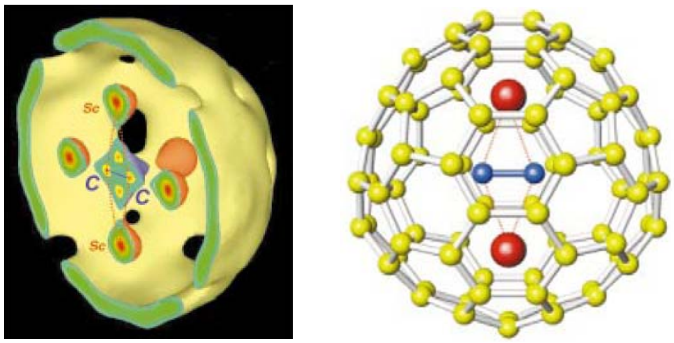

Figure 1-38. Left: The half section of the iso-electronic density (1.9 e $Å^{-3}$) surface of $Sc_2C_2@C_{84}$ (D_{2d}). Right: The structure of $Sc_2C_2@C_{84}$ (D_{2d}). Sc-Sc, C-C, and Sc-C distances in the Sc_2C_2 core cluster are 4.29(2) Å, 1.42(6) Å, and 2.26(3) Å, respectively. For comparison, the C-C distance connecting two pentagons in C_{60} and the Sc-C distance in ScC_2 cluster are 1.43Å and 2.135Å, respectively (reprinted from Ref.[167]).

1.3.4.3 The Structure of $Sc_3C_2@C_{80}$ (I_h)

The existence of $Sc_3@C_{82}$ was first reported by the Shinohara group in 1992,[168] but its structural determination using MEM/Rietveld analysis was not reported until 1999.[169] As they documented in 1999, an equilateral triangle of the Sc_3 trimer was encapsulated in an IPR C_{82} (C_{3v}) cage and the Sc-Sc distance was 2.3(3) Å. From an MEM charge density analysis, its electronic structure was presented as $Sc_3^{3+}@C_{82}^{3-}$.[169] However, prior theoretical calculations had anticipated different electronic and geometric structures,[170] namely an electronic structure of $[Sc_3]^{6+}@C_{82}^{6-}$ and a much longer Sc-Sc distance (about 3.6 Å). They also predicted that encapsulation of the Sc_3 trimer in the IPR C_{82} (C_{3v}) would not be the most favorable structure.[170]

As indicated above, theoretical calculations and MEM/Rietveld analyses delivered completely different electronic and geometric structures, prompting further investigation of this interesting molecule. Akasaka and Nagase, in fact, presented a revised research result for Sc_3C_{82} molecule in 2005.[171] Since the Sc_3C_{82} is an EPR active molecule, it is a paramagnetic molecule. Thus, obtaining its ^{13}C NMR spectrum is challenging. However, by reducing Sc_3C_{82} to its

diamagnetic anion $[Sc_3C_{82}]^-$ form, an NMR spectrum of $[Sc_3C_{82}]^-$ was obtained. This ^{13}C NMR spectrum clearly suggested that the fullerene cage of $[Sc_3C_{82}]^-$ is a C_{80} (I_h) cage with 2 peaks showing a ratio of 3:1 peak areas (see Figure 1-39).[171] Therefore, its structure should be $Sc_3C_2@C_{80}$ (I_h) with an electronic state of $[Sc_3C_2]^{6+}@[C_{80}(I_h)]^{6-}$. This structure was confirmed by the single crystal X-ray diffraction measurement of its functionalized product (see Figure 1-40).[171] Later on, the structure of $Sc_3C_2@C_{80}$ (I_h) was also confirmed by the MEM/third generation synchrotron radiation X-ray powder diffraction (see Figure 1-41), which documented that the Sc-Sc distance was 3.61(3) Å in the Sc_3 triangle, while the distance between the Sc and the center of C_2 in the core Sc_3C_2 cluster was 2.07(1) Å.[172]

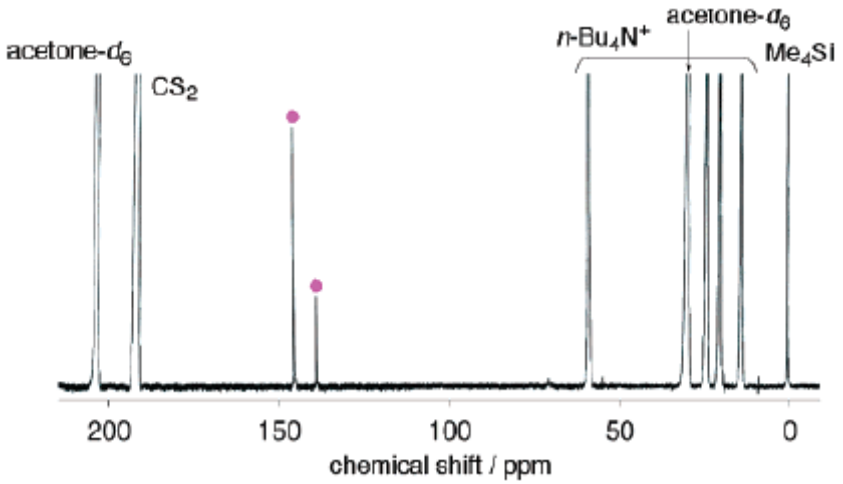

Figure 1-39. ^{13}C NMR spectrum of [n-Bu_4N]+[$Sc_3C_2@C_{80}$ (I_h)]$^-$. The peaks marked with • are due to the sixty [665] and twenty [666] carbon atoms of C_{80} (I_h) (reprinted from Ref. [171]).

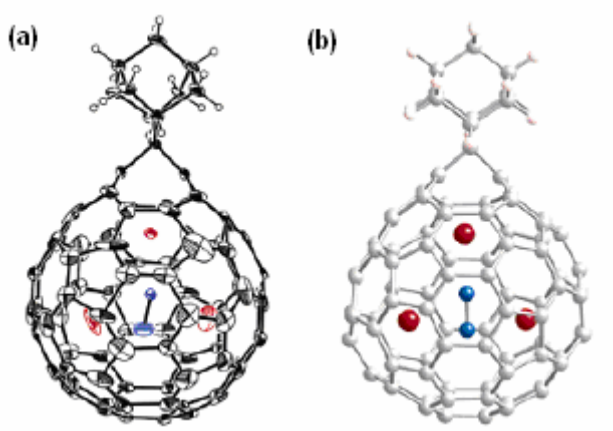

Figure 1-40. (a) Single crystal X-ray diffraction structure of the adamantylidene carbine functionalized $Sc_3C_2@C_{80}$ (I_h). (b) Optimized structure of (a). (reprinted from Ref. [171])

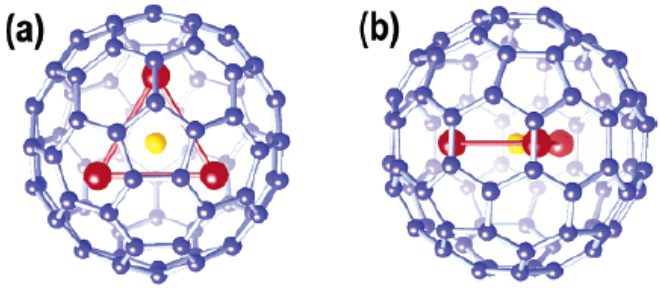

Figure 1-41. Two views of the molecular structure of $Sc_3C_2@C_{80}$ (I_h) determined by the MEM/Rietveld analysis using third generation synchrotron radiation X-ray powder diffraction (reprinted from Ref. [172]).

1.4. Endohedral Metalloheterofullerenes

"Heterofullerenes are fullerenes in which one or more carbon atoms on the cage structure are replaced by non-carbon atoms, i. e. by heteroatoms such as nitrogen, boron, silicon, etc." [78] Replacing carbon atoms with heteroatoms on a fullerene cage will result in significant modifications of its geometry, as well as the chemical functionality and electronic characteristics of the fullerenes. Thus, the resulting heterofullerenes are likely to possess new physico-chemical properties,[77, 173, 174] including altered electronegativity, better funtionalization ability, etc.

When a carbon atom is replaced by a nitrogen atom and a boron atom, the resulting molecules are called azafullerenes and borafullerenes, respectively. Although heterofullerenes have been synthesized via the laser-ablation method [175] and the arc-discharge method,[176] neither

of them have been shown to produce macroscopic yields.[78, 82] Most of the heterofullerene research focuses on the azafullerenes since the macroscopic yield is available by conventional organic synthetic processes.[78, 79, 173, 175]

Although several empty azafullerenes or dimers have been reported, endohadral metalloazafullerenes have only rarely been discussed. In fact, $La@C_{81}N$ and $La_2@C_{79}N$ are the only endohedral metalloazafullerenes reported so far.[21] The mass signals of $La@C_{81}N^+$ and $La_2@C_{79}N^+$ were observed in the gas phase by firing their corresponding adducts, $La@C_{82}(NCH_2Ph)$ and $La_2@C_{80}(NCH_2Ph)$, respectively, via fast atom bombardment mass (FABMS) fragmentation (see Figure 1-42).[21] The replacement of one carbon atom with a nitrogen atom on the cages of $La@C_{82}$ and $La_2@C_{80}$ (I_h) have been confirmed by the FABMS fragmentations of their ^{15}N isotope labeled adducts, $La@C_{82}(^{15}NCH_2Ph)$ and $La_2@C_{80}(^{15}NCH_2Ph)$, respectively (see Figure 1-43). Due to their special structures and potential applications in the field of quantum dots, endohedral metalloazafullerene are likely to be more fully investigated in the future.

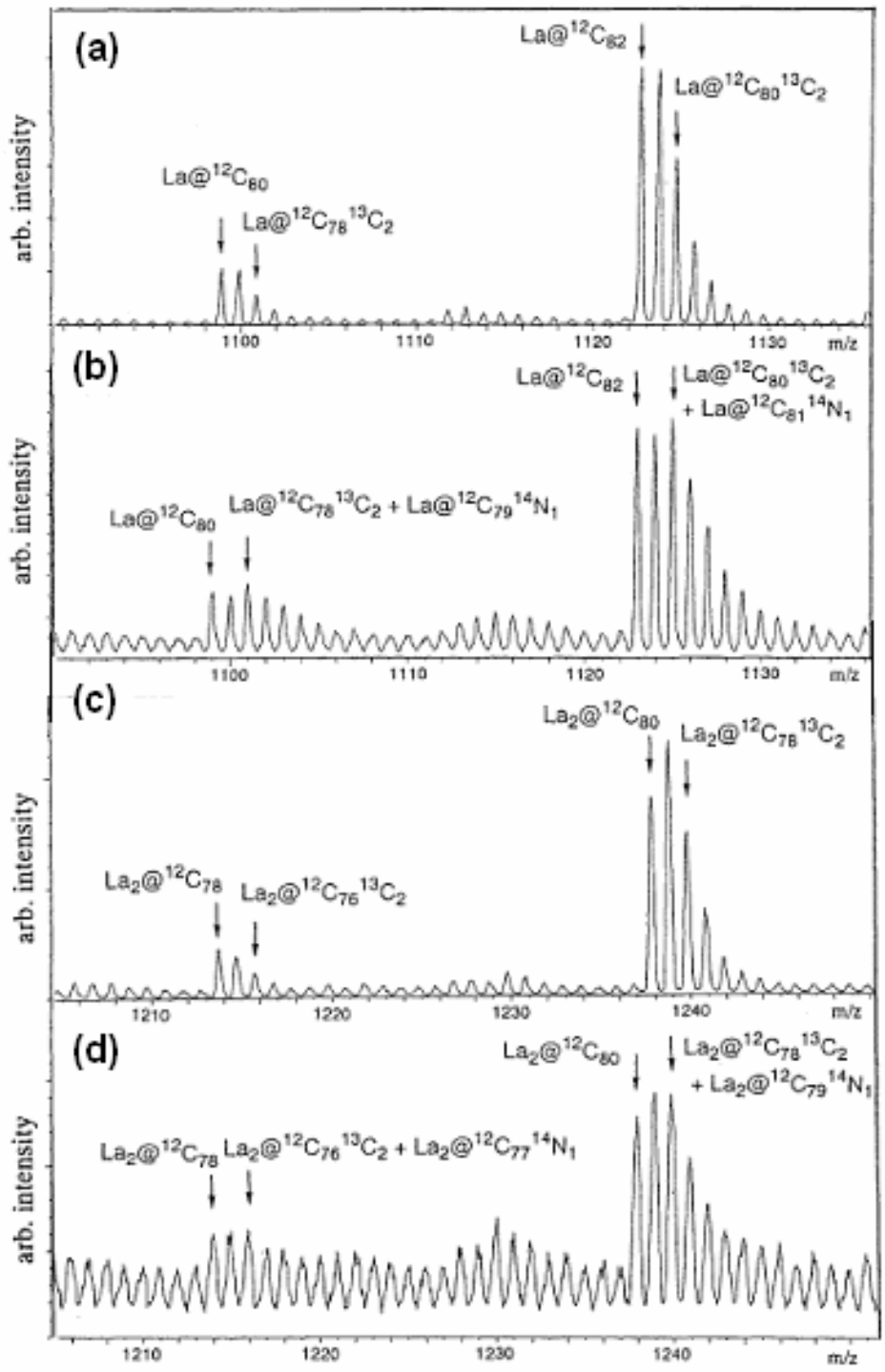

Figure 1-42. FABMS fragmentation spectra of (a) La@C_{82}, (b) La@C_{82}(NCH_2Ph), (c) La_2@C_{80}, and (d) La_2@C_{80}(NCH_2Ph) (reprinted from Ref. 21). By comparison of (a) and (b) as well as (c) and (d), the replacement of a carbon atom with a nitrogen atom on the cages of La@C_{82} and La_2@C_{80} was clearly demonstrated by the enhancement of the (M+2) peak.

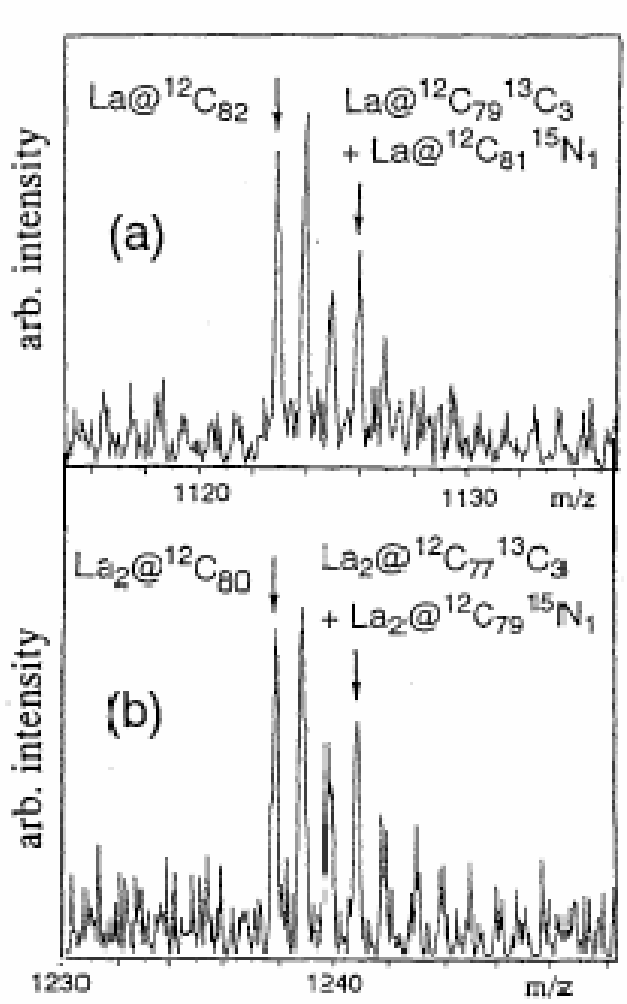

Figure 1-43. FABMS fragmentation spectra of (a) La@C_{82}($^{15}NCH_2Ph$), (b) La_2@C_{80}($^{15}NCH_2Ph$), (reprinted from Ref. 21). The replacement of a carbon atom with a nitrogen atom on the cages of La@C_{82} and La_2@C_{80} was clearly demonstrated by the enhancement of the (M+3) peak due to their ^{15}N isotope labeled adducts.

Chapter 2 — Research Overview

Based on a comprehensive review of the literature, it is clear that the TNT-EMF family of endofullerenes produces higher yields and exhibits better air and temperature stability[31, 107, 177, 178] compared to other endohedral metallofullerenes. These attractive features make them ideal candidates for a variety of important applications.[179, 180] Among the TNT-EMFs reported thus far, the following well-characterized compounds have had their structures fully documented: $M_3N@C_{80}$ (I_h) (M=Sc,[107] Tb,[181] Lu,[182] Gd,[183] Dy[129]), $M_3N@C_{80}$ (D_{5h}) (M=Sc,[121] Tb[181]), $Sc_3N@C_{68}$ (D_3),[28] $Sc_3N@C_{78}$ (D_{3h}),[109] $Er_2ScN@C_{80}$ (I_h),[108] and $CeSc_2N@C_{80}$ (I_h).[177] In the current research effort, $M_3N@C_{80}$ (D_{5h}) (M=Sc, Tb), $Tb_3N@C_{80}$ (I_h), and $CeSc_2N@C_{80}$ (I_h) have been characterized. Except for $Sc_3N@C_{68}$ (D_3), $Sc_3N@C_{78}$ (D_{3h}), and $M_3N@C_{80}$ (D_{5h}) (M=Sc, Tb), these well-characterized structures all have a C_{80} (I_h) cage with the formula $A_{3-x}B_xN@C_{80}$ (I_h) (x = 0 ~ 3), which is the most abundant structure due to the outstanding thermodynamic and kinetic stability of C_{80}^{6-}(I_h).

Recently, other investigators have reported two families of Tm and Dy based TNT-EMFs, namely $Tm_3N@C_{2n}$ ($39 \le n \le 43$)[184] and $Dy_3N@C_{2n}$ ($39 \le n \le 44$),[116] despite the fact that experimental evidence for these two families of molecules was confirmed by HPLC traces, mass spectra, and UV-Vis spectra, their structures were not elucidated. This study, therefore, has focused on the Tb and Y based TNT-EMFs, with the goal of determining the structures for these TNT-EMFs and their related dimetallic endohedral metalloazafullerenes.

The challenges for this research are to obtain enough isomerically pure samples and to characterize their structures based on the limited amount of sample. Following the research process, the research focus and challenges are as follows.

2.1 Research Focus on Synthesis and Isolations

With respect to "obtaining enough isomerically pure sample," this research faces several barriers. First, the yield of endohedral metallofullerenes is very low, which has frustrated scientists working in fullerene research—especially those engaged in applied research.[108] Although $Sc_3N@C_{80}$ (I_h) (also $Lu_3N@C_{80}$ (I_h)) has the highest yield among all the endohedral metallofullerenes, its yield is still only about 10~15 % of the total fullerene mixture under optimized experimental conditions according to the peak areas in HPLC chromatograms of toluene extracts from the raw soots.[54] Generally, the total fullerene mixture yield is 5~15% for metal Sc and Lu via the TNT process; but for other Group III B elements and lanthanides, the total fullerene mixture yield is suppressed to less than 1%. For Y, and Tb in this research, the yield for even the most abundant component, $M_3N@C_{80}$ (I_h) (M=Y, and Tb), was only about 1~3% of the total fullerene mixture in the extract. Furthermore, this research mostly focused on the larger cage (> C_{80}) TNT-EMFs. However, the yields for these larger cage TNT-EMFs generally represented only about 1~5% of the corresponding $M_3N@C_{80}$ (I_h), which is the most abundant component of the selected metal-based TNT-EMFs. For the Y, and Tb based larger cage TNT-EMFs in this research, the final available amount was about 0.1~0.3 mg, which was separated from the fullerene mixture in raw soot extract by vaporizing about 100 quarter inch rods (6.4 mm in diameter×152 mm in length) packed with selected metal oxides and catalyst. Obtaining even this small amount of sample required intensive lab work, synthesis and isolation over the course of several months. Second, the components of the extract were quite complicated. For example, the extract from the raw soot produced via the TNT process by vaporizing metal-doping graphite rods generally contained C_{2n} ($n \geq 30$) empty cage fullerenes (~ 95%),[54] $M_x@C_{2n}$ ($x = 1 \sim 3$, $n \geq 30$) classical endohedral metallofullerenes, and $M_3N@C_{2n}$ (M is the Group III B and lanthanide) TNT-EMFs (about 1 ~ 3%). TNT-EMFs are normally co-eluted

with large empty cage fullerenes and classical endohedral metallofullerenes, which may exist as several isomers. Therefore, the purification process for each isomeric sample was very difficult at best, and practically impossible in some cases. The primary chemical separation process utilized in this research kinetically removed the reactive empty cage fullerenes and reactive classical endohedral metallofullerenes.[185] Using such a process, the co-elution behavior of TNT-EMFs became much simpler than that of the original extract. Furthermore, after removing most of the abundant empty cage fullerenes, the surviving TNT-EMFs could be concentrated by vaporizing the solvent. As a result, the isolation process using HPLC became much more efficient. However, the process of chemical separation was only the first step in accessing a viable sample. In order to isolate an isomerically pure samples, a two-stage HPLC process involving complementary columns and cycling processes was used. Separations easily accounted for 40% to 50% of this research work. Third, the air stability of some components in the samples was uncertain. During the HPLC purification process, in fact, frequent filtration of the injection samples was required, suggesting that some components of the samples were not very stable in air and were oxidized or polymerized to insoluble materials.[108]

2.2 Research Focus on Structural Characterization

Even after a pure isomeric sample was obtained, another challenge involved the structural characterization of the molecule. Since the available amount of a pure sample was often only in the 0.1~0.3 mg range, available methods for its structural determination were quite limited. Generally, due to a sample's paramagnetic property, the limited sample size, and the lower symmetries of the large cage endofullerenes, NMR spectroscopy was often useless for most of the samples in this research. Therefore, we often had to rely on structural characterization via single crystal X-ray diffraction. The quasi-spherical shape of a fullerene molecule makes it rotate

with a very small energy barrier.[107, 108] Consequently, crystallizing the fullerenes themselves will result in the disorder of their structural data. Therefore, the co-crystallization of fullerene molecules and organometallic agents by means of inter-molecular interactions, which fix the orientations of fullerene cages, led to the success in the structural characterization of several larger cage TNT-EMFs in this research work in spite of the failure to do so in some other very precious samples.[31, 181] Via use of a home-made crystallization device, this research was most productive in obtaining the single crystal for the X-ray diffraction analysis in the field of fullerene research, especially using trace amounts of sample at 0.1 mg levels.[31, 121, 177, 181]

In addition to isolating the novel TNT-EMFs, other new classical endohedral metallofullerenes have also been isolated. The structural characterization of the new classical endohedral metallofullerenes may demonstrate new fascinating aspects for this seemingly well-developed research field.

With the isolation and characterization data of several series of TNT-EMFs and consideration of the retention mechanism of the different HPLC columns, this research also endeavored to associate the retention behavior of the isolated endohedral metallofullerenes with their geometric and electronic structures.[186] Understanding these associations will enable researchers to obtain valuable structural information—even during the sample purification stage—based on these retention behavior and mass spectrum data.

Heterofullerenes are fullerenes in which one or more carbon atoms on the cage are replaced by non-carbon atoms, e.g. heteroatoms such as nitrogen. The substitution of a carbon atom by a nitrogen atom leads to an unstable radical structure, and dimerization of two unstable radicals forms a dumbbell-like stable structure as typified by $(C_{59}N)_2$.[79] Interestingly, however, the metal-doped azafullerenes have rarely been reported. In effect, the only reported

azafullerenes were $[La_2@C_{79}N]^+$ and $[La@C_{81}N]^+$ fragments, which were observed in the gas phase via fast atom bombardment (FABMS) fragmentation by bombing their corresponding precursors.[21] Therefore, actual endohedral metalloazafullerenes have never been isolated. Due to the special electronic states of endohedral metalloazafullerenes, they are expected to have novel properties. In order to develop their potential applications, it would be essential to isolate these metal-doped azafullerenes. Therefore, another important aspect of this research involved the introduction of a nitrogen source in the TNT process to synthesize endohedral metalloazafullerenes. The identification and isolation of this type of molecule represents an important chapter in this research.

As computational chemistry becomes more important and technologically more powerful in the 21st century,[43] tremendous efforts have also been made in theoretical calculations to understand and interpret the novel structures and properties of the new types of endohedral metallofullerenes disclosed in this research.

2.3 Outline of Current research

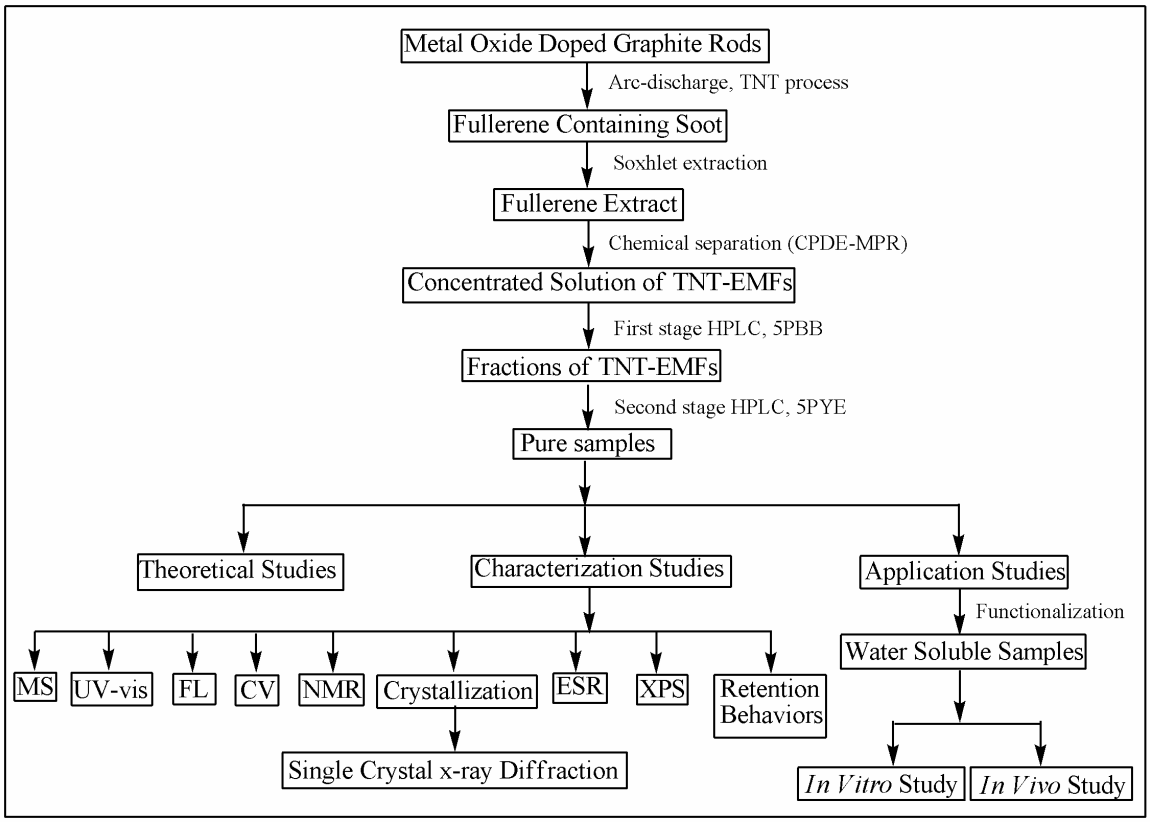

Figure 2-1. Outline of current research.

In summary, this research emphasizes the exploration and well-structured characterization of novel endohedral metallofullerenes and endohedral metalloheterofullerenes which are typically in the nanometer scale. Specifically, well developed synthesis, separation, and crystallization processes, as well as the theoretical calculations and other analytical techniques in this research provide an effective way to further explore previously unknown, and now highly intriguing, nanometer sized novel endohedral metallofullerenes. These novel nano-particles may have special potential applications in electronic, material, and medical fields in the future.

2.4 The Highlights of Research Results

The highlights of results in this research are listed below:

Published structures of endohedral metallofullerenes:

$Tb_3N@C_{80}$ (I_h) $Tb_3N@C_{80}$ (D_{5h}) $Tb_3N@C_{86}$ (D_3) $Tb_3N@C_{88}$ (D_2)	*JACS*, **2007**, *129*, 2035~2043
$Tb_3N@C_{84}$ (C_s)	JACS, **2006**, *128*, 11352~11353
$CeSc_2N@C_{80}$ (I_h)	*JACS*, **2006**, *128*, 8884~8889
$Sc_3N@C_{80}$ (D_{5h})	*JACS*, **2006**, *128*, 8581~8589
Methano monoadducts of $Sc_3N@C_{80}$ (I_h)	*JACS*, **2007**, *129*, 15710~15717
$Tm_3N@C_{84}$ (C_s)	*Chem. Comm.,* In press

To be published structures of new endohedral metallofullerenes:

$Tm_2@C_{82}$ (C_s)	$Y_3N@C_{80}$ (I_h)
$Tm@C_{94}$ (C_{3v})	$Y_3N@C_{84}$ (C_s)
$Tm_3N@C_{80}$ (I_h)	$Y_3N@C_{86}$ (D_3)
$Tm_3N@C_{80}$ (D_{5h})	$Y_3N@C_{88}$ (D_2)
$Tm_3N@C_{86}$ (D_3)	$Ho_3N@C_{80}$ (I_h)
$Tm_3N@C_{88}$ (D_2)	$Er_3N@C_{80}$ (I_h)

To be published novel structures of endohedral metalloazafullerenes and metallic oxide endohedral metallofullerenes:

$Tb_2@C_{79}N$	$Y_2@C_{79}N$
$La_2@C_{79}N$	$Y_2O@C_{74}$
$Tb@C_{81}N$	$La@C_{81}N$

Patent (Pending):

(a) A New Class of Endohedral Metalloheterofullerenes, $M_2@C_{79}N$ (M=Group III B or Lanthanide Metal)

(b) Trimetallic Nitride Clusters Entrapped within C_nN Heteroatom Cages and Method for Making the Same using Oxidizing Gas and Combustion

Chapter 3 — Synthesis, Isolation, and Characterization of Tb-based TNT-EMFs, $Tb_3N@C_{2n}$ ($40 \leq n \leq 44$)

3.1 Introduction

Endofullerenes represent atoms and/or clusters encapsulated inside a fullerene carbon cage and have been the focus of many recent investigations.[6, 86, 107, 160, 178] During the past 10-15 years, several Group III B and lanthanide ions[187] encapsulated inside carbon cages have been prepared via the Krätchmer-Huffman electric arc-process. Due to their *f*-electron configurations, the lanthanides have many special physico-chemical properties such as magnetic properties, unique optical properties (fluorescence, activator/sensitizer for laser host materials, and luminescence), as well as large atomic cross sections.[188] Also, gadolinium containing endohedral metallofullerenes have been reported as promising next generation magnetic resonance imaging (MRI) contrast agents.[179]

In 1999, $Sc_3N@C_{80}$ was discovered in the Dorn laboratory, and numerous other trimetallic nitride template endohedral metallofullerenes (TNT-EMFs) have also been reported.[54, 107, 108, 189] The initially discovered TNT-EMFs were documented to have eighty carbons and I_h symmetry, but other cage sizes have also been reported, including $Sc_3N@C_{68}$ (D_3)[28] in 2000 and $Sc_3N@C_{78}$ (D_{3h})[109] in 2001. Recently, the existence of additional isomer, D_{5h}, of the $Sc_3N@C_{80}$ has been confirmed by X-ray crystallography.[121] Detailed single-crystal X-ray structural information about lanthanide TNT-EMFs has been limited to $Gd_3N@C_{80}$ (I_h),[183] $Lu_3N@C_{80}$ (I_h)[182] and mixed metal $CeSc_2N@C_{80}$ (I_h)[177] and $Er_2ScN@C_{80}$ (I_h).[108] The TNT-EMFs with C_{80} (I_h) generally have the highest yields compared to other related TNT-EMFs, therefore, it is

generally easier to obtain necessary amounts of samples for growing crystals and subsequent crystallographic analysis.

Two families of TNT-EMFs, Tm-based and Dy-based, with C_{80} and larger cages have been reported by Dunsch and coworkers.[116, 184, 190, 191] However, their characterization methods, including mass spectrum, UV-Vis, FTIR, Raman, XPS spectroscopy, and cyclic voltametry, have been unable to provide any conclusive structural information for these larger cage TNT-EMFs. In summary, besides the relatively abundant C_{80} (I_h) caged TNT-EMFs, the only other family of TNT-EMFs that has been structurally well characterized is the Sc-based TNT-EMFs, including $Sc_3N@C_{80}$ (I_h and D_{5h}), $Sc_3N@C_{68}$ (D_3), and $Sc_3N@C_{78}$ (D_{3h}).

With respect to the four-member Sc-based TNT-EMF family, the Sc_3N cluster always maintains a planar structure in the fullerene cages because of the small size of the Sc atom. Except for the $Sc_3N@C_{68}$ (D_3), the other three members all have a fullerene cage obeying IPR. The fullerene cage of $Sc_3N@C_{68}$, however, is a non-IPR structure because all fullerene cages smaller than C_{70} cannot satisfy IPR— the only exception being C_{60} (I_h). Based on these observations, we have attempted to answer the following research questions during the course of this investigation:

1. When larger lanthanide metals form TNT-EMFs, what size fullerene cage will they choose?

2. If IPR fullerene cages are available, does the M_3N cluster always choose the IPR-obeying fullerene cages?

3. Does an M_3N cluster always maintain a planar structure?

To further explore these issues, we selected the middle-sized lanthanide metal, Tb, to synthesize the corresponding TNT-EMFs and to carry out systematic studies of Tb-based TNT-EMFs.

3.2 Results and Discussions

3.2.1 Preparation of $Tb_3N@C_{2n}$ (n = 40 ~ 44)

Raw soot containing the $Tb_3N@C_{2n}$ (n = 40 - 44) family of endofullerenes was synthesized in an arc-discharge generator by vaporizing composite graphite rods containing a mixture of Tb_4O_7, graphite powder, and iron nitride (Fe_xN) with a weight ratio of 2.03:1.0:0.4, respectively. Together with the graphite tube for packing the mixture, the molar ratio of Tb:C was about 3%. The arc-discharge process was conducted in a dynamic flow of helium (280 Torr) and dinitrogen (20 Torr). The pressure was ~ 300 Torr at the start of the arc-discharge. The raw soot was extracted using toluene as a solvent in a Soxhlet extractor for 20 hours. In order to compare the synthesis effect, we also conducted a controlled arc discharge experiment without packing Tb_4O_7. The HPLC chromatograms of the extracts are shown in Figure 3-1. By comparing (a) and (b) of Figure 3-1, one peak after C_{84} in Figure 3-1b showed some bulging. The mass spectrum in Figure 3-2 confirmed that the Tb-related endofullerenes were synthesized.

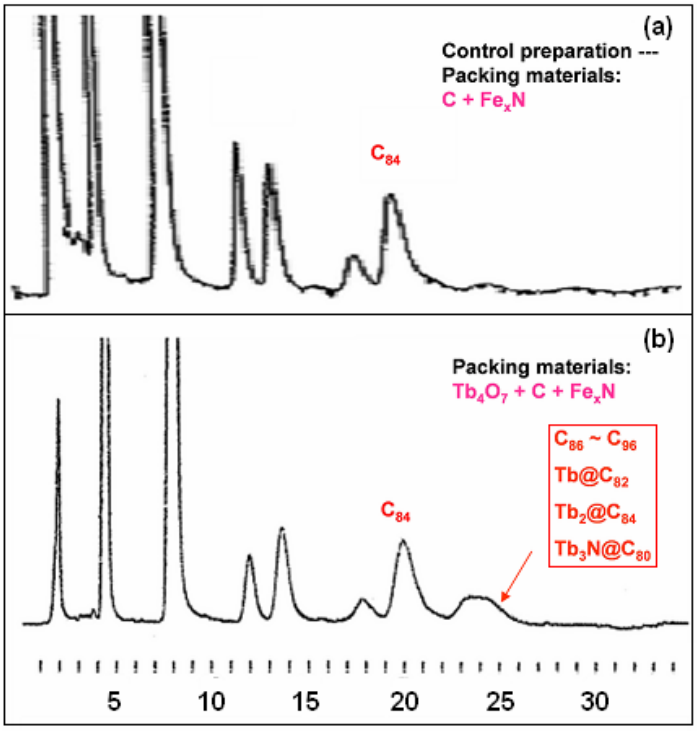

Figure 3-1. HPLC chromatograms of the control experiment extract (a) and the Tb-based extract (b). The peak containing $Tb_3N@C_{80}$ after C_{84} in (b) is generally about 2~3% of the total peak area.

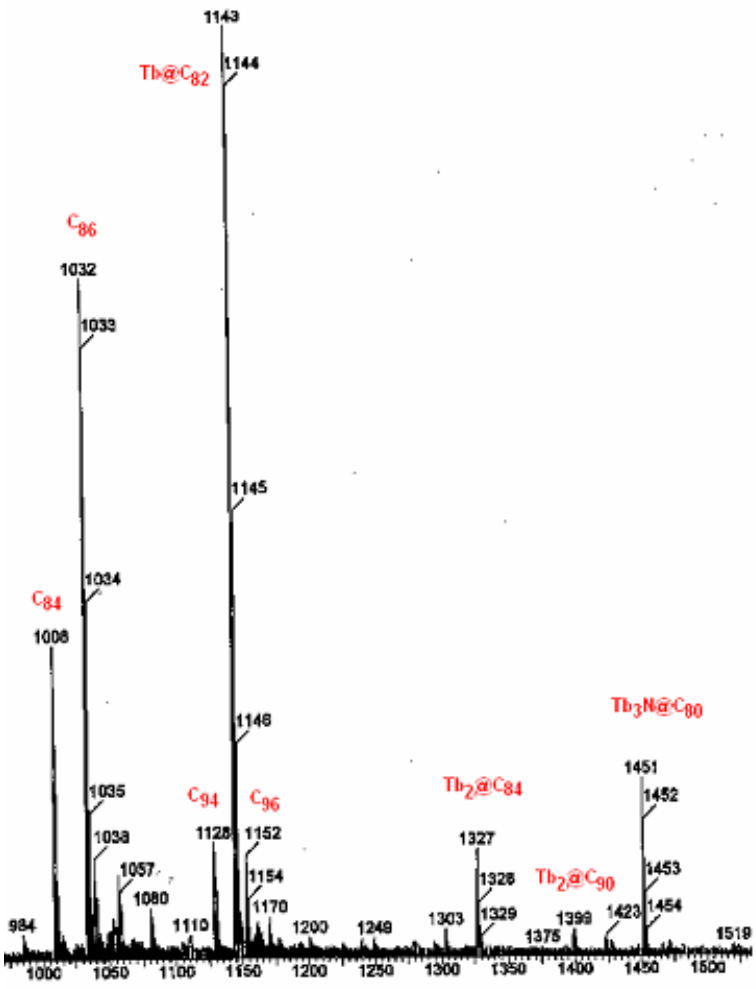

Figure 3-2. The negative DCI mass spectrum of the peak after C_{84} in Figure 3-1b.

Figure 3-2 demonstrates that $Tb_3N@C_{80}$ was not a main component in the peak after C_{84} in Figure 3-1b, as its yield was generally very low. To achieve higher TNT-EMFs yields, synthetic conditions were optimized in the following way.

3.2.1.1 Optimization of Synthesis Conditions

The synthesis of macroscopic amounts of fullerenes generally uses the arc-discharge method, which features a variety of important factors. These include choice of cooling gas and its supply method, total cooling gas pressure, partial pressure of dinitrogen in TNT process, packing materials, pre-processing of the packed rod, catalyst, electric current and voltage, etc.

With respect to the choice of cooling gas, helium typically affords a much higher fullerene yield than other noble gases such as argon. Electric current and voltage were generally set at 105 Amperes and 32 Volts (controlling the gap between the anode and cathode) for a high enough temperature of vaporizing graphite rod, maintaining stable plasma, and consuming speed of the packed rods. The other variables are discussed in greater detail below.

Static Method versus Kinetic Method: Supplying the cooling gas and the nitrogen source of dinitrogen can use the static or dynamic method. For the synthesis of Tb-based TNT-EMFs, the dynamic method provides much higher yield of extract than static method. The relative yield refers to the normalized peak area to C_{84} peak area. The ratio of $(A_1/C_{84})_{static}$: $(A_2/C_{84})_{dynamic}$ was about 0.5 in Figure 3-3. Thus, taking into account the extract yield and the relative yield of the peak containing $Tb_3N@C_{80}$, the dynamic method affords a much higher yield of TNT-EMF than the static method.

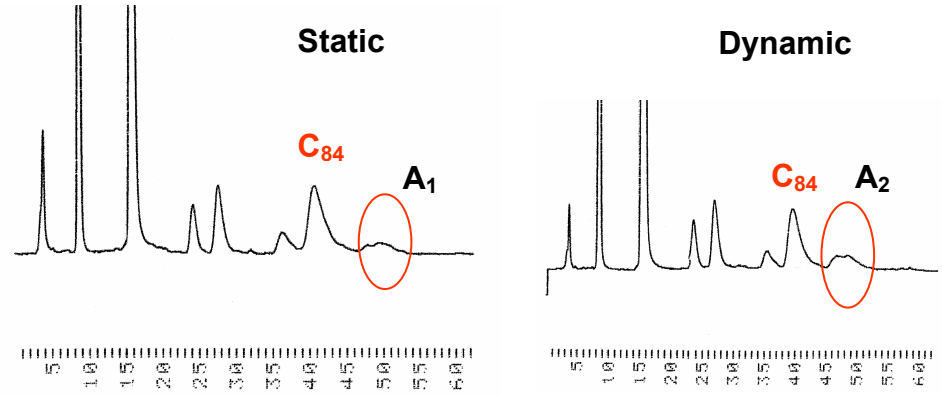

Figure 3-3. Comparison of the relative yields of Tb-based TNT-EMF in static and dynamic methods.

Pre-processing of the Packed Rods — Temperature Effect: The packed rods were preheated at 600 °C and 1000 °C in a dinitrogen atmosphere for 12 hours. The extract yields for both kinds of rods, which were processed at different temperatures, were very good. However, the ratio of relative yields of $(A_2/C_{84})_{1000\ °C}$ to $(A_1/C_{84})_{600\ °C}$, was about 1.5, suggesting that the preheating

process at a higher temperature was better than at a lower temperature. Possible reasons for this include the fact that the packed materials (carbon, Tb_4O_7, and Fe_xN) may have reacted to produce terbium carbide or nitride at a high temperature and that the terbium carbide or nitride may have functioned as seeds in the formation process of classical endofullerenes and TNT-EMFs. Nevertheless, the packed rods preheated at a higher temperature produced higher yields of endofullerenes.

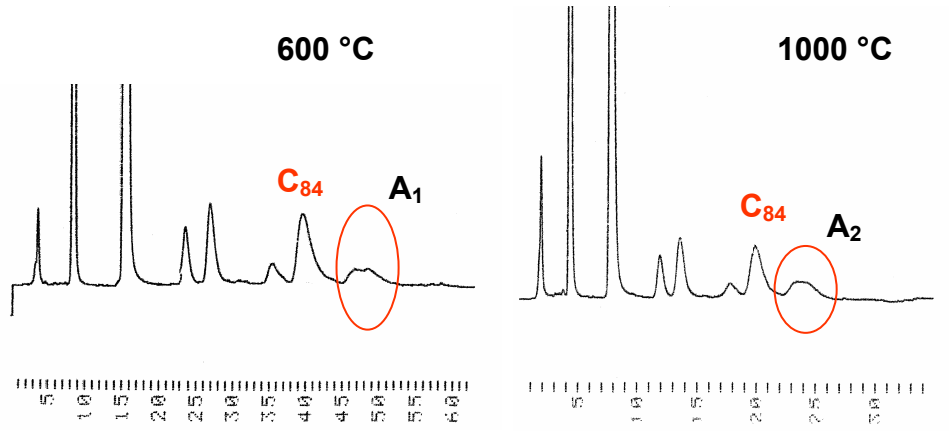

Figure 3-4. Comparison of the temperature effect in the pre-processing of packed rods.

Plasma modifier: Fe_XN (x = 2 ~ 4) versus CuO. The plasma modifiers used in this experiment, Fe_xN and CuO, afforded similar extract yields and similar relative yields (see Figure 3-5). The ratio of relative yields of $(A_2/C_{84})_{FexN}$ to $(A_1/C_{84})_{CuO}$ was about 1.0. These results suggest that there was no difference between the selected plasma modifiers.

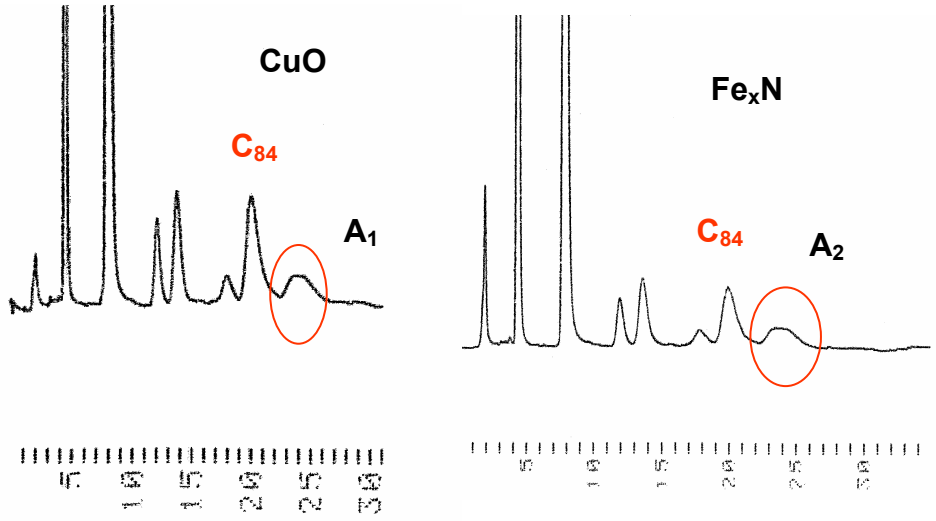

Figure 3-5. Comparison of the relative yield of endofullerenes using different plasma modifiers.

Other variables: Tb:C molar ratio, total cooling gas pressure, and partial pressure of dinitrogen. Tb:C molar ratios of 1:100, 3:100, and 5:100 were tested. There were no apparent differences in their fullerene extract yields and in their HPLC chromatograms for these various packing mixtures. Thus, the Tb:C molar ratio of 3:100 was used for the packing mixture. With respect to total cooling gas pressures, 150, 300, and 600 Torr of total cooling gas pressure were tested. As expected, while the lowest pressure (150 Torr) was suitable for the production of empty cage fullerenes, it was inappropriate for the production of endofullerenes. The highest pressure (600 Torr), however, suppressed the productions of both empty cage fullerenes and endofullerenes. Thus, a 300 Torr cooling gas was chosen for the synthesis of the endofullerenes in this research. With respect to the partial pressure of the nitrogen source, dinitrogen, 10, 20, 40, 80, and 160 Torr were tested while the total gas pressure was maitained at 300 Torr. The results showed that 10 Torr of dinitrogen produced the most abundant amount of empty cage fullerenes; 20 Torr of dinitrogen afford a relatively high yield of endofullerenes; 40 and 80 Torr of dinitrogen suppressed the total extract yield; while 160 Torr of dinitrogen almost completely extinguished the production of fullerenes.

In summary, the optimized conditions for Tb-based TNT-EMF synthesis were as follows: the packing material was a mixture of Tb_4O_7, graphite powder, and Fe_xN with the mass formula of 2.03:1.0:0.4, respectively. The packed rods were preheated at 1000 °C in a steady dinitrogen flow and then vaporized in the dynamic atmosphere of a mixture of helium and dinitrogen in a Kratschmer-Huffman generator. The total gas pressure was 300 Torr with 20 Torr of dinitrogen and 280 Torr of helium. Under these optimized conditions, the yield of $Tb_3N@C_{80}$ was around 0.1 mg per quarter inch rod (6.4 mm in diameter × 153mm in length).

3.2.2 Separation of $Tb_3N@C_{2n}$ (n = 40 ~ 44)

3.2.2.1 Chemical Separation Approach

The primary purification process was carried out using a chemical separation method. The toluene extract was subject to chemical separation on a cyclopentadiene functionalized Merrifield peptide resin (CPDE-MPR) column.[185, 192] The HPLC chromatogram of the effluent after the chemical separation utilizing the CPDE-MPR column is shown in Figure 3-6b. In general, this approach relies on the inherent chemical kinetic stability of trimetallic nitride template endohedral metallofullerenes (TNT-EMFs) relative to empty-cage fullerenes and non-TNT-EMFs. Since the TNT-EMFs, $M_3N@C_{2n}$ ($78 \leq 2n \leq 88$), are all large-gap compounds (HOMO-LUMO gap > 1.0 eV),[37] they are all relatively kinetic stable species (although their individual kinetic stabilities may differ). The synthesis of the CPDE-MPR and the chemical separation approach are shown in Figure 1-26.

Synthesis of CPDE-MPR.[192] To prepare CPDE-MPR, 25 g (30 mmol Cl) of Merrifield peptide resin was suspended in 600 mL toluene in a 1 L flask. The mixture was cooled to -20 °C and held at that temperature using a dry ice and an ethyl alcohol bath. A 60 mL portion of a sodium cyclopentadienide solution (2 M in tetrahydrofuran, total 120 mmol CPDE ion) was added

dropwise to the stirred suspension. After the addition was complete, the suspension was stirred at -20 °C for 2 hours. The suspension was collected by vacuum filtration on a Buchner funnel and washed with water until the filtrate was colorless. Then the filtration and washing processes were repeated using toluene. The sample of CPDE-MPR was dried under a N_2 flow in the hood and kept in glove box. The resulting product was a light brown solid.

Chemical Separation of $Tb_3N@C_{2n}$: The toluene extract was applied to a glass column (22 mm in diameter by 280 mm in length) packed with approximately 20 grams of cyclopentadiene-functionalized Merrifield peptide resin (CPDE-MPR) in toluene. Toluene extract was flushed through by gravity feed (about 20 mL/hour). The effluent was collected and the toluene solvent of the effluent was vaporized to obtain the concentrated solution containing TNT-EMFs and other EMFs.

3.2.2.2 HPLC Separations

The concentrated effluent from the chemical separation was further separated using a two-stage HPLC approach. First, the pentabromobenzyloxypropyl silica, 5PBB, column (4.6 mm by 250 mm, Alltech Associates) was employed with toluene as the mobile phase. The flow rate was 2.0 mL/minute and the detection wavelength of the UV detector was 390 nm. The seven fractions from Tb1 to Tb7 with this 5PBB column were collected. Second, the 2-(1-pyrenyl)ethyl silica, 5PYE, column (10 mm by 250 mm, Nacalai Tesque) was employed for further separation of the seven fractions obtained from the first HPLC stage using 5PBB column. The pure samples of $Tb_3N@C_{2n}$, $Tb_2@C_{79}N$, and Tb_2C_{2n} were obtained with repeated cycling separation of the samples on 5PYE column. Toluene was also used as the mobile phase (2.0 mL/minute). The detection wavelength was 390 nm.

First Stage of HPLC Using 5PBB Column: By comparing Figure 3-6a and 3-6b, we know that the chemical separation process concentrated the TNT-EMFs by getting rid of most of the reactive fullerenes. If the CPDE-MPR column approached saturation, peaks due to C_{60} and C_{70} appeared in the subsequent chromatogram of the effluent as shown in Figure 3-6b. The larger cage TNT-EMFs ($Tb_3N@C_{2n}$, $2n > 80$) also passed through the CPDE-MPR column and were eluted. In Figure 3-6b, there are seven fractions that are labeled Tb1 to Tb7. The main components of each fraction are indicated in Figure 3-6b. For example, fraction Tb2 contains $Tb_3N@C_{80}$ (I_h and D_{5h} isomers); fraction Tb5 contains $Tb_3N@C_{86}$ and Tb_2C_{90}; and fraction Tb6 contains $Tb_3N@C_{88}$ and Tb_2C_{92}.

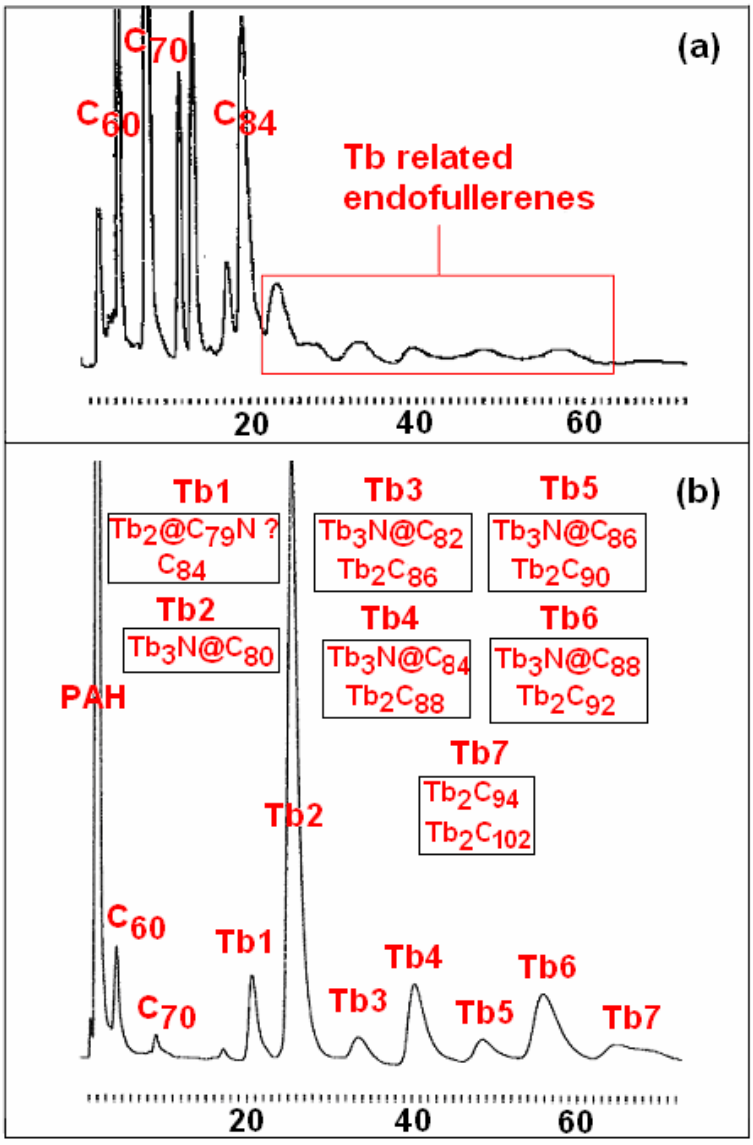

Figure 3-6. Chemical separation effects for removing the reactive empty cage fullerenes. (a) HPLC chromatogram of the original toluene extract of the raw soot. (b) HPLC chromatogram of effluent from the chemical separation column filled with CPDE-MPR. Column: 5PBB column (4.6 mm by 250 mm); Mobile phase: toluene; Flow rate: 2.0 mL/minute; Detection wavelength: 390 nm.

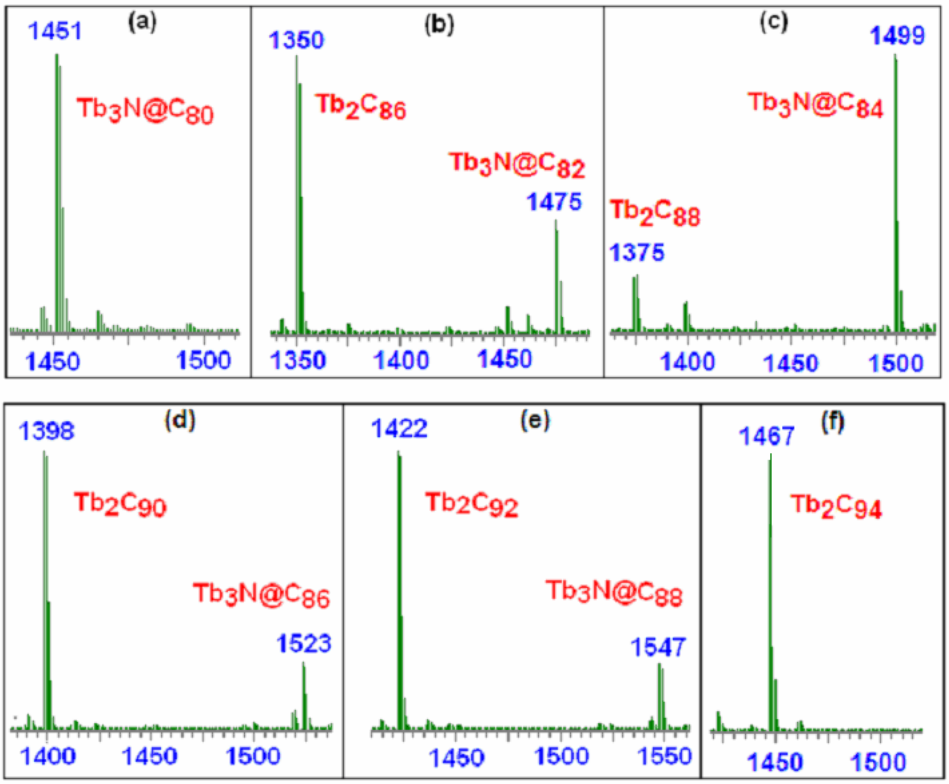

Figure 3-7. Negative DCI mass spectra of the Tb-fractions: Tb2 (a), Tb3 (b), Tb4 (c), Tb5 (d), Tb6 (e), and Tb7 (f).

The mass spectra of material present in fractions from Tb2 to Tb7 are shown in Figure 3-7. Fraction Tb1 will be discussed separately in Chapter 4. From these mass spectra, we know that each fraction still represents a mixture of endofullerenes. However, with the help of the chemical separation approach, the components of each fraction are not very complicated. Specifically,the main components of each fraction are TNT-EMFs and dimetallic endofullerenes. The co-elution of the TNT-EMF and dimetallic endofullerenes in each fraction has a clear pattern in their fullerene cage sizes. For example, $Tb_3N@C_{82}$ co-eluted with Tb_2C_{86} in Fraction Tb3 while $Tb_3N@C_{84}$ co-eluted with Tb_2C_{88} in Fraction Tb4. As the cage size of the TNT-EMF increases by two, the cage size of its co-eluted dimetallic endofullerene also increases by two. This pattern suggests that the retention behavior of fullerenes is closely related to their fullerene cage size on

a 5PBB column, as shown Table 3-1. The retention behavior of these fullerenes will be discussed in greater detail in Chapter 5.

Table 3- 1. Comparisons of the cage sizes of the co-eluted TNT-EMFs and dimetallic EMFs

Fractions	TNT-EMFs	Dimetallic EMFs
Tb2	$Tb_3N@C_{80}$	Tb_2C_{84}
Tb3	$Tb_3N@C_{82}$	Tb_2C_{86}
Tb4	$Tb_3N@C_{84}$	Tb_2C_{88}
Tb5	$Tb_3N@C_{86}$	Tb_2C_{90}
Tb6	$Tb_3N@C_{88}$	Tb_2C_{92}
Tb7	N/A	Tb_2C_{94}

The Second Stage of HPLC Using a 5PYE Column: The fractions from Tb2 to Tb7 were further purified using a 5PYE column. Since each fraction is still a mixture of endofullerenes and their isomers, the second stage HPLC on a 5PYE column involves the repeated cycling processes. HPLC chromatograms of the first cycling process for these fractions are documented in Figures 3-8 through 3-13.

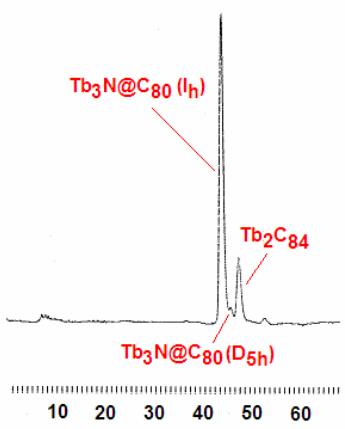

Figure 3-8. HPLC chromatograms of fraction Tb2 in the first cycling process on a 5PYE column. Mobile phase: toluene; Flow rate: 2.0 mL/minute; Detection wavelength: 390 nm.

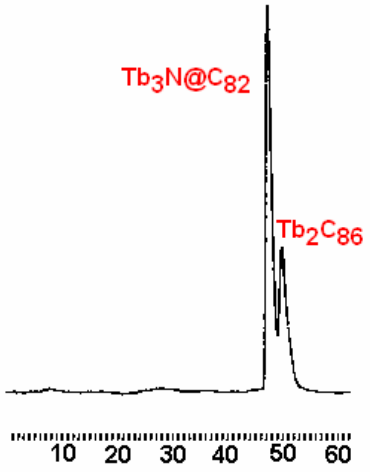

Figure 3-9. HPLC chromatograms of fraction Tb3 in the first cycling process on a 5PYE column. Mobile phase: toluene; Flow rate: 2.0 mL/minute; Detection wavelength: 390 nm.

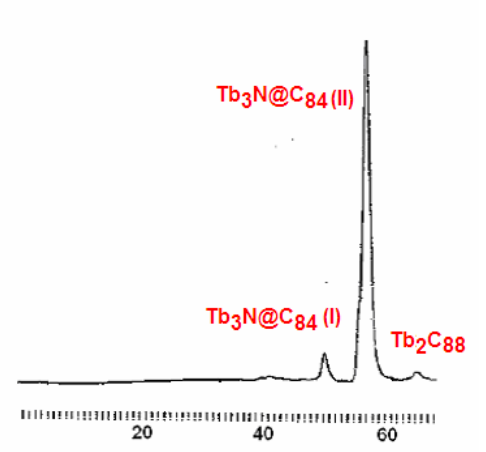

Figure 3-10. HPLC chromatograms of fraction Tb4 in the first cycling process on a 5PYE column. Mobile phase: toluene; Flow rate: 2.0 mL/minute; Detection wavelength: 390 nm.

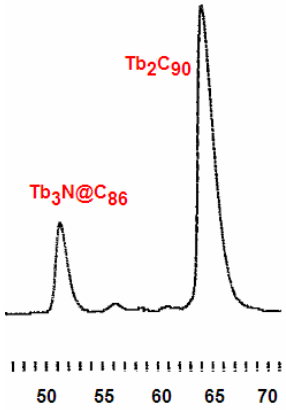

Figure 3-11. HPLC chromatograms of fraction Tb5 in the first cycling process on a 5PYE column. Mobile phase: toluene; Flow rate: 2.0 mL/minute; Detection wavelength: 390 nm.

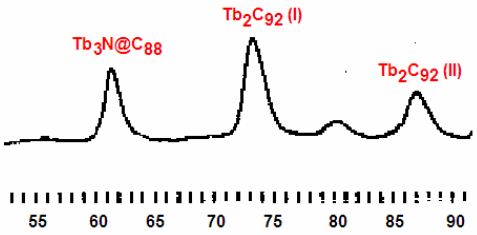

Figure 3-12. HPLC chromatograms of fraction Tb6 in the first cycling process on a 5PYE column. Mobile phase: toluene; Flow rate: 2.0 mL/minute; Detection wavelength: 390 nm.

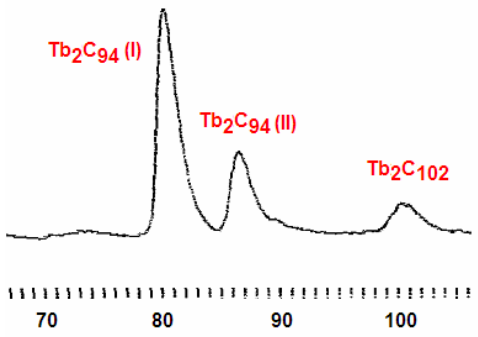

Figure 3-13. HPLC chromatograms of fraction Tb7 in the first cycling process on a 5PYE column. Mobile phase: toluene; Flow rate: 2.0 mL/minute; Detection wavelength: 390 nm.

Each peak in the chromatograms of these fractions during the first cycling process on a 5PYE column was collected and was further cycled on the 5PYE column until its purity was satisfied via the inspection of mass spectra. In this fashion, Tb-based TNT-EMF pure samples, including the I_h and D_{5h} isomers of $Tb_3N@C_{80}$, $Tb_3N@C_{82}$, $Tb_3N@C_{84}$ (two isomers), $Tb_3N@C_{86}$, and $Tb_3N@C_{88}$, and Tb-based dimetallic endofullerene pure samples, including Tb_2C_{86}, Tb_2C_{90}, Tb_2C_{92}, and Tb_2C_{94} (two isomers), were obtained. Their HPLC chromatograms are shown in Figure 3-14 and Figure 3-15, respectively. The images of the pure TNT-EMFs are shown in Figure 3-16.

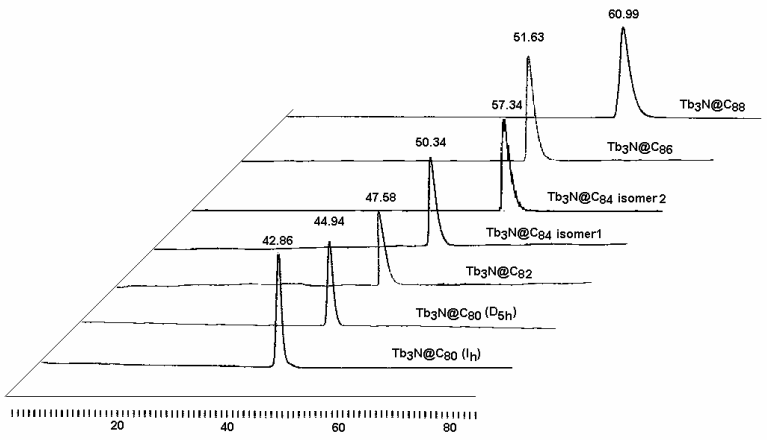

Figure 3-14. HPLC chromatograms of pure Tb-based TNT-EMFs on a 5PYE column. Mobile phase: toluene; Flow rate: 2.0 mL/minute; Detection wavelength: 390 nm.

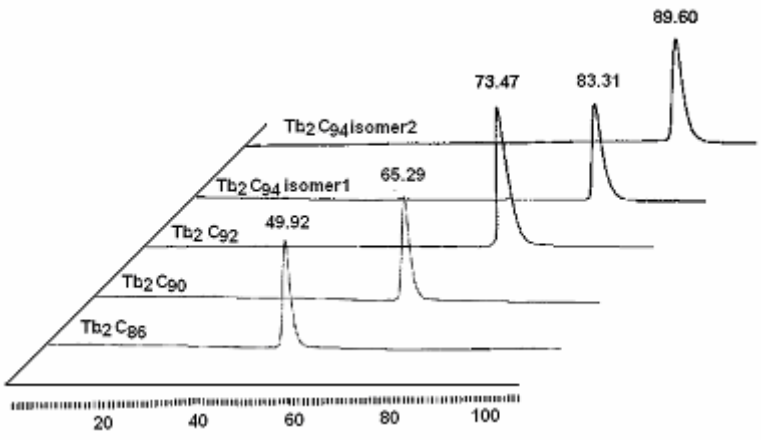

Figure 3-15. HPLC chromatograms of pure Tb-based dimetallic EMFs on a 5PYE column. Mobile phase: toluene; Flow rate: 2.0 mL/minute; Detection wavelength: 390 nm.

Figure 3-16. Images of the pure Tb-based TNT-EMFs in toleune.

3.2.3 Characterization of Tb-based Endofullerenes

3.2.3.1 Negative DCI Mass Spectra of Pure TNT-EMFs

The following five figures (Figure 3-17 through Figure 3-21) depict negative DCI mass spectra for a variety of pure TNT-EMFs.

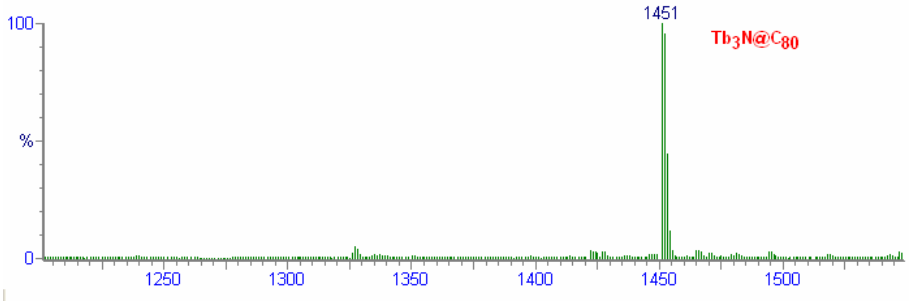

Figure 3-17. Negative DCI mass spectrum of $Tb_3N@C_{80}$.

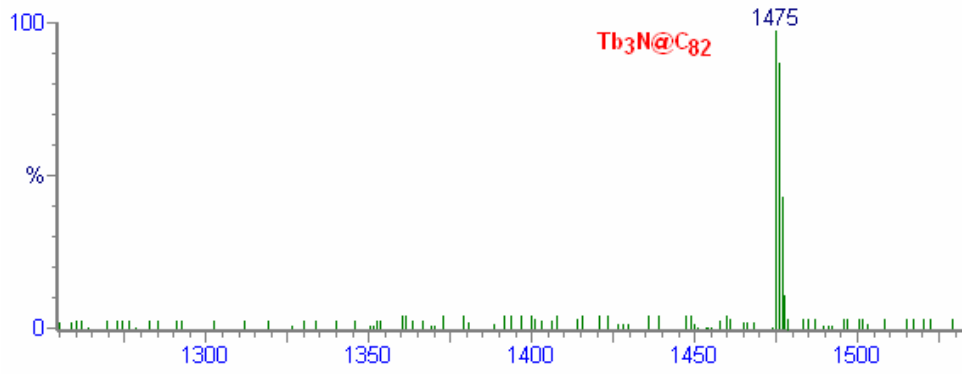

Figure 3-18. Negative DCI mass spectrum of $Tb_3N@C_{82}$.

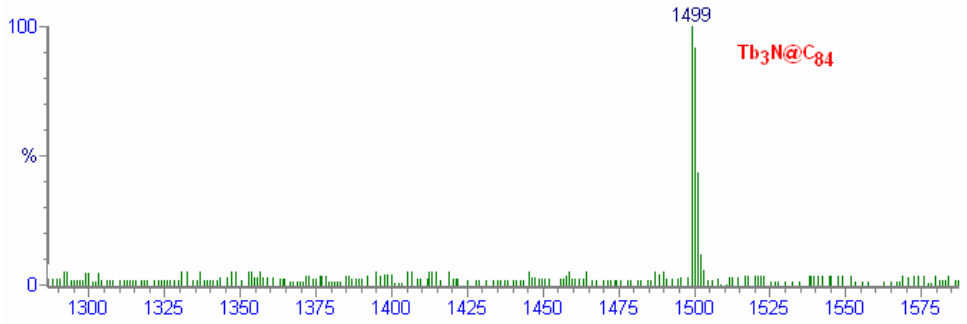

Figure 3-19. Negative DCI mass spectrum of $Tb_3N@C_{84}$.

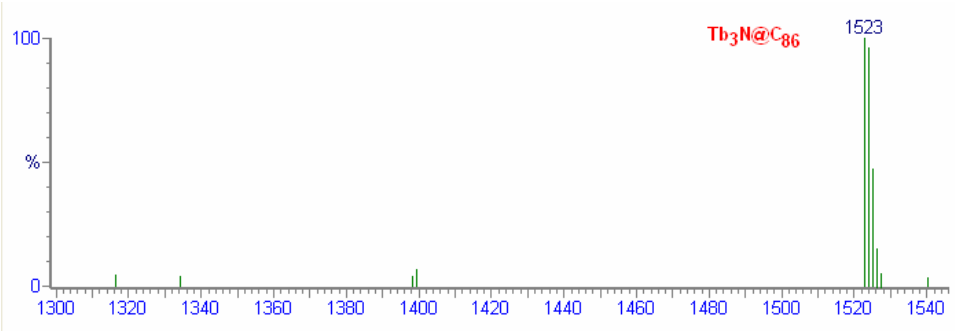

Figure 3-20. Negative DCI mass spectrum of $Tb_3N@C_{86}$.

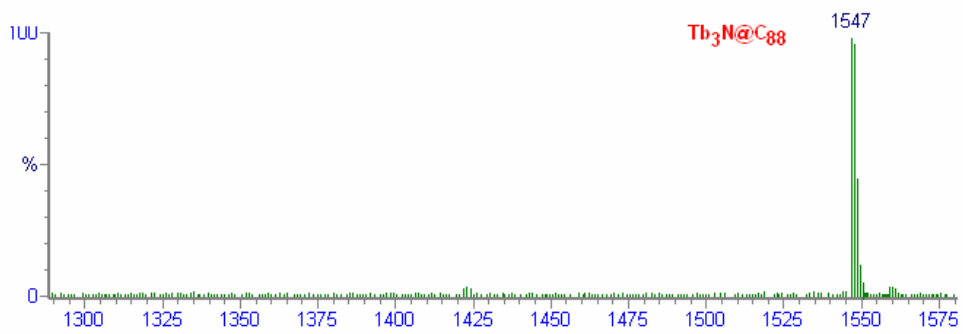

Figure 3-21. Negative DCI mass spectrum of $Tb_3N@C_{88}$.

3.2.3.2 UV-Vis Spectra of Pure TNT-EMFs

Generally, the electronic structure of an endohedral metallofullerene depends on its cage structure (size and symmetry) and charges on the cage. The UV-Vis spectrum, a valence electronic spectrum, is particularly advantageous for identifying cage structure and charges on it. For example, many publications about $M_3N@C_{80}$ (I_h and D_{5h}) have been reported. Although the M_3N cluster inside the C_{80} cage changes depending on the type of metal ion, their UV-Vis spectra between the I_h isomers and between the D_{5h} isomers are very similar to each other. Therefore, UV-Vis spectra mainly reflect the electronic structure of a fullerene cage. Given the availability of different UV-Vis spectra, comparing them will be valuable for structural characterization and determining purity. For example, for many years fullerene Sc_3C_{82} had been reported as $Sc_3@C_{82}$. However, more precise findings have since determined that its UV-Vis spectrum is actually quite different from other C_{82} cage endofullerenes—but very similar to those of endofullerenes with $C_{80}^{6-}(I_h)$ cage. Indeed, fullerene Sc_3C_{82} was found later to have a $Sc_3C_2@C_{80}$ (I_h) structure via ^{13}C NMR and single crystal X-ray diffraction crystallography.

Another important aspect of the UV-Vis spectra of endofullerenes is the concept of onset absorption. The onset absorption in UV-Vis spectroscopy reflects the electronic transition energy. The band gap (HOMO-LUMO gap) and electronic transition energy are approximately

related according to the following formula: ε_k-ε_i (Band-gap, or HOMO-LUMO gap) = $\Delta E_{i\rightarrow k}$ +constant. The states of the transition electron are indicated by i and k.[112] The constant is a positive value and changes with different compounds. Since the constant is unknown, we cannot quantitatively calculate the band gap directly just using the onset wavelength. However, when similar structures are compared, onset absorption data can still provide useful qualitative information about the kinetic stability of compounds. For example, the onset absorptions of the I_h and D_{5h} samples of $Tb_3N@C_{80}$ in Figure 3-22 are approximately 760 nm and 900 nm, respectively. The onset absorptions of isomer 1 and isomer 2 of $Tb_3N@C_{84}$ in Figure 3-24 are around 980 nm and 850 nm, respectively. These data suggest that the I_h isomer of $Tb_3N@C_{80}$ is kinetically more stable than its D_{5h} isomer, and isomer 2 of $Tb_3N@C_{84}$ is kinetically more stable than its isomer 1. These observations are consistent with their relative ease of production in high yields, as well as with theoretical calculations for their kinetic stability. Moreover, the 980 nm onset absorption of $Tb_3N@C_{82}$ is consistent with its low synthetic yields compared to $Tb_3N@C_{80}$ (I_h and D_{5h}), $Tb_3N@C_{84}$ (II, C_s), $Tb_3N@C_{86}$ (D_3), and $Tb_3N@C_{88}$ (D_2).

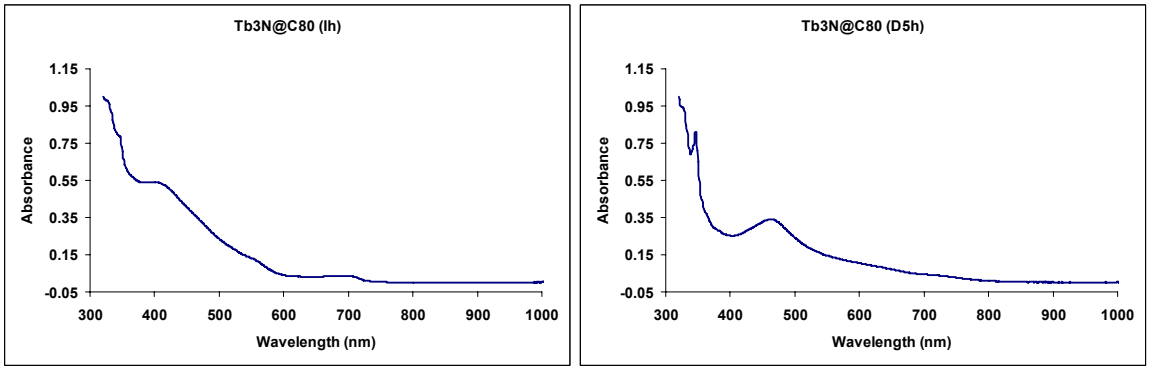

Figure 3-22. UV-Vis spectra of pure I_h and D_{5h} samples of $Tb_3N@C_{80}$.

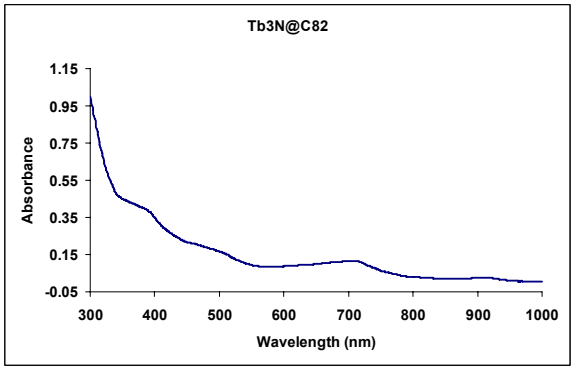

Figure 3-23. UV-Vis spectrum of $Tb_3N@C_{82}$.

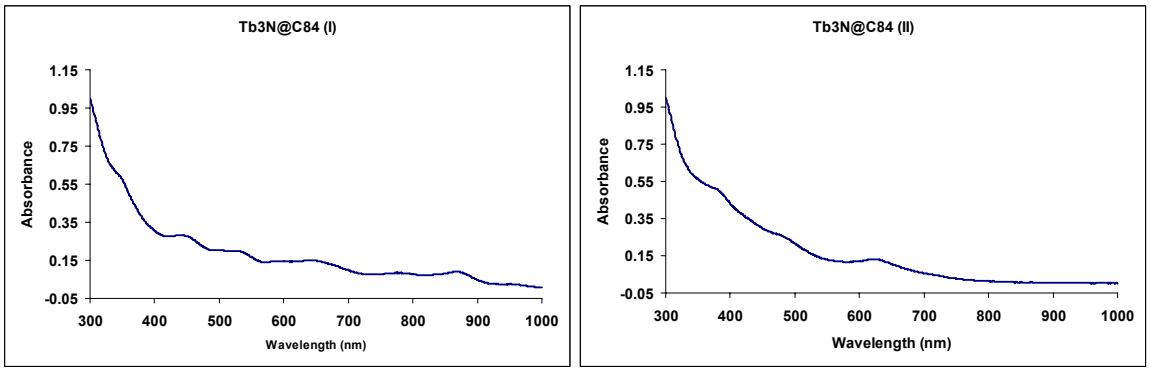

Figure 3-24. UV-Vis spectra of $Tb_3N@C_{84}$ (I and II).

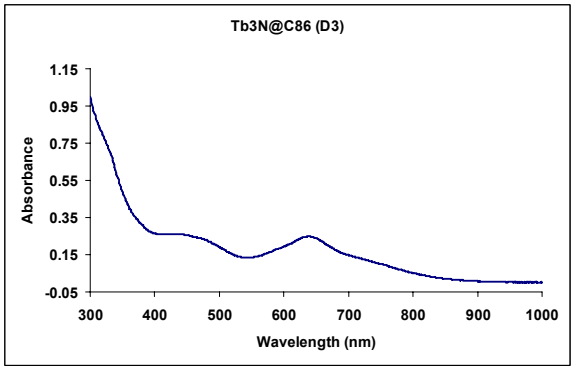

Figure 3-25. UV-Vis spectrum of $Tb_3N@C_{86}$ (D_3).

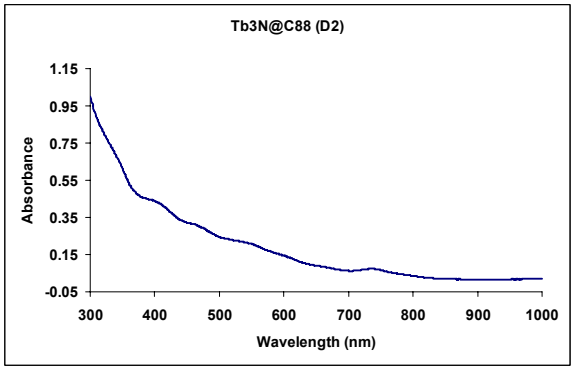

Figure 3-26. UV-Vis spectrum of $Tb_3N@C_{88}$ (D_2).

3.2.3.3 Negative DCI Mass Spectra of Pure Tb-based Dimetallic EMFs

The following four figures (Figure 3-27 through Figure 3-30) depict negative DCI mass spectra for a variety of pure Tb-based dimetallic EMFs.

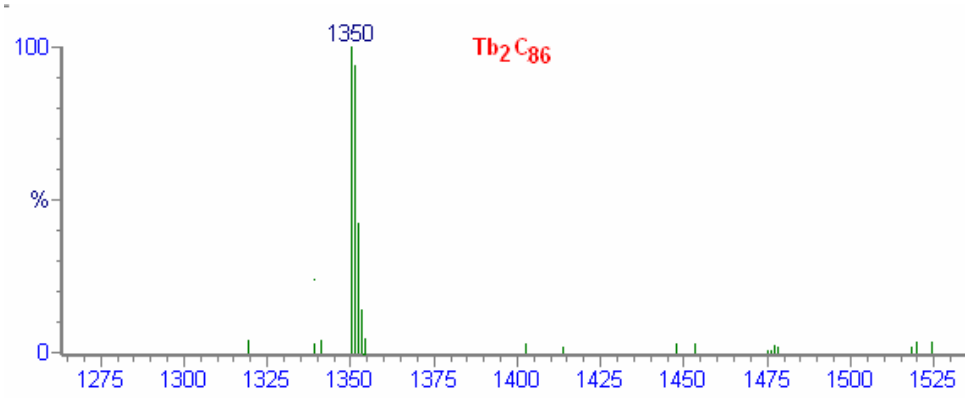

Figure 3-27. Negative DCI mass spectrum of Tb_2C_{86}.

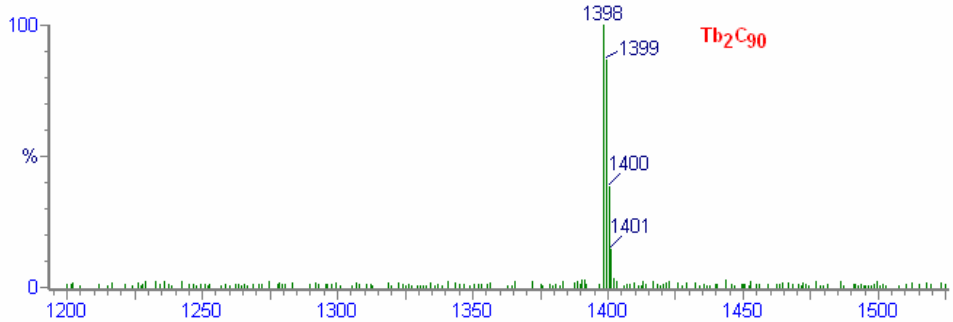

Figure 3-28. Negative DCI mass spectrum of Tb_2C_{90}.

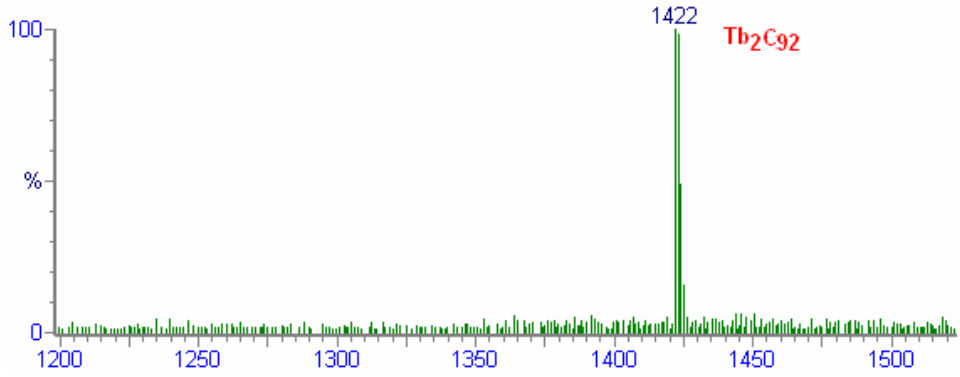

Figure 3-29. Negative DCI mass spectrum of Tb_2C_{92}.

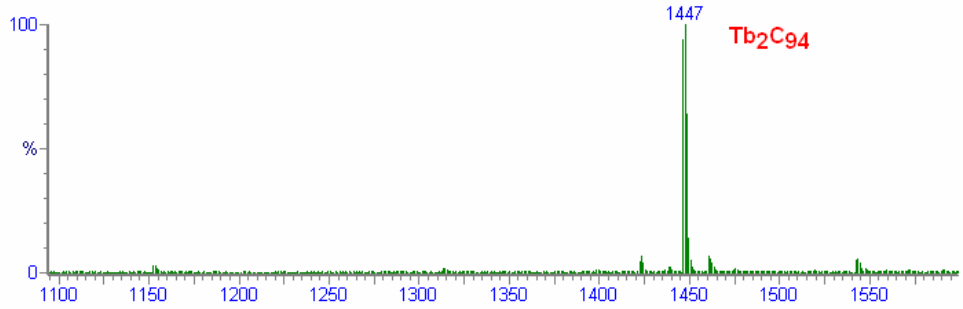

Figure 3-30. Negative DCI mass spectrum of Tb_2C_{94}.

3.2.3.4 UV-Vis Spectra of Pure Tb-based Dimetallic EMFs

The following five figures (Figure 3-31 through Figure 3-35) depict UV-Vis spectra for a variety of pure Tb-based dimetallic EMFs.

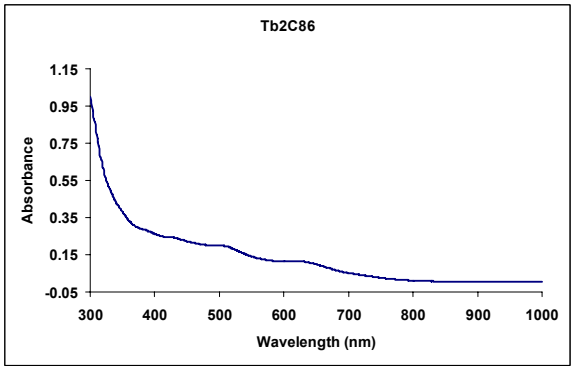

Figure 3-31. UV-Vis spectrum of Tb_2C_{86}.

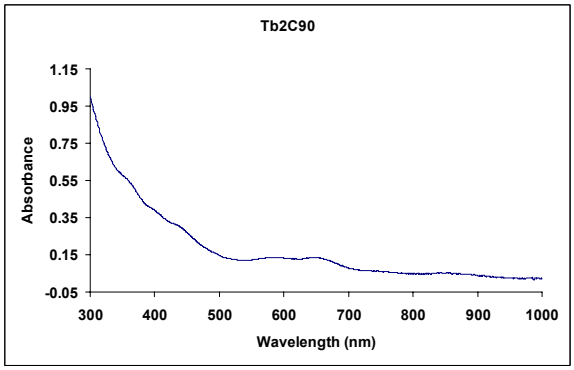

Figure 3-32. UV-Vis spectrum of Tb_2C_{90}.

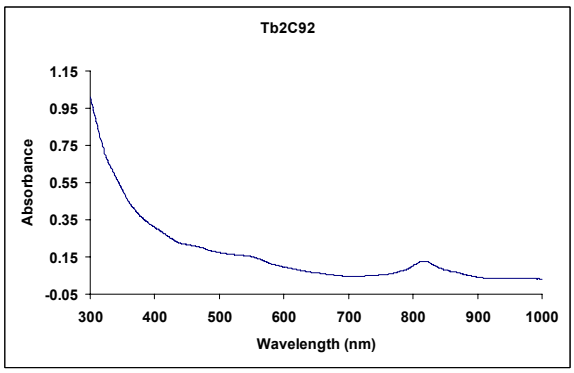

Figure 3-33. UV-Vis spectrum of Tb_2C_{92}.

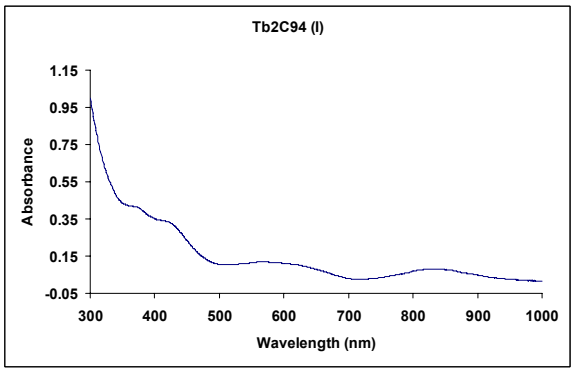

Figure 3-34. UV-Vis spectrum of Tb_2C_{94} (I).

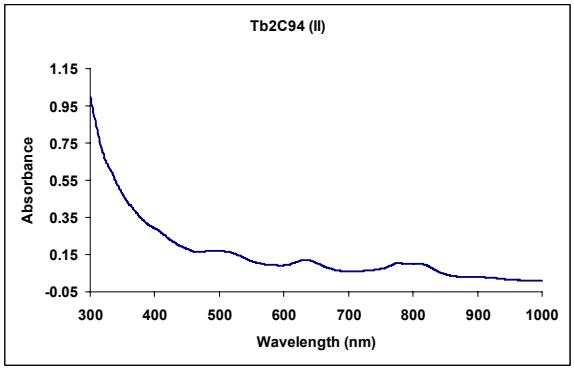

Figure 3-35. UV-Vis spectrum of Tb_2C_{94} (II).

3.2.3.5 Crystallographic Structures of the Tb-based TNT-EMFs

TNT-EMFs have an electronic state of $[M_3N]^{6+}@C_{2n}^{6-}$, with the metal ion in the +3 valence state. The electronic state of Tb^{3+} is f^8, with 6 unpaired electrons in its *f* orbitals. As a result, $Tb_3N@C_{2n}$ is paramagnetic. Due to the paramagnetic property of $Tb_3N@C_{2n}$, a ^{13}C NMR spectrum of the fullerene cage is very difficult to obtain—even for the highest symmetry I_h isomer of $Tb_3N@C_{80}$. Even if ^{13}C NMR data were available for other diamagnetic TNT-EMFs, detailed structural data for the M_3N cluster inside the fullerene cage, as well as the structural relationship between the M_3N cluster and the fullerene cage, still cannot be clearly determined by ^{13}C NMR. The most powerful method for structural determination is crystallography, i.e. single crystal X-ray diffraction. As described earlier in the research overview of this thesis (Chapter 2), scientists face two challenges when using single crystal X-ray diffraction method: obtaining enough pure sample and growing the qualify crystal. Using a homemade device, we developed a method for growing the suitable crystals using very small amounts of pure sample (<0.1 mg). With expertise in the structural determination of fullerene samples using single crystal X-ray diffraction crystallography, the Balch and Olmstead research group at the

University of California, Davis, revealed the structures of a series of our fullerene crystal samples. The Tb-based TNT-EMFs are among these samples.

Crystal Growth for Tb-based TNT-EMFs:[107, 139] Co-crystals of $Tb_3N@C_{2n}$ and $Ni^{II}(OEP)$ (OEP is the dianion of octaethylporphyrin) were obtained by layering a solution of $Tb_3N@C_{2n}$ in 0.5 mL benzene over a red benzene solution of $Ni^{II}(OEP)$ in a glass tube placed in the homemade device. Over a 14-day period, the two solutions diffused together and black crystals were harvested.

X-ray Crystallography and Data Collection.[107-109] The crystals were removed from the glass tubes in which they were grown in a small amount of mother liquor and immediately coated with hydrocarbon oil on the microscope slide. Suitable crystals were mounted on glass fibers with silicone grease and placed in the cold dinitrogen stream of a Bruker ApexII diffractometer with graphite-monochromatic Mo Kα radiation at 90(2) K. No decay was observed in 50 duplicate frames at the end of each data collection. The structures were solved by direct methods and refined using all data (based on F^2) using the software SHELXTL 5.1. A semi-empirical method utilizing equivalents was employed to correct for absorption. Hydrogen atoms were located in a difference map, added geometrically, and refined with a riding model.

Structural Studies:[31, 181] All Tb-based TNT-EMFs were stoichiometrically co-crystalized with benzene and $Ni^{II}(OEP)$ molecules. The stoichiometry of fullerene, $Ni^{II}(OEP)$, and benzene was 1:1:2, respectively, except for the crystal of $Tb_3N@C_{88}$ where the stoichiometry of fullerene, $Ni^{II}(OEP)$, and benzene was 1:1:2.5. In every case, a nearly planar porphyrin portion and eight ethyl groups at the rim of porphyrin formed a cradle. This was similar to that observed in the triclinic form of $Ni^{II}(OEP)$[193] rather than the S_4 distorted structure found in the tetragonal polymorph of pristine $Ni^{II}(OEP)$.[194] The cradle structure of $Ni^{II}(OEP)$ enhances the

intermolecular interaction between the TNT-EMFs and Ni^{II}(OEP) so that the orientation of TNT-EMFs is largely fixed. Fullerene molecules are quasi-spherical structures with relatively small intermolecular interactions. Consequently, their spin movement hinders their structural determination if they are measured in the form of bare fullerene molecules.

Another effective way for determining a fullerene's structure is to exo-functionalize the fullerene molecule and crystallize the functionalized product. Due to the exo-group in the fullerene cage, the functionalized fullerenes will tend to assume a similar orientation, thereby reducing the disorder of the crystallization. However, there are a number drawbacks associated with the exo-functionalization method. First, it may distort or even damage the structure of the fullerene cage.[195] As a result, structural data may not reflect the actual structures of the bare fullerene molecules. Second, multi-functional sites on a fullerene cage will produce a mixture of products. Third, the low yield of endofullerene and the small sample size may be insufficient to conduct a functionalization reaction.

The π-π stacking between the large conjugated π-systems of porphyrin portion and fullerene cage as well as the dispersive interactions between the ethyl groups and fullerene cage can effectively fix the orientation of the fullerene cage, and in so doing reduce the crystallization disorder. Moreover, these interactions are intermolecular interactions in nature (which can be inferred from the distances between Ni^{II}(OEP) and the fullerene cage), and thus the fullerene structure can be maintained in an almost intact form. Since the intermolecular interactions between Ni^{II}(OEP) and the Tb-based TNT-EMFs will make their relative orientations with lowest energy, the orientations of the Tb_3N groups inside the cages will depend on the orientations of their corresponding fullerene cages. Thus, they will vary from one compound to another.

As shown below, each of the structures displays some degree of disorder, which is a common phenomenon in crystallography. Therefore, only the major orientation of the fullerene and its contents are discussed in detail. Table 3-2 contains comparative interatomic distance and angle information for the Tb_3N units inside the cages. Table 3-3 shows the average geometric information of the Tb_3N clusters in different cages, which demonstrates that as the cage size increases, the Tb-N bond elongates while the Tb-C shortens. It should be noted, however, that the Tb-C distance is always longer than Tb-N bond length. Thus, no chemical bond forms between Tb and C atoms. The pyramidal shape of the Tb_3N cluster in C_{80} becomes planar when the cage size is C_{84} or larger. This suggests that when a fullerene cage becomes larger, it releases the strain on the Tb_3N cluster so that the Tb_3N cluster stretches out to form a less strained structure.

Table 3- 2. Selected interatomic distances and angles

	$Tb_3N@C_{88}$ • $Ni^{II}(OEP)$ • $2.5C_6H_6$	$Tb_3N@C_{88}$ • $Ni^{II}(OEP)$ • $2.5C_6H_6$	$Tb_3N@C_{86}$ • $Ni^{II}(OEP)$ • $2C_6H_6$	$Tb_3N@C_{86}$ • $Ni^{II}(OEP)$ • $2C_6H_6$
site occupancy	site 1 0.43	site 2 0.40	site 1 0.60(2)	site 2 0.40(2)
distances (Å)				
Tb1-N1	2.207(3)	2.175(3)	2.158(6)	2.165(7)
Tb2-N1	2.171(3)	2.209(3)	2.159(3)	2.148(7)
Tb3-N1	2.180(3)	2.175(3)	2.159(3)	2.151(7)
Tb1-C	2.333(10)	2.418(8)	2.454(13)	2.36(2)
Tb2-C	2.430(9)	2.337(10)	2.398(19)	2.383(19)
Tb3-C	2.328(8)	2.382(9)	2.398(19)	2.373(17)
angles (deg)				
Tb1-N1-Tb2	117.26(12)	116.46(13)	119.53(14)	119.1(3)
Tb1-N1-Tb3	117.40(13)	125.22(14)	119.53(14)	118.8(3)
Tb2-N1-Tb3	125.23(13)	118.23(13)	120.3(3)	121.7(3)
Σ(Tb-N-Tb)	359.89	359.91	359.36	359.6

Table 3-2 Selected interatomic distances and angles (continued)

	D_{5h} Isomer of $Tb_3N@C_{80}$ • $Ni^{II}(OEP)$ • $2C_6H_6$	I_h Isomer of $Tb_3N@C_{80}$ • $Ni^{II}(OEP)$ • $2C_6H_6$	I_h Isomer of $Tb_3N@C_{80}$ • $Ni^{II}(OEP)$ • $2C_6H_6$	Isomer 2 $Tb_3N@C_{84}$ • $Ni^{II}(OEP)$ • $2C_6H_6$
site occupancy	site 1 0.341(2)	site 1, N1A 0.60	site 2, N1B 0.40	site 1 0.512(3)
distances (Å)				
Tb1-N1	2.008(8)	2.056(4)	2.038(6)	2.182(4)
Tb2-N1	2.026(6)	2.089(4)	2.085(6)	2.130(4)
Tb3-N1	2.130(6)	2.077(4)	2.089(4)	2.120(4)
Tb1-C	2.287(17)	2.423(3)		2.483(6)
Tb2-C	2.315(15)	2.434(3)		2.406(6)
Tb3-C	2.18(2)	2.404(3)		2.333(6)
angles (deg)				
Tb1-N1-Tb2	125.0(3)	116.78(18)	117.8(3)	124.5(2)
Tb1-N1-Tb3	110.8	117.65(19)	118.8(3)	114.6(2)
Tb2-N1-Tb3	111.9	111.63(18)	112.1(3)	120.7(2)
Σ(Tb-N-Tb)	347.7	346.06	348.7	359.8

Table 3- 3. Average Tb-N and Tb-C distances (Å)

	$Tb_3N@C_{88}$ (D_2)	$Tb_3N@C_{86}$ (D_3)	$Tb_3N@C_{84}$ (C_s)	$Tb_3N@C_{80}$ (I_h)	$Tb_3N@C_{80}$ (D_{5h})
Tb-N	2.186	2.157	2.144	2.072	2.055
Tb-C	2.372	2.394	2.407	2.420	2.261
Tb_3N	Planar	Planar	Planar	Pyramidal	Pyramidal

The Structure of $Tb_3N@C_{80}$ (I_h): The major site for Tb atoms exhibits 97% occupancy, while the N atom has two occupancies of 60% for N1A and 40% for N1B (Figure 3-37). As a consequence, there are two predominant sites for the Tb_3N cluster. The sum of the three Tb-N-Tb angles is 346.06° and 348.7° for the Tb_3N (1A) and the Tb_3N (1B) cluster sites, respectively. Therefore, the Tb_3N cluster inside the C_{80} (I_h) assumes a pyramidal shape. Compared with the planar shape of the Sc_3N cluster in $Sc_3N@C_{80}$ (I_h and D_{5h}), $Sc_3N@C_{78}$ (D_{3h}), and $Sc_3N@C_{68}$ (D_3), it is clear that the Tb_3N cluster size is much larger than the Sc_3N cluster, which is due to the larger size of the Tb atom relative to the Sc atom. The orientation of the Tb_3N cluster is almost perpendicular to the Ni(OEP) plane. This orientation is the same as other M_3N clusters relative to the Ni(OEP) plane among all the TNT-EMFs with C_{80} cage crystallographically characterized thus far. For fullerene C_{80}, there are a total of 31,924 isomers, but only 7 isomers obey the IPR. C_{80} (I_h) isomer is one of those 7 IPR structures. Its pentagon ring spiral code is: 1 8 10 12 14 16 28 30 32 34 36 42. Due to its high symmetry, there are only two kinds of carbon atoms in a C_{80} (I_h) cage: Sixty carbon atoms are at the junctions of two hexagons and one pentagon (665, corannulene site), and another twenty carbon atoms are at the junctions of three hexagons (666, pyrene site) (see Figure 3-40). Consequently, its ^{13}C NMR pattern is very simple: two peaks with a 3:1 ratio. However, due to the paramagnetic property of Tb^{3+} (f^8), a ^{13}C NMR spectrum of

$Tb_3N@C_{80}$ (I_h) is generally difficult to obtain. In fact, the C_{80} (I_h) isomer exhibits the least stability among the 7 IPR isomers; thus, it has not yet been separated as an empty cage. However, upon accepting 6e as in the TNT-EMF model, $[M_3N]^{6+}@[C_{80}(I_h)]^{6-}$, $[C_{80}(I_h)]^{6-}$ becomes thermodynamically and kinetically stable (see Section 1.3.3.2.1 in Chapter 1). Therefore, $M_3N@$ C_{80} (I_h) has a very high yield compared with other EMFs.

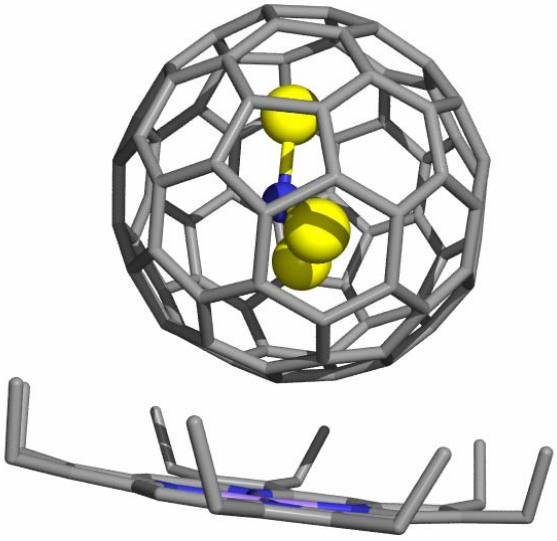

Figure 3-36. Illustration of the relative spatial orientations of $Tb_3N@C_{80}$ (I_h) and Ni^{II}(OEP) in $Tb_3N@C_{80}$ (I_h)• Ni^{II}(OEP)•$2C_6H_6$. Only one position of the fullerene cage and the major Tb_3N cluster site are shown. Benzene molecules are omitted for illustration effect. R1 is 0.035.

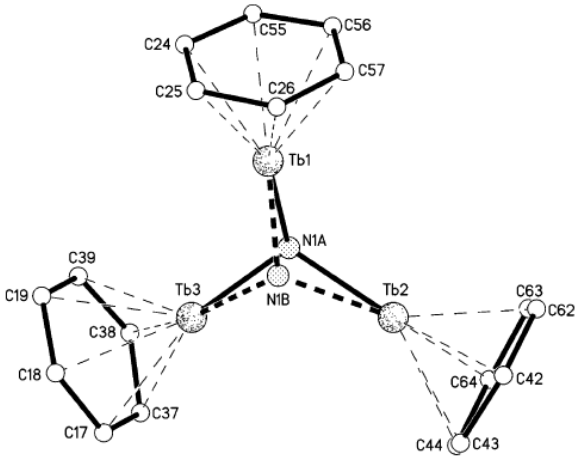

Figure 3-37. The spatial relationship between Tb atoms and the two locations of N atom and between Tb atoms and C atoms of the fullerene cage in $Tb_3N@C_{80}$ (I_h)• Ni^{II}(OEP)•$2C_6H_6$.

The Structure of $Tb_3N@C_{80}$ (D_{5h}): There are four sites for the Tb_3N cluster in $Tb_3N@C_{80}$ (D_{5h})•Ni^{II}(OEP)•$2C_6H_6$. The populations in these sites are 68.2%, 7%, 12.4%, and 12.4%. The sums of the three Tb-N-Tb angles of the Tb_3N cluster in the four sites are 347.8°, 358.9°, 350.8°, and 349.5°. The scattered values for the sums of the Tb-N-Tb angles suggest that the C_{80} (D_{5h}) cage is longitudinal in shape compared with the C_{80} (I_h) cage. Figure 3-39 shows the two orthogonal views of $Tb_3N@C_{80}$ (D_{5h}) with respect to the C_5 axis. The C_{80} (D_{5h}) isomer is also one of the 7 IPR isomers of C_{80}. Its pentagon ring spiral code is: 1 7 10 12 14 19 26 28 32 34 39 42. The structures of the I_h and D_{5h} isomers are closely related. The C_{80} (I_h) isomer can be obtained from the D_{5h} isomer by slicing the D_{5h} isomer along its horizontal mirror plane, rotating one-half by 36°, and putting the two halves back together.[110] Due to the 36° rotation, the D_{5h} isomer has a much lower symmetry than its I_h counterpart. There are a total of six kinds of carbon atoms in its fullerene cage, as labeled in Figure 3-40. Thus, the ^{13}C NMR spectrum of the D_{5h} isomer has 6 peaks with 1:1:2:2:1:1.

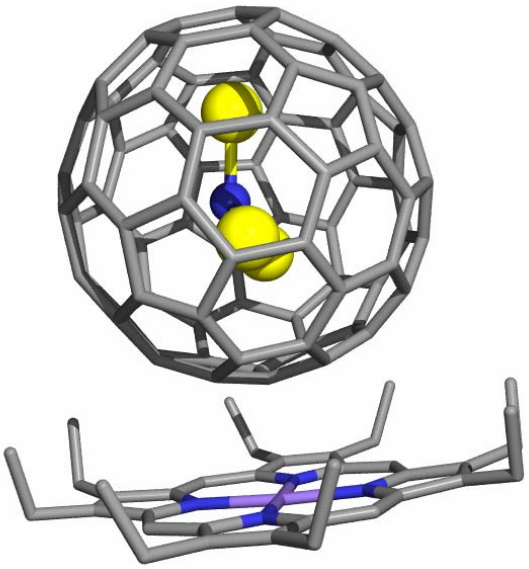

Figure 3-38. Illustration of the relative spatial orientations of $Tb_3N@C_{80}$ (D_{5h}) and Ni^{II}(OEP) in $Tb_3N@C_{80}$ (D_{5h})•Ni^{II}(OEP)•$2C_6H_6$. Only one position of the fullerene cage and the major Tb_3N cluster site are shown. Benzene molecules are omitted for illustration effect. R1 is 0.079.

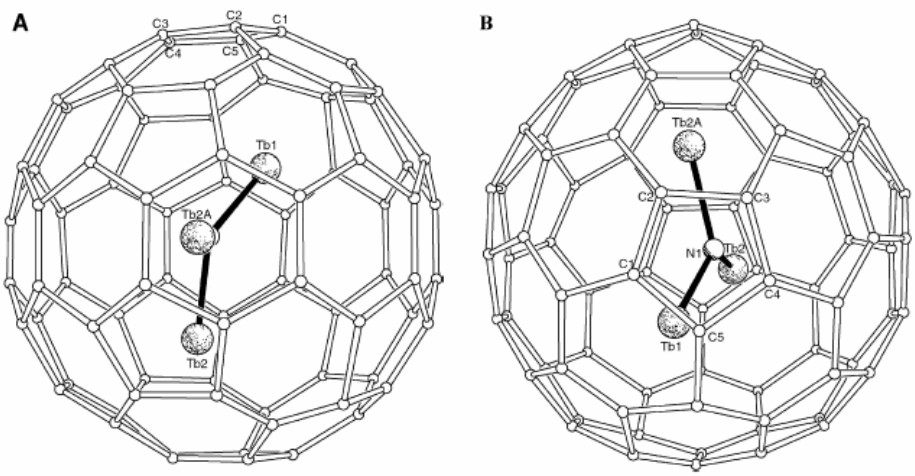

Figure 3-39. Two views of $Tb_3N@C_{80}$ (D_{5h}) with respect to its C_5 axis. A is with the C_5 axis in the paper plane while B is with the C_5 axis perpendicular to the paper plane.

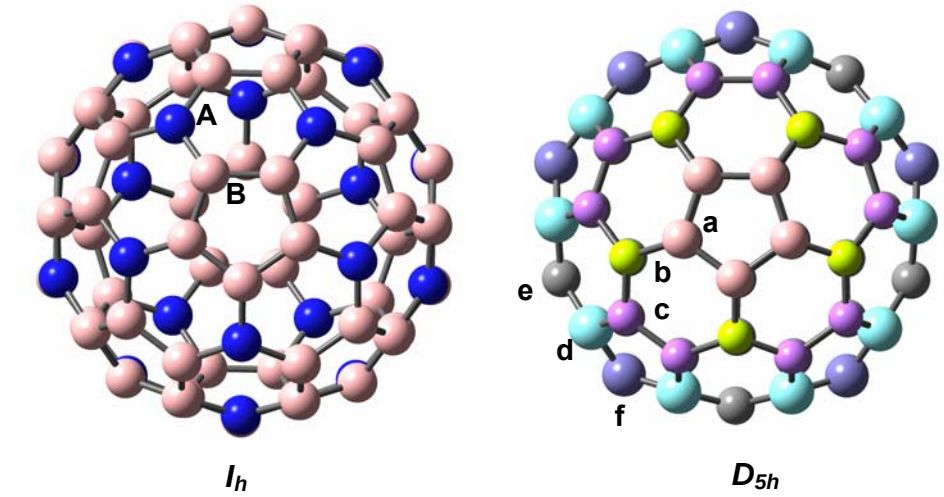

Figure 3-40. An illustration of the symmetry of the I_h and D_5h isomers of C_{80} with labels for the different kinds of carbon atoms based on symmetry considerations.

The Structure of $Tb_3N@C_{84}$ (C_s):

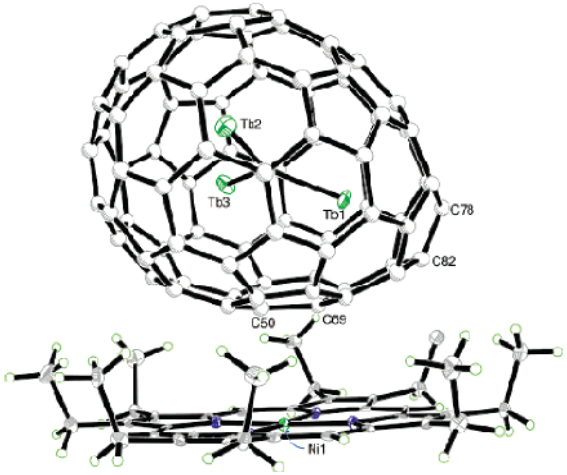

Figure 3-41. An illustration of the relative spatial orientations of $Tb_3N@C_{84}$ (II, C_s) and Ni^{II}(OEP) in $Tb_3N@C_{84}$ (C_s)• Ni^{II}(OEP)•$2C_6H_6$ with uniform arbitrarily sized circle for cage carbon atoms and 50% thermal contours for other atoms. Only one position of the fullerene cage and the major Tb_3N cluster site are shown. Benzene molecules are omitted for illustration effect. R1 is 0.047.

Figure 3-41 illustrates the spatial relationship between $Tb_3N@C_{84}$ (II, C_s) and Ni^{II}(OEP). It clearly demonstrates that $Tb_3N@C_{84}$ (II) assumes an egg-shape, which rests in the cradle of Ni^{II}(OEP) in such a way that the contact (interaction) between $Tb_3N@C_{84}$ (II) and Ni^{II}(OEP) is maximized. The placement of $Tb_3N@C_{84}$ (II) in the cradle of Ni^{II}(OEP) is very similar to the orientation of a real egg on a planar surface. The most significant part of the $Tb_3N@C_{84}$ (II) structure is that the fullerene cage does not obey IPR as evidenced by the fact that there is a fused pentagon pair in the fullerene cage of $Tb_3N@C_{84}$ (II)! For a C_{84}, there are a total of 51,592 isomers. Twenty-four isomers are IPR structures, while the other 51,568 isomers are non-IPR structures. The fullerene cage of $Tb_3N@C_{84}$ (II) is No. 51,365 among the 51,568 non-IPR isomers in Fowler and Manolopoulos' sequence. This non-IPR No.51365 isomer is in C_s symmetry. Its pentagon ring spiral code is: 1 2 11 13 16 18 29 31 33 35 37 44. From this spiral code, it is also clear that the first and the second pentagons adjoin each other. Prior to this finding, other reported non-IPR endohedral metallofullerenes, $Sc_3N@C_{68}$ (D_3) and $Sc_2C_2@C_{66}$

(C_{2v}), are all with a fullerene cage smaller than C_{70}. Their non-IPR structures are not surprising because fullerenes smaller than C_{70} cannot obey IPR except in the case of C_{60} (I_h). In other words, $Sc_3N@C_{68}$ (D_3) and $Sc_2C_2@C_{66}$ (C_{2v}) have no chance to adopt IPR structures. However, with respect to $Tb_3N@C_{84}$ (II), the situation is quite different because there are twenty-four IPR structures available for $Tb_3N@C_{84}$ (II) to choose. This finding concerning the non-IPR structure of $Tb_3N@C_{84}$ (II) suggests that IPR is no longer the only criteria to follow for the selection of fullerene structure. Another important aspect is the full occupation of one Tb^{3+} ion in the pentalene fold formed by a pair of fused pentagons. Among all the non-IPR endohedral metallofullerenes reported so far, the pentalene fold always coordinated with a metal ion. The full occupation of one Tb^{3+} ion in the case of $Tb_3N@C_{84}$ (II) may suggest the necessity of coordination between the metal ion and a fused pentagon pair for a non-IPR structure. Theoretical calculations show that the charge transferred from the metal atom to the fullerene cage mainly focuses on the pentalene patch of the non-IPR cage. As a result, the antiaromatic pentalene patch became aromatic and therefore stabilized.[27]

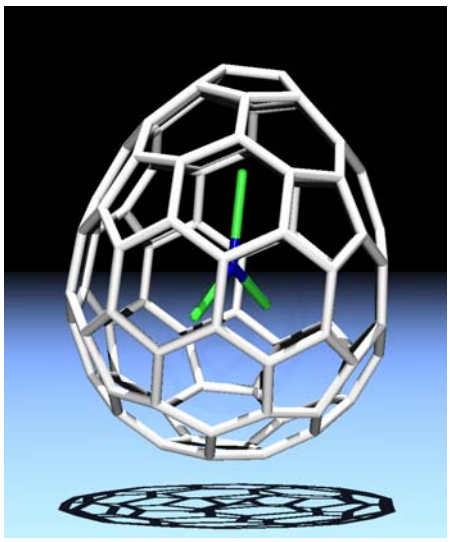

Figure 3-42. Illustration of the egg-shaped $Tb_3N@C_{84}$ (II, C_s) and the planar Tb_3N cluster. Only the major Tb_3N site is shown.

As we determined, the Tb_3N cluster inside the egg-shaped fullerene cage is disordered. As shown in Figure 3-43, while Tb1 has full occupation, the site of the Tb2 and Tb3 pair has 0.512 occupancy. Other sites of Tb4 and Tb5, Tb6 and Tb7, and Tb8 and Tb9, in pair, have occupancies of 0.212 (2), 0.229 (3), and 0.047, respectively. These results suggest that the Tb_3N cluster spins along the Tb1-N bond inside the fullerene cage. The sums of Tb-N-Tb bond angles in Tb_3N cluster sites are very close to 360° (for example, 359.8° for the major site), suggesting that the Tb_3N cluster is planar inside the egg shaped C_{84} (C_s) fullerene cage. The bond lengths (Å) in the major site of Tb_3N cluster are as follows: Tb1-N: 2.182(4), Tb2-N: 2.130(4), and Tb3-N: 2.120(4). Tb1-N is significantly longer than Tb2-N and Tb3-N due to the coordination of Tb1 and the pentalene fold.

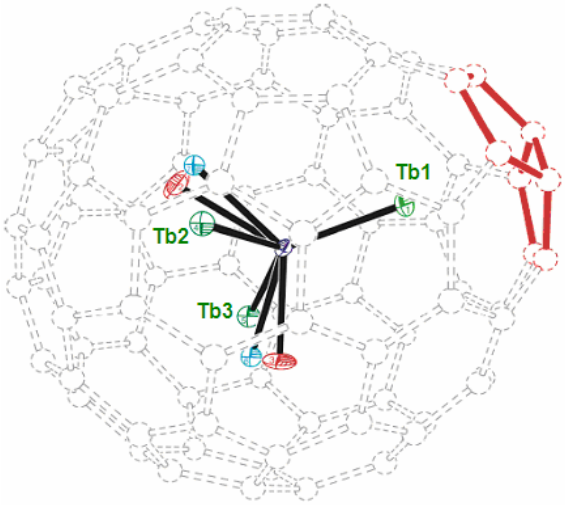

Figure 3-43. Emphasized illustrations of the fused pentagon pair (pentalene fold is in red color), full occupation of Tb1 in the pentalene fold, and disorder sites of other Tb atoms.

The disorder of the cage carbons of $Tb_3N@C_{84}$ (II, C_s) is shown in Figure 3-44. While the 64 carbon atoms around the pentalene fold are well behaved, the other twenty carbon atoms at the opposite end of the pentalene fold of the egg-shaped cage are disordered and form two sets. These two sets of 20 carbons are related by a C_2 axis (rotation 180°).

There are two isomers of $Tb_3N@C_{84}$, which were co-eluted in the 5PBB column. This suggests that their fullerene cages (P_π electrons) are the same size. Their retention times on a 5PYE column, however, displayed a seven minute gap, with $Tb_3N@C_{84}$ (II) eluted later, suggesting the $Tb_3N@C_{84}$ (II) has a much lower symmetry than $Tb_3N@C_{84}$ (I). Although $Tb_3N@C_{84}$ (I) was not fully characterized, the primary crystallographic data suggested a D_2 symmetry (No. 21 isomer of 24 IPR isomers). After the structural determinations of many novel endofullerenes in this thesis, some experimental results need to be rationally interpreted using their electronic structures, which are normally generated by computational method. Liaosa Xu in Dorn group graciously cooperated and undertook all the calculation work while the proposal of initial electronic structures and interpretations of the calculation results were originated and performed by myself.

Theoretical calculations were conducted for the $C_{84}^{6-}(D_2)$ and the $C_{84}^{6-}(C_s)$ cages. As shown in Figure 3-45, while $C_{84}^{6-}(C_s)$ was similar to $C_{84}^{6-}(D_2)$ in thermodynamic energy, the HOMO-LUMO gap of $C_{84}^{6-}(C_s)$ was much larger than that of $C_{84}^{6-}(D_2)$, suggesting $C_{84}^{6-}(C_s)$ is more kinetically stable than $C_{84}^{6-}(D_2)$. These results are consistent with the dominant yield of $Tb_3N@C_{84}$ (II, C_s) over that of $Tb_3N@C_{84}$ (I, D_2) in Figure 3-10.

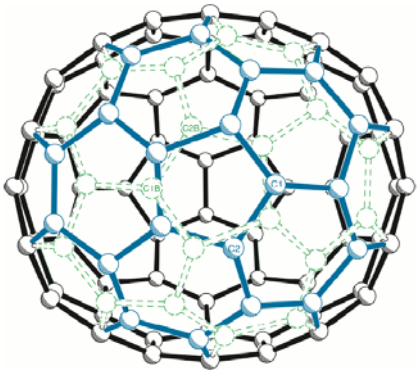

Figure 3-44. Illustration of the disorder of the cage carbon atoms of $Tb_3N@C_{84}$ (C_s). Sixty-four carbon atoms around pentalene fold are well behaved. Twenty carbon atoms at the opposite end of the pentalene fold are disordered and form two sets. One set of twenty carbon atoms are connected with a solid line while the other set of twenty carbon atoms are connected with a dash line. The two sets of twenty carbon atoms are related by rotating 180°.

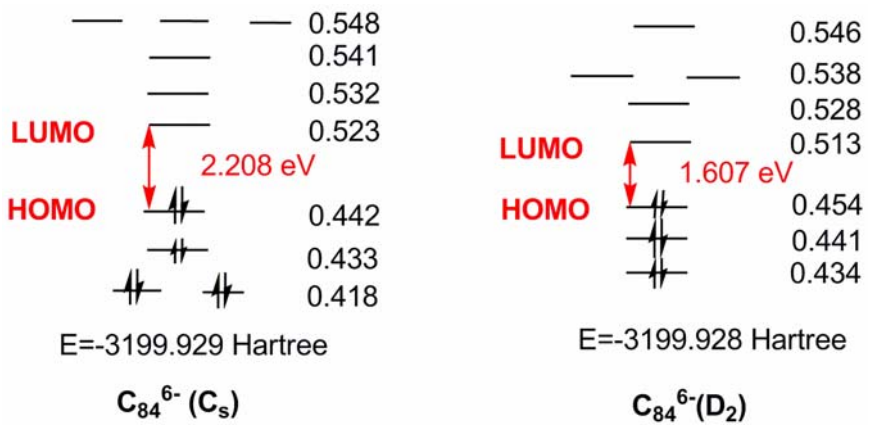

Figure 3-45. Theoretical calculations for C_{84}^{6-} (D_2) of $Tb_3N@C_{84}$ (I) and C_{84}^{6-}(C_s) of $Tb_3N@C_{84}$ (II).

Structure of $Tb_3N@C_{86}$: The orientation of the Tb_3N cluster and C_{86} (D_3) relative to the Ni(OEP) is shown in Figure 3-46. As we documented, the Tb_3N cluster is planar inside the fullerene cage and is parallel to the plane of Ni^{II}(OEP). The average Tb-N distance was longer than that in $Tb_3N@C_{84}$ (II). The C_{86} (D_3) cage is placed in the cradle of Ni^{II}(OEP) with its flat surface in contact with the plane of Ni^{II}(OEP), reflecting the maximum interaction between the C_{86} (D_3) fullerene cage and Ni^{II}(OEP). The flattened C_{86} (D_3) cage shape is shown in Figure 3-47. The surface-to-surface distance (C_1 - C_{82}) along its C_3 axis was 7.353 Å, while the distances along its three D_2 axis were 8.516Å, 8.555 Å, and 8.553 Å. These structural data of the C_{86} (D_3) cage demonstrated that the C_{86} (D_3) cage is flattened in the direction along its C_3 axis.

The C_{86} (D_3) cage is a chiral structure. The two enantiomers of $Tb_3N@C_{86}$ (D_3) are shown in Figure 3-47. Since the separation of any fullerene enantiomers has not yet been reported, the separation of enantioners of $Tb_3N@C_{86}$ (D_3) is a new challenge for chemists. The fullerene cage of $Tb_3N@C_{86}$ (D_3) is an IPR structure. It is the No. 19 isomer of the total 19 IPR isomers of C_{86} in the sequence proposed by Fowler and Manolopoulos. Its pentagon ring spiral code is: 1 7 10 12 14 19 28 33 35 37 40 45. The Tb_3N cluster relative to the C_3 (along C_1 and C_{82}) axis of C_{86} (D_3) is shown in Figure 3-48. The N atom of the Tb_3N cluster in the major site is

at the middle point between the C_1 and C_{82} atoms. The interactions between the three Tb ions of the Tb_3N cluster in the major site and their closest carbon atoms are shown in Figure 3-49—namely, that the three Tb ions all coordinate over the 6:6 ring junctions. Theoretical calculations in Figure 3-50 show that the neutral C_{86} (D_3) has a small HOMO-LUMO gap. Upon accepting 6e, however, the HOMO-LUMO gap becomes very large, which accounts for the stability of $Tb_3N@C_{86}$ (D_3).

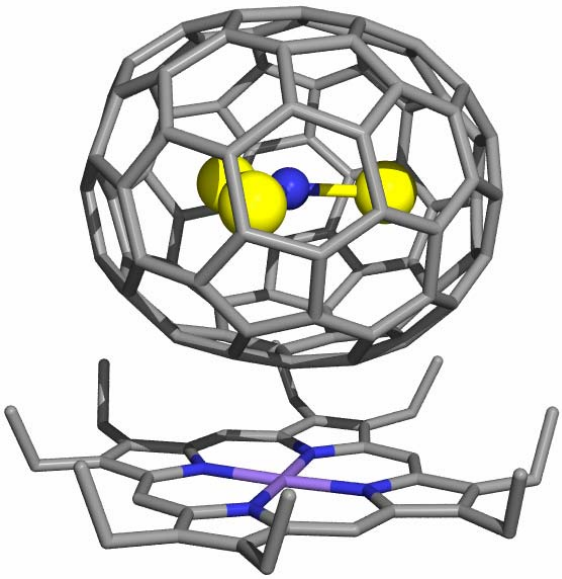

Figure 3-46. Illustration of the relative spatial orientations of $Tb_3N@C_{86}$ (D_3) and Ni^{II}(OEP) in $Tb_3N@C_{86}$ (D_3)•Ni^{II}(OEP)•$2C_6H_6$. Only one position of the fullerene cage and the major Tb_3N cluster site are shown. Benzene molecules are omitted for illustration effect. R1 is 0.054.

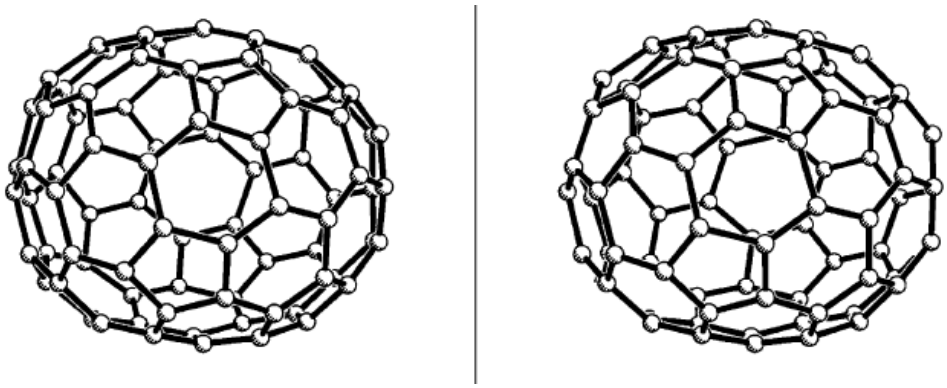

Figure 3-47. Illustrations of the two enantiomers of the C_{86} (D_3) cage of $Tb_3N@C_{86}$ (D_3). The C_{86} (D_3) cage is flattened in the direction of its C_3 axis which is in the plane of the paper.

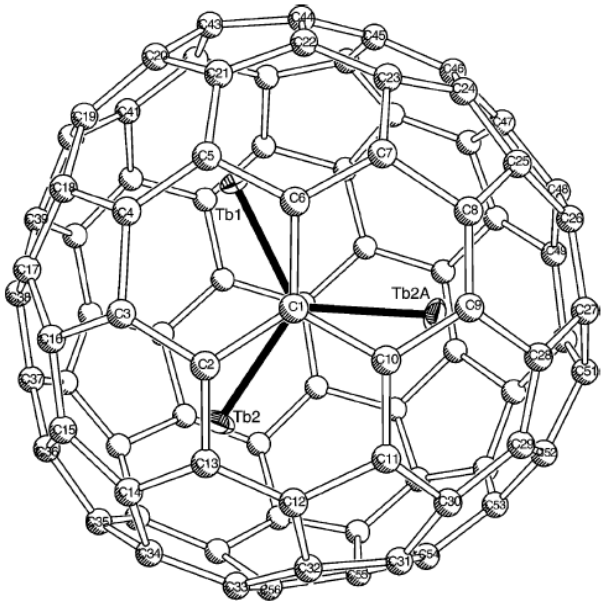

Figure 3-48. Illustration of the Tb_3N cluster in its major site relative to the C_3 axis of the C_{86} (D_3) cage.

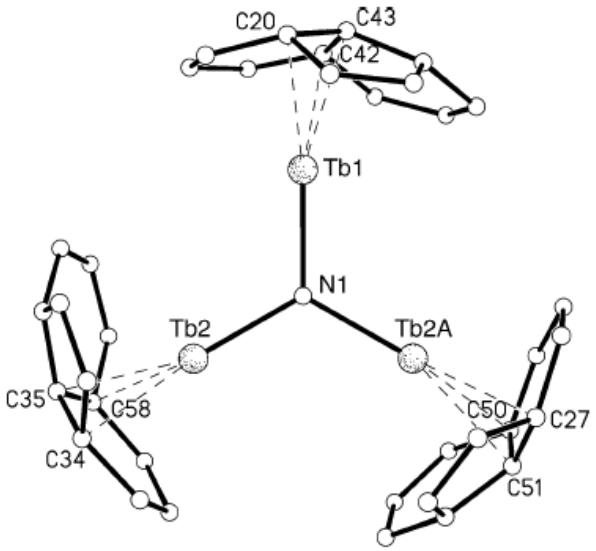

Figure 3-49. Illustrations of interactions between the three Tb ions of the Tb_3N cluster and their closest carbon atoms. The three Tb ions of the Tb_3N cluster coordinate over three 6:6 ring junctions.

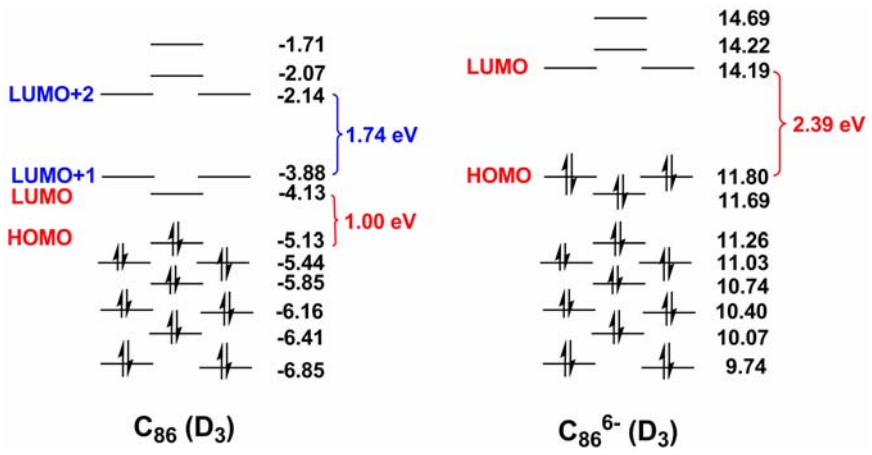

Figure 3-50. Illustration of the stabilization of the neutral C_{86} (D_3) upon accepting 6e and becoming C_{86}^{6-} (D_3).

Structure of $Tb_3N@C_{88}$: Figure 3-51 shows the spatial relationships of the Tb_3N cluster and the C_{86} (D_2) cage relative to the Ni^{II}(OEP) plane. The fullerene cage of $Tb_3N@C_{88}$ (D_2) is the largest cage crystallographically characterized so far. In fact, the fullerene cage of $Tb_3N@C_{88}$ (D_2) is so large that it cannot be fully placed in the cradle of Ni^{II}(OEP). Consequently, the fullerene cage, along with the Tb_3N cluster inside, is canted relative to the plane of Ni^{II}(OEP). Due to this change, $Tb_3N@C_{88}$ (D_2) and Ni^{II}(OEP) co-crystalize with the 2.5 C_6H_6 molecules rather than $2C_6H_6$ molecules, as the stoichiometry in the cases of $Tb_3N@C_{80}$, $Tb_3N@C_{84}$, and $Tb_3N@C_{86}$. The C_{88} (D_2) of $Tb_3N@C_{88}$ (D_2) is the No. 35 of a total of 35 IPR isomers of C_{88} in the list of Fowler and Manolopoulos' book.[12] Its pentagon ring spiral code is: 1 7 10 12 14 19 28 34 36 40 42 45. The C_{88} (D_2) cage is also a chiral structure. The cage of $Tb_3N@C_{88}$ (D_2) is disordered with two enantiomers residing at a common site. Similar to the fullerene cage of $Tb_3N@C_{86}$ (D_3), the C_{88} (D_2) cage is also flattened. The shortest distance between two surfaces along a C_2 axis of C_{88} (D_2) is 7.245Å. The longer C-C distance along the other two C_2 axes are 8.839 Å and 8.531 Å. The Tb_3N cluster is also planar, indicated by the sums of the Tb-N-Tb angles (359.90 and 359.86 for the two major sites) in $Tb_3N@C_{88}$ (D_2). The Tb_3N cluster is disordered. The two major sites of the Tb_3N cluster have 0.43 and 0.40 occupancies. Other four minor sites have 0.07, 0.04, 0.03,

and 0.03 occupancies. The average Tb-N distance (See Table 3-3) is even longer than that of $Tb_3N@C_{86}$, suggesting that the fullerene cage releases strain when the cage becomes larger. Figure 3-53 demonstrates the electronic structures of neutral C_{88} (D_2) and C_{88}^{6-} (D_2). Neutral C_{88} (D_2) has a relative small HOMO-LUMO gap. Upon accepting 6e, however, the HOMO-LUMO gap becomes significantly larger, which accounts for the stability of $Tb_3N@C_{88}$ (D_2).

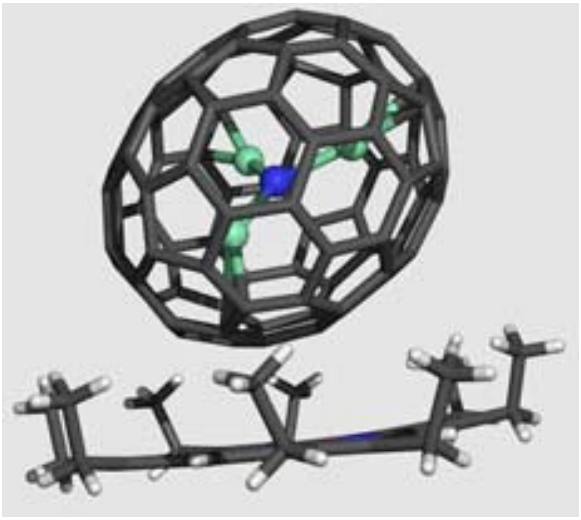

Figure 3-51. Illustration of the relative spatial orientations of $Tb_3N@C_{88}$ (D_2) and Ni^{II}(OEP) in $Tb_3N@C_{88}$ (D_2)•Ni^{II}(OEP)•$2.5C_6H_6$. Only one position of the fullerene cage and the major Tb_3N cluster site are shown. Benzene molecules are omitted for illustration. R1 is 0.056.

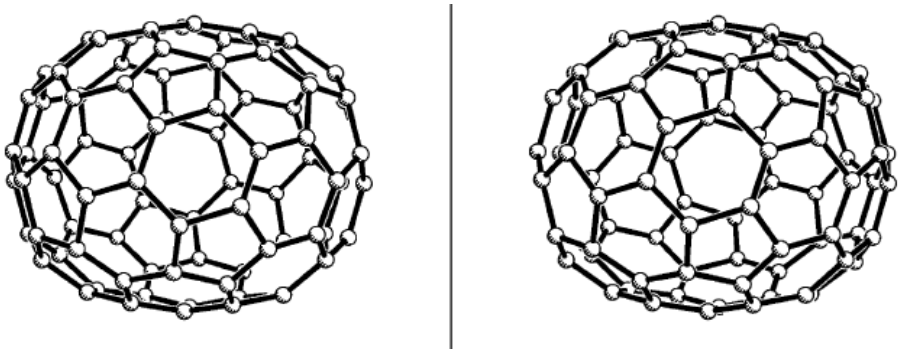

Figure 3-52. Illustrations of the two enantiomers of the C_{88} (D_2) cage of $Tb_3N@C_{88}$ (D_2). The C_{88} (D_2) cage is flattened in the direction of its one C_2 axis which is in the plane of the paper.

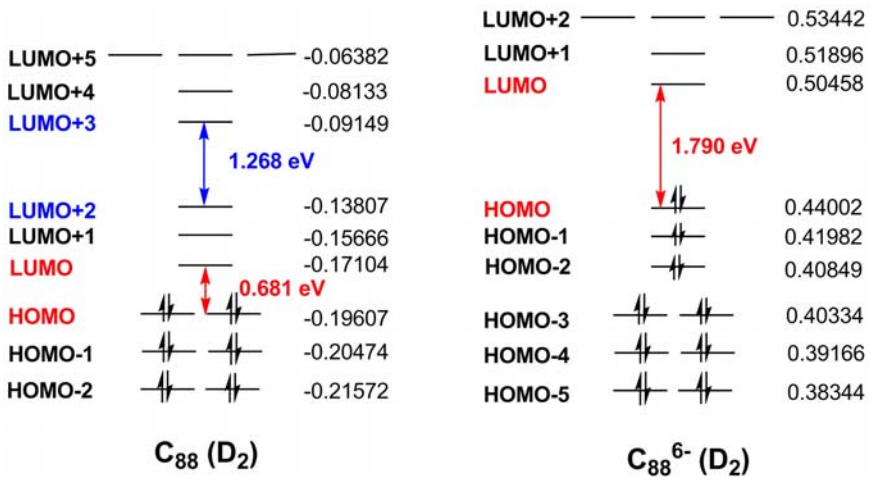

Figure 3-53. Theoretical calculations of neutral C_{88} (D_2) and C_{88}^{6-}(D_2).

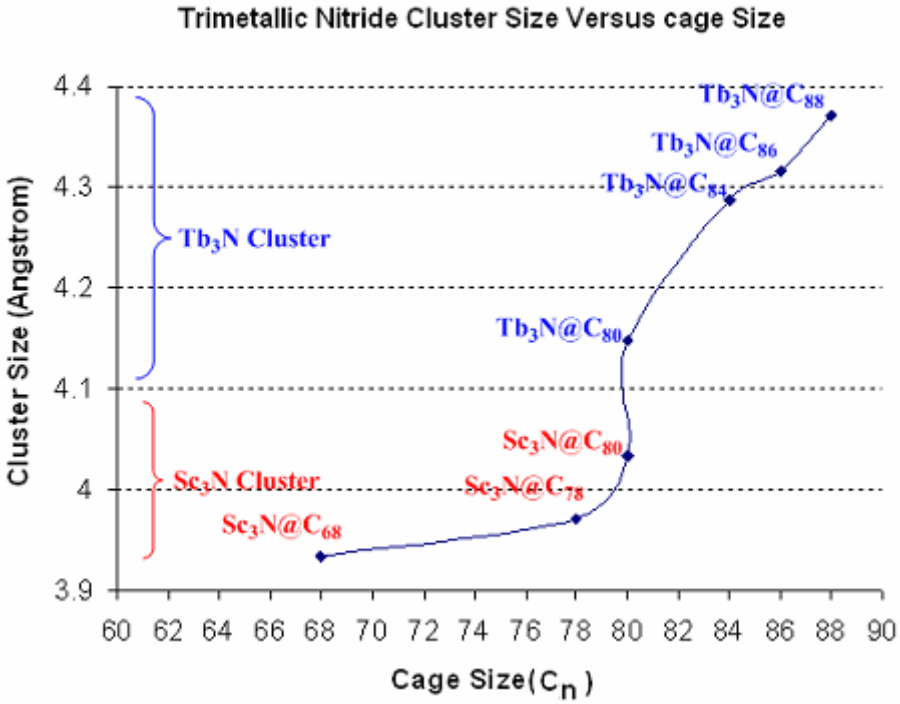

Figure 3-54. The relationship between the M_3N cluster sizes and fullerene cage sizes in TNT-EMFs, $M_3N@C_{2n}$ (M=Group III B and lanthanides). A larger size Tb_3N cluster can only be encapsulated in larger fullerene cages (≥C80) while smaller Sc_3N cluster can only be encapsulated in smaller fullerene cages. When fullerene size increases, it releases the strain on the M_3N cluster and the size of the M_3N cluster becomes larger. These results strongly support the trimetallic nitride template (TNT) formation mechanism for TNT-EMFs, $M_3N@C_{2n}$.

3.2.4 Fluorescence of a Hydrogenated $Tb_3N@C_{80}$ Sample

Because many lanthanide ion compounds display fluorescence, lanthanide-based endohedral metallofullerenes were also expected to have fluorescence. If proven, this could be significant for a number of applications. However, fluorescent endofullerenes have rarely been reported. Solid $Tb@C_{82}$ was reported to fluoresce at 544 nm with excitation wavelength at 270 nm,[196] possibly due to the first overtone of the excitation light (270 nm). Moreover, $Y@C_{82}$ in polar solvent (DMSO) was reported to have fluorescence at 490 and 570 nm, with excitation wavelengths in the ranges of 405 to 420 nm and 500 to 530 nm, respectively. The 490 nm fluorescence was attributed to $Y@C_{82}$ itself while the fluorescence at 570 nm was attributed to the nanoparticles formed by the aggregation of the $Y@C_{82}$ molecules.[197] Mixed metal TNT-EMFs, $Er_xSc_{3-x}N@C_{80}$ (x=1~3), have been reported to exhibit fluorescence in a CS_2 solid solution at a very low temperature (1.6 K), which was attributed to the Er^{3+} ions in the fullerene molecule.[198] Apparently, however, none of these reports measured the fluorescence in non-polar solvents at room temperature.

As discussed earlier with respect to the UV-Vis spectra (see Section 3.2.3.2 of Chapter 3), the UV-Vis spectra of TNT-EMFs depend on the electronic structure of fullerene cage, but is independent of the trimetallic nitride cluster. This observation suggests that the trimetallic nitride cluster inside the fullerene cage is shielded from the incoming UV-Vis light. Due to this shielding, the lanthanide ions in the cluster cannot be excited and thus no fluorescence will be detected from them. This shielding may be attributed to two conditions: the conjugated π electron system in the fullerene cage and the rapid spinning of the fullerene cage. With reference to the first condition, the incoming excitation light of UV-Vis is absorbed by the outer spherical conjugated π electron system in the fullerene cage and thus cannot reach the trimetallic nitride cluster inside. Second, the rapid spinning movement of the fullerene cage enhances the shielding

effect from the incoming excitation light. Based on these two suppositions, we proposed the following solution in order to observe fluorescence from an M_3N cluster: *reduce cage symmetry by external functionalization (to slow down the spin movement of the fullerene molecules) and partially destroy the conjugated π-electron system in the fullerene cage.* To test this proposal, we hydrogenated a $Tb_3N@C_{80}$ sample and measured its fluorescence. The hydrogenation reaction of the $Tb_3N@C_{80}$ is as follows:

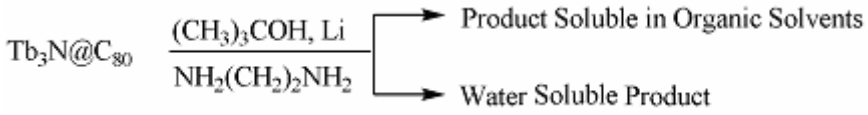

The hydrogenated product, soluble in organic solvents, was provided by Wujun Fu in Dorn group. The sample was dissolved and vaporized in CS_2 several times to remove the original toluene solvent. The resulting CS_2 solution was used to measure fluorescence. The fluorescence spectra were measured with two different wavelength regions of excitation light. The shorter wavelength region of the excitation light is from 260 to 290 nm, while the longer wavelength region of the excitation light is from 360 to 420 nm.

3.2.4.1 Fluorescence at Shorter Wavelength Excitations

Fluorescence spectra of shorter wavelength excitation are shown in Figure 3-55 through Figure 3-58. For short wavelength excitation (260~290 nm), three wavelengths were used: 260, 275, and 290 nm. With the wavelength change in this range, steady fluorescence spectra were observed with the maximum fluorescence at about 460 nm. Even after subtracting the solvent background, the resulting fluorescence spectrum maintains the same maximum fluorescence wavelength (460 nm). Figure 3-56 shows a comparison of the fluorescence spectra of a $Tb_3N@C_{80}$ sample and the hydrogenated product of $Tb_3N@C_{80}$ obtained using 275 nm excitation

light. While the hydrogenated product demonstrated strong fluorescence, the fluorescent intensity of the intact $Tb_3N@C_{80}$ sample was even lower than that of CS_2 solvent.

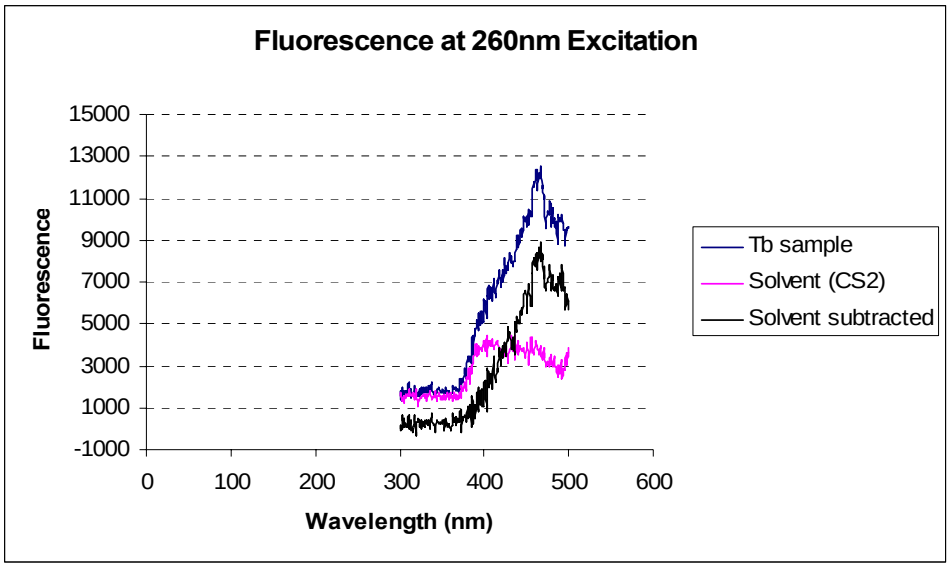

Figure 3-55. Fluorescence spectra for excitation at 260 nm. Tb sample was the hydrogenated product of $Tb_3N@C_{80}$. Even after subtracting the solvent fluorescence background, the resulted fluorescence spectrum maintained the same maximum fluorescence wavelength (460 nm).

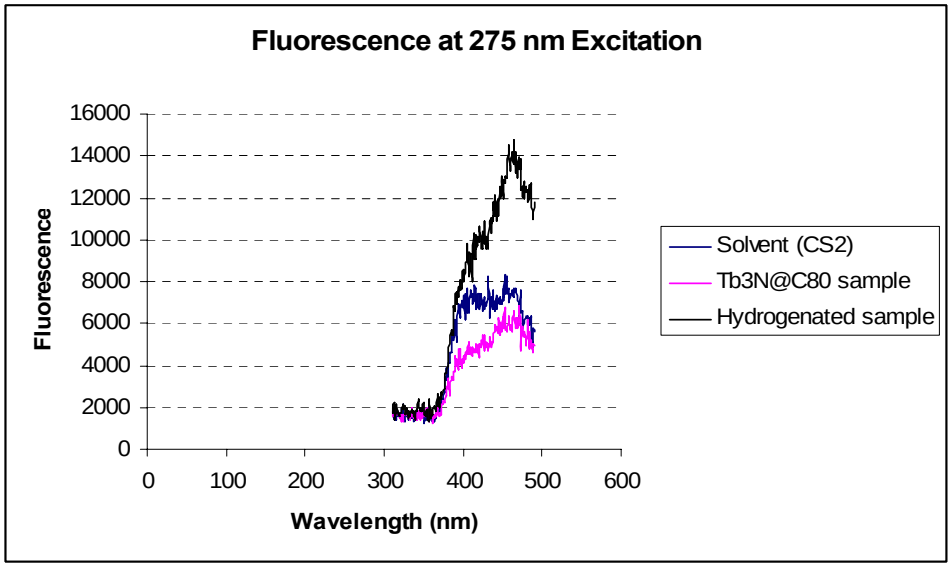

Figure 3-56. Comparison of the fluorescence spectra of the $Tb_3N@C_{80}$ sample and the hydrogenated product of $Tb_3N@C_{80}$ obtained using 275 nm excitation light.

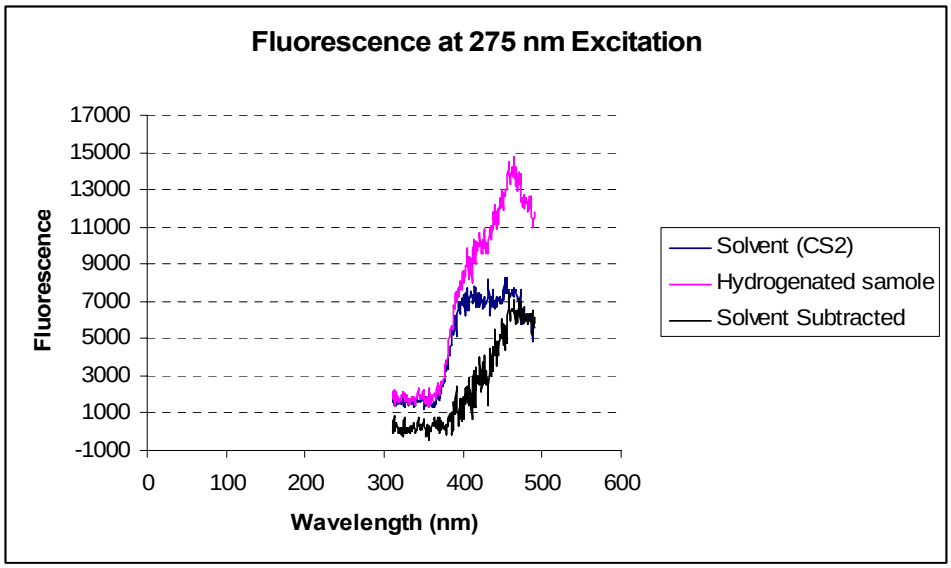

Figure 3-57. Fluorescence spectra for excitation at 275 nm. Even after subtracting the solvent fluorescence background, the resulting fluorescence spectrum maintained the same maximum fluorescence wavelength (460 nm).

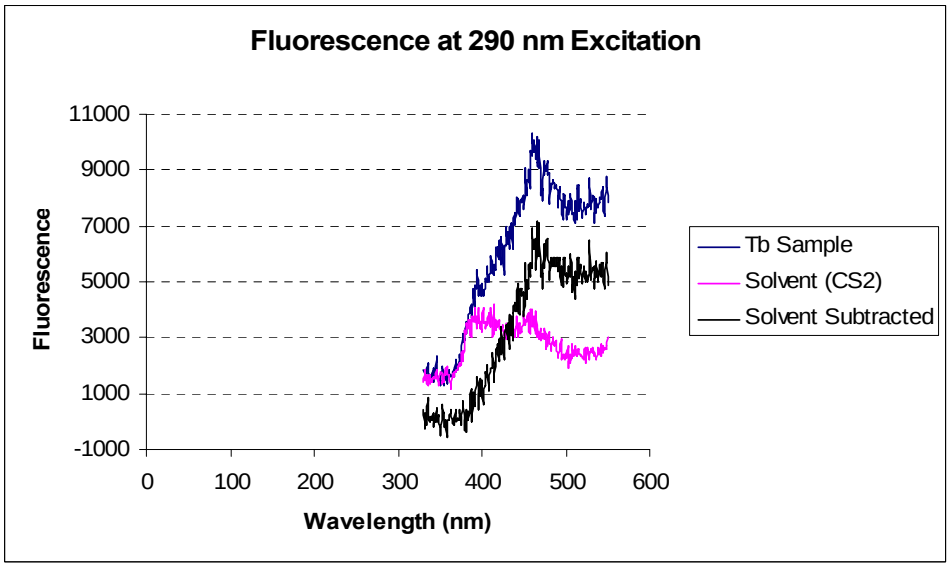

Figure 3-58. Fluorescence spectra for excitation at 290 nm. Tb sample was the hydrogenated product of $Tb_3N@C_{80}$. Even after subtracting the solvent fluorescence background, the resulting fluorescence spectrum maintained the same maximum fluorescence wavelength (460 nm).

3.2.4.2 Fluorescence at Longer Wavelength Excitations

Fluorescence spectra from longer wavelength excitation are shown in Figure 3-59 to Figure 3-62. With respect to the longer excitation wavelength (360~420 nm), four wavelengths

were used: 360, 380, 400, and 420 nm. Regarding the wavelength change in this range, steady fluorescence spectra were also observed with the maximum fluorescence at about 540 nm. No fluorescence was observed at 360 nm excitation. Fluorescence at 380 nm excitation was much weaker than those observed at 400 and 420 nm excitations. An excitation wavelength of 400 nm was chosen for further fluorescence study. Even after subtracting the solvent fluorescence background, the resulting fluorescence spectrum maintained the same maximum fluorescence wavelength (540 nm), as shown in Figure 3-60 and Figure 3-61. With the 400 nm excitation, fluorescence at 460 nm was also observed in the fluorescence spectrum after subtracting the solvent effect. Figure 3-60 and Figure 3-61 display the results of repeated experiments, while Figure 3-62 shows a comparison of the fluorescence spectra of the $Tb_3N@C_{80}$ sample and the hydrogenated product of $Tb_3N@C_{80}$ obtained using 400 nm excitation light. While the hydrogenated product demonstrates the strong fluorescence, the fluorescence intensity of the intact $Tb_3N@C_{80}$ sample was even lower than that of the CS_2 solvent.

The fluorescence of the hydrogenated product of $Tb_3N@C_{80}$ at 460 and 540 nm were assigned to the transitions from $^5D_4$ to $^7F_6$ and from $^5D_4$ to $^7F_5$, respectively. The quantum yields of these transitions, as well as the lifetimes of the fluorescence decay, required additional quantitative studies.

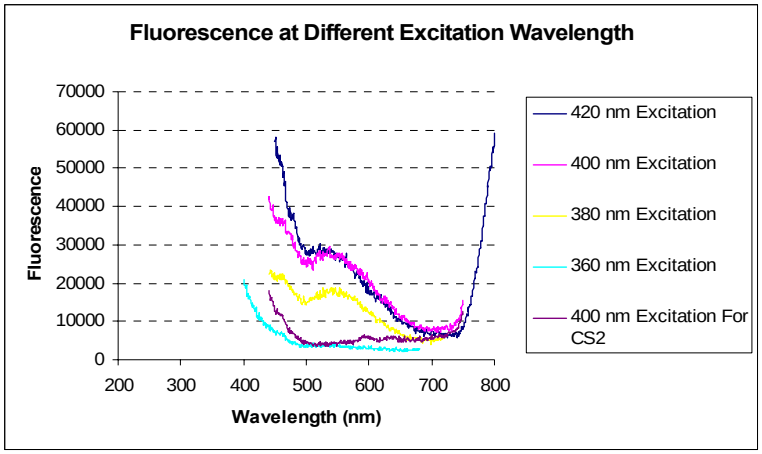

Figure 3-59. Fluorescence spectra of solvent (CS_2) and the hydrogenated product of $Tb_3N@C_{80}$ obtained using excitation light of longer wavelength (360 to 420 nm). The maximum fluorescence wavelength occurred at about 540 nm.

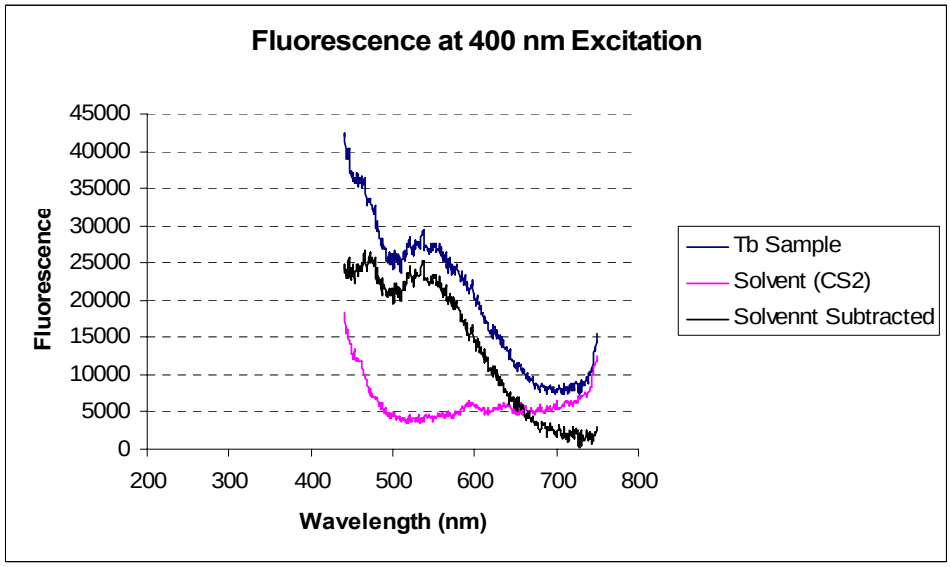

Figure 3-60. Fluorescence spectra for excitation at 400 nm. Tb sample was the hydrogenated product of $Tb_3N@C_{80}$. Even after subtracting the solvent fluorescence background, the resulting fluorescence spectrum maintained the same maximum fluorescence wavelength (540 nm).

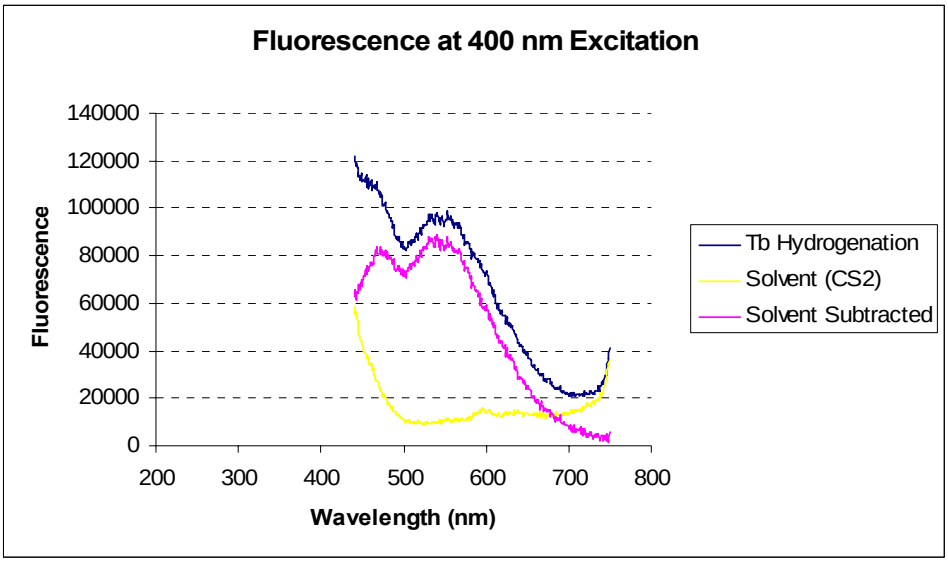

Figure 3-61. Fluorescence spectra for excitation at 400 nm. Even after subtracting the solvent fluorescence background, the resulting fluorescence spectrum maintained the same maximum fluorescence wavelength (540 nm).

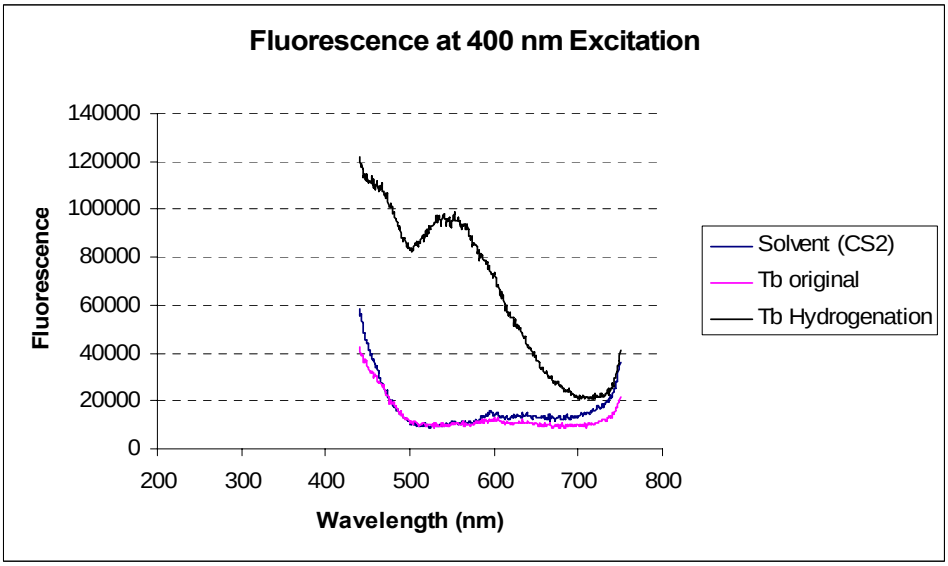

Figure 3-62. Comparison of the fluorescence spectra of the $Tb_3N@C_{80}$ sample and the hydrogenated product of $Tb_3N@C_{80}$ obtained using 400 nm excitation.

3.3 Summary

For the first time, a family of novel larger cage Tb-based TNT-EMFs $Tb_3N@C_{2n}$ ($40 \leq n \leq 44$) was, systematically synthesized, isolated, and crystallographically characterized. The protocol developed in this thesis also provides an effective and systematic method for the

synthesizing, purifying, and characterizing TNT-EMFs and other novel EMFs. The structural information of the larger cage Tb-based TNT-EMFs $Tb_3N@C_{2n}$ ($40 \leq n \leq 44$) and the small cage Sc-based TNT-EMFs $Sc_3N@C_{2n}$ (n = 34, 39, & 40) provides us for the first time an opportunity to build the relationship between sizes of trimetallic nitride clusters and sizes of fullerene cages. As documented earlier in Figure 3-54, the cage size of TNT-EMF is clearly dependent on the size of trimetallic nitride clusters. Specifically, larger cage TNT-EMFs require larger templates of trimetallic nitride clusters. Therefore, the successful structural characterization of a family of Tb-based TNT-EMFs has provided strong support for the trimetallic nitride template (TNT) formation mechanism of TNT-EMFs. The structures of TNT clusters inside the fullerene cages are either planar or pyramidal, depending on the size ratio of the cluster to the fullerene cage. With respect to the structure of the fullerene cage, EMFs may not necessarily choose an IPR-obeying cage, as does the non-IPR $Tb_3N@C_{84}$ (II, C_s), even if the IPR cages are available. At room temperature and in a non-polar organic solvent, the fluorescence of the hydrogenated product of $Tb_3N@C_{80}$ was, for the first time, successfully obtained. This outcome was based on the idea of de-shielding and mitigating screening effect of the fullerene cage on the metal ions or clusters inside the fullerene cage. The maximum fluorescence at 460 and 540 nm were assigned to the transitions from $^5D_4$ to $^7F_6$ and from $^5D_4$ to $^7F_5$, respectively.[199-204] As a result of this new protocol, the fluorescence spectra of many other lanthanide-based endohedral metallofullerenes are expected. The fluorescence of the lanthanide-based endohedral metallofullerenes is anticipated to have many promising applications in medical and optical fields in the future.

Chapter 4 — A New Class of Endohedral Metalloheterofullerenes --- A Low-lying Spin-Doped Dimetallic Cluster Inside Aza[80]fullerenes: $M_2@C_{79}N$ (M = Tb, Y, and La)

4.1. Introduction

Fullerenes are quasi-spherical carbon cages with each sp^2 hybrid carbon atom tri-valently connecting to three other carbon atoms.[12, 39] According to valence-bond theory each carbon atom on the fullerene cage has one electron in its P_π orbital, which radiantly orients to the fullerene cage. These P_π electrons thus form a conjugated system in a fullerene cage.[25, 68] The substitution of a carbon atom with a heteroatom, such as a nitrogen atom, will partially damage the π conjugation system and result in a radical heterofullerene cage that is energetically unstable.[205, 206] The dimerization of the two unstable radicals forms a dumbbell-like stable structure, as exemplified by the molecule $(C_{59}N)_2$.[79, 173] Thus, the existence of a single heterofullerene structure remains unclear. Upon encapsulating metal atoms or a cluster, however, the electronic structure of the fullerene cage will dramatically change as a result of charge transfer between the captive and the capturer.[74, 107] Therefore, the supposition that a stable endohedral metalloheterofullerene can exist is reasonable.

Due to the special electronic states associated with endohedral metalloheterofullerenes, they were expected to have novel electronic and magnetic properties and very important potential applications. Therefore, exploring metal doped heterofullerenes was intriguing to many scientists, although the research results had rarely been reported. In fact, the only reported endohedral metalloazafullerenes were $[La_2@C_{79}N]^+$ and $[La@C_{81}N]^+$ fragments, which were observed in the gas phase by bombarding their corresponding precursors via fast atom bombardment mass spectrum (FABMS) fragmentation.[21] Therefore, actual endohedral metalloazafullerenes had not yet been isolated.

We previously reported the preparation and novel properties of a new family of stable endohedral metallofullerenes (EMFs), $A_{3-x}B_xN@C_{80}$ (x = 0 ~ 3, A and B are Group III B and lanthanide metals), formed via a trimetallic nitride template (TNT) process.[31, 107, 177, 181] The introduction of the nitrogen source in this TNT methodology may facilitate the synthesis of the endohedral metalloazafullerenes. While synthesizing these TNT-EMFs, therefore, we paid particular attention to the interesting family of endohedral metalloazafullerenes. Herein, we report the synthesis, isolation, and experimental and theoretical characterization of a new class of dimetallic endohedral metalloazafullerenes: $M_2@C_{79}N$ (M = Tb, Y, and La).

4.2. Experimental Results and Discussions

4.2.1 Synthesis and Isolation

The process utilized to prepare $M_2@C_{79}N$ (M=Tb, Y, and La) was analogous to the one used for TNT-EMFs described in Chapter 3. To reiterate briefly, the core-drilled graphite rods (6.4 mm in diameter ×152 mm in length) were packed with a mixture of M_2O_3 (Tb_4O_7 for $Tb_2@C_{79}N$), graphite powder and iron nitride (Fe_xN, x = 2 ~ 4). The total M:C molar ratios were about 3:100. In previous studies, we established that iron nitride functions as a modifier of the electric-arc plasma.[181] The packed rods were pre-heated to about 1000°C under N_2 flow for about 10 hours to remove air and moisture. The rods were then vaporized in a Krätschmer -Huffman arc-discharge fullerene generator filled with a mixture of 20 Torr dinitrogen and 280 Torr helium gases. The raw soot was extracted in a Soxhlet extractor using toluene as solvent for approxiately 20 hours to obtain the extract. The extract was initially separated utilizing a cyclopentadiene functionalized Merrifield peptide resin (CPDE-MPR) column as previously described. With chemical separation, most of the empty cages and reactive classical endofullerenes are retained on the CPDE-MPR and thus cannot be eluted. The HPLC chromatograms of the Y-based sample

before and after chemical separation are shown in Figure 4-1. The HPLC traces of Tb- and La-based sample before and after chemical separations are shown in Figure 3-6 and Figure 4-21, respectively.

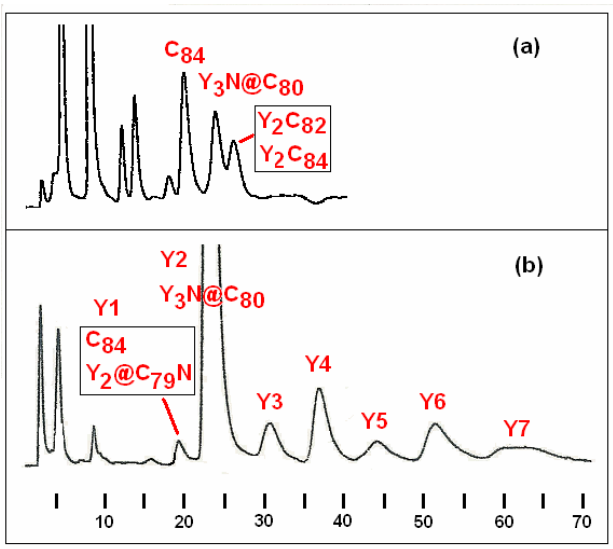

Figure 4-1. HPLC chromatograms of Y-based samples on 5PBB column (4.6 mm×250 mm). (a) and (b) are HPLC traces before and after the chemical separations, respectively. Flow rate: 2.0 ml toluene /minute; Detection: 390 nm.

As shown in Figure 4-1b, there were seven fractions from Y1 to Y7. Fraction Y1 contained C_{84} and $Y_2@C_{79}N$. The Tb-based sample after chemical separation had a similar HPLC trace, and also had seven fractions from Tb1 to Tb7. Fraction Tb1 contained C_{84} and $Tb_2@C_{79}N$ (see Figure 3-6). Fraction Y1 and Fraction Tb1 were collected and were further separated using a 5PYE column. C_{84} was easily separated from $Y_2@C_{79}N$ and $Tb_2@C_{79}N$ since their retention times on a 5PYE column were very different (see Figure 4-2 and Figure 4-3). The HPLC chromatograms of the pure $Y_2@C_{79}N$ and $Tb_2@C_{79}N$ samples are shown in Figure 4-4.

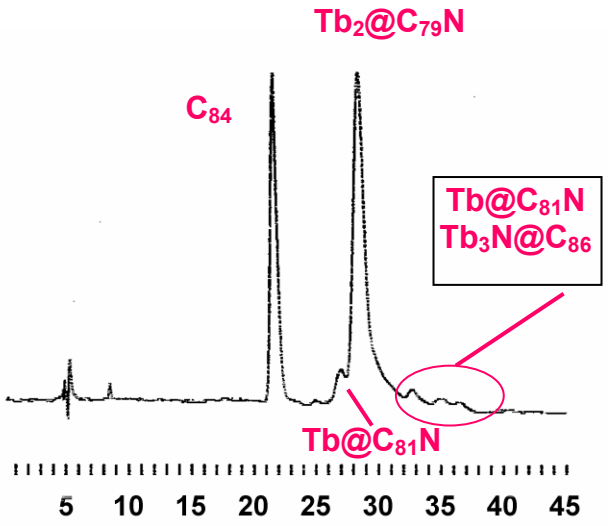

Figure 4-2. Separation of $Tb_2@C_{79}N$ from C_{84} on a 5PYE column (10mm×250mm). Flow rate: 3.0 ml toluene /minute; Detection: 390 nm.

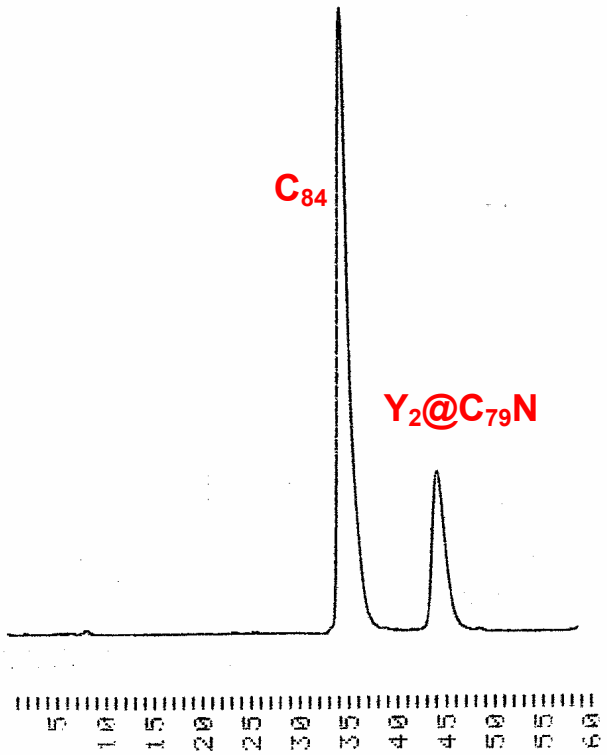

Figure 4-3. Separation of $Y_2@C_{79}N$ from C_{84} on a 5PYE column (10mm×250mm). Flow rate: 2.0 ml toluene /minute; Detection: 390 nm.

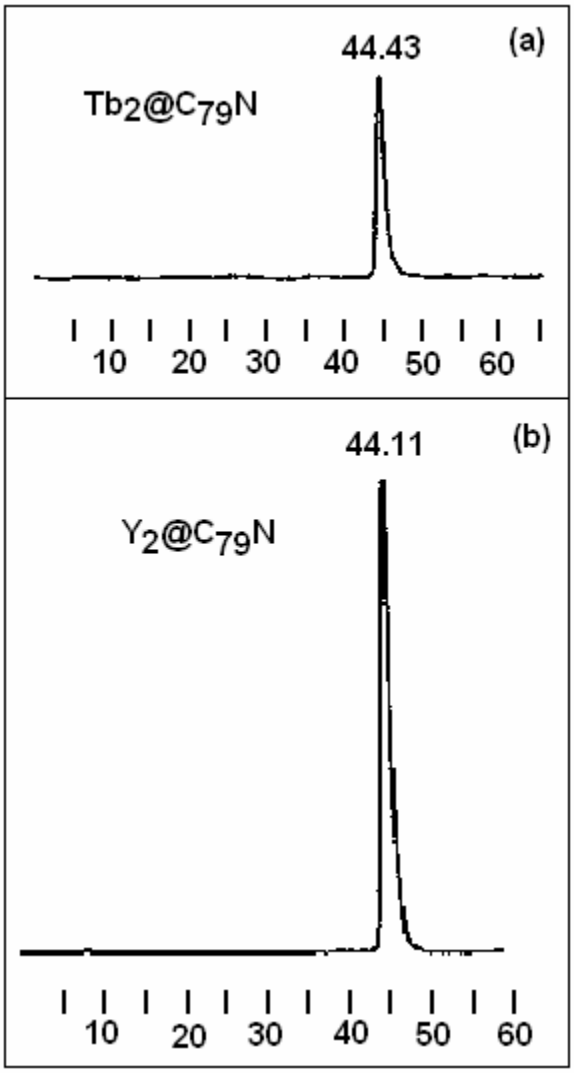

Figure 4-4. HPLC chromatograms of the pure $Y_2@C_{79}N$ and $Tb_2@C_{79}N$ samples on a 5PYE column (10mm×250mm). Flow rate: 2.0ml toluene /minute; Detection: 390 nm.

4.2.2 Characterization

4.2.2.1 UV-Vis, Mass Spectra, and Retention Behavior

After obtaining the pure samples, we measured the UV-Vis of both the $Y_2@C_{79}N$ and $Tb_2@C_{79}N$ samples. The similarity in UV-Vis spectra (see Figure 4-6) of these samples suggested that they have the same fullerene cage structure. This was consistent with the fact that $Y_2@C_{79}N$ and $Tb_2@C_{79}N$ samples had the similar retention behavior on both PBB and PYE columns. We had established the relationship between the retention behavior and the fullerene

cage sizes on 5PBB column. By this relationship, both $Y_2@C_{79}N$ and $Tb_2@C_{79}N$ had a fullerene cage size of about 85 P_π electrons, which was consistent with our calculation for a model of $[M_2]^{5+}@[C_{79}N]^{5-}$ (M = Y, Tb, and La). This cage size of about 85 P_π electrons also suggests that the N atom would be located in the fullerene cage rather than inside the cage. Since a fullerene cage requires an even number of atoms, the other possible molecular formula is $M_2CN@C_{78}$. However, the structure of $M_2CN@C_{78}$ can only result in a maximum cage size of about 82 P_π electrons.

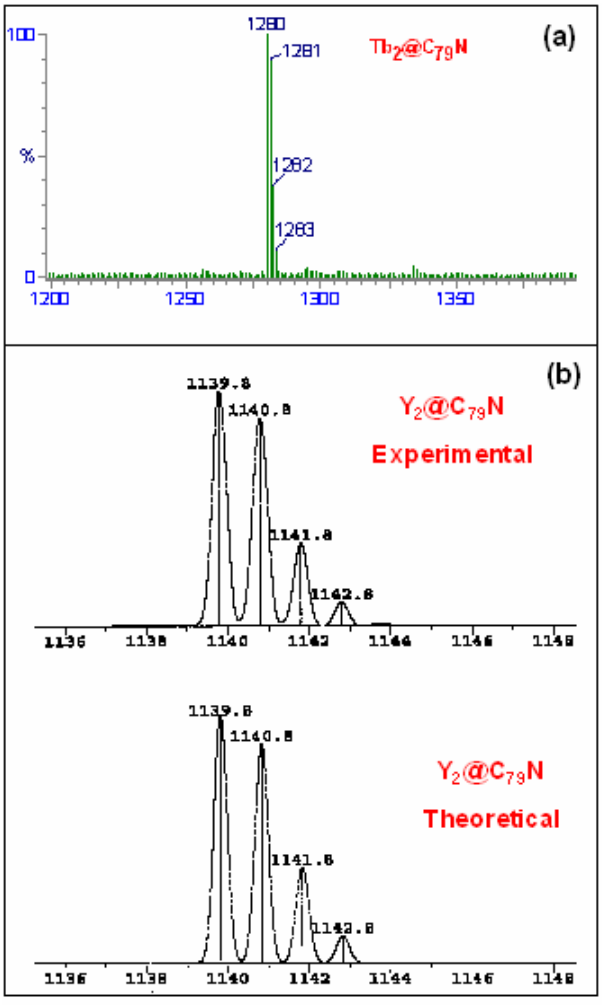

Figure 4-5. Negative DCI mass spectra of the pure $Tb_2@C_{79}N$ and $Y_2@C_{79}N$ samples.

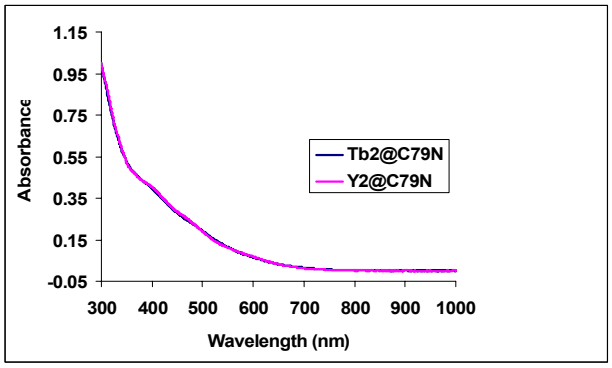

Figure 4-6. The UV-Vis spectra of the pure $Y_2@C_{79}N$ and $Tb_2@C_{79}N$ samples.

4.2.2.2 Mass Spectra of ^{15}N Isotopic Labeled $Tb_2@C_{79}N$ Sample

To verify the existence of the N atom in $Tb_2@C_{79}N$, we labeled the molecule with ^{15}N. The mass spectrum of the ^{15}N labeled sample is shown in Figure 4-7. The ^{15}N labeled $Tb_3N@C_{80}$ sample is an internal reference.

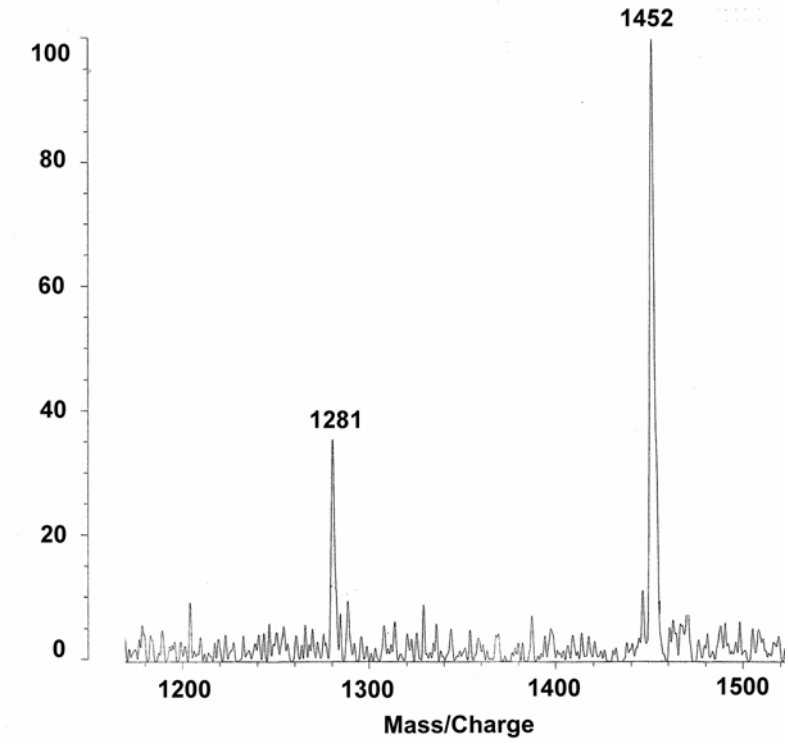

Figure 4-7. LD-TOF mass spectrum of ^{15}N labeled $Tb_2@C_{79}N$ and $Tb_3N@C_{80}$. $Tb_2@C_{79}N$ and $Tb_3N@C_{80}$ samples with natural abundant nitrogen have molecular weights of 1280 and 1451, respectively.

4.2.2.3 Crystallographic Structure of $Tb_2@C_{79}N$

From the HPLC separation chromatograms of $Tb_2@C_{79}N$ and $Y_2@C_{79}N$ shown in Figures 3-6, 4-1, 4-2, and 4-3, we knew that the yields of both $Tb_2@C_{79}N$ and $Y_2@C_{79}N$ were very low. However, the yield of $Tb_2@C_{79}N$ was slightly higher than that of $Y_2@C_{79}N$. Thus, we chose the $Tb_2@C_{79}N$ molecule for growing the single crystal sample. The methodology for growing crystals is very similar to that described in Chapter 3. Unfortunately, the available amount of the $Tb_2@C_{79}N$ sample was even much lower than those for the larger cage TNT-EMF samples—namely, only about 5 micrograms. The crystal sample was harvested after a 45-day crystallization process using our homemade device. As it turned out, utilizing the specialized conditions controlled in our homemade device, only one small crystal was produced. This observation suggests that a $Tb_2@C_{79}N$ sample was not wasted for multiple crystallizations, but was adequately utilized for growing the single observed crystal.

The space group for the black prism crystal of $Tb_2@C_{79}N$•Ni(OEP)•$2C_6H_6$ was C2/m. The orientation of the $Tb_2@C_{79}N$ molecule relative to Ni(OEP) is depicted in Figure 4-8. As a result of this disorder, the crystallographic data could not specifically identify the site of the nitrogen atom in the cage. Moreover, because of the similar sizes and scattering power of carbon and nitrogen, differentiation between C and N atom sites was challenging in such a high symmetry environment. The X-ray crystal structure of the carbocation , $(C_{59}N)^+$, also displayed disorder in the position of the nitrogen atom.[207] The possibility of a specific interaction between the nitrogen atom of the cage and the Ni(OEP) molecule was also examined and rejected. The closest contacts for atoms in the cage with the nickel atom were shown to be 3.044(8) and 2.805(3) Å for the two cage orientations. These distances were within the range found for numerous analogous structures associated with all-carbon cages. If the N atom site was ignored

and viewed as a carbon site, the fullerene cage had a structure of C_{80} (I_h). There were two orientations of the C_{80} (I_h) cages in the collected crystallographic data set. One of the two balls, which was present half the time, displayed crystallographic mirror symmetry. The other half of the time, the C_{80} was disordered with respect to the mirror plane. As shown in Figure 4-8b, there were 11 pairs of Tb atom sites, most of which were in a circle, although they did seem to avoid the Ni atom of Ni(OEP). Ten of the 11 pairs had occupancies ranging from 0.029 to 0.102. However, there was one major pair of Tb1-Tb1A, as shown in Figure 4-8a, that had an occupancy of 0.43. In Figure 4-8a, the mirror plane was vertical and came off the page. The Tb1-Tb1A distance was 3.9020(10) Å. Each of Tb1 and Tb1A atoms coordinated in an η^6 fashion to a hexagon of the fullerene cage. The Tb-C distances ranged from 2.366(10) to 2.523(11) Å with the Tb to ring centroid distance of 1.969(10) Å. The placement of the Tb atoms above the hexagons was remarkably similar to the location of the three Tb atoms in $Tb_3N@C_{80}$-I_h, where the Tb-C distances ranged from 2.404(3) to 2.518(3) Å and the Tb to ring centroid distance was 1.975(3) Å.[181]

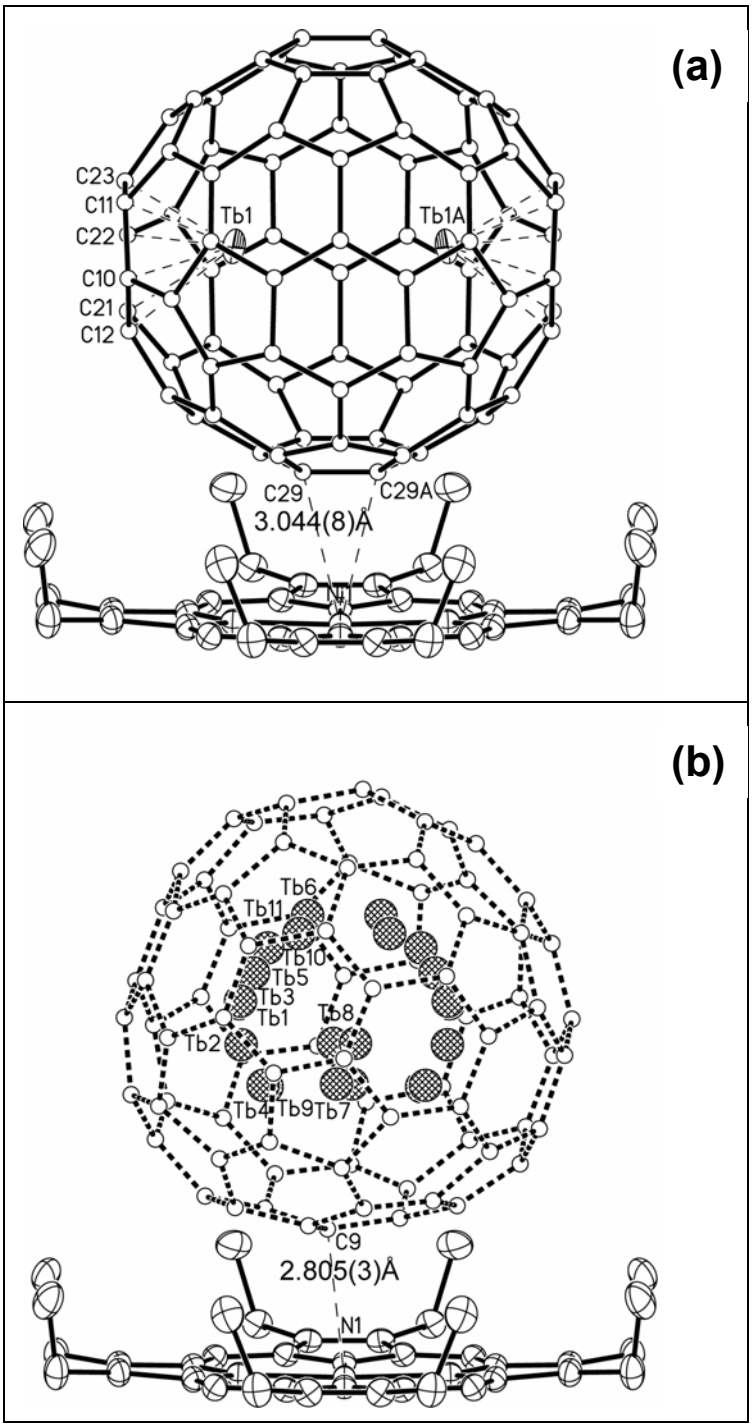

Figure 4-8. Illustrations of the $Tb_2@C_{79}N$ molecule relative to Ni(OEP) in the co-crystal of $Tb_2@C_{79}N$•Ni(OEP)•$2C_6H_6$ with uniform arbitrarily sized circle for cage carbon atoms and 50% thermal contours for other atoms. Benzene molecules were omitted for clarity.

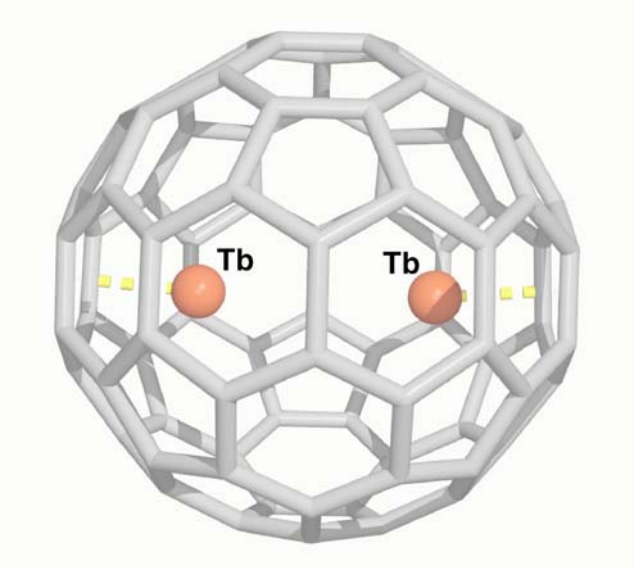

Figure 4-9. Illustration of the positions of the Tb atoms in the major site inside the fullerene cage determined crystallographically. At this site there is a crystallographic mirror plane which lies perpendicular to the plane of the paper and bisects the line between the two terbium atoms. R1 is 0.0844.

4.2.2.4 DFT Theoretical Studies: Structure of $M_2@C_{79}N$

The structure of $C_{79}N$ can be thought of as a C_{80} (I_h) cage with one N atom replacing a C atom. There are two types of carbon atoms in C_{80} (I_h), i. e. a three hexagon junction and a two-hexagon and one-pentagon junction. Therefore, the N atom can only have two possible positions, a three hexagon junction (666 junction) and a two-hexagon and one-pentagon junction (665 junction). The structures of $M_2@C_{79}N$ with 666 and 665 junctions are depicted in Figure 4-10. $[C_{79}N]^{5-}$ and $[C_{80}]^{6-}$ are isoelectronic molecules. This, we believe, explains the stability of $[C_{79}N]^{5-}$. Our theoretical calculations using density function theory (DFT, B3LYP/6-31G*)[208-211] were initially carried out on both the 666 junction and 665 junction structures of $[C_{79}N]^{5-}$, and these results are shown in Figure 4-11. As depicted, the 665 junction structure was shown to be more thermodynamically and kinetically stable than the 666 junction structure. The thermodynamic energy difference was 12.6 kcal/mol with the 665 junction structure in the lower

level. The HOMO-LUMO gaps were 2.388 and 2.684 eV for the 666 junction structure and 665 junction structure, respectively, while that of $[C_{80}]^{6-}$ was 2.99 eV at the same calculation level.

We also carried out theoretical calculations for the $Y_2@C_{79}N$ molecule at the same level. Our computational approach for $Y_2@C_{79}N$ predicted significantly higher thermodynamic and kinetic stability for the 665 structure in comparison to the 666 species. In fact, the 665 structure turned out to be 14.05 kcal/mol more stable than the 666 species. Moreover, the HOMO-LUMO gaps were relatively large 2.43 eV and 2.50 eV for the 666 and 665 junction structures, respectively. Clearly, calculations for $[C_{79}N]^{5-}$ and $Y_2@C_{79}N$ predicted similar results, i. e. a 665 junction structure was favored over its 666 counterpart based on both thermodynamic and kinetic considerations. Therefore, our subsequent calculations for molecular orbital and spin density focused on the 665 structures.

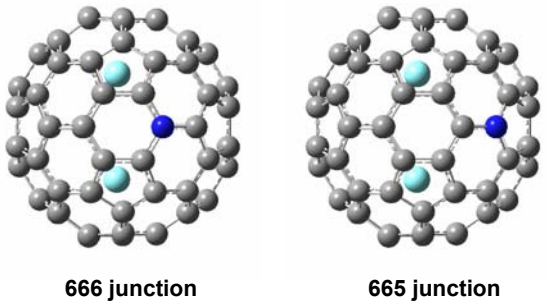

Figure 4-10. Illustration of $M_2@C_{79}N$ (M=Y, Tb, and La). N atom is placed at two possible positions: three hexagon (666) junction and two hexagon and one pentagon (665) junction.

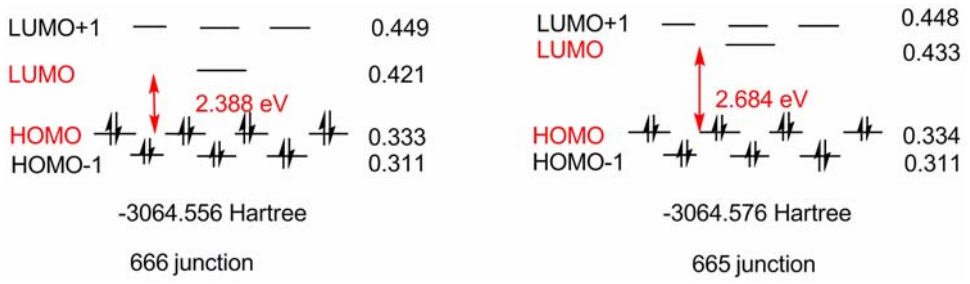

Figure 4-11. DFT calculations of 666 junction and 665 junction structures of $[C_{79}N]^{5-}$.

4.2.2.5 Electron Spin Resonance (ESR) Measurements of $Y_2@C_{79}N$ Sample in Solution, Solid, and Solid Solution

The $[M_2]^{5+}@[C_{79}N]^{5-}$ (M=Y, Tb, and La) model suggests that there is an unpaired electron in this type of molecule and they should be ESR active. Indeed, the electron spin resonance (ESR) measurements of $Y_2@C_{79}N$ confirmed this conjecture, and this is shown in Figure 4-12. However, in the case of the $Tb_2@C_{79}N$ sample, no ESR signal was detected, which we believe was due to the paramagnetic property of Tb^{3+} and the associated short electron relaxation time for the Tb^{+3} ion.[212, 213] The electronic configuration of Tb^{3+} was $4f^8$ and there were 6 unpaired electrons in the *4f* orbital.

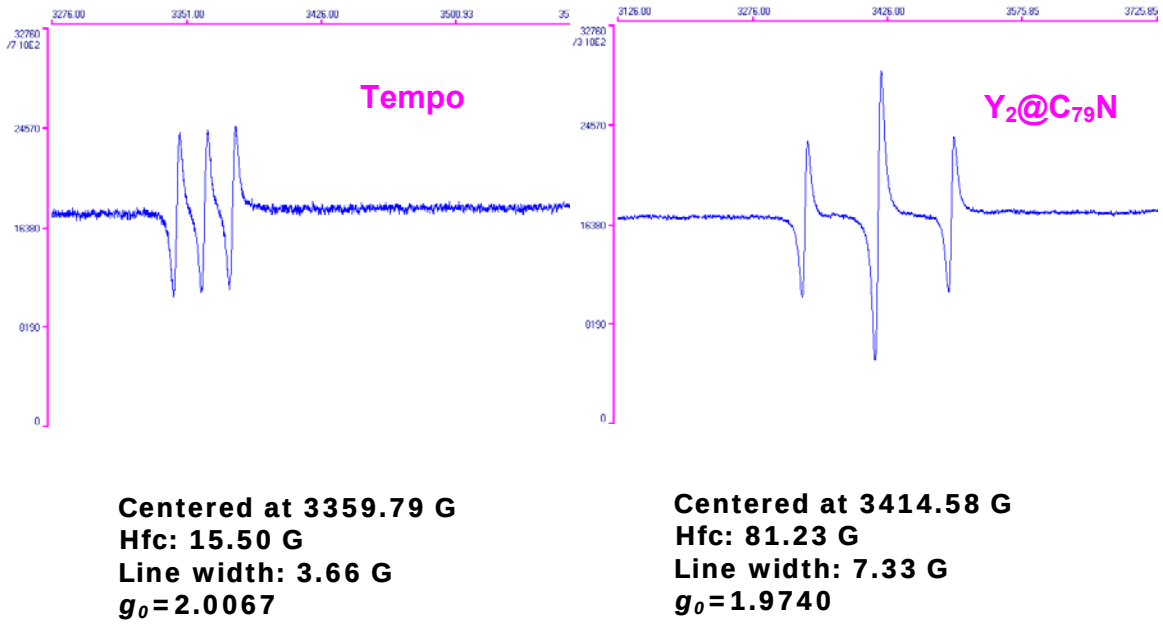

Figure 4-12. ESR measurements of $Y_2@C_{79}N$ and 2,2,6,6-Tetramethyl-piperidinyl-l-oxy (Tempo). The g-factor (g_0) value for nitrogen radicals is slightly larger than 2.0 with a hyperfine coupling constant (hfc) typically around 15 Gauss.

Figure 4-12 shows ESR measurements of $Y_2@C_{79}N$ and 2,2,6,6-Tetramethyl-piperidinyl-l-oxy (Tempo) samples. The g-factor (g_0 = 1.9740) suggests that the ESR signals were not due to the nitrogen atom (as g_0 = 2.0067 in Tempo sample) but rather to the metal atoms inside the

fullerene cage. The assignment of spin density on metals was also consistent with the large hyperfine coupling constant (81.23 G).[214, 215] The nuclear spin number of yttrium is $I = 1/2$, and the total nuclear spin number of the two yttrium atoms is 1. The unpaired electron of $Y_2@C_{79}N$ molecule was shared by the two yttrium atoms and formed a single-electron chemical bond between them. According to the $(2I + 1)$ rule, the ESR signals will demonstrate 3 peaks with 1:2:1 ratios of peak areas, which was confirmed by the experimental observations.

To further test the assignment of the spin location, ESR measurements of the solid $Y_2@C_{79}N$ sample were carried out. As expected, a singlet ESR signal with the same g_0 value was observed, which was associated with the Heisenberg spin exchange effect. Diluted with C_{84}, a solid solution of $Y_2@C_{79}N$ in excess of C_{84} again demonstrated ESR signals of three peaks. The corresponding 1:2:1 ratio of peak areas was similar to the results of the sample in toluene. These results of ESR measurements can only be explained by the fact that the cluster inside the fullerene cage is a spin-doped dimetallic cluster. A comparison of the ESR measurements of the $Y_2@C_{79}N$ sample in different states is demonstrated in Figure 4-13.

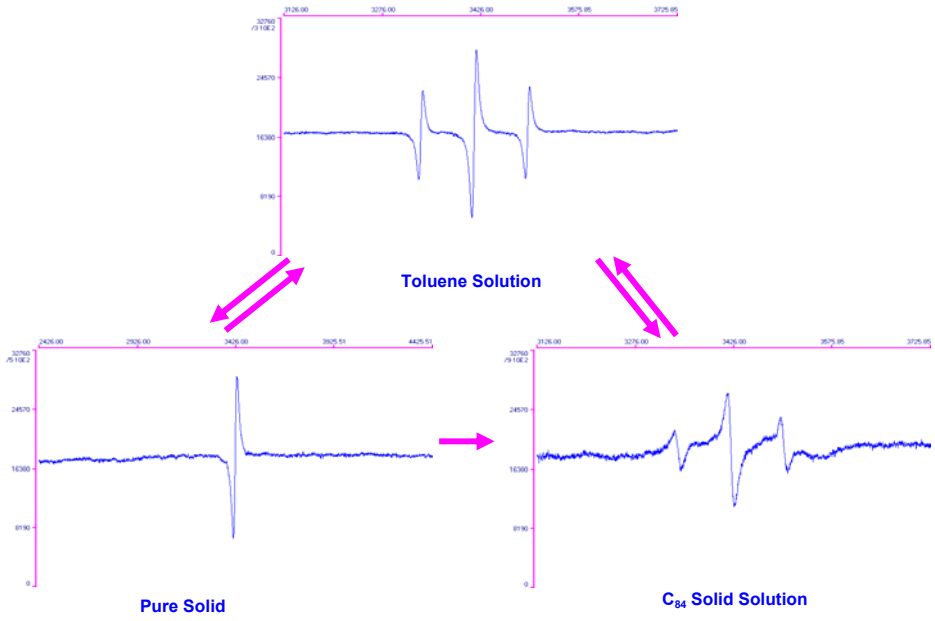

Figure 4-13. Comparison of the ESR measurements of $Y_2@C_{79}N$ in different states.

4.2.2.6 DFT Theoretical Studies: Low-lying Single-electron Orbital and Spin Density

The density functional theory (DFT, B3LYP) calculations, with basis sets of 6-31G* for the C and N atoms, and DZVP (DFT orbital) for the Y atom,[216] showed that Y-Y distance was 3.864 Å. The orientation of the two Y atoms relative to the N atom is illustrated in Figure 4-14.

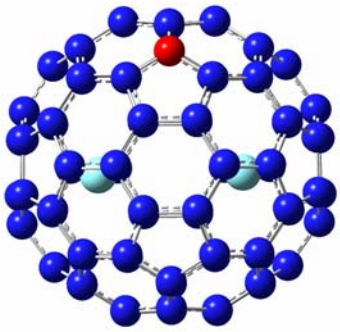

Figure 4-14. The orientation of the two Y atoms relative to the N atom in the 665 junction structure.

The single-electron orbital between the two Y atoms was low-lying at the HOMO -2 orbital. This low-lying single-electron orbital— together with the large HOMO-LUMO gap (2.50 eV)—are responsible for the stability of the $Y_2@C_{79}N$ molecule. The calculated isotropic Fermi contact coupling was 65.79 G, which is very close to the experimental hyperfine coupling constant (81.23 G). Moreover, the lack of an observed ^{14}N nitrogen hyperfine coupling for the cage nitrogen atom is consistent with the small calculated value 0.03 G. We also calculated the $Y_2@C_{80}$ (I_h) molecule at same level. The LUMO of $Y_2@C_{80}$ (I_h) corresponds to the empty orbital between the two Y atoms and had a very low level of energy. As a consequence, $Y_2@C_{80}$ (I_h) exhibited a small HOMO-LUMO gap of 0.92 eV, suggesting that $Y_2@C_{80}$ (I_h) molecule is not stable, which is consistent with missing observation of the $Y_2@C_{80}$ (I_h) molecule.

Notice that the $Y_2@C_{79}N$ molecule has one more electron than $Y_2@C_{80}$ (I_h). Upon accepting one electron, $Y_2@C_{80}$ (I_h) becomes $[Y_2@C_{80}\ (I_h)]^-$, which is the isoelectronic molecule of $Y_2@C_{79}N$. The low-level energy LUMO of $Y_2@C_{80}$ (I_h) with the single electron accepted will

be further lying down to the HOMO -2 of $[Y_2@C_{80}\ (I_h)]^-$, resulting in a large HOMO-LUMO gap, as well as the same molecular orbital distributions as those of $Y_2@C_{79}N$. A comparison of the molecular orbital distributions between $[Y_2@C_{80}\ (I_h)]^-$ and $Y_2@C_{79}N$ and the indication of the low-lying process of $Y_2@C_{80}\ (I_h)$'s LUMO upon accepting one electron are shown in Figure 4-15. Electrons in the $Y_2@C_{80}\ (I_h)$ molecule are all coupled, thus there is no spin density associated with it. However, there is an uncoupled electron in both the $[Y_2@C_{80}]^-$ and $Y_2@C_{79}N$ molecules. The single electron in both the $[Y_2@C_{80}]^-$ and $Y_2@C_{79}N$ molecules is located in the HOMO-2 orbital for the two molecules. The HOMO-2 orbitals in the $[Y_2@C_{80}]^-$ and $Y_2@C_{79}N$ molecules are mainly contributed by the two Y atoms, as shown in Figure 4-15. Moreover, the spin density of $[Y_2@C_{80}]^-$ and $Y_2@C_{79}N$ molecules are concentrated between the two Y atoms and have a very similar shape to the HOMO-2 orbital. This observation suggests that the spin density of the two molecules is due to the uncoupled electron at the HOMO-2 orbital. These calculated results were confirmed by the ESR signals demonstrated in Figure 4-13.

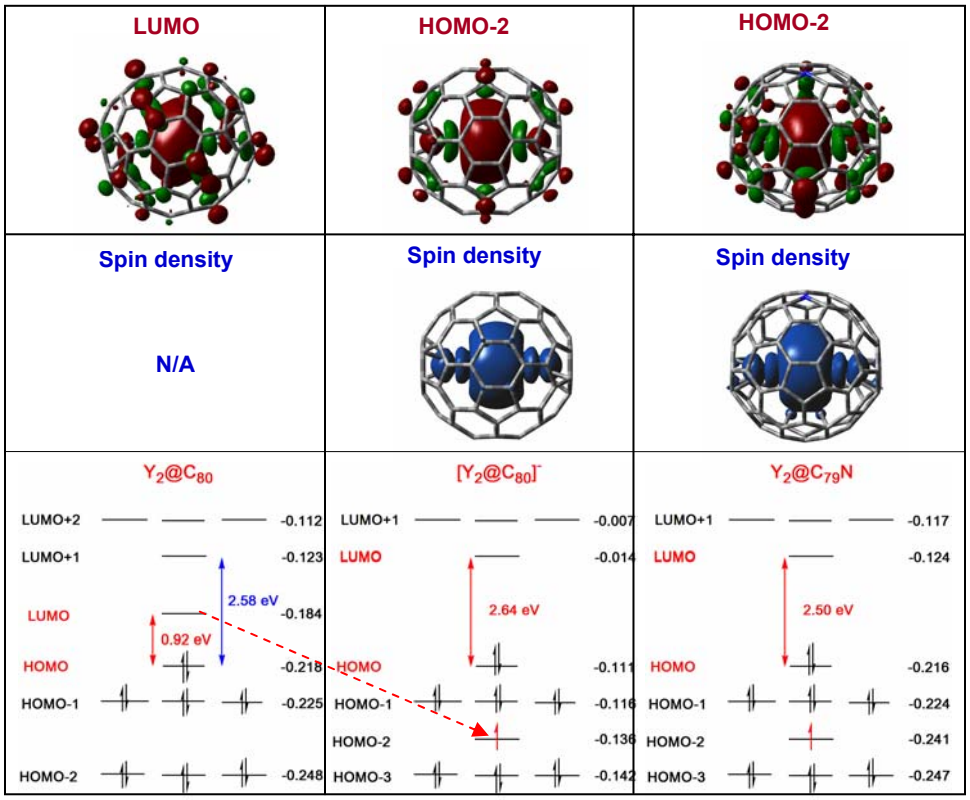

Figure 4-15. Illustrations of the low-lying process of $Y_2@C_{80}$ (I_h)'s LUMO upon accepting one electron, and comparison of the molecular orbital distributions between $Y_2@C_{79}N$ and $[Y_2@C_{80}]^-$, as well as comparisons of HOMO-2 and spin density of $Y_2@C_{79}N$ and $[Y_2@C_{80}]^-$.

Calculation of $[Y_2@C_{79}N]^+$ showed that when one electron was removed from $Y_2@C_{79}N$, the electron was from the HOMO of $Y_2@C_{79}N$, not from the single electron occupied HOMO-2. In order to further establish that the single electron at the HOMO-2 orbital was truly at low energy level, the $[Y_2@C_{79}N]^{2+}$ was calculated. This was done to ascertain the location where the two electrons could eventually be removed from the $Y_2@C_{79}N$ molecule. As expected, the two electrons were removed from the HOMO orbital of the $Y_2@C_{79}N$ molecule. The single electron was still there, but now it was located in the HOMO-1 of $[Y_2@C_{79}N]^{2+}$ molecular ion, confirming that the single electron was truly low-lying in a low-energy orbital. The comparison of the HOMO-1 orbital and spin density of the $[Y_2@C_{79}N]^{2+}$ molecular ion is shown in Figure 4-16.

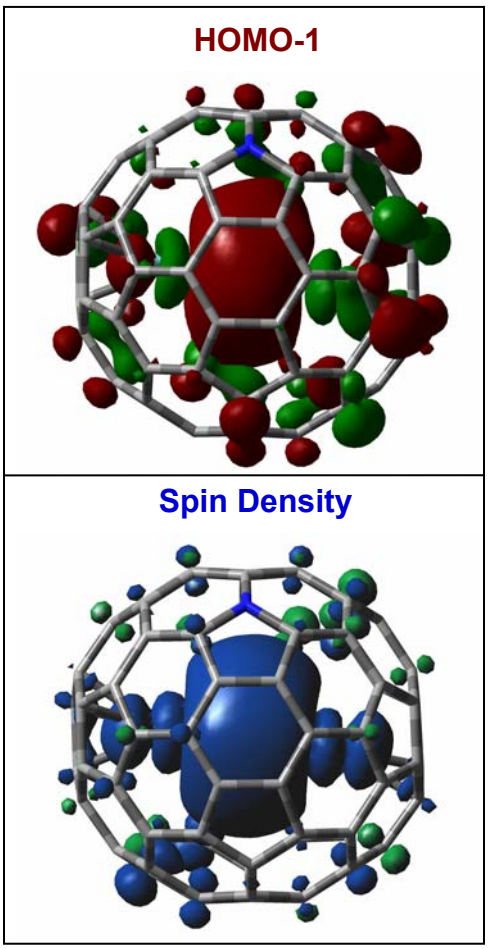

Figure 4-16. Comparison of the HOMO-1 orbital and spin density of $[Y_2@C_{79}N]^{2+}$ molecular ion. The HOMO-1 orbital of $[Y_2@C_{79}N]^{2+}$ corresponding to the HOMO-2 orbital of $Y_2@C_{79}N$.

Important comparisons among the HOMO of $[Y_2@C_{80}]^{2-}$, the LUMO of $Y_2@C_{80}$ (I_h), and the HOMO -2 of $[Y_2@C_{80}]^{-}$ are depicted in Figure 4-17. In particular, by comparing the symmetries of the molecular orbitals, we determined that the low-lying HOMO-2 orbital of $[Y_2@C_{80}$ (I_h)$]^{-}$ was from the LUMO of $Y_2@C_{80}$ (I_h). Upon accepting one electron, the LUMO with the single electron of is low-lying to HOMO-2 of $[Y_2@C_{80}$ (I_h)$]^{-}$. The small HOMO-LUMO gap (0.92 eV) of $Y_2@C_{80}$ (I_h) thereby becomes the large HOMO-LUMO gap (2.64 eV) of $[Y_2@C_{80}$ (I_h)$]^{-}$(see Figure 4-15). Upon accepting two electrons, however, the LUMO remained but became the HOMO of $[Y_2@C_{80}$ (I_h)$]^{2-}$ with smaller HOMO-LUMO gap of 2.00 eV. These

results suggested that single electron bond between the two Y metal atoms is favored, while a two electron bond between the two Y metal atoms is not.

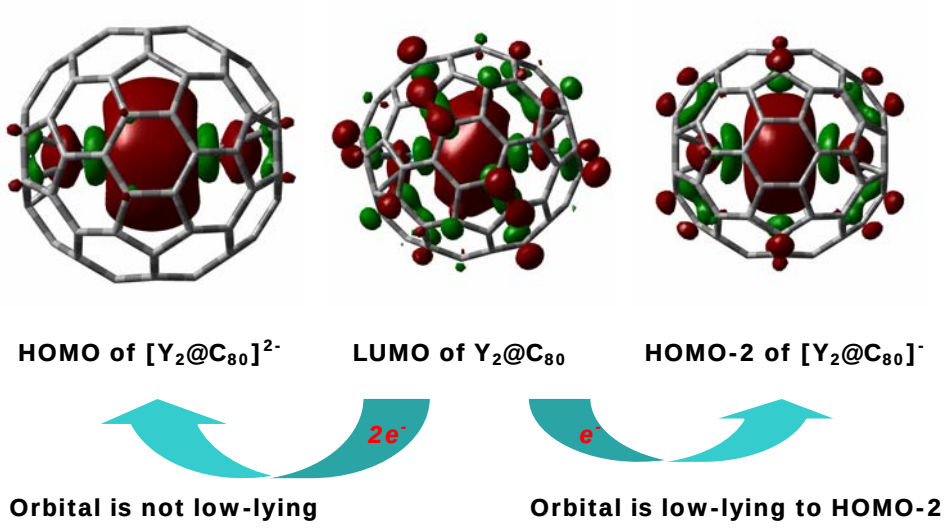

Figure 4-17. Comparisons of HOMO of $[Y_2@C_{80}]^{2-}$, LUMO of $Y_2@C_{80}$, and HOMO-2 of $[Y_2@C_{80}]^{-}$.

In order to confirm the kinetic stabilization energy of the single-electron bond between dimetallic clusters inside a fullerene cage, theoretical calculations were also conducted on $[Y_2@C_{79}N]^{-}$, which is an isoelectronic molecule of $[Y_2@C_{80}]^{2-}$. The molecular orbital diagram of $[Y_2@C_{79}N]^{-}$ and its HOMO orbital are shown in Figure 4-18. Since $Y_2@C_{79}N$ has a single-electron bond between its two Y atoms, $[Y_2@C_{79}N]^{-}$ should have two electrons shared by the two Y atoms. As shown in Figure 4-18, the two-electron orbital between the two Y atoms was not low-lying and remained as the HOMO of $[Y_2@C_{79}N]^{-}$. Consequently, the HOMO-LUMO gap (1.89 eV) was much smaller than that (2.50 eV) of $Y_2@C_{79}N$ molecule.

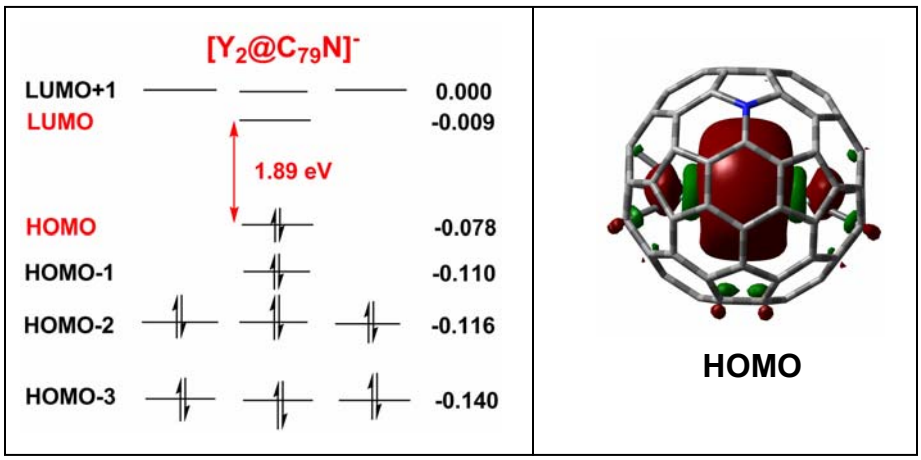

Figure 4-18. Molecular orbital diagram and the HOMO of $[Y_2@C_{79}N]^-$. The HOMO of $[Y_2@C_{79}N]^-$ was mainly contributed by two Y atoms.

Table 4- 1 Comparisons of Y-Y bond lengths and hybrids on bonding Y atoms

	Y-Y Distance (Å)	Hybrid on Bonding Y	Orbital
$[Y_2@C_{79}N]^-$	3.613	$5s4d^{0.75}$	HOMO, 2e Bonding
$Y_2@C_{79}N$	3.864	$5s4d^{1.59}$	HOMO-2, 1e Bonding
$[Y_2@C_{80}]^{2-}$	3.640	$5s4d^{0.86}$	HOMO, 2e Bonding
$[Y_2@C_{80}]^-$	3.893	$5s4d^{1.63}$	HOMO-2, 1e Bonding
$Y_2@C_{80}$	3.941	No bonding	LUMO, no bonding
Y_2^{5+}	No minimum point	N/A	N/A

As shown in Table 4-1, the Y-Y distances in the relative molecules clearly demonstrate the formation of the metal-metal bond between the two Y atoms. Since no fullerene cage constrains for two yttrium cations, Y_2^{5+} cannot exist due to the strong electrostatic repulsion between the two Y cations. In $Y_2@C_{80}$ molecule, the two Y cations participate in LUMO. Thus, no bonding was formed between them. Its Y-Y distance was 3.941 Å. Upon accepting 1e and 2e, $Y_2@C_{80}$ became $[Y_2@C_{80}]^-$and $[Y_2@C_{80}]^{2-}$ and their Y-Y distances were 3.893 Å and 3.640 Å,

respectively. The decrease trend of Y-Y distances from $Y_2@C_{80}$ to $[Y_2@C_{80}]^-$ and from $[Y_2@C_{80}]^-$ to $[Y_2@C_{80}]^{2-}$ supported that a single-electron bond and a two-electron bond were formed between the two Y cations in the $[Y_2@C_{80}]^-$ and $[Y_2@C_{80}]^{2-}$, respectively. The cases of $Y_2@C_{79}N$ and $[Y_2@C_{79}N]^-$ were similar. Their Y-Y distances (3.864 Å in $Y_2@C_{79}N$ and 3.613 Å in $[Y_2@C_{79}N]^-$) also decreased, suggesting the metal-metal bond became stronger from the $Y_2@C_{79}N$ to $[Y_2@C_{79}N]^-$, where there were a single-electron bond and a two-electron bond between the two Y^{3+} cations, respectively. The inspection of the hybrid on the bonding Y atoms demonstrated that the bonding between the two Y cations was primarily between their 5s and 4d atomic orbitals.

We also calculated $La_2@C_{79}N$. The La-La distance (3.638 Å) was much shorter than the Y-Y distance (3.864 Å) in $Y_2@C_{79}N$ as well as Tb-Tb distance (3.902 Å) in $Tb_2@C_{79}N$. In addition, the single-electron occupied LUMO was not low-lying. As a result, its HOMO-LUMO gap (2.08 eV) of $La_2@C_{79}N$ was much smaller than that (2.64 eV) of $Y_2@C_{79}N$. This observation also suggests that the single-electron bond between two metals is very sensitive to the distance between those two metals. This smaller HOMO-LUMO gap is consistent with the much smaller yield of $La_2@C_{79}N$ compared with $Tb_2@C_{79}N$ and $Y_2@C_{79}N$. The molecular orbital diagram of $La_2@C_{79}N$ is shown in Figure 4-19, while comparisons of its α-HOMO, β-LUMO, and spin density are shown in Figure 4-20. Since the total number of electrons in the $La_2@C_{79}N$ molecule is odd, the uncoupled electron is in the α-HOMO orbital. Therefore, we anticipated that the α-HOMO and β-LUMO would have the same symmetry, and that the spin density would reflect the symmetry of the α- HOMO.

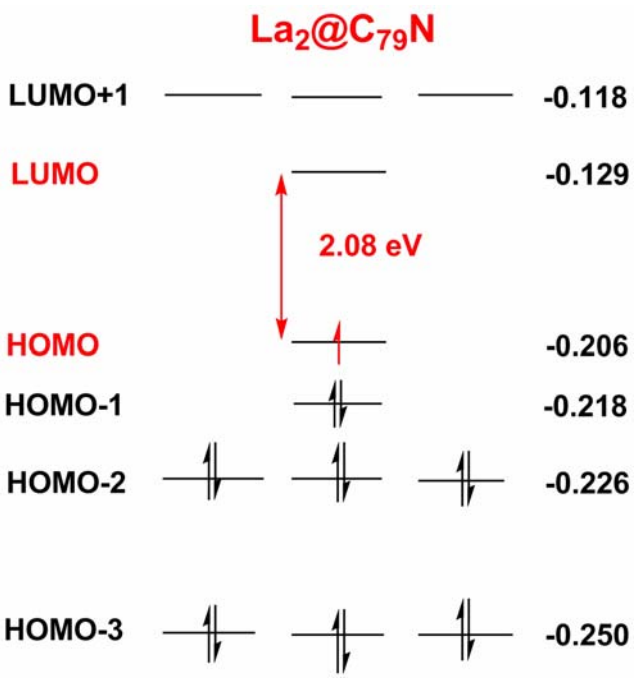

Figure 4-19. Molecular orbital diagram of $La_2@C_{79}N$. Contrast to those of $Y_2@C_{79}N$ and $[Y_2@C_{80}]^-$, the uncoupled electron was not low-lying and remained at the HOMO, resulting in a smaller HOMO-LUMO gap.

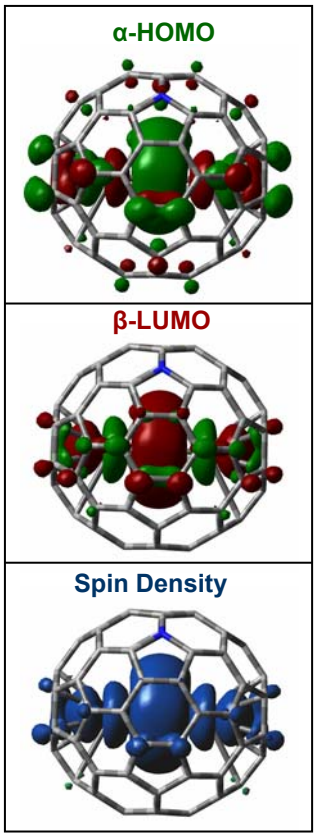

Figure 4-20. Comparison of α-HOMO, β-LUMO, and spin density of $La_2@C_{79}N$.

4.2.2.7 Synthesis and Separation of $La_2@C_{79}N$ and $La@C_{81}N$

The synthesis and isolation of $La_2@C_{79}N$ was very similar to procedures used for both $Tb_2@C_{79}N$ and $Y_2@C_{79}N$. However, due to the large size of the lanthanum atom, La-based TNT-EMFs were not found. Thus, the HPLC trace of effluent after chemical separation was different from those of the Tb- and Y-based samples. Based on the known methodology of separating $Tb_2@C_{79}N$ and $Y_2@C_{79}N$, we knew that $La_2@C_{79}N$ would co-elute with C_{84} on a 5PBB column if it existed. Therefore, the peaks around C_{84} were collected in wide range to avoid the loss of the $La_2@C_{79}N$ sample, as shown in Figure 4-21.

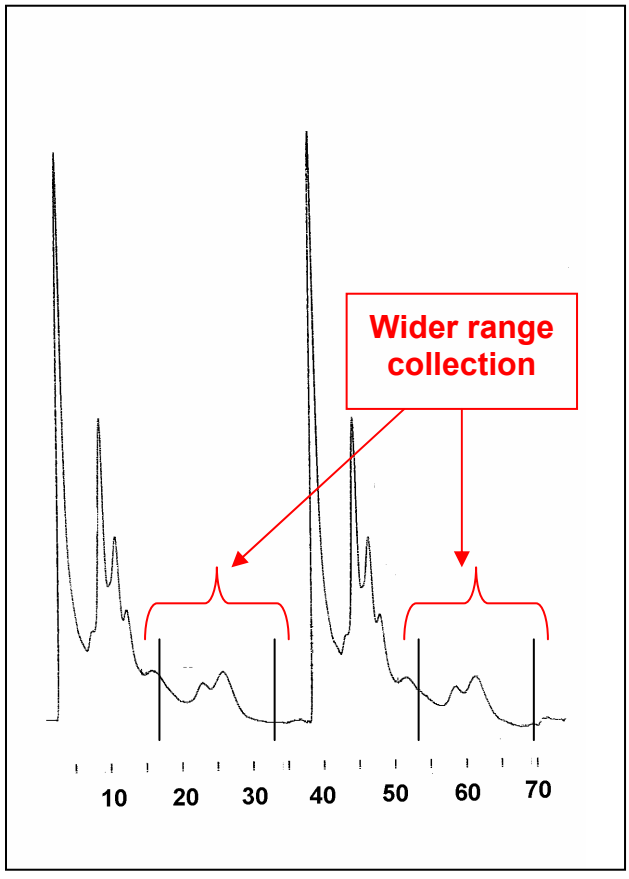

Figure 4-21. HPLC chromatograms of effluent after chemical separation on a 5PBB column (4.6 mm × 250mm). It shows the two traces of continuous sample injections. Flow rate: 2.0 ml toluene /minute; Detection: 390 nm.

The sample collected during the first stage of HPLC using a 5PBB column was further separated on a 5PYE column. This HPLC chromatogram is shown in Figure 4-22. There were

three peaks in the 5PYE trace. C_{84} was expected because it had always co-eluted with $M_2@C_{79}N$ molecules. Samples La 1 and La 2 were collected and further cycled on a 5PYE column. Their HPLC chromatograms are shown in Figures 4-23 and 4-24.

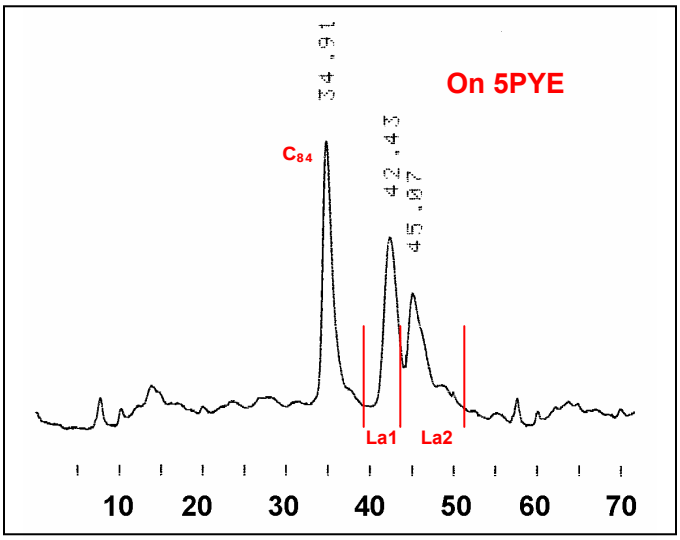

Figure 4-22. HPLC chromatogram on a 5PYE column (10 mm × 250mm) of the C_{84} portion collected during the first separation stage on a 5PBB column. Flow rate: 2.0 ml toluene /minute; Detection: 390 nm.

Surprisingly, the La 1 portion was identified as $Tb_3N@C_{80}$, which was confirmed by mass spectrum. Upon further investigation, however, we ascertained that it had been contaminated—probably as a result of the reclaimed extraction solvent. Due to the very low yield of $La_2@C_{79}N$, the contamination became even more significant when we concentrated the La-based sample by vaporizing the solvent. We also purified the La 2 sample by cycling on a 5PYE column. The resulting mass spectrum demonstrates that it contained both $La_2@C_{79}N$ and $La@C_{81}N$. To further confirm the presence of $La_2@C_{79}N$, the La 2 portion was characterized via high resolution LD-TOF mass spectrometry, which is shown in Figure 4-25.

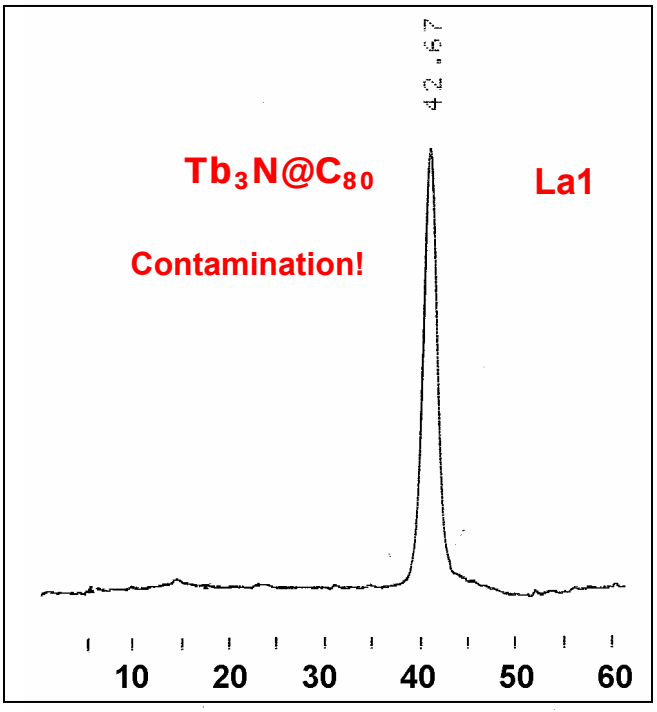

Figure 4-23. HPLC chromatogram of the La 1 portion on a 5PYE column (10 mm × 250mm). Flow rate: 2.0 ml toluene /minute; Detection: 390 nm.

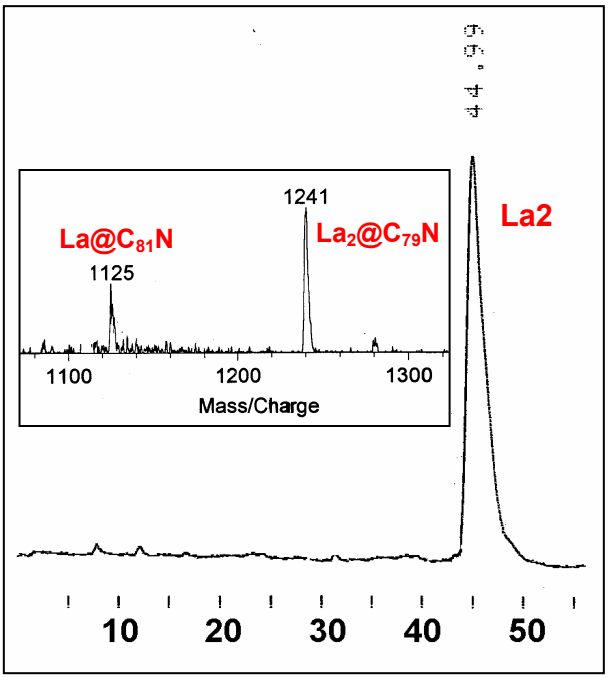

Figure 4-24. HPLC chromatogram of the La 2 portion on a 5PYE column (10 mm × 250 mm). The inserted mass spectrum confirms that it contains both $La_2@C_{79}N$ and $La@C_{81}N$. Flow rate: 2.0 ml toluene /minute; Detection: 390 nm.

4.2.2.8 High Resolution LD-MS Spectra of $La_2@C_{79}N$ and $La@C_{81}N$

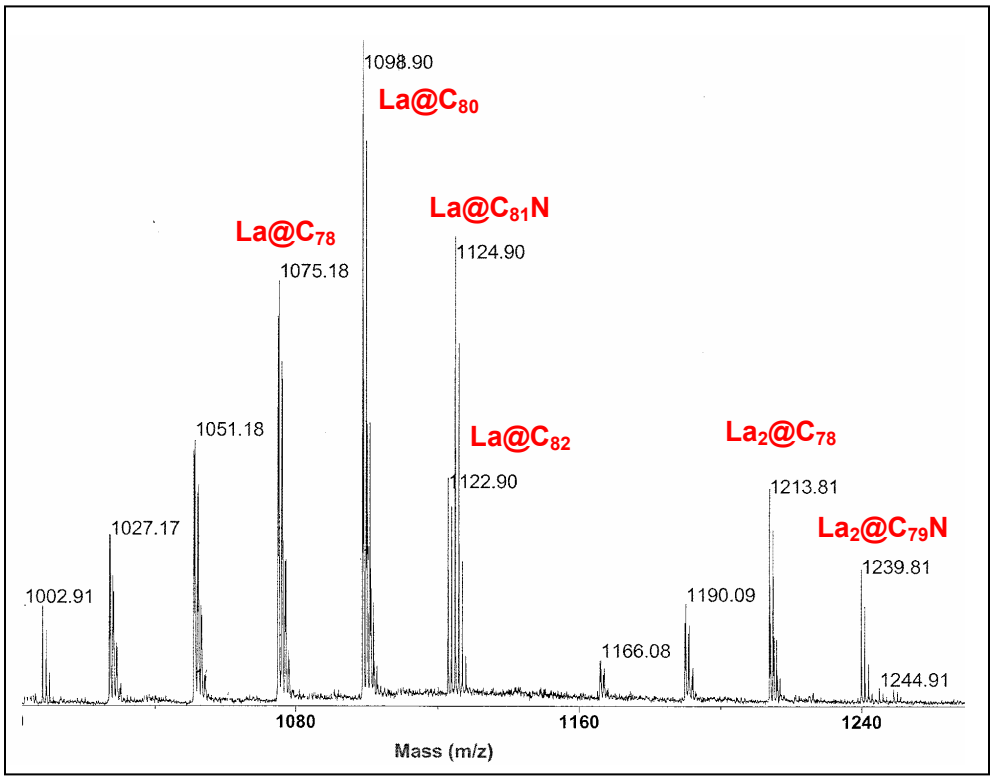

Figure 4-25. High resolution LD-TOF mass spectrum of La 2 portion. It demonstrates that in addition to the existence of both $La_2@C_{79}N$ and $La@C_{81}N$, there are a series of $La@C_{2n}$ ($2n \leq 82$) and a series of $La_2@C_{2n}$ ($2n \leq 78$) presenting in the La2 portion.

High resolution LD-TOF mass spectrum of the La 2 portion shown in Figure 4-25 confirms the existence of $La_2@C_{79}N$ and $La@C_{81}N$ (as shown in Figure 4-24). In addition to the existence of both $La_2@C_{79}N$ and $La@C_{81}N$, it also demonstrates the presence of a series of $La@C_{2n}$ ($2n \leq 82$) and a series of $La_2@C_{2n}$ ($2n \leq 78$) in the La 2 portion. Comparisons of the experimental mass spectra and theoretical isotopic distributions of $La_2@C_{79}N$ and $La@C_{81}N$ are shown in Figure 4-26 and Figure 4-27, respectively.

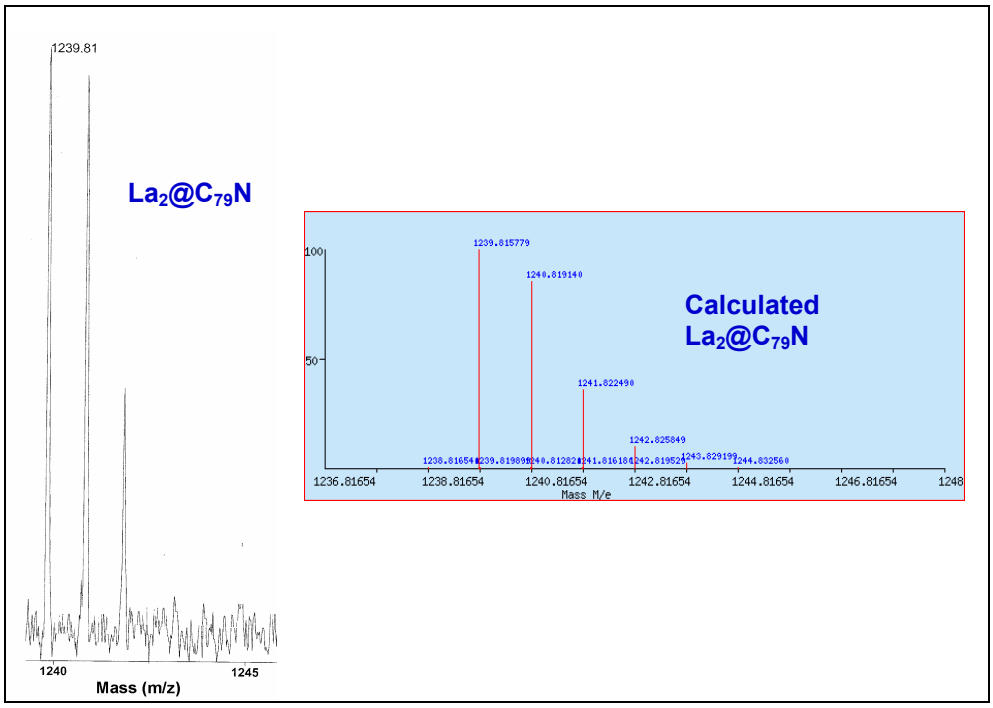

Figure 4-26. Comparison of the experimental mass spectrum of $La_2@C_{79}N$ and its theoretical isotope distribution.

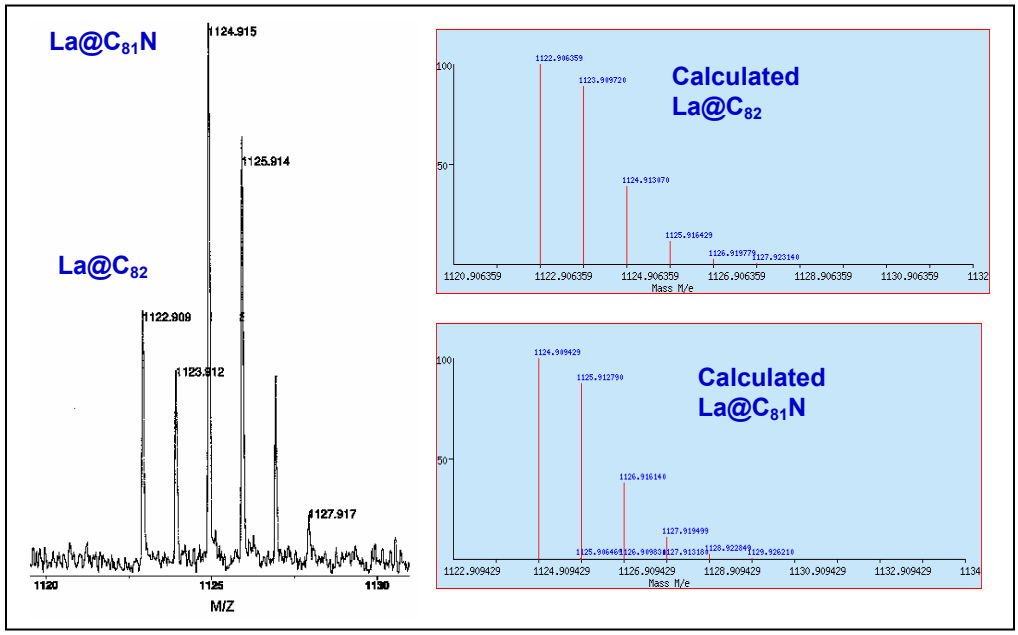

Figure 4-27. Comparisons of experimental mass spectra of $La@C_{81}N$ and $La@C_{82}$ and their theoretical isotope distributions.

2.2.9 DFT Theoretical Studies: Stability of $M_2@C_{80}$ (I_h)

Due to the small size of $La_2@C_{79}N$ sample, it could not be completely isolated. Instead, it was mixed with $La@C_{81}N$ and series of $La_2@C_{2n}$ ($2n \leq 78$) and $La@C_{2n}$ ($2n \leq 82$), as shown in Figure 4-25. It should be noted, however, that the well-characterized $La_2@C_{80}$ (molar mass: 1238) in literature is missing from the mass spectrum in Figure 4-25, suggesting that $La_2@C_{80}$ (I_h) is not a very stable species and cannot compete with $La_2@C_{79}N$ in the process of synthesis and chemical separation. Our theoretical calculations show that $La_2@C_{80}$ (I_h) exhibited a much smaller HOMO-LUMO gap (1.30 eV) than $La_2@C_{79}N$ (2.08 eV). The electrochemical gap of $La_2@C_{80}$ (I_h) was 0.87 V. These data suggests that $La_2@C_{80}$ (I_h) is kinetically much less stable than the members of the C_{80} cage TNT-EMFs, whose electrochemical gaps and HOMO-LUMO gaps are generally around 1.8 V and 2.5 eV, respectively. This also explains why the yield of $La_2@C_{80}$ (I_h) was much smaller than other $M_3N@C_{80}$ (I_h). Although $La_2@C_{80}$ (I_h) has the fullerene cage C_{80}^{6-} (I_h), which is the same as that of TNT-EMFs, its stability was not the same as that of C_{80}^{6-} (I_h) because the La_2 cluster also participates in the frontier molecular orbitals, and thus affects the HOMO-LUMO gap. The molecular orbital diagram and the LUMO orbital of $La_2@C_{80}$ (I_h) are shown in Figure 4-28. Clearly, the LUMO of the $La_2@C_{80}$ was mainly contributed by La_2 cluster. Due to the low-energy level of the LUMO, the HOMO-LUMO gap of $La_2@C_{80}$ (I_h) is much smaller than that of C_{80}^{6-} (I_h).

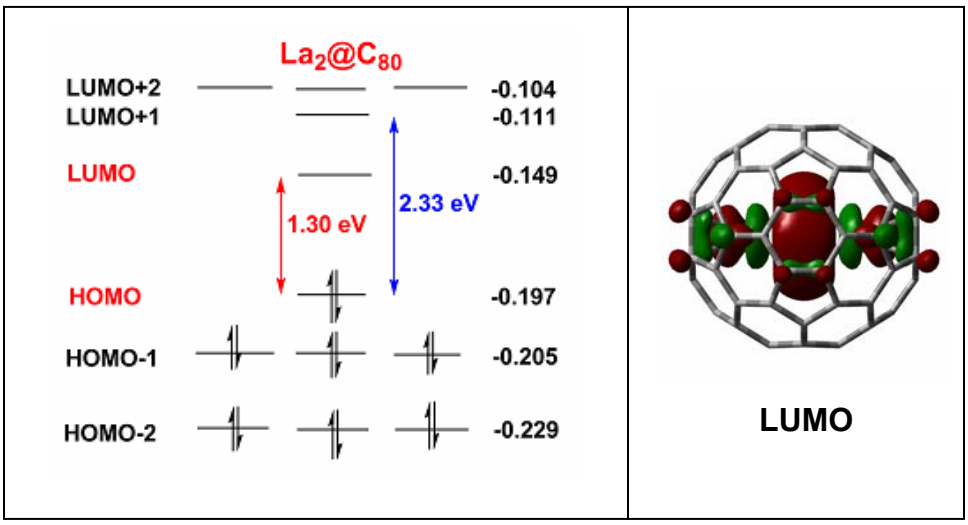

Figure 4-28. Molecular orbital diagram and LUMO of $La_2@C_{80}$. The LUMO of $La_2@C_{80}$ (I_h) was mainly contributed by two La atoms.

Although the HOMO-LUMO gap (1.30 eV) of $La_2@C_{80}$ (I_h) was much smaller than those of either $La_2@C_{79}N$ (2.08 eV) or $Y_2@C_{79}N$ (2.50 eV), it was significantly larger than the HOMO-LUMO gap (0.92 eV) of $Y_2@C_{80}$ (I_h). These results are consistent with experimental observations, namely that $La_2@C_{80}$ (I_h) has been synthesized and well characterized in many reports[120, 151, 160, 165] while $Y_2@C_{80}$ (I_h) is a missing molecule. These results strongly suggest that the kinetic stability of $M_2@C_{80}$ (I_h) is metal dependent. Since the LUMO of $M_2@C_{80}$ (I_h) is primarily impacted by (1) the dimetallic cluster (M_2) inside the C_{80} (I_h) fullerene cage, and (2) the fact that generally the LUMO is at a low-energy level, $M_2@C_{80}$ (I_h) is less stable than its $M_2@C_{79}N$ counterpart. Thus far, the reported $M_2@C_{80}$ (I_h) molecules include $La_2@C_{80}$ (I_h), $Ce_2@C_{80}$ (I_h), $Pr_2@C_{80}$ (I_h), and $Gd_2@C_{80}$ (I_h). However, due to the complicated isotope distribution in mass spectrum of $Gd_2@C_{80}$ (I_h), the assignment of $Gd_2@C_{80}$ (I_h) by only mass spectrum characterization is questionable. Apparently, other three members of the $M_2@C_{80}$ (I_h) family (M=La, Ce, and Pr) are the largest (or light) lanthanide-based dimetallic endofullerenes.

4.3 Summary

In summary, a family of novel dimetallic endohedral metalloazafullerenes with the molecular formula of $M_2@C_{79}N$ (M=Y, Tb, and La) was synthesized, isolated, and characterized for the first time. Mass spectra also demonstrated the existence of $La@C_{81}N$ and $Tb@C_{81}N$. The structural characterization of $Tb_2@C_{79}N$ using single crystal X-ray diffraction demonstrated that its fullerene cage was an I_h eighty-atom cage and thus excluded the possibility of $Tb_2CN@C_{78}$. The presence of the N atom in the molecule was further confirmed by mass spectrum of ^{15}N labeled sample. Based on their similar retention behavior and/or similar UV-Vis spectra, its Y- and La-based counterparts should also have formula of $Y_2@C_{79}N$ and $La_2@C_{79}N$, respectively. Our ESR data demonstrated that there was a single electron between two Y atoms in the $Y_2@C_{79}N$ molecules. Our calculations supported the experimental observation and showed that the single electron was low-lying at HOMO -2 orbital and thus resulted in a large HOMO-LUMO gap for $Y_2@C_{79}N$. The large HOMO-LUMO gap and the low-lying single-electron orbital (hidden at HOMO-2) were responsible for the stability of $Y_2@C_{79}N$. Theoretical calculations of $Y_2@C_{79}N$ vs. $[Y_2@C_{80}]^-$ and $[Y_2@C_{79}N]^-$ vs. $[Y_2@C_{80}]^{2-}$ demonstrated that the single-electron-two-metal-center bond inside the fullerene cages was favored while the two-electron-two-metal-center bond was not. The single-electron-two-metal-center bond was sensitive to the distance between the two metal centers. While the larger distance between the two metal centers in $Y_2@C_{79}N$ and $[Y_2@C_{80}]^-$ rendered the low-lying of the single-electron occupied orbital and thereby resulted in large HOMO-LUMO gaps (2.50 eV and 2.64 eV for $Y_2@C_{79}N$ and $[Y_2@C_{80}]^-$, respectively), the smaller distance between the two metal centers in $La_2@C_{79}N$ did not have the low-lying phenomenon of the single-electron occupied orbital and thus resulted in a small HOMO-LUMO gap (2.08 eV). These calculation results were consistent with experimental results of ESR signals, sample stability, and synthesis yields. The low-lying

orbital at lower energy level was further confirmed by the calculated results of their oxidized counterparts.

Theoretical calculations also showed that the kinetic stability of $M_2@C_{80}$ (I_h) was metal dependent since M_2 cluster participate in a frontier orbital, LUMO, of $M_2@C_{80}$ (I_h). Because larger lanthanide-based $M_2@C_{80}$ (M=La, Ce, and Pr) had reasonable HOMO-LUMO gap (such as 1.30 eV for $La_2@C_{80}$), they were isolated and characterized. However, smaller size metal-based $Y_2@C_{80}$ was not experimentally observed. This was consistent with its smaller HOMO-LUMO gap (0.92 eV).

Due to the special magnetic properties and novel electronic structures, $M_2@C_{79}N$ (M=Y, Tb, and La) are expected to have many potential applications, such as nano-scale molecule electronics, molecular semiconductors, and quantum computers.[217, 218] With the disclosure of their structures in current research, more discoveries about the new nano-particles of $M_2@C_{79}N$ are anticipated.[219, 220]

Chapter 5 — HPLC Retention Behavior of TNT-EMFs

5.1 Introduction

Fullerene synthesis via the arc-discharge method produces a mixture of both empty cage fullerenes and endohedral metallofullerenes, with the former as dominant components. In the current research, even after primary chemical separation using CPDE-MPR which removes most of the reactive empty cage fullerenes,[185] the surviving solutes were still mixed together and had to be further separated. Due to this, the HPLC separation process generally is a necessary part of fullerene research. Using modern techniques, HPLC can quantitatively provide precise and reproducible chromatography for studying the intermolecular interactions between the solute and the mobile and stationary phases.[66, 221] At a constant temperature, the HPLC retention behavior of solutes, which reflect the intermolecular interactions, depend on the three variables: the physicochemical properties of the mobile phase, the physicochemical properties of the stationary phase, and the nature (chemical structure) of the solute.[221-224] The physicochemical properties of both mobile and stationary phases can be controlled once these phases are selected and the flow rate of the mobile phase is determined. Under controlled conditions, the only independent variable is the chemical structure of the solutes being studied. Therefore, HPLC was used in this study not only as a method of isolating specific structural isomers, but also as one way of studying the various mechanisms associated with chromatographic separations and the relationships between the retention behavior and the chemical structures of the solutes.[186, 225] The columns used in this study were the 5PBB (4.6mm×250mm) and the 5PYE (10mm×250mm) columns. The mobile phase was toluene, in which fullerenes generally have a moderate solubility. Flow rate was 2.0 ml/minute. The UV-Vis detector was set at 390 nm for detection.

In general, intermolecular interactions are due to intermolecular forces. In our study using non-polar solvents and phenyl stationary phases, we focused primarily on the dispersive force (London effect), the inductive force (Debye effect), and the directional force between dipoles (Keesom effect).[221]

5.2 Results and Discussions

Based on the literature and our current research results, there are two families of Sc- and Tb-based TNT-EMFs and a series of TNT-EMFs with C_{80} (I_h and D_{5h}) cages, whose structures have been well characterized.[28, 31, 107, 109, 121, 181] These structural data will be very helpful in understanding the HPLC retention behavior of these TNT-EMFs of interest. Figure 5-1 shows the structures of the Sc- and Tb-based TNT-EMFs.

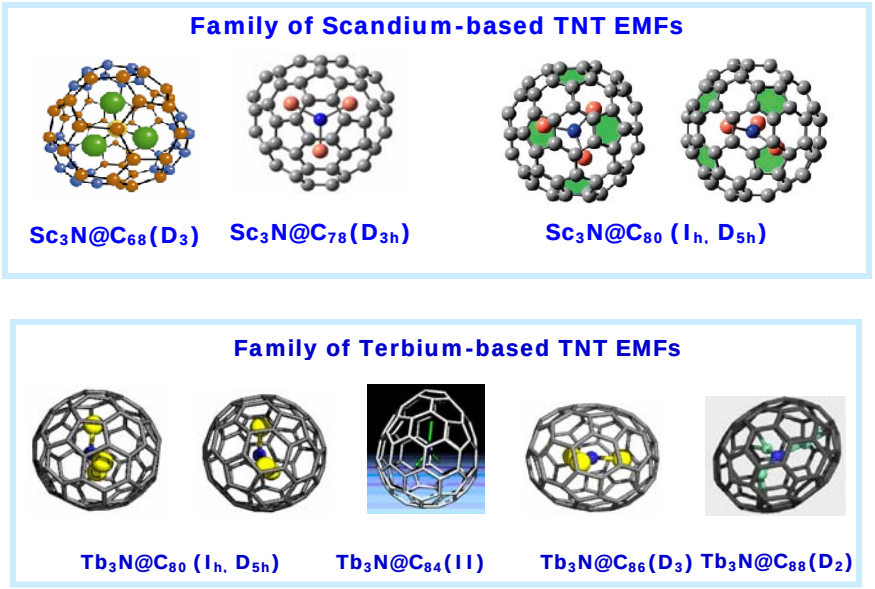

Figure 5-1. Structures of the Sc- and Tb-based TNT-EMFs.

2.1 Electronic Structures and Properties of 5PBB[64] and 5PYE Columns[65]

The structural and electronic properties of the 5PBB and 5PYE stationary phases were calculated using density functional theory (DFT, B3LYP/6-31G*).The electrostatic potential mapped onto the total electron density isosurface of 0.0004 is shown in Figure 5-2. The 5PYE

stationary phase was the pyrene moiety with a non-polar conjugated π-electron system. The electrostatic potential of the conjugated π-electron system was negative, suggesting the electron richness of the pyrene moiety.[226] This conjugated π-electron system of the pyrene moiety was much larger than that of the benzene ring moiety of the 5PBB stationary phase. Therefore, intermolecular interactions between the 5PYE stationary phase and the fullerene cages (fullerene cages also have conjugated π-electron systems) were expected to the dispersive π-π stacking interaction (London effect). Moreover, the larger conjugated π-electron system, as well as the electron rich properties of the pyrene moiety of the 5PYE stationary phase, increased the shape (geometry) selectivity of the fullerene solutes. The later was also governed by the density and distribution of the π-electron system on the fullerene cages.[221] Consequently, a 5PYE column or a column with similar stationary phases (such as a Buckyprep column) is often used for final isolation of structural isomers.

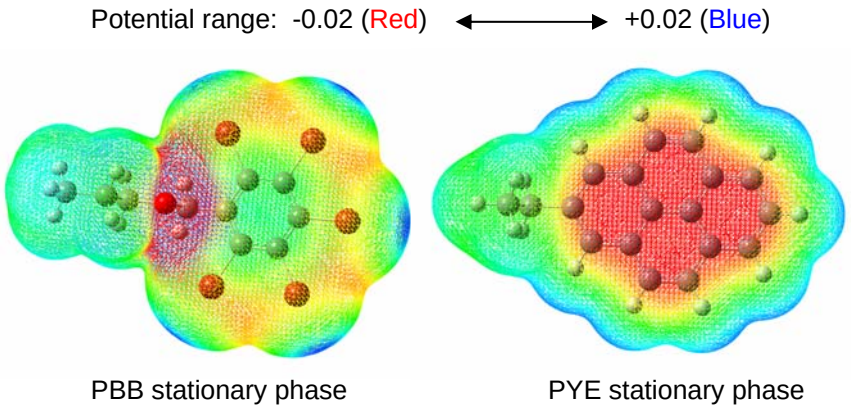

Figure 5-2. The structures and electronic properties of the stationary phases of 5PBB and 5PYE columns.[43]

With respect to the stationary phase of a 5PBB column, the electrostatic potential surface of the pentabromobenzyl moiety forms two concentric bands. The electrostatic potential of the central area of the benzene ring is positive, while that of the outer band containing five bromine atoms is negative.[226] Therefore, when a fullerene cage interacts with the pentabromobenzyl

moiety the outer band will repel the π electrons of the fullerene cage, while the central area will attract the π electrons of the fullerene cage. As a result, the conjugated π-electron system of a fullerene cage will be distorted or polarized, and the π-π stacking effect between a fullerene cage and the pentabromobenzyl moiety will be greatly enhanced. This inductive molecular interaction (Debye effect) mainly depends on the polarizability of the conjugated π-electron system of the fullerene cage, which is directly proportional to the total number of the π electrons in the conjugated system.[186, 221, 225] As a result, the retention behavior of fullerenes on a 5PBB column will reflect the sizes of the cages (predicted cage sizes or total P_π electrons).

5.2.2 Comparison of the Retention Order of $M_3N@C_{80}$ (I_h) (M=Group III B and lanthanide)

The following represents the retention order of TNT-EMFs with a C_{80} (I_h) cage on a 5PBB column:

$Sc_3N@C_{80}$< $Y_3N@C_{80}$ <$Lu_3N@C_{80}$< $Tm_3N@C_{80}$ < $Er_3N@C_{80}$< $Ho_3N@C_{80}$< $Tb_3N@C_{80}$< $Gd_3N@C_{80}$

While the sequence shown below represents the retention order of TNT-EMFs with a C_{80} (I_h) cage on a 5PYE column:

$Y_3N@C_{80}$< $Lu_3N@C_{80}$< $Tm_3N@C_{80}$ < $Er_3N@C_{80}$ < $Ho_3N@C_{80}$< $Tb_3N@C_{80}$< $Gd_3N@C_{80}$<$Sc_3N@C_{80}$

By comparing these retention orders, we determined that they were actually quite similar, which we believe reflects the common phenyl properties of the two stationary phases. One exception with respect to both of retention orders involved $Sc_3N@C_{80}$. The retention orders of $Sc_3N@C_{80}$ on the two columns were opposite—namely, it has the shortest retention time on the 5PBB column, and the longest retention time on the 5PYE column. Table 5.1 provides the retention times of various TNT-EMFs with a C_{80} (I_h) cage and the corresponding experimental uncertainties.

Table 5- 1. I_h isomer retention time (minute) on 5PBB and 5PYE columns

TNT EMFs	t_R (5PBB)	t_R (5PYE)
$Sc_3N@C_{80}$	25.10 ± 0.05	44.00 ±0.02
$Y_3N@C_{80}$	27.64 ± 0.05	38.92 ± 0.12
$Lu_3N@C_{80}$	27.85 ± 0.20	40.06 ± 0.04
$Tm_3N@C_{80}$	27.93 ± 0.09	40.18 ± 0.11
$Er_3N@C_{80}$	28.43 ± 0.05	41.09 ± 0.06
$Ho_3N@C_{80}$	28.45 ± 0.06	41.25 ± 0.05
$Tb_3N@C_{80}$	29.40 ± 0.08	41.50 ± 0.04
$Gd_3N@C_{80}$	29.62 ± 0.23	43.12 ± 0.16

5.2.3 The Relationships between the Retention Behavior of Fullerenes and Their Structures

Fullerene separations generally use four HPLC columns, including the 5PBB, 5PYE, Buckyprep, and Buckyclutcher columns. These columns all have a phenyl-type stationary phase. The elution trends of fullerenes on these columns generally share some common characteristics, including the fact that larger fullerene cages are eluted with longer retention times than smaller ones, as well as the fact that endohedral metallofullerenes are elute later than their corresponding empty cages. These retention trends suggest a common retention mechanism shared by these columns, i.e. π-π stacking. However, the structures of the phenyl moieties of these columns were very different and thus would demonstrate specific retention behavior for separations of different fullerenes.

5.2.3.1 Retention Behavior and Predicted Cage Sizes

Figure 5-3 shows the relationship between the capacity factors (K) and the fullerene cage sizes on both 5PBB and 5PYE columns. Based on this relationship, we calculated the predicted cage sizes of $M_3N@C_{80}$ (M=Group III B and lanthanide) using their retention behavior on the

5PBB column. The results are listed in Table 5.2, which shows that all the TNT-EMFs (except for the $Sc_3N@C_{80}$) have predicted cage sizes of about 86 π electrons and are consistent with the electronic model of TNT-EMFs, $[M_3N]^{6+}@C_{80}^{6-}$.

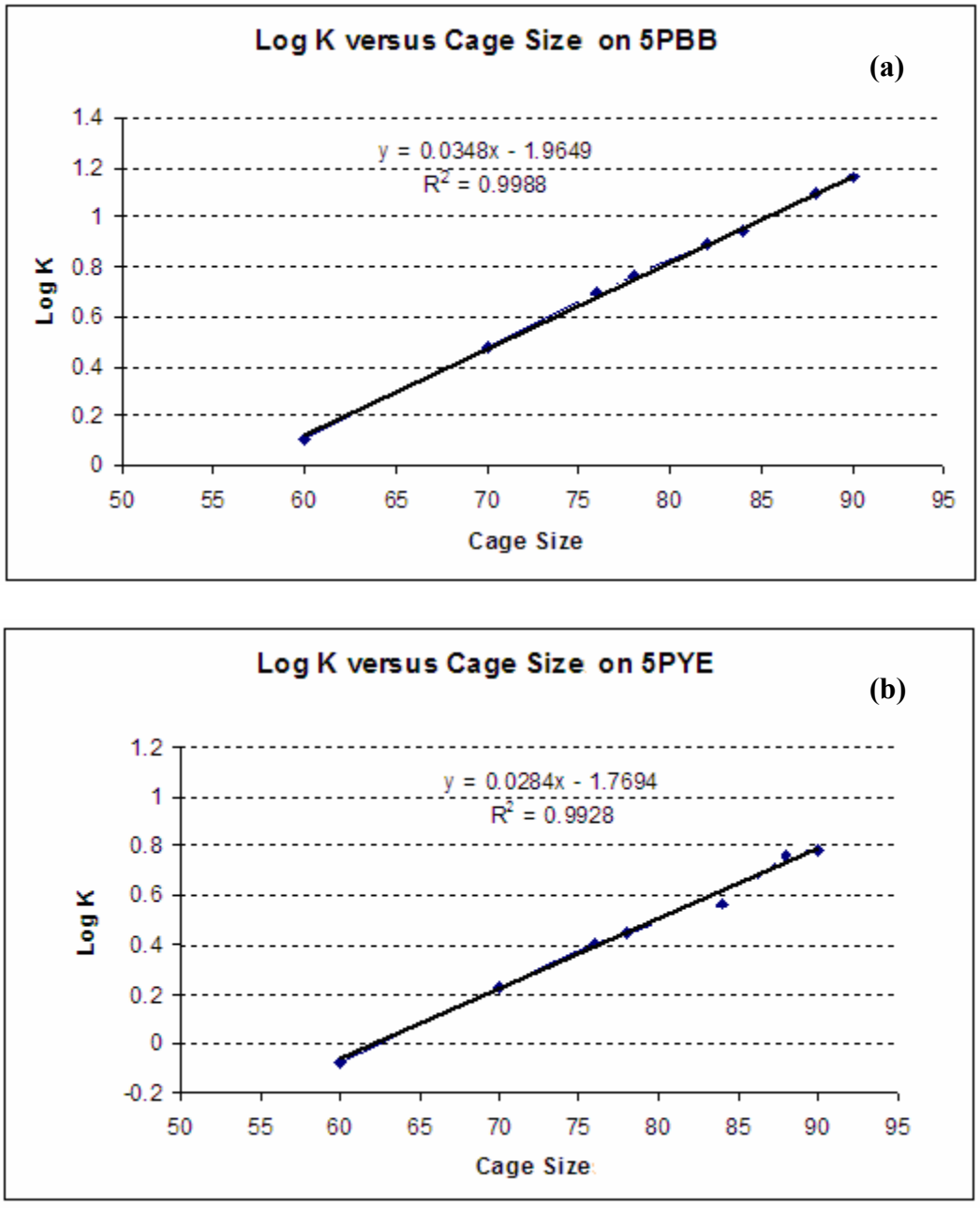

Figure 5-3. The relationship between the capacity factors and the fullerene cage sizes on 5PBB (a) and 5PYE (b) columns.[66, 186]

5.2.3.2 Retention Behavior of $M_3N@C_{80}$ (I_h) on 5PBB Column

Table 5- 2. Predicted cage sizes of $M_3N@C_{80}$ on a 5PBB column

TNT-EMFs	Log K	Predicted Cage Size
$Sc_3N@C_{80}$	0.935 ± 0.002	83.3 ± 0.1
$Y_3N@C_{80}$	1.021 ± 0.006	85.8 ± 0.2
$Lu_3N@C_{80}$	1.014 ± 0.002	85.6 ± 0.1
$Tm_3N@C_{80}$	1.018 ± .006	85.7 ± 0.2
$Er_3N@C_{80}$	1.035 ± 0.006	86.2 ± 0.2
$Ho_3N@C_{80}$	1.026 ± 0.003	85.9 ± 0.1
$Tb_3N@C_{80}$	1.023 ± 0.006	85.9 ± 0.2
$Gd_3N@C_{80}$	1.014 ± 0.004	85.6 ± 0.1

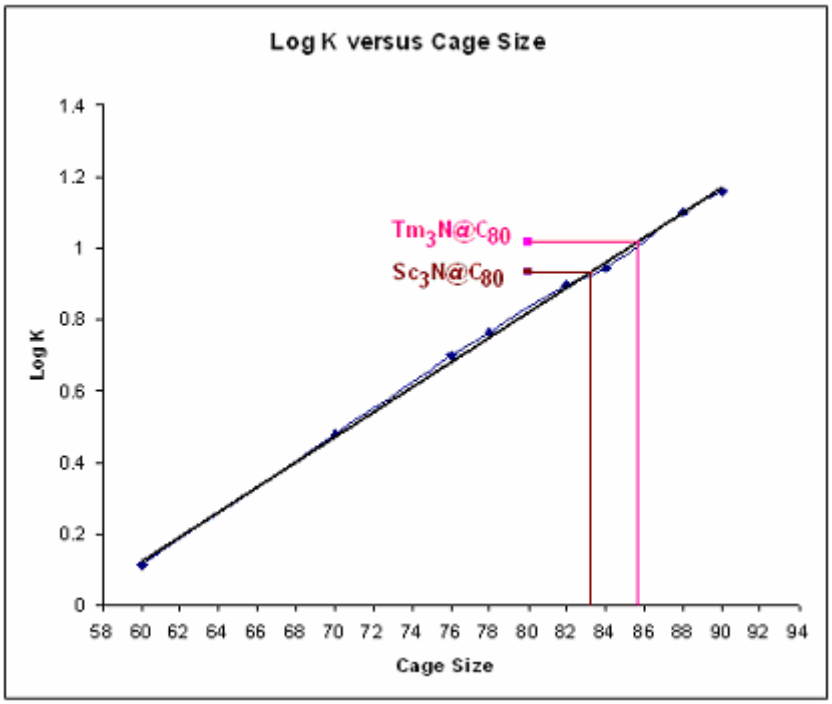

Figure 5-4. HPLC retention behavior on 5PBB column of $Tm_3N@C_{80}$ and $Sc_3N@C_{80}$.

5.2.3.3 Special Retention Behavior of Sc-based TNT-EMFs on 5PBB Column: Effect of p-d Orbital Interactions

Figure 5-4 shows the difference of the predicted cage sizes between the $Sc_3N@C_{80}$ and one of the lanthanide-based TNT-EMFs, $Tm_3N@C_{80}$. Although both $Sc_3N@C_{80}$ and $Tm_3N@C_{80}$ molecules have a C_{80} fullerene cage, their predicted cage sizes are very different. The predicted cage sizes of the $Tm_3N@C_{80}$ and $Sc_3N@C_{80}$ suggest that the Tm_3N and Sc_3N clusters transfer about 5.8e and 3.3e to their C_{80} fullerene cages, respectively. In order to understand why $Sc_3N@C_{80}$ deviated so markedly from the typical electronic model of TNT-EMFs, $[M_3N]^{6+}@C_{80}^{6-}$, the retention behavior of Sc-containing TNT-EMFs on a 5PBB column were systematically studied and listed in Table 5.3.

Table 5- 3. HPLC characterization of TNT EMFs containing Sc on a 5PBB column

TNT EMFs	Predicted Cage Size	Charge Transferred
$Sc_3N@C_{68}$	74.6 ± 0.3	6.6e
$Sc_3N@C_{78}$	82.3 ± 0.0	4.3e
$Sc_3N@C_{80}$	83.5 ± 0.0	3.5e
$CeSc_2N@C_{80}$	84.3 ± 0.1	4.3e
$Gd_2ScN@C_{80}$	84.9 ± 0.2	4.9e
$Gd_3N@C_{80}$	85.6 ± 0.1	5.6e

Table 5-3 is easier to comprehend if one uses the graphic information provided in Figure 5-5 and Figure 5-6. Specifically, Figure 5-5 shows that the Sc atom transfers fewer electrons to the C_{80} fullerene cage compared with the lanthanide elements, such as the Gd atom. The more Sc atoms, the less charge transfer in the series of TNT-EMFs, $Gd_{(3-x)}Sc_xN@C_{80}$. The calculations

show that there is a *p-d* orbital interaction between the C_{80} cage and the Sc metal ions.[27, 126] Because this interaction feeds back some electrons from the C_{80} cage to the Sc metal ions, the 5PBB column feels fewer π electrons in the fullerene cage of the $Sc_3N@C_{80}$ and $Sc_3N@C_{80}$ elutes earlier than other TNT-EMFs. With a Gd atom as a reference, the charge feedback from the C_{80} fullerene cage to each Sc metal ion via the *p-d* orbital interactions between the two was about 0.7e.

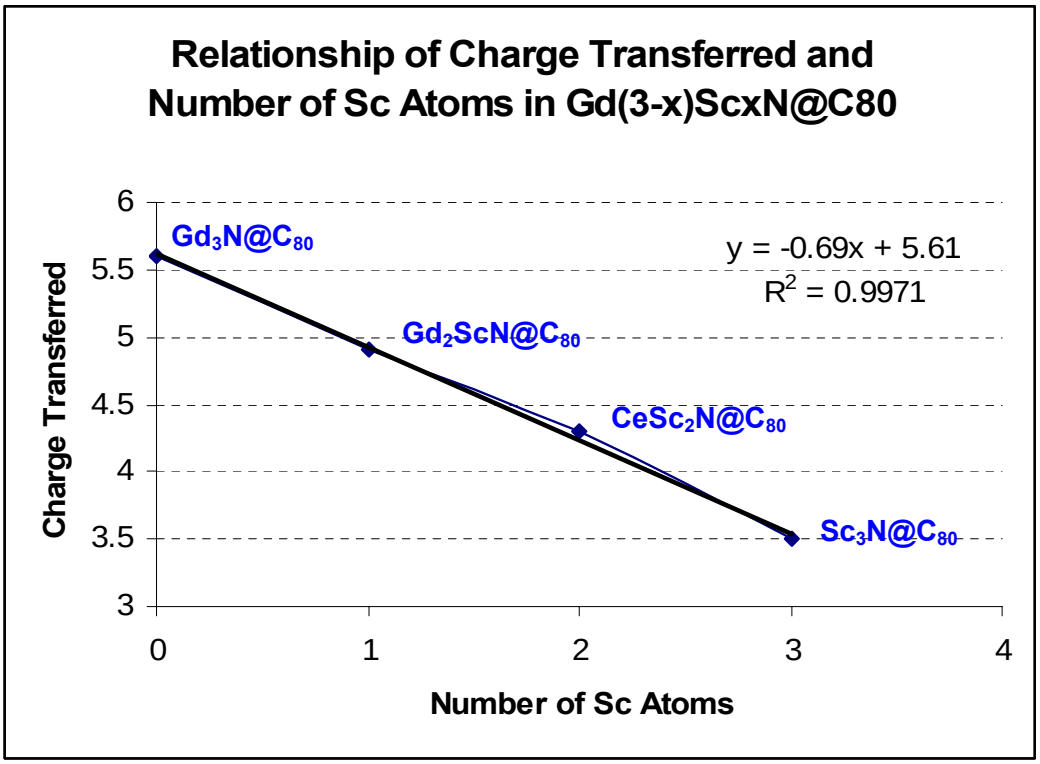

Figure 5-5. HPLC characterization of the relationship between charge transfer and the number of Sc atoms in $Gd_{(3-x)}Sc_xN@C_{80}$ (x = 0 ~ 3).

5.2.3.4 Special Retention Behavior on a 5PBB Column of Sc-based TNT-EMFs: Ratio of Cluster and Fullerene cage sizes

The charge transfer effect of Sc_3N cluster versus fullerene cage size is documented in Figure 5-6. It demonstrates the interaction effect between the Sc_3N cluster and fullerene cage. It also suggests that the *p-d* orbital interaction between the C_{2n} cage and the Sc metal ions require a

proper ratio between Sc_3N and fullerene C_{2n} cage size. From $Sc_3N@C_{80}$ to $Sc_3N@C_{78}$, the charge feed back effect of *p-d* orbital interactions became smaller (2.5e versus1.7e based on $[Sc_3N]^{6+}@[C_{2n}]^{6-}$ model). Moreover, in the case of $Sc_3N@C_{68}$, the charge transferred from the Sc_3N cluster to the C_{68} cage was about 6e, which suggests that the charge feed back effect of *p-d* orbital interactions was no longer present. Among all the TNT-EMFs discovered so far, $Sc_3N@C_{80}$ was shown to have the highest yield. The size ratio of the Sc_3N cluster to the C_{80} fullerene cage, as well as its resulting charge feed back effect of *p-d* orbital interactions, may play a critical role in the trimetallic nitride template formation mechanism of the TNT-EMFs. It may also explain the reason for the high yield of $Sc_3N@C_{80}$.

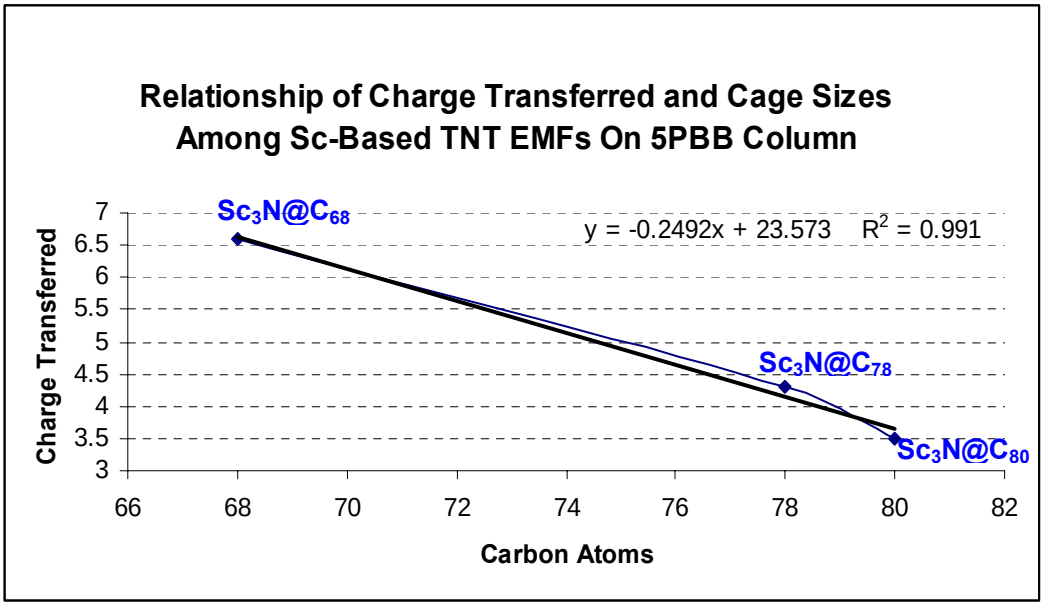

Figure 5-6. HPLC characterization of the relationship between charge transfer and fullerene cage size in the family of $Sc_3N@C_{2n}$ (n=34, 39, and 40).

5.2.3.5 Retention Behavior of Large Cage TNT-EMFs on 5PBB Column

The retention behavior on a 5PBB column of the Tb-based TNT EMFs with the molecular formula of $Tb_3N@C_{2n}$ ($41 \leq n \leq 44$) were also studied. The results are listed in Table 5.4.

Table 5- 4. Retention behavior of large cage Tb-based TNT EMFs on 5PBB column

TNT-EMFs	Capacity Factors (K)	Predicted Cage Sizes	Charges Transferred
$Tb_3N@C_{82}$	14.79 ± 0.18	90.1 ± 0.1	8.1e
$Tb_3N@C_{84}$ (I)	18.16 ± 0.23	92.6 ± 0.2	8.6e
$Tb_3N@C_{84}$ (II) (C_s)	18.42 ± 0.52	92.8 ± 0.3	8.8e
$Tb_3N@C_{86}$ (D_3)	21.25 ± 0.20	94.6 ± 0.1	8.6e
$Tb_3N@C_{88}$ (D_2)	24.39 ± 0.17	96.3 ± 0.1	8.3e

When the two isomers of the $Tb_3N@C_{84}$ were isolated in the second stage HPLC using a 5PYE column, the difference in their retention times was about 7 minutes. This relatively large difference suggests that isomer 1 maintains much higher cage symmetry than isomer 2 (egg-shaped cage with C_s symmetry). However, the two isomers co-eluted on a 5PBB column, suggesting that their cage sizes were actually quite similar. As documented in Table 5.4, the predicted cage sizes of isomer 1 and isomer 2 were 92.6 ± 0.2 and 92.8 ± 0.3, respectively. Within the experimental uncertainties, their predicted cage sizes were identical. These experimental data also suggest that the 5PPB column was sensitive to fullerene cage size but indifferent to cage symmetry. The charge transferred from the Tb_3N cluster to the larger fullerene cages ($\geq C_{82}$) was about 8e, which significantly deviates from the electronic model of $[M_3N]^{6+}@C_{2n}^{6-}$ for TNT-EMFs. Although the reason for this deviation is not clear, theoretical calculations in the literature have shown that in the case of $La_3N@C_{80}$, 8e were transferred from the La_3N cluster to the C_{80} cage.[111]

5.2.3.6 Retention Behavior of Tb-based Dimetallic Endofullerenes on a 5PBB Column

Table 5- 5. HPLC characterization of some Tb-based dimetallic endofullerenes on a 5PBB

Endofullerenes	Capacity Factors	Predicted cage sizes	Charges Transferred	
			$Tb_2@C_{2n}$ Model	$Tb_2C_2@C_{2n}$ Model
Tb_2C_{86}	15.2 ± 0.1	90.5 ± 0.1	4.5e	6.5e
Tb_2C_{90}	20.4 ± 0.8	94.1 ± 0.5	4.1e	6.1e
Tb_2C_{92}	24.0 ± 1.0	96.1 ± 0.5	4.1e	6.1e
Tb_2C_{94}	28.5 ± 0.0	98.3 ± 0.0	4.3e	6.3e

In addition to isolating Tb-based TNT-EMFs, some dimetallic endohedral metallofullerenes were also obtained. Their retention behavior on a 5PBB column is listed in Table 5-5. As shown in Table 5-5, the dimetallic endofullerenes may exhibit one of the molecular formulas, either $Tb_2@C_{2n}$ or $Tb_2C_2@C_{2n}$. The charges transferred from the endo-cluster to the fullerene cages were about 4e for the $Tb_2@C_{2n}$ model and 6e for the $Tb_2C_2@C_{2n}$ model. Since the dimetallic endofullerenes listed in Table 5-5 displayed similar retention behavior, they should have the same pattern of molecular formula—namely, either $Tb_2@C_{2n}$ or $Tb_2C_2@C_{2n}$. Thus, if the structure of one molecule is crystallographically determined, the formula of other molecules will also be clear. The relationship between the retention behavior on a 5PBB column and the total P_π electrons in their fullerene cages was also demonstrated for these classical dimetallic endofullerenes.

5.2.3.7 Effect of Fullerene Cage Symmetry on a 5PYE Column

Table 5- 6. Retention behavior of $M_3N@C_{80}$ (I_h and D_{5h}) on a 5PYE column

TNT-EMFs		t_R (minute)	Δt_R (minute)	K	ΔK
$Gd_3N@C_{80}$	I_h	43.12 ± 0.16	1.72 ± 0.22	4.91± 0.02	0.24 ± 0.03
	D_{5h}	44.84 ± 0.15		5.15 ± 0.02	
$Tb_3N@C_{80}$	I_h	41.50 ± 0.04	1.79 ± 0.06	4.58 ± 0.00	0.24 ± 0.00
	D_{5h}	43.29 ± 0.04		4.82 ± 0.00	
$Ho_3N@C_{80}$	I_h	41.25 ± 0.05	2.15 ± 0.07	4.68 ± 0.02	0.30 ± 0.03
	D_{5h}	43.40 ± 0.05		4.98 ± 0.02	
$Er_3N@C_{80}$	I_h	41.09 ± 0.06	1.91 ± 0.08	4.66 ± 0.02	0.26 ± 0.03
	D_{5h}	43.00 ± 0.05		4.92 ± 0.02	
$Tm_3N@C_{80}$	I_h	40.18 ± 0.11	1.53 ± 0.16	4.50 ± 0.03	0.21 ± 0.04
	D_{5h}	41.71 ± 0.11		4.71 ± 0.03	
$Lu_3N@C_{80}$	I_h	40.06 ± 0.04	1.75 ± 0.10	4.49 ± 0.04	0.24 ± 0.06
	D_{5h}	41.81 ± 0.07		4.73 ± 0.04	
$Y_3N@C_{80}$	I_h	38.92 ± 0.12	1.57 ± 0.18	4.28 ± 0.02	0.21 ± 0.03
	D_{5h}	40.49 ± 0.13		4.49 ± 0.02	
$Sc_3N@C_{80}$	I_h	44.00 ±0.02	1.38 ± 0.03	4.53 ± 0.03	0.17 ± 0.04
	D_{5h}	45.38 ± 0.02		4.70 ± 0.03	

Table 5- 7. Retention behavior of large cage $Tb_3N@C_{2n}$ on a 5PYE column

TNT EMFs	K	Predicted Cage Size	Charges Transferred
$Tb_3N@C_{82}$	5.69 ± 0.01	88.9 ± 0.0	6.9e
$Tb_3N@C_{84}$ (I)	6.13 ± 0.02	90.0 ± 0.1	6.0e
$Tb_3N@C_{84}$ (II) (C_s)	7.12 ± 0.04	92.3 ± 0.1	8.3e
$Tb_3N@C_{86}$ (D_3)	6.28 ± 0.05	90.4 ± 0.1	4.4e
$Tb_3N@C_{88}$ (D_2)	7.58 ± 0.02	93.3 ± 0.0	5.3e

Tables 5-6 and 5-7 show the retention behavior of TNT-EMFs on a 5PYE column. The retention behavior of the $M_3N@C_{80}$ (M=Group III B and lanthanide) with I_h and D_{5h} cage symmetries are listed in Table 5-6. As documented, Table 5-6 shows that the D_{5h} isomers were always eluted behind their corresponding I_h isomers. In addition, the gaps in both the retention

times and capacity factors between the I_h and D_{5h} isomers remained nearly constant (within the experimental uncertainties) with the exception of the $Sc_3N@C_{80}$ (I_h and D_{5h}) molecules. These constant gaps suggest that the 5PYE column is sensitive to the symmetries of fullerene cages. The data in Table 5-7 show retention behavior of Tb-based larger cage TNT-EMFs with different cage symmetries. In contrast to the retention behavior of the TNT-EMFs on 5PBB columns—which is typified by the model of $[Tb_3N]^{8+}@C_{2n}^{8-}$ for these larger cage TNT-EMFs—the retention behavior of these samples varied with their cage symmetries and no relationship could be patterned between the retention behavior and the total P_π electrons in their fullerene cages.

5.3 Summary

In summary, the retention behavior of two TNT-EMFs families, Sc and Tb-based, were systematically studied in this research. Their retention mechanisms using both 5PBB and 5PYE columns are discussed based on theoretical and experimental data. Although these fullerenes displayed similar overall elution orders on both columns as a result of the common properties of their phenyl stationary phases, their detailed retention behavior on the two columns were quite different.[221] The 5PBB column was sensitive to the fullerenes' predicted cage sizes, but indifferent to their cage symmetries. Therefore, the fullerenes with a similar predicted cage size were co-eluted on the 5PBB column. Once the retention behavior of a fullerene was obtained from its chromatogram on a 5PBB column, its real and predicted cage sizes, as well as the charges transferred from the endo-clusters to the fullerene cages could be calculated based on the relationship equation between capacity factors and fullerene cage size. The resulting structural and electronic information associated with their retention behavior were very useful in the determining fullerene structures. For example, when a pure sample was characterized by mass spectrometry, there were often several candidates with a molecular formula matching the

molecular peak in the mass spectrum. By checking their retention behavior on a 5PBB column, however, most of them could be easily ruled out because their fullerene cage sizes did not match the calculated predicted cage sizes. 5PYE column has a stationary phase of pyrene moiety with a large conjugated π electron system and electron richness, it was more sensitive to the density and distributions of π electrons in the fullerene cages. The distribution of π electrons in a fullerene cage primarily depends on the geometric structures of the fullerene cages. Therefore, the 5PYE column was more suitable for the separating structural isomers. Combining separation process with first stage HPLC using a 5PBB column and the second stage HPLC using a 5PYE column provided an effective way for the isolating specific isomers.

References

(1) Kroto, H. W.; Heath, J. R.; O'Brien, S. C.; Curl, R. F.; Smalley, R. E. C_{60}: Buckminsterfullene *Nature* **1985,** *318*, 162-163.

(2) Kroto, H. W. Symmetry, Space, Stars and C_{60}. http://nobelprize.org/chemistry/laureates/1996/kroto-lecture.html (08/19/2004),

(3) Smalley, R. E. Discovering the Fullerenes. http://nobelprize.org/chemistry/laureates/1996/smalley-lecture.html (08/19/2004),

(4) Kroto, H. W.; Allaf, A. W.; Balm, S. P. C_{60}: Buckminsterfullene *Chem. Rev.* **1991,** *91*, 1213-1235.

(5) Rohlfing, E. A.; Cox, D. M.; Kaldor, A. Production and characterization of supersonic carbon cluster beams *J. Chem. Phys.* **1984,** *81*, 3322-3330.

(6) Heath, J. R.; O'Brien, S. C.; Zhang, Q. L.; Liu, Y.; Curl, R. F.; Kroto, H. W.; Tittel, F. K.; Smalley, R. E. Lanthanum Complexes of Spheroidal Carbon Shells *J. Am. Chem. Soc.* **1985,** *107*, 7779-7780.

(7) Cox, D. M.; Reichmann, K. C.; Kaldor, A. Carbon clusters revisited: the "special" behavior of carbon sixty-atom molecule and large carbon clusters *J. Chem. Phys.* **1988,** *88*, 1588-1597.

(8) Kratschmer, W.; Lamb, L. D.; Fostiropoulos, K.; Huffman, D. R. Solid C_{60}: A New Form of Carbon *Nature* **1990,** *347*, 354-358.

(9) Hawkins, J. M.; Meyer, A.; Lewis, T. A.; Loren, S.; Hollander, F. J. Crystal structure of osmylated C_{60}: confirmation of the soccer ball framework *Science* **1991,** *252*, 312-313.

(10) Brinkmann, G.; Fowler, P. W. A Catalogue of Growth Transformations of Fullerene Polyhedra *J. Chem. Inf. Comput. Sci.* **2003,** *43*, 1837-1843.

(11) Haymet, A. D. J. C_{120} and C_{60}: Archimedean Solids Constructed from sp^2 Hybridized Carbon Atoms *Chem, Phys. Lett.* **1985,** *122*, 421-424.

(12) Fowler, P. W.; Manolopoulos, D. E. *An Atlas of Fullerene* Oxford University Press: New York, 1995.

(13) Higgins, T. Definition of Steradian. http://whatis.techtarget.com/definition/0,,sid9_gci528813,00.html (05/15/2004),

(14) Kroto, H. W. The Stability of the Fullerenes C_n, with n=24, 28, 32, 36, 50, 60 and 70 *Nature* **1987,** *329*, 529-531.

(15) Wang, G.-W.; Komatsu, K.; Murata, Y.; Shiro, M. Synthesis and X-ray Structure of Dumb-bell-shaped C_{120} *Nature* **1997,** *387*, 583-586.

(16) Schmalz, T. G.; Seitz, W. A.; Klein, D. J.; Hite, G. E. Elemental Carbon Cages *J. Am. Chem. Soc.* **1988,** *110*, 1113-1127.

(17) Gao, Y.-D.; Herndon, W. C. Fullerenes with Four-Membered Rings *J. Am. Chem. Soc.* **1993,** *115*, 8459-8460.

(18) Johnson, R. D.; Bethune, D. S.; Yannoni, C. S. Fullerene Structure and Dynamics: A Magnetic Resonance Potpourri *Acc.Chem. Res.* **1992,** *25*, 169-175.

(19) Taylor, R.; Hare, J. P.; Abdul-Sada, A. K.; Kroto, H. W. Isolation, separation and characterization of the fullerenes C_{60} and C_{70}: the third form of carbon *J. Chem. Soc., Chem. Comm.* **1990,** *20*, 1423-1425.

(20) Lagow, R. J.; Kampa, J. J.; Wei, H.-C.; Battle, S. L.; Genge, J. W.; Laude, D. A.; Harper, C. J.; Bau, R.; Stevens, R. C. Synthesis of linear acetylenic carbon: the "sp" carbon allotrope *Science* **1995,** *267*, 362-367.

(21) Akasaka, T.; Okubo, S.; Wakahara, T.; Yamamoto, K.; Kobayashi, K.; Nagase, S.; Kato, T.; Kako, M.; Nakadaira, Y.; Kitayama, Y.; Matsuura, K. Endohedrally metal-doped heterofullerenes: La@C_{81}N and La_2@C_{79}N *Chem. Lett.* **1999,** *9*, 945-946.

(22) Haddon, R. C. Chemistry of the Fullerenes: The Manifestation of Strain in a Class of Continuous Aromatic Molecules *Science* **1993,** *261*, 1545-1550.

(23) Haddon, R. C.; Brus, L. E.; Raghavachari, K. Electronic Structure and Bonding in Icosahedral C_{60} *Chem, Phys. Lett.* **1986,** *125*, 459-464.

(24) Newton, M. D.; Stanton, R. E. Stability of Buckminsterfullerene and Related Carbon Clusters *J. Am. Chem. Soc.* **1986,** *108*, 2469-2470.

(25) Fowler, P. W.; Soncini, A. Aromaticity, Polarisability and Ring Current *Chem, Phys. Lett.* **2004,** *383*, 507-511.

(26) Xie, S.-Y.; Gao, F. L., X.; Huang, R.-B.; Wang, C.-R.; Zhang, X.; Liu, M.-L.; Deng, S.-L.; Zheng, L.-S. Capturing the Labile Fullerene[50] as $C_{50}C_{110}$ *Science* **2004,** *304*, 699.

(27) Park, S. S.; Liu, D.; Hagelberg, F. Comparative Investigation on Non-IPR C_{68} and IPR C_{78} Fullerenes Encaging Sc_3N Molecules *J. Phys. Chem. A* **2005,** *109*, 8865-8873.

(28) Stevenson, S.; Fowler, P. W.; Heine, T.; Duchamp, J. C.; Rice, G.; Glass, T.; Harich, K.; Hajdu, E.; Bible, R.; Dorn, H. C. Materials science: A stable non-classical metallofullerene family *Nature* **2000,** *408*, 427-428.

(29) Campbell, E. E. B.; Fowler, P. W.; Mitchell, D.; Zerbetto, F. Increasing cost of pentagon adjacency for larger fullerenes *Chem. Phys. Lett.* **1996,** *250*, 544-548.

(30) Troshin, P. A.; Avent, A. G.; Darwish, A. D.; Martsinovich, N.; Abdul-Sada, A. K.; Street, J. M.; Taylor, R. Isolation of Two Seven-Membered Ring C_{58} Fullerene Derivatives: $C_{58}F_{17}CF_3$ and $C_{58}F_{18}$ *Science* **2005,** *309*, 278-281.

(31) Beavers, C. M.; Zuo, T.; Duchamp, J. C.; Harich, K.; Dorn, H. C.; Olmstead, M. M.; Balch, A. L. $Tb_3N@C_{84}$: An Improbable, Egg-Shaped Endohedral Fullerene that Violates the Isolated Pentagon Rule *J. Am. Chem. Soc.* **2006,** *128*, 11352-11353.

(32) Shi, Z.-Q.; Wu, X.; Wang, C.-R.; Lu, X.; Shinohara, H. Isolation and characterization of $Sc_2C_2@C_{68}$: a metal-carbide endofullerene with a non-IPR carbon cage *Angew. Chem. Int. Ed. Eng.* **2006,** *45*, 2107-2111.

(33) Aihara, J.-i. Bond Resonance Energy and Verification of the Isolated Pentagon Rule *J. Am. Chem. Soc.* **1995,** *117*, 4130-4136.

(34) Cioslowski, J. *Electronic Structure Calculations on Fullerenes and Their Derivatives*. Oxford University Press: New York, 1995.

(35) Aihara, J.-i. Kinetic Stability of Metallofullerenes as Predicted by the Bond Resonance Energy Model *Phys. Chem. Chem. Phys.* **2001,** *3*, 1427-1431.

(36) Henderson, C. C.; Rohlfing, C. M.; Cahill, P. A. Theoretical Studies of Selected C60H2 and $C_{70}H_2$ Isomers *Chem. Phys. Lett.* **1993,** *213*, 383-388.

(37) Aihara, J.-i. Kinetic Stability of Carbon Cages in Non-classical Metallofullerenes *Chem, Phys. Lett.* **2001,** *343*, 465-469.

(38) Manolopoulos, D. E.; May, J. C.; Down, S. E. Theoretical Studies of the Fullerenes: C_{34} to C_{70} *Chem, Phys. Lett.* **1991,** *181*, 105-111.

(39) Fowler, P. W.; Manolopoulos, D. E.; Redmond, D. B.; Ryan, R. P. Possible symmetries of fullerene structures *Chem. Phys. Lett.* **1993,** *202*, 371-378.

(40) Manolopoulos, D. E.; Fowler, P. W. Molecular graphs, point groups, and fullerenes *J. Chem. Phys.* **1992,** *96*, 7603-7614.

(41) Voytekhovsky, Y. L.; Stepenshchikov, D. G. C_{72} to C_{100} fullerenes: combinatorial types and symmetries *Acta Crystallographica, Section A: Foundations of Crystallography* **2003,** *A59*, 283-285.

(42) Rauk, A.; Cannings, R. The Simple Huckel Molecular Orbital Theory Calculator. http://www.chem.ucalgary.ca/SHMO/ (06/10/2004),

(43) Foresman, J. B.; Frisch, A. *Exploring Chemistry with Electronic Structure Method* 2nd ed ed.; Gaussian, Inc.: Pittsburgh, 1996.

(44) Schwarz, H. The Mechanism of Fullerence Formation *Angew. Chem. Int. Ed. Engl.* **1993,** *32*, 1412-1415.

(45) Mishra, R. K.; Lin, Y.-T.; Lee, S.-L. Theoretical studies of the fullerene growth mechanism: Ring-collapse model to C_{28} and cascade bond formation *J. Chem. Phys.* **2000,** *112*, 6355-6364.

(46) Churilov, G. N.; Novikov, P. V.; Tarabanko, V. E.; Lopatin, V. A.; Vnukova, N. G.; Bulina, N. V. On the mechanism of fullerene formation in a carbon plasma *Carbon* **2002,** *40*, 891-896.

(47) Strout, D. L.; Scuseria, G. E. J. P. C. A Cycloaddition Model for Fullerene Formation *J. Phys. Chem.* **1996,** *100*, 6492-6498.

(48) Haufler, R. E.; Chai, Y.; Chibante, L. P. F.; Conceicao, J.; Jin, C.; Wang, L.; Maruyama, S.; Smalley, R. E. Carbon-arc generation of carbon sixty-atom molecules. *Mat. Res. Soc. Symp. Proc.* **1991,** *206*, 627-637.

(49) Hua, X.; Gagin, T.; Che, J.; Goddard III, W. A. *Nanotechnology* **2000,** *11*, 85-88.

(50) Zhang, Q. L.; O'Brien, S. C.; Heath, J. R.; Liu, Y.; Curl, R. F.; Kroto, H. W.; Smalley, R. E. Reactivity of large carbon clusters: spheroidal carbon shells and their possible relevance to the formation and morphology of soot *J. Phys. Chem.* **1986,** *90*, 525-528.

(51) Shvartsburg, A. A.; Hudgins, R. R.; Dugourd, P.; Gutierrez, R.; Frauenheim, T.; Jarrold, M. F. Observation of "Stick" and "Handle" Intermediates along the Fullerene Road *Phys. Rev. Lett.* **2000,** *84*, 2421-2424.

(52) Curl, R. F. Dawn of the Fullerenes: Experiment and Conjecture. http://nobelprize.org/chemistry/laureates/1996/curl-lecture.html (08/19/2004),

(53) Newton, M. D.; Stanton, R. E. Stability of Buckminsterfullerene and Related Carbon Clusters *J. Am. Chem. Soc.* **1986,** *108*, 2469-2470.

(54) Dorn, H. C.; Duchamp, J. C. In *Endofullerene: A New Family of Carbon Clusters*; Akasaka, T.,Nagase, S., Eds. Kluwer Academic Publishers: Dordrecht, The Netherlands, 2002; pp 121-132.

(55) McElvany, S. W.; Dunlap, B. I.; O'Keefe, A. Ion molecule reactions of carbon cluster ions with deuterium and oxygen *J. Chem. Phys.* **1987,** *86*, 715-725.

(56) Meijer, G.; Bethune, D. S. Laser deposition of carbon clusters on surfaces: a new approach to the study of fullerenes *J. Chem. Phys.* **1990,** *93*, 7800-7802.

(57) Ebbesen, T. W.; Tabuchi, J.; Tanigaki, K. The mechanistics of fullerene formation *Chem. Phys. Lett.* **1992,** *191*, 336-338.

(58) Scott, L. T.; Boorum, M. M.; McMahon, B. J.; Hagen, S.; Mack, J.; Blank, J.; Wegner, H.; de Meijere, A. A rational chemical synthesis of C_{60} *Science* **2002,** *295*, 1500-1503.

(59) Diogo, H. P.; Minas da Piedade, M. E.; Dennis, T. J. S.; Hare, J. P.; Kroto, H. W.; Taylor, R.; Walton, R. W. Enthalpies of Formation of Buckminsterfullerene (C_{60}) and of the

Parent Ions C_{60}^{+}, C_{60}^{2+}, C_{60}^{3+} and C_{60}^{-} *J. Chem. Soc. Faraday Trans.* **1993,** *89*, 3541-3544.

(60) Korobov, M. V.; Smith, A. L. In *Fullerenes-Chemistry, Physics, and Technology*; Kadish, K. M.,Ruoff, R. S., Eds. A John Wiley and Sons, Inc.: New York, 2000.

(61) Parker, D. H.; Wurz, P.; Chatterjee, K.; Lykke, K. R.; Hunt, J. E.; Pellin, M. J.; Hemminger, J. C.; Gruen, D. M.; Stock, L. M. High-Yield Synthesis, Separation, and Mass-Spectrometric Characterization of Fullerenes C_{60} to C_{266} *J. Am. Chem. Soc.* **1991,** *113*, 7499-7503.

(62) Beailey, J. A. Novel Preparation of Endohedral Metallofullerenes via Laser Vaporization of Fullerene/Metal Pellets. Virginia Polytechnic Institute and State University, Blacksburg, VA, 1996.

(63) Isaacs, L.; Wehrsig, A.; Diederich, F. Improved Purification of C_{60} and Formation of Sigma- and Pi- Homoaromatic Methano-Bridged Fullerenes by Reaction with Alkyl Diazoacetates *Helv. Chim. Acta.* **1993,** *76*, 1231-1250.

(64) Tanaka, N.; Kimura, H.; Tokuda, D.; Hosoya, K.; Ikegami, T.; Ishizuka, N.; Minakuchi, H.; Nakanishi, K.; Shintani, Y.; Furuno, M.; Cabrera, K. Simple and Comprehensive Two-Dimensional Reversed-Phase HPLC Using Monolithic Silica Columns *Anal. Chem.* **2004,** *76*, 1273-1281.

(65) HPLCweb Specialty Columns PYE, NPE column. http://shop.hplcweb.com/product_details/PYE-NPE.htm (07/08/2004),

(66) Stevenson, S. Chromatography and Purification of Endohedral Metallofullerenes. Virginia Polytechnic Institute and State University, Blacksburg, VA, 1995.

(67) Elliott, B.; Yu, L.; Echegoyen, L. A Simple Isomeric Separation of D5h and Ih $Sc_3N@C_{80}$ by Selective Chemical Oxidation *J. Am. Chem. Soc.* **2005,** *127*, 10885-10888.

(68) Fowler, P. W.; Ceulemans, A. Electron Deficiency of the Fullerenes *J. Phys. Chem.* **1995,** *99*, 508-510.

(69) Mestres, J.; Duran, M.; Sola, M. Theoretical Study of Diels-Alder Cycloadditions of Butadiene to C_{70}: An Insight into the Chemical Reactivity of C_{70} as Compared to C_{60} *J. Phys. Chem.* **1996,** *100*, 7449-7454.

(70) Meier, M. S.; Spielmann, H. P.; Haddon, R. C.; Bergosh, R. G.; Gallagher, M. E.; Hamon, M. A.; Weedon, B. R. Reactivity, Spectroscopy, and Structure of Reduced Fullerenes *Carbon* **2000,** *38*, 1535-1538.

(71) Sun, G.; Kertesz, M. Theoretical ^{13}C NMR Spectra of IPR Isomers of Fullerene C_{80}: A Density Functional Theory Study *Chem, Phys. Lett.* **2000,** *328*, 387-395.

(72) Nagase, S.; Kobayashi, K.; Akasaka, T. In *The Electronic Properties and Reactivities of Metallofullerenes*, Electrochem. Soc. Proceedings, 1995; 1995; pp 747-762.

(73) Nagase, S.; Kobayashi, K.; Akasaka, T. Recent Advances in the Structural Determination of Endohedral Metallofullerenes *J. comput. Chem.* **1998,** *19*, 232-239.

(74) Kobayashi, K.; Nagase, S. Structures and Electronic States of Endohedral Dimetallofullerenes: $M_2@C_{80}$ (M=Sc, Y, La, Ce, Pr, Eu, Gd, Yb, and Lu) *Chem, Phys. Lett.* **1996,** *262*, 227-232.

(75) Patchkovskii, S.; Thiel, W. How Does Helium Get into Buckminsterfullerene? *J. Am. Chem. Soc.* **1996,** *118*, 7164-7172.

(76) Son, M.-S.; Sung, Y. K. The Atom-atom Potential. Exohedral and Endohedral Complexation Energies of Complexes of $X@C_{60}$ between Fullerene and Rare-gas Atoms (X=He, Ne, Ar, Kr, and Xe) *Chem, Phys. Lett.* **1995,** *245*, 113-118.

(77) Andreoni, W.; Curioni, A.; Holczer, K.; Prassides, K.; Keshavarz-K, M.; Hummelen, J.-C.; Wudl, F. Unconventional Bonding of Azafullerenes: Theory and Experiment *J. Am. Chem. Soc.* **1996,** *118*, 11335-11336.

(78) Hirsch, A.; Nuber, B. Nitrogen Heterofullerenes *Acc.Chem. Res.* **1999,** *32*, 795-804.

(79) Hummelen, J.-C.; Knight, B.; Pavlovich, J.; Gonzalez, R.; Wudl, F. Isolation of the Heterofullerene $C_{59}N$ as its dimer *Science* **1995,** *269*, 1554.

(80) Aihara, J.-i. Kinetic Instability of Azafullerenes *J. Mol. Struc.(Theochem)* **2000,** *532*, 95-102.

(81) Billas, I. M. L.; Tast, F.; Branz, W.; Malinowski, N.; Heinebrodt, M.; Martin, T. P.; Broero, M.; Marssobrio, C.; Parrinello, M. Experimental and Computational Studies of Si-doped Fullerenes *Eur. Phys. J. D* **1999,** *9*, 337-340.

(82) Hirsch, A. *Fullerenes and Related Structures*. Springer-Verlag Berlin Heidelberg: Berlin, Germany, 1999.

(83) Weiss, F. D.; Elkind, J. L.; O'Brien, S. C.; Curl, R. F.; Smalley, R. E. Photophysics of metal complexes of spheroidal carbon shells *J. Am. Chem. Soc.* **1988,** *110*, 4464-4465.

(84) Saunders, M.; Jimenez-Vazquez, H. A.; Cross, R. J.; Poreda, R. J. Stable Compounds of Helium and Neon: HeC_{60} and NeC_{60} *Science* **1993,** *259*, 1428.

(85) Johnson, R. D.; De Vries, M. S.; Salem, J.; Bethune, D. S.; Yannoni, C. S. Electron paramagnetic resonance studies of lanthanum-containing C_{82} *Nature* **1992,** *355*, 239-240.

(86) Beyers, R.; Kiang, C.-H.; Johnson, R. D.; Salem, J. R.; de Vries, M. S.; Yannoni, C. S.; Bethune, D. S.; Dorn, D.; Burbank, P.; Harich, K.; Stevenson, S. Preparation and structure of crystals of the metallofullerene $Sc_2@C_{84}$ *Nature* **1994,** *370*, 196-199.

(87) Takata, M.; Umeda, B.; Nishibori, E.; Sakat, M.; Saito, Y.; Ohno, M.; Shinohara, H. Confirmation by X-ray diffraction of the endohedral nature of the metallofullerene $Y@C_{82}$ *Nature* **1995,** *377*, 46.

(88) Laasonen, K.; Andreoni, W.; Parrinello, M. Structural and electronic properties of lanthanum-doped fullerene C_{82} ($La@C_{82}$) *Science* **1992,** *258*, 1916-1918.

(89) Nagase, S.; Kobayasi, K. Metallofullerenes MC_{82} (M = Sc, Y, and La). A theoretical study of the electronic and structural aspects *Chem. Phys. Lett.* **1993,** *214*, 57-63.

(90) Syamala, M. S.; Cross, R. J.; Saunders, M. ^{129}Xe NMR Spectrum of Xenon Inside C_{60} *J. Am. Chem. Soc.* **2002,** *124*, 6216-6219.

(91) Saunders, M.; Jimenez-Vazquez, H. A.; Cross, R. J. Incorporation of Heium, Neon, Argon, Krypton, and Xenon into Fullerenes Using High Pressure *J. Am. Chem. Soc.* **1994,** *116*, 2193-2194.

(92) DiCamillo, B. A.; Hettich, R. L.; Guiochon, G.; Compton, R. N.; Saunders, M.; Jimenez-Vazquez, H. A.; Khong, A.; Cross, R. J. Enrichment and Charaterization of a Noble Gas Fullerene: $Ar@C_{60}$ *J. Phys. Chem.* **1996,** *100*, 9197-9201.

(93) Saunders, M.; Cross, R. J. In *Endofullerenes: A New Family of Carbon Clusters*; Akasaka, T.,Nagase, S., Eds. Kluwer Academic Publishers: Dordrecht, The Netherlands, 2002; pp 1-12.

(94) Braun, T. The World Inside Fullerene Cages: The Physical Chemistry of Endohedral $X@C_n$ Compounds *ACH-Models Chem.* **1995,** *132*, 245-263.

(95) Gadd, G. E.; Elcombe, M. M.; Dennis, J.; Morrica, S.; Webb, N.; Cassidy, D.; Evans, P. J. Novel Rare Gas Interstitial Fullerenes of C_{70} *J. Phys. Chem. Solids* **1998,** *59*, 937-944.

(96) Ito, S.; Takeda, A.; Miyazaki, T.; Yokoyama, Y.; Saunders, M.; Cross, R. J.; Hakagi, H.; Berthet, P.; Dragoe, N. Kr Extended X-ray Absorption Fine Structure Study of Endohedral Kr@C_{60} *J. Phys. Chem.* **2004,** *108*, 3191-3195.

(97) Sears, D. N.; Jameson, C. J. Calculation of the 129Xe Chemical Shift in Xe@C_{60} *J. Chem. Phys.* **2003,** *118*, 9987-9989.

(98) Buhl, M.; Patchkovskii, S.; Thiel, W. Interaction Energies and NMR Chemical Shifts of Noble Gases in C_{60} *Chem, Phys. Lett.* **1997,** *275*, 14-18.

(99) Cherubini, A.; Bifone, A. Hyperpolarized Xenon in Biology. *Prog. Nucl. Magn. Reson. Spectrosc.* **2003,** *42*, 1-30.

(100) Knapp, C.; Dinse, K.-P.; Pietzak, B.; Waiblinger, M.; Weiginger, A. Fourier transform EPR study of N@C_{60} in solution *Chem, Phys. Lett.* **1997,** *272*, 433.

(101) Weiginger, A.; Waiblinger, M.; Pietzak, B.; Murphy, T. A. Atomic nitrogen in C_{60}: N@C_{60} *Appl. Phys. A* **1998,** *66*, 287.

(102) Murphy, T. A.; Pawlik, T.; Weiginger, A.; Hohne, M.; Alcala, R.; Spaeth, J.-M. Observation of Atomlike Nitrogen in Nitrogen-Implanted Solid C_{60} *Phys. Rev. Lett.* **1996,** *77*, 1075.

(103) Mauser, H.; van Eikema Hommes, N. J. R.; Clark, T.; Hirsch, A.; Pietzak, B.; Weiginger, A.; Dunsch, A. Stabilization of Atomic Nitrogen Inside C_{60} *Angew. Chem. Int. Ed. Engl.* **1997,** *36*, 2835.

(104) Pietzak, B.; Waiblinger, M.; Murphy, T. A.; Weiginger, A.; Hohne, M. D., E.; Dunsch, A. Buckminsterfullerene C_{60}: a chemical Faraday cage for atomic nitrogen *Chem, Phys. Lett.* **1997,** *279*, 259.

(105) Pietzak, B.; Weidinger, A.; Dinse, K.-P.; Hirsh, A. In *Endofullerenes: A New Family of Carbon Clusters*; Akasaka, T.,Nagase, S., Eds. Kluwer Academic Publishers: Dordrecht, The Netherlands, 2002; pp 13-66.

(106) Ltd., T. U. o. S. a. W. Physical Properties of Xenon. http://www.webelements.com/webelements/scholar/elements/xenon/physical.html (06/10/2004),

(107) Stevenson, S.; Rice, G.; Glass, T.; Harich, K.; Cromer, F.; Jordan, M. R.; Craft, J.; Hajdu, E.; Bible, R.; Olmstead, M. M.; Maitra, K.; Fischer, A. J.; Balch, A. L.; Dorn, H. C. Small-bandgap endohedral metallofullerenes in high yield and purity *Nature* **1999,** *401*, 55.

(108) Olmstead, M. M.; de Bettencourt-Dias, A.; Duchamp, J. C.; Stevenson, S.; Dorn, H. C.; Balch, A. L. Isolation and Crystallographic Characterization of $ErSc_2N@C_{80}$: an Endohedral Fullerene Which Crystallizes with Remarkable Internal Order. *J. Am. Chem. Soc.* **2000,** *122*, 12220-12226.

(109) Olmstead, M. M.; de Bettencourt-Dias, A.; Duchamp, J. C.; Stevenson, S.; Marciu, D.; Dorn, H. C.; Balch, A. L. Isolation and Structural Characterization of the Endohedral Fullerene $Sc_3N@C_{78}$ *Angew. Chem. Int. Ed. Engl.* **2001,** *40*, 1223-1227.

(110) Duchamp, J. C.; Demorter, A.; Fletcher, K. R.; Dorn, D.; Iezzi, E. B.; Glass, T.; Dorn, H. C. An Isomer of the Endohedral Metallofullerene $Sc_3N@C_{80}$ with D_{5h} Symmetry *Chem, Phys. Lett.* **2003,** *375*, 655-659.

(111) Kobayashi, K.; Nagase, S. In *Endofullerene: A New Family of Carbon Clusters*; Akasaka, T.,Nagase, S., Eds. Kluwer Academic Publishers: Dordrecht, The Netherlands, 2002; pp 99-119.

(112) Dunsch, L.; Krause, M.; Noack, J.; Georgi, P. Endohedral Nitride Cluster Fullerenes Formation and Spectroscopic Analysis of $L_{3-x}M_xN@C_{2n}$ *J. Phys. Chem. Solids* **2004,** *65*, 309-315.

(113) Kiang, C.-H.; van Loosdrecht, P. H. M.; Beyers, R.; Salem, J. R.; Bethune, D. S.; Goddard III, W. A.; Dorn, H. C.; Burbank, P.; Stevenson, S. Novel Structures from Arc-Vaporized Carbon and Metals: Single-layer Carbon Nanotubes and Metallofullerenes *Surf. Rev.Lett.* **1996,** *3*, 765-769.

(114) Shinohara, H.; Hayashi, N.; Sato, H. Direct STM imaging of spherical endohedral discandium fullerenes ($Sc_2@C_{84}$) *J. Phys. Chem.* **1993,** *97*, 13438-13440.

(115) Krause, M.; Wong, J.; Dunsch, L. Expanding the world of endohedral fullerenes-the $Tm_3N@C_{2n}$ ($39 \le n \le 43$) clusterfullerene family *Chem. Eur. J.* **2005,** *11*, 706-711.

(116) Yang, S.; Dunsch, L. A Large Family of Dysprosium-based Trimetallic Nitride Endohedral Fullerenes: $Dy_3N@C_{2n}$ ($39 \le n \le 44$) *J. Phys. Chem. B* **2005,** *109*, 12320-12328.

(117) Diener, M. D.; Alford, J. M. Isolation and Properties of Small-Bandgap Fullerenes *Nature* **1998,** *393*, 668-671.

(118) Ge, Z.; Duchamp, J. C.; Cai, T.; Gibson, H. W.; Dorn, H. C. Purification of Endohedral Trimetallic Nitride Fullerenes in a Single, Facile Step *J. Am. Chem. Soc.* **2005,** *127*, 16292-16298.

(119) Krause, M.; Kuzmany, H.; Georgi, P.; Dunsch, L.; Vietze, K.; Seifert, G. Structure and Stability of Endohedral Fullerene $Sc_3N@C_{80}$: A Raman, Infrared, and Theoretical Analysis *J. Chem. Phys.* **2001,** *115*, 6596-6605.

(120) Kobayashi, K.; Nagase, S.; Akasaka, T. Endohedral dimetallofullerenes $Sc_2@C_{84}$ and $La_2@C_{80}$. Are the metal atoms still inside the fullerene cages? *Chem. Phys. Lett.* **1996,** *261*, 502-506.

(121) Cai, T.; Xu, L.; Anderson, M. R.; Ge, Z.; Zuo, T.; Wang, X.; Olmstead, M. M.; Balch, A. L.; Gibson, H. W.; Dorn, H. C. Structure and enhanced reactivity rates of the D5h $Sc_3N@C_{80}$ and $Lu_3N@C_{80}$ metallofullerene isomers: the importance of the pyracylene motif. *J. Am. Chem. Soc.* **2006,** *128*, 8581-8589.

(122) Campanera, J. M.; Bo, C.; Olmstead, M. M.; Balch, A. L.; Poblet, J. M. Bonding within the Endohedral Fullerenes $Sc_3N@C_{78}$ and $Sc_3N@C_{80}$ as Determined by Density Functional Calculations and Reexamination of the Crystal Structure of $\{Sc_3N@C_{78}\}\times\{Co(OEP)\}\times1.5(C_6H_6)\times0.3(CHCl_3)$ *J. Phys. Chem. A* **2002,** *106*, 12356-12364.

(123) Wang, C.-R.; Kai, T.; Tomiyama, T.; Yoshida, T.; Kobayashi, Y.; Nishibori, E.; Takata, M.; Sakata, M.; Shinohara, H. C_{66} fullerene encaging a scandium dimer *Nature* **2000,** *408*, 426-427.

(124) Shi, Z.-Q.; Wu, X.; Wang, C.-R.; Lu, X.; Shinohara, H. Isolation and characterization of $Sc_2C_2@C_{68}$: a metal-carbide endofullerene with a non-IPR carbon cage *Angew. Chem. Int. Ed.* **2006,** *45*, 2107-2111.

(125) Kobayashi, K.; Sano, Y.; Nagase, S. Theoretical study of endohedral metallofullerenes: $Sc_{3-n}La_nN@C_{80}$ (n=0-3) *J. Comput. Chem.* **2001,** *22*, 1353-1358.

(126) Campanera, J. M.; Bo, C.; Olmstead, M. M.; Balch, A. L.; Poblet, J. M. Bonding within the Endohedral Fullerenes $Sc_3N@C_{78}$ and $Sc_3N@C_{80}$ as Determined by Density Functional Calculations and Reexamination of the Crystal Structure of $\{Sc_3N@C_{78}\}\times\{Co(OEP)\}\times1.5(C_6H_6)\times0.3(CHCl_3)$ *J. Phys. Chem. A* **2002,** *106*, 12356-12364.

(127) Melin, F.; Chaur, M. N.; Engmann, S.; Elliott, B.; Kumbhar, A.; Athans, A. J.; Echegoyen, L. The large $Nd_3N@C_{2n}$ ($40 \le n \le 49$) cluster fullerene family: Preferential templating of a C_{88} cage by a trimetallic nitride cluster *Angew. Chem. Int. Ed.* **2007,** *46* 9032-9035.

(128) Krause, M.; Liu, X.; Wong, J.; Pichler, T.; Knupfer, M.; Dunsch, L. The electronic and vibrational structure of endohedral $Tm_3N@C_{80}$ (I) fullerene--proof of an encaged Tm^{3+} *J. phys. chem. A* **2005,** *109*, 7088-7093.

(129) Yang, S.; Troyanov, S.; Popov, A.; Krause, M.; Dunsch, L. Deviation from the Planarity-a Large Dy_3N Cluster Encapsulated in an I_h-C_{80} Cage: An X-ray Crystallographic and Vibrational Spectroscopic Study *J. Am. Chem. Soc.* **2006,** *128*, 16733-16739.

(130) Yang, S.; Dunsch, L. Expanding the number of stable isomeric structures of the C_{80} Cage: A new fullerene $Dy_3N@C_{80}$ *Chemistry--A European Journal* **2006,** *12*, 413-419.

(131) Stevenson, S.; Phillips, J. P.; Reid, J. E.; Olmstead, M. M.; Rath, S. P.; Balch, A. L. Pyramidalization of Gd_3N inside a C_{80} cage. The synthesis and structure of $Gd_3N@C_{80}$ *Chem. Comm.* **2004,** *24*, 2814-2815.

(132) Krause, M.; Dunsch, L. Gadolinium nitride Gd_3N in carbon cages: The influence of cluster size and bond strength *Angew. Chem. Int. Ed.* **2005,** *44*, 1557-1560.

(133) Echegoyen, L.; Chancellor, C. J.; Cardona, C. M.; Elliott, B.; Rivera, J.; Olmstead, M. M.; Balch, A. L. X-Ray crystallographic and EPR spectroscopic characterization of a pyrrolidine adduct of $Y_3N@C_{80}$ *Chem. Comm.* **2006,** *25*, 2653-2655.

(134) Cardona, C. M.; Elliott, B.; Echegoyen, L. Unexpected Chemical and Electrochemical Properties of $M_3N@C_{80}$ (M = Sc, Y, Er) *J. Am. Chem. Soc.* **2006,** *128*, 6480-6485.

(135) Chen, N.; Fan, L.-Z.; Tan, K.; Wu, Y.-Q.; Shu, C.-Y.; Lu, X.; Wang, C.-R. Comparative Spectroscopic and Reactivity Studies of $Sc_{3-x}Y_xN@C_{80}$ (x = 0-3). *J. Phys. Chem. C* **2007,** *111*, 11823-11828.

(136) Gan, L.-H.; Yuan, R. Influence of cluster size on the structures and stability of trimetallic nitride fullerenes $M_3N@C_{80}$ *ChemPhysChem* **2006,** *7*, 1306-1131.

(137) Ichikawa, T.; Kodama, T.; Suzuki, S.; Fujii, R.; Nishikawa, H.; Ikemoto, I.; Kikuchi, K.; Achiba, Y. Isolation and characterization of a new isomer of $Ca@C_{72}$ *Chem. Lett.* **2004,** *33*, 1008-1009.

(138) Wan, T. S. M.; Zhang, H.-W.; Nakane, T.; Xu, Z.; Inakuma, M.; Shinohara, H.; Kobayashi, K.; Nagase, S. Production, Isolation, and Electronic Properties of Missing Fullerenes: $Ca@C_{72}$ and $Ca@C_{74}$ *J. Am. Chem. Soc.* **1998,** *120*, 6806-6807.

(139) Reich, A.; Panthoefer, M.; Modrow, H.; Wedig, U.; Jansen, M. The Structure of $Ba@C_{74}$ *J. Am. Chem. Soc.* **2004,** *126*, 14428-14434.

(140) Cao, B.; Hasegawa, M.; Okada, K.; Tomiyama, T.; Okazaki, T.; Suenaga, K.; Shinohara, H. EELS and ^{13}C NMR characterization of pure $Ti_2@C_{80}$ metallofullerene *J. Am. Chem. Soc.* **2001,** *123*, 9679-9680.

(141) Tan, K.; Lu, X. Ti2C80 is more likely a titanium carbide endohedral metallofullerene $(Ti_2C_2)@C_{78}$ *Chem. Comm.* **2005**, 4444-4446.

(142) Huang, H.; Ata, M.; Yoshimoto, Y. Cu@C_{60} formation in rf-plasma and ring-current induced magnetism of C_{60} *Chem. Comm.* **2004**, 1206-1207.

(143) Elliott, B.; Yang, K.; Rao, A. M.; Arman, H. D.; Pennington, W. T.; Echegoyen, L. A reassignment of the EPR spectra previously attributed to Cu@C_{60} *Chem. Comm.* **2007**, 2083-2085.

(144) Ettl, R.; Chao, I.; Diederich, F.; Whetten, R. L. Isolation of C_{76}, a chiral (D_2) allotrope of carbon *Nature* **1991**, 353.

(145) Diederich, F.; Whetten, R. L.; Thilgen, C.; Ettl, R.; Chao, I.; Alvarez, M. M. Fullerene isomerism: isolation of C_{2v}-C_{78} and D_3-C_{78} *Science* **1991,** *254*, 1768-1770.

(146) Kikuchi, K.; Nakahara, N.; Wakabayashi, T.; Honda, M.; Matsumiya, H.; Moriwaki, T.; Suzuki, S.; Shiromaru, H.; Saito, K.; Isolation and identification of fullerene family: the carbon seventy-six-, seventy-eight, eighty-two-, eighty-four, ninety-, and ninety-six-atom molecules (C_{76}, C_{78}, C_{82}, C_{84}, C_{90}, and C_{96}) *Chem Phys. Lett.* **1992,** *188*, 177-180.

(147) Kikuchi, K.; Nakahara, N.; Wakabayashi, T.; Suzuki, S.; Shiromaru, H.; Miyake, Y.; Saito, K.; Ikemoto, I.; Kainosho, M.; Achiba, Y. NMR characterization of isomers of C_{78}, C_{82} and C_{84} fullerenes *Nature* **1992,** *357*, 142-145.

(148) Taylor, R.; Langley, G. J.; Avent, A. G.; Dennis, J. S.; Kroto, H. W.; Walton, D. R. M. Carbon-13 NMR spectroscopy of fullerenes C_{76}, C_{78}, C_{84} and mixtures of C_{86}-C_{102}; anomalous chromatographic behavior of C_{82}, and evidence for $C_{70}H_{12}$. *J. Chem. Soc. Perkin Trans. 2: Phys. Org. Chem.* **1993,** *6*, 1029-1036.

(149) Lian, Y.; Yang, S.; Yang, S. Revisiting the Preparation of La@C_{82} (I and II) and La_2@C_{80}: Efficient Production of the "Minor" Isomer La@C_{82} (II) *Journal of Physical Chemistry B* **2002,** *106*, 3112-3117.

(150) Suzuki, T.; Maruyama, Y.; Kato, T.; Kikuchi, K.; Nakao, Y.; Achiba, Y.; Kobayashi, K.; Nagase, S. Electrochemistry and ab initio study of the dimetallofullerene $La_2@C_{80}$ *Angew. Chem. Int. Ed.* **1995,** *34*, 1094-1096.

(151) Kobayashi, K.; Nagase, S.; Akasaka, T. A theoretical study of C_{80} and $La_2@C_{80}$ *Chem. Phys. Lett.* **1995,** *245*, 230-236.

(152) Manolopoulos, D. E.; Fowler, P. W. Structural proposals for endohedral metal-fullerene complexes *Chem. Phys. Lett.* **1991,** *187*, 1-7.

(153) Fowler, P. W.; Ceulemans, A. Electron Deficiency of the Fullerenes *J. Phys. Chem.* **1995,** *99*, 508-510.

(154) Fowler, P. W.; Zerbetto, F. Charging and equilibration of fullerene isomers. *Chem. Phys. Lett.* **1995,** *243*, 36-41.

(155) Alvarez, M. M.; Gillan, E. G.; Holczer, K.; Kaner, R. B.; Min, K. S.; Whetten, R. L. La_2C_{80},: A Soluble Dimetallofullerene *J. Phys. Chem.* **1991,** *95*, 10561-10563.

(156) Akasaka, T.; Nagase, S.; Kobayashi, K.; Walchli, M.; Yamamoto, K.; Funasaka, H.; Kako, M.; Hoshino, T.; Erata, T. ^{13}C and ^{139}La NMR studies of $La_2@C_{80}$: first evidence for circular motion of metal atoms in endohedral dimetallofullerenes *Angew. Chem. Int. Ed.* **1997,** *36*, 1643-1645.

(157) Nishibori, E.; Takata, M.; Sakata, M.; Taninaka, A.; Shinohara, H. Pentagonal-dodecahedral La_2 charge density in [80-I_h]fullerene: $La_2@C_{80}$ *Angew. Chem. Int. Ed.* **2001,** *40*, 2998-2999.

(158) Shinohara, H.; Sato, H.; Ohkohchi, M.; Ando, Y.; Kodama, T.; Shida, T.; Kato, T.; Saito, Y. Encapsulation of a scandium trimer in C_{82} *Nature* **1992,** *357*, 52-54.

(159) Stevenson, S.; Dorn, H. C.; Burbank, P.; Harich, K.; Sun, Z.; Kiang, C. H.; Salem, J. R.; DeVries, M. S.; van Loosdrecht, P. H. M. Isolation and Monitoring of the Endohedral Metallofullerenes $Y@C_{82}$ and $Sc_3@C_{82}$: Online Chromatographic Separation with EPR Detection *Anal. Chem.* **1994,** *66*, 2680-2685.

(160) Iiduka, Y.; Wakahara, T.; Nakahodo, T.; Tsuchiya, T.; Sakuraba, A.; Maeda, Y.; Akasaka, T.; Yoza, K.; Horn, E.; Kato, T.; Liu, M. T. H.; Mizorogi, N.; Kobayashi, K.; Nagase, S. Structural Determination of Metallofullerene Sc_3C_{82} Revisited: A Surprising Finding. *J. Am. Chem. Soc.* **2005,** *127*, 12500-12501.

(161) Nishibori, E.; Terauchi, I.; Sakata, M.; Takata, M.; Ito, Y.; Sugai, T.; Shinohara, H. High-resolution analysis of $(Sc_3C_2)@C_{80}$ metallofullerene by third generation synchrotron radiation X-ray powder diffraction *J. phys. chem. B* **2006,** *110*, 19215-19219.

(162) Wang, C.-R.; Inakuma, M.; Shinohara, H. Metallofullerenes $Sc_2@C_{82}$(I, II) and $Sc_2@C_{86}$(I, II): isolation and spectroscopic studies *Chem. Phys. Lett.* **1999,** *300*, 379-384.

(163) Wang, C.-R.; Kai, T.; Tomiyama, T.; Yoshida, T.; Kobayashi, Y.; Nishibori, E.; Takata, M.; Sakata, M.; Shinohara, H. A scandium carbide endohedral metallofullerene: $(Sc_2C_2)@C_{84}$ *Angew. Chem. Int. Ed.* **2001,** *40*, 397-399.

(164) Yamamoto, E.; Tansho, M.; Tomiyama, T.; Shinohara, H.; Kawahara, H.; Kobayashi, Y. ^{13}C-NMR Study on the Structure of Isolated $Sc_2@C_{84}$ Metallofullerene. *J. Am. Chem. Soc.* **1996,** *118*, 2293-2294.

(165) Iiduka, Y.; Wakahara, T.; Nakajima, K.; Tsuchiya, T.; Nakahodo, T.; Maeda, Y.; Akasaka, T.; Mizorogi, N.; Nagase, S. ^{13}C NMR spectroscopic study of scandium dimetallofullerene, $Sc_2@C_{84}$ vs. $Sc_2C_2@C_{82}$ *Chem. Comm.* **2006**, 2057-2059.

(166) Nishibori, E.; Ishihara, M.; Takata, M.; Sakata, M.; Ito, Y.; Inoue, T.; Shinohara, H. Bent (metal)2C2 clusters encapsulated in $(Sc_2C_2)@C_{82}$(III) and $(Y_2C_2)@C_{82}$(III) metallofullerenes *Chem. Phys. Lett.* **2006,** *433*, 120-124.

(167) Wang, C.-R.; Kai, T.; Tomiyama, T.; Yoshida, T.; Kobayashi, Y.; Nishibori, E.; Takata, M.; Sakata, M.; Shinohara, H. A scandium carbide endohedral metallofullerene: $(Sc_2C_2)@C_{84}$ *Angew. Chem. Int. Ed.* **2001,** *40*, 397-399.

(168) Shinohara, H.; Sato, H.; Ohkohchi, M.; Ando, Y.; Kodama, T.; Shida, T.; Kato, T.; Saito, Y. Encapsulation of a scandium trimer in C_{82} *Nature* **1992,** *357*, 52-54.

(169) Takata, M.; Nishibori, E.; Sakata, M.; Inakuma, M.; Yamamoto, E.; Shinohara, H. Triangle Scandium Cluster Imprisoned in a Fullerene Cage *Phys. Rev. Lett.* **1999,** *83*, 2214-2217.

(170) Kobayashi, K.; Nagase, S. Theoretical study of structures and dynamic properties of $Sc_3@C_{82}$ *Chem. Phys. Lett.* **1999,** *313*, 45-51.

(171) Iiduka, Y.; Wakahara, T.; Nakahodo, T.; Tsuchiya, T.; Sakuraba, A.; Maeda, Y.; Akasaka, T.; Yoza, K.; Horn, E.; Kato, T.; Liu, M. T. H.; Mizorogi, N.; Kobayashi, K.; Nagase, S. Structural Determination of Metallofullerene Sc_3C_{82} Revisited: A Surprising Finding *J. Am. Chem. Soc.* **2005,** *127*, 12500-12501.

(172) Nishibori, E.; Terauchi, I.; Sakata, M.; Takata, M.; Ito, Y.; Sugai, T.; Shinohara, H. High-Resolution Analysis of $(Sc_3C_2)@C_{80}$ Metallofullerene by Third Generation Synchrotron Radiation X-ray Powder Diffraction *J. Phys. Chem. B* **2006,** *110*, 19215-19219.

(173) Prassides, K.; Keshavarz-K, M.; Hummelen, J.-C.; Andreoni, W.; Giannozzi, P.; Beer, E.; Bellavia, C.; Cristofolini, L.; Gonzalez, R.; Lappas, A.; Murata, Y.; Malecki, M.;

Srdanov, V.; Wudl, F. Isolation, Structure, and Electronic Calculations of the Heterofullerene Salt $K_6C_{59}N$ *Science* **1996,** *271*, 1833-1835.

(174) Averdung, J.; Luftmann, H.; Schlachter, I.; Mattay, J. Aza-Dihydro[60]fullerene in the Gas Phase. A Mass-Spectrometric and Quantumchemical Study *Tetrahedron* **1995,** *51*, 6977-6982.

(175) Ying, Z. C.; Hettich, R. L.; Compton, R. N.; Haufler, R. E. Synthesis of Nitrogen-doped Fullerenes by Laser Ablation *J. Phys. B: At. Mol. Opt. Phys.* **1996,** *29*, 4935-4942.

(176) Yu, R.; Zhan, M.; Cheng, D.; Yang, S.; Liu, Z.; Zheng, L.-S. Simultaneous Synthesis of Carbon Nanotubes and Nitrogen-Doped Fullerenes in Nitrogen Atmosphere *J. Phys. Chem.* **1995,** *99*, 1818-1819.

(177) Wang, X.; Zuo, T.; Olmstead, M. M.; Duchamp, J. C.; Glass, T. E.; Cromer, F.; Balch, A. L.; Dorn, H. C. Preparation and Structure of $CeSc_2N$ @ C_{80} : An Icosahedral Carbon Cage Enclosing an Acentric $CeSc_2N$ Unit with Buried f Electron Spin. *J. Am. Chem. Soc.* **2006** *128* 8884-8889.

(178) Murata, Y.; Murata, M.; Komatsu, K. 100% Encapsulation of a Hydrogen Molecule into an Open-Cage Fullerene Derivative and Gas-Phase Generation of H_2@C_{60} *J. Am. Chem. Soc.* **2003,** *125*, 7152 - 7153.

(179) Kato, H.; Kanazawa, Y.; Okumura, M.; Taninaka, A.; Yokawa, T.; Shinohara, H. Lanthanoid Endohedral Metallofullerenols for MRI Contrast Agents. *J. Am. Chem. Soc.* **2003,** *125*, 4391-4397.

(180) Bolskar, R. D.; Benedetto, A. F.; Husebo, L. O.; Price, R. E.; Jackson, E. F.; Wallace, S.; Wilson, L. J.; Alford, J. M. First Soluble M@C_{60} Derivatives Provide Enhanced Access

to Metallofullerenes and Permit in Vivo Evaluation of $Gd@C_{60}$[C(COOH)2]10 as a MRI Contrast Agent *J. Am. Chem. Soc.* **2003,** *125*, 5471-5478.

(181) Zuo, T.; Beavers, C. M.; Duchamp, J. C.; Campbell, A.; Dorn, H. C.; Olmstead, M. M.; Balch, A. L. Isolation and Structural Characterization of a Family of Endohedral Fullerenes Including the Large, Chiral Cage Fullerenes $Tb_3N@C_{88}$ and $Tb_3N@C_{86}$ as well as the I_h and D_{5h} Isomers of $Tb_3N@C_{80}$. *J. Am. Chem. Soc.* **2007,** *129*, 2035-2043.

(182) Stevenson, S.; Lee, H.; Olmstead, M. M.; Kozikowski, C.; Stevenson, P.; Balch, A. L. Preparation and Crystallographic Characterization of a New Endohedral, $Lu_3N@C_{80}$5(o-xylene), and Comparison with $Sc_3N@C_{80}$5 (o-xylene) *Chem. Eur. J.* **2002,** *8*, 4528-4535.

(183) Stevenson, S.; Phillips, J. P.; Reid, J. E.; Olmstead, M. M.; Rath, S. P.; Balch, A. L. Pyramidalization of Gd_3N inside a C_{80} cage. The synthesis and structure of $Gd_3N@C_{80}$ *Chem. Comm.* **2004,** *24*, 2814-2815.

(184) Krause, M.; Liu, X.; Wong, J.; Pichler, T.; Knupfer, M.; Dunsch, L. The electronic and vibrational structure of endohedral $Tm_3N@C_{80}$ (I) fullerene--proof of an encaged Tm^{3+} *J. phys. chem. A* **2005,** *109*, 7088-7093.

(185) Ge, Z.; Duchamp, J. C.; Cai, T.; Gibson, H. W.; Dorn, H. C. Purification of Endohedral Trimetallic Nitride Fullerenes in a Single, Facile Step *J. Am. Chem. Soc.* **2005,** *127*, 16292-16298.

(186) Stevenson, S.; Burbank, P.; Harich, K.; Sun, Z.; Dorn, H. C.; van Loosdrecht, P. H. M.; deVries, M. S.; Salem, J. R.; Kiang, C.-H.; Johnson, R. D.; Bethune, D. S. $La_2@C_{72}$: Metal-Mediated Stabilization of a Carbon Cage. *J. Phys. Chem. A* **1998,** *102*, 2833-2837.

(187) Cotton, F. A.; Wilkinson, G. *Advanced Inorganic Chemistry*. 5th ed. ed.; Wiley & Son, Inc.: New York, 1988; p 955.

(188) Iezzi, E. B.; Duchamp, J. C.; Fletcher, K. R.; Glass, T. E.; Dorn, H. C. Lutetium-based Trimetallic Nitride Endohedral Metallofullerenes: New Contrast Agents. *Nano Lett.* **2002,** *2*, 1187-1190.

(189) MacFarlane, R. M.; Bethune, D. S.; Stevenson, S.; Dorn, H. C. Fluorescence spectroscopy and emission lifetimes of Er^{3+} in $Er_xSc_{3-x}N@C_{80}$ (x=1-3) *Chem. Phys. Lett.* **2001,** *343*, 229-234.

(190) Krause, M.; Dunsch, L. Gadolinium nitride Gd_3N in carbon cages: The influence of cluster size and bond strength *Angew. Chem. Int. Ed.* **2005,** *44*, 1557-1560.

(191) Krause, M.; Wong, J.; Dunsch, L. Expanding the world of endohedral fullerenes-the $Tm_3N@C_{2n}$ ($39 \leq n \leq 43$) clusterfullerene family *Chem. Eur. J.* **2005,** *11*, 706-711.

(192) Guhr, K. I.; Greaves, M. D.; Rotello, V. M. Reversible Covalent Attachment of C_{60} to a Polymer Support *J. Am. Chem. Soc.* **1994,** *116*, 5997-5998.

(193) Brennan, T. D.; Scheidt, W. R.; Shelnutt, J. A. New crystalline phase of (octaethylporphinato)nickel(II): effects of .pi.-.pi. interactions on molecular structure and resonance Raman spectra *J. Am. Chem. Soc.* **1988,** *110*, 3919 - 3924

(194) Meyer, E. F., Jr. *Acta Crystallogr., Sect. B* **1972,** *28*, 2162.

(195) Echegoyen, L.; Chancellor, C. J.; Cardona, C. M.; Elliott, B.; Rivera, J.; Olmstead, M. M.; Balch, A. L. X-Ray crystallographic and EPR spectroscopic characterization of a pyrrolidine adduct of $Y_3N@C_{80}$ *Chem. Comm.* **2006,** *25*, 2653-2655.

(196) Sun, D.; Liu, Z.; Guo, X.; Xu, W.; Liu, S. Electronic structure and fluorescent property of endohedral terbium fullerenes *Chinese Science Bulletin* **1997,** *42*, 1798-1802.

(197) Nath, S.; Pal, H.; Sapre, A. V.; Bubnov, V. P.; Estrin, Y. I.; Parnyuk, T. A.; Koltover, V. K. Aggregation of Endometallofullerene Y@C_{82} in Polar Solvents *Fullerenes, Nanotubes, and Carbon Nanostructures* **2004,** *12*, 53-57.

(198) MacFarlane, R. M.; Bethune, D. S.; Stevenson, S.; Dorn, H. C. Fluorescence spectroscopy and emission lifetimes of Er^{3+} in $Er_xSc_{3-x}N@C_{80}$ (x=1-3) *Chem. Phys. Lett.* **2001,** *343*, 229-234.

(199) Dawson, W. R.; Kropp, J. L.; Windsor, M. W. Internal-energy transfer efficiencies in Eu^{3+} and Tb^{3+} chelates using excitation to selected ion levels *J. Chem. Phys.* **1966** *45*, 2410-2418.

(200) Luo, L.; Lai, W. P.-W.; Wong, K.-L.; Wong, W.-T.; Li, K.-F.; Cheah, K.-W. Green upconversion fluorescence in terbium coordination complexes. *Chem. Phys. Lett.* **2004,** *398*, 372-376.

(201) Ringer, D. P.; Etheredge, J. L.; Dalrymple, B. L.; Niedbalski, J. S. Fluorescence of phosphotyrosine-terbium(III) complexes. *Biochem. Biophys. Res. Comm.* **1990,** *168*, 267-273.

(202) Kong, D. Y.; Wang, Z. L.; Lin, C. K.; Quan, Z. W.; Li, Y. Y.; Li, C. X.; Lin, J. Biofunctionalization of CeF_3:Tb^{3+} nanoparticles. *Nanotechnology* **2007,** *18*, 075601/075601-075601/075607.

(203) Zhao, Y.-L.; An, X.-P.; Zhao, F.-Y.; Yan, L.; Bao, J.-R. Fluorescence property of the complexes of the RE(Eu-Tb)-18-crown-6-p-phthalic acid. *Faguang Xuebao* **2004,** *25*, 551-555.

(204) Kato, D.; Shimoda, K. Fluorescence spectrum of Tb^{3+} in the phosphorus oxychloride-tin(IV) chloride liquid. *Japanese J. Appl. Phys.* **1970,** *9*, 581-582.

(205) Pichler, T.; Knupfer, M.; Golden, M. S.; Haffner, S.; Friedlein, R.; Fink, J.; Andreoni, W.; Curioni, A.; Keshavarz-K, M.; Bellavia-Lund, C.; Sastre, A.; Hummelen, J.-C.; Wudl, F. On-ball doping of fullerenes: the electronic structure of $C_{59}N$ dimers from experiment and theory *Phys. Rev. Lett.* **1997,** *78*, 4249-4252.

(206) Vostrowsky, O.; Hirsch, A. Heterofullerenes *Chem. Rev.* **2006,** *106*, 5191-5207.

(207) Kim, K.-C.; Hauke, F.; Hirsch, A.; Boyd, P. D. W.; Carter, E.; Armstrong, R. S.; Lay, P. A.; Reed, C. A. Synthesis of the $C_{59}N^+$ Carbocation. A Monomeric Azafullerene Isoelectronic to C_{60} *J. Am. Chem. Soc.* **2003,** *125*, 4024.

(208) Becke, A. D. A new mixing of Hartree-Fock and local-density-functional theories *J. Chem. Phys.* **1993,** *98*, 1372-1377.

(209) Becke, A. D. Density-functional thermochemistry. III. The role of exact exchange *J. Chem. Phys.* **1993,** *98*, 5648-5652.

(210) Stephens, P. J.; Devlin, F. J.; Chabalowski, C. F.; Frisch, M. J. Ab Initio Calculation of Vibrational Absorption and Circular Dichroism Spectra Using Density Functional Force Fields *J. Phys. Chem.* **1994,** *98*, 11623-11627.

(211) Lee, C.; Yang, W.; Parr, R. G. Development of the Colle-Salvetti correlation-energy formula into a functional of the electron density *Phys. Rev. B* **1988,** *37*, 785-789.

(212) Wortman, D. E. Analysis of the Ground Term of Triply Ionized Terbium in Calcium Tungstate *Phys. Rev.* **1968,** *175*, 488-498.

(213) Gafurov, M. R.; Ivanshin, V. A.; Kurkin, I. N.; Rodionova, M. P.; Keller, H.; Gutmann, M.; Staub, U. *J. Magn. Reson.* **2003,** *161*, 210-214.

(214) Knight, L. B., Jr.; Woodward, R. W.; Van Zee, R. J.; Weltner, W., Jr. Properties of scandium (Sc_3), yttrium (Y_3), and scandium (Sc_{13}) molecules at low temperatures, as determined by ESR. *J. Chem. Phys.* **1983,** *79*, 5820-5827.

(215) Kikuchi, K.; Nakao, Y.; Suzuki, S.; Achiba, Y.; Suzuki, T.; Maruyama, Y. Characterization of the Isolated $Y@C_{82}$ *J. Am. Chem. Soc.* **1994,** *116*, 9367-9368.

(216) Godbout, N.; Salahub, D. R.; Andzelm, J.; Wimmer, E. Optimization of Gaussian-type basis sets for local spin density functional calculations. Part I. Boron through neon, optimization technique and validation *Can. J. Chem.* **1992**, *70*, 560.

(217) Benjamin, S. C.; Ardavan, A.; Briggs, A. G.; A., B. D.; Gunlycke, D.; Jefferson, J.; Jones, M. A.; Leigh, D. F.; Lovett, B. W.; Khlobystov, A. N.; Lyon, S. A.; Morton, J. J.; Porfyrakis, K.; Sambrook, M. R.; Tyryshkin, A. M. *J. Phys.-Cond. Matter* **2006,** *18*, S867-S883.

(218) Twamley, J. Quantum-cellular-automata quantum computing with endohedral fullerenes *Phys. Rev. A* **2003,** *67*, 052318: 052311-052312.

(219) Lloyd, S. A Potentially Realizable Quantum Computer *Science* **1993,,** *261*, 1569-1571.

(220) Lukin, M. D.; Hemmer, P. R. Quantum Entanglement via Optical Control of Atom-Atom Interactions *Phys. Rev. Lett.* **2000,** *84*, 2818-2821.

(221) Kaliszan, R. *Quantitative Structure-Chromatographic Retention Relationships*. John Wiley & Sons: New York, 1987; Vol. 93, p 8.

(222) Taylor, L. T.; Calvey, E. M. Supercritical fluid chromatography with FT-IR detection. *Anal. Supercrit. Fluids: Extr. Chromatogr.* **1992**, 178-189.

(223) Taylor, L. T. Trends in supercritical fluid chromatography: 1997 *J. Chromatogr. Sci.* **1997,** *35*, 374-382.

(224) Jinno, K.; Bidlingmeyer, B.; Rabel, F. In *Chromatography Fundamentals, Applications, and Troubleshooting*; Walker, J. Q., Ed. Preston Publications: Niles, 1996; p 81.

(225) Fuchs, D.; Rietschel, H.; Michel, R. H.; Fischer, A.; Weis, P.; Kappes, M. M. Extraction and Chromatographic Elution Behavior of Endohedral Metallofullerenes: Inferences Regarding Effective Dipole Moments *J. Phys. Chem.* **1996,** *100*, 725-729.

(226) Murray, J. S.; Peralta-Inga, Z.; Politzer, P.; Ekanayake, K.; Lebreton, P. *Int. J. Quantum Chem.* **2001,** *83*, 245-254.